Aus dem ‚Mannheim Center for Translational Neuroscience' (MCTN)
der Universität Heidelberg und dem
‚Center for Mass Spectrometry and Optical Spectroscopy' (CeMOS)
(Leiter: Prof. Dr. rer. nat. Carsten Hopf) der Hochschule Mannheim

Spatial Probabilistic Mapping of Biomolecular Ensembles in Tissue via Mass Spectrometry Imaging

Inauguraldissertation
zur Erlangung des Doctor scientiarum humanarum (Dr. sc. hum)
an der
Medizinischen Fakultät Mannheim
der Ruprecht-Karls-Universität
zu
Heidelberg

vorgelegt von
Denis Abu Sammour

aus
Rostov
2023

Dekan: Prof. Dr. med. Sergij Goerdt
Referent: Prof. Dr. rer. nat. Carsten Hopf

*To my wife Mariam, the co-first author
of all my life achievements . . .*

Contents

List of Abbreviations

MS(I)	Mass Spectrometry (Imaging)
MALDI	Matrix-Assisted Laser Desorption/Ionization
LC-MS	Liquid Chromatography-Mass Spectrometry
IS	Internal Standard
SIMS	Secondary Ion Mass Spectrometry
DESI	Desorption Electrospray Ionization
m/z	Mass-to-charge Ratio
MOI	Molecule-of-interest
POI	Peak-of-Interest
FFPE	Formalin-fixed and Paraffin-embedded
MPM	Molecular Probabilistic Map
CSR	Complete Spatial Randomness
CT-MPM	cross-tissue Molecular Probabilistic Map
CPPM	Collection Projection Probability Map
TOF	Time-of-Flight
FTICR	Fourier Transform Ion Cyclotron Resonance
UHPLC	Ultra-High Performance Liquid Chromatography
ESI-QTOF	Electrospray-ionization Quadrupole Time-of-Flight
FWHM	Full-width at Half-maximum
R$_{FWHM}$	Mass Resolving Power obtained from the peak's FWHM
PCA	Principal Component Analysis
NNMF	Non-negative Matrix Factorization
t-SNE	t-distributed Stochastic Neighbor Embedding
TEC	Tissue Extinction Coefficient
GIST	Gastrointestinal Stromal Tumor
GB	Glioblastoma
IDH-WT	Isocitrate Dehydrogenase-Wild Type
IDH-MUT	Isocitrate Dehydrogenase-Mutant
FTIR	Fourier transform infrared
H&E	Hematoxylin and Eosin
Imatinib-D8	Deuterated imatinib
DHB	2,5-Dihydroxybenzoic acid
9AA	9-Aminoacridine
ITO	Indium-tin-oxide

1,5-DAN	1,5-Diaminonaphthalene
Trp	Tryptophan
R-2-HG	R-2-Hydroxyglutarate
PhCCAA	4-Phenyl-α-Cyanocinnamic Acid Amide
timsTOF	Trapped Ion Mobility Spectrometry Time-of-Flight
LOESS	Locally-Estimated Scatter-plot Smoothing
TIC	Total Ion Count
MFC	Median Fold Change
SPP	Spatial Point Pattern
KDE	Kernel Density Estimation
eCDF	Empirical Cumulative Distribution Function
DSC	Dice Similarity Coefficient
arb. units	Arbitrary Units
LOD	Limit of Detection
LOQ	Limit of Quantification
MSE	Mean Squared Error
RSE	Residual standard error
SNR	Signal to Noise Ratio
TKI	Tyrosine Kinase Inhibitor
CI	Confidence Interval
MRI	Magnetic Resonance Imaging
MRMS	Magnetic Resonance Mass Spectrometry

Chapter 1

Introduction

Tissues are a major focus of clinical research and diagnosis for a wide range of diseases. Understanding the complex biomolecular manifestations of disease within tissues by characterizing its morphology and biomolecular content paves the way for exploring fundamental mechanisms of pathogenesis and for identifying diagnostic and prognostic biomarkers and potential therapeutic targets.[1] Among the many tissue-investigation techniques, mass spectrometry imaging (MSI) has evolved into a label-free core technology for visualization and spatially-resolved *ex vivo* analysis of biomolecules directly from tissue samples.[2] Biomolecules are essential cellular components that regulate different processes important for function, communication and cellular structure. These include, for instance, proteins, glycans, metabolites and lipids which can be readily probed by MSI.[3]

Among the different MSI technologies, matrix-assisted laser desorption/ionization (MALDI) MSI has seen a steep growth and adoption in various biomedical research areas.[4] The first demonstration of MALDI-based time-of-flight (TOF) MSI has been conducted in 1995 by Gusev et al., where MALDI MSI was used to image the position of various compounds (including dyes and peptides) from thin layer chromatography plates.[5] In a landmark study published in 1997, Caprioli et al. introduced a MALDI-MSI measurement of a tissue section for the first time.[6] Some years later, Stoeckli et al. went on to publish one of the most highly cited studies in the field of MSI, which presented MALDI-MSI protein ion images obtained from brain and brain tumor tissues, achieving a spatial resolution of 25 μm.[7] In the recent years the field of MSI has been rapidly expanding, as enormous advances in speed, sensitivity and spatial resolution of MSI instruments have been witnessed.[8] Due to its high versatility and capability of measuring different biomolecular classes, MALDI-MSI has seen a widespread adoption in the fields of spatial proteomics, metabolomics, lipidomics and drug discovery.[3] In the latter case, MALDI-MSI has found its way into pharmaceutical research and development, where disposition of drugs and their formulations can be monitored alongside their pharmacodynamic and toxic effects.[9–12] Importantly, MALDI MSI has been successfully applied for probing tissue-biomolecular profiles particularly in cancer research. Here, MALDI MSI has helped in uncovering molecular

mechanisms concerning tumor microenvironment, immunosupression and metabolic activity.[13–15]

Strong advances in MSI technology have also been accompanied by rapid development of cutting-edge computational analysis tools and machine learning methods custom-tailored for MSI data. MSI data for tissues is typically memory-demanding sparse hyperspectral imaging data encoding molecular profiles (mass spectra) of spatial units (pixels) arranged on a spatial grid.[16] To address the increasing need to handle and analyze this complex data, several open source tools and packages have been developed (R/python) providing researchers and bioinformaticians with valuable methods for MSI data handling, cleaning and pre-processing.[17–23] Computational methods concerning dimensionality reduction, clustering and segmentation have been proposed continuously accompanying the ever-increasing complexity of MSI data.[24] Machine and deep learning approaches have also been applied for dimensionality reduction, peak learning and tissue classification and profiling.[25–28]

Reproducibility of research methods, data and findings has been gaining ever more increasing attention in science and is subject to constant discussions.[29,30] In this regard, the MSI community invested and continues to invest efforts to improve the reproducibility and integrity of MSI experiments. Site-to-site MSI experiments' reproducibility has been thoroughly investigated by comparing results obtained from MALDI MSI measurements of clinical tissue samples collected at different facilities, measured at different sites with standard protocols.[31] Computational and statistical scores have been proposed to compare standard sample preparation protocols for processing formaline-fixed, paraffin-embedded human biopsy tissues prior to MSI measurements.[32] Quality control[22,23,33], standard data formats[34], spectral alignment[35,36] and normalization methods[37–39] have also been continuously developed to ensure reproducibility, data comparability and reduce technical variability. Batch effects, i.e. systemic sources of technical variability affecting MSI studies particularly for tissue cohorts, have been thoroughly studied and described in a recent study providing concrete recommendations aimed to downplaying the impact of this undesired phenomena on the reliability of MSI experiments.[40]

MSI has also been increasingly applied in pharmaceutical research for quantifying tissue-drug content. Until recently MSI was described as a semi-quantitative technology and has been predominantly used for the spatial assessment of compounds' presence in tissues and their relative change in concentrations across samples.[16,41,42] However, several studies have attempted to bridge this gap describing MSI-based quantification protocols and demonstrating that MSI can achieve quantification with high agreement with liquid chromatography–mass spectrometry (LC-MS), the gold-standard for quantification in tissues.[43,44] To account for the inherently high technical variability of MALDI-MSI data, quantification based on tissue mimetic models or compound dilution series spotted onto tissue, as well as signal normalization against stable isotope-labeled internal standards (IS) and the calculation of tissue extinction

coefficients were introduced.[45,46] Inspired by LC-MS-based quantification, linear calibration models have been predominantly used in MALDI-MSI-based quantification.[3] However, batch effects and the limited understanding of the ionization pathways, in-source fragmentation and cluster formation still hinder a wider adoption of MALDI-MSI for quantification in (clinical) pharmacology, specifically when it comes to tissue cohorts.[21,40] While Several computational tools, which provide quantitation capabilities, have been previously proposed[47,48], developing computational and analytical methods specifically suited for spatial quantification via MSI is an active area of research and development[49–51].

1.1 Mass Spectrometry Imaging Basic Principles

The mass spectrometer is comprised of three distinct components: the ion source, which ionizes the analytes (i.e. molecules such as proteins, glycans, metabolites, lipids or drugs); the mass analyzer, which separates the analytes according to their molecular weight; and the detector, which identifies the various analytes present in the sample.[4] There are three primary desorption/ionization methods that are commonly utilized for obtaining MSI data from different surfaces: secondary ion mass spectrometry (SIMS), MALDI MS, and desorption electrospray ionization (DESI) MS. The chosen ionization technique determines which analytes can be detected (e.g., polar, non-polar, small molecules or proteins) as well as the spatial resolution of the MSI measurement.[52] SIMS was the first technique used to acquire images from various surfaces including tissue sections, and it is used to analyze the composition of solid surfaces and thin films by sputtering the surface of the specimen with a focused primary ion beam and collecting and analyzing ejected secondary ions by MS.[4] Instead of irradiating the sample with a focused ion beam, in MALDI MSI the biological tissues are irradiated with a laser beam after being coated with with a matrix, typically an organic acid, which absorbs the laser energy and aids molecular ionization.[6] On the other hand, DESI imaging, which was introduced in 2004[53], involves the application of an electrically charged solvent mist (electrospray) onto the sample causing the ionization and desorption of the surface molecules which are then transported into the mass analyzer inlet.

MALDI-based MSI has seen a wide-spread adoption of this technology in the fields of proteomics, metabolomics, lipidomics and drug discovery. It is considered to be a soft ionization technique that produces ions of biomolecules with minimal fragmentation and primarily single-charged ions when induced by the energy delivered by a laser.[3,54] MALDI MSI starts with the deposition of a dissolved chemical matrix onto a tissue sample. This matrix is a chemical solution that, upon crystallization, possesses high energy absorbance for a certain laser wavelength. The deposited matrix solution mixes with the sample causing the biomolecular tissue content to dissolve in it depending on the matrix type. To avoid imaging artifacts arising from matrix application, the matrix is homogeneously applied across the tissue sample, which is

commonly carried out by robotic sprayers[55] but also via sublimation[56] or inkjet[57] or 3D printers[58]. After solvents evaporate, the matrix crystallizes together with tissue biomolecules which are then trapped within the co-crystals. By selecting different matrices and depending on the technology used (e.g. MALDI-TOF or MALDI-FTICR), different biomolecule classes can be targeted in MSI measurements.[59–61] Moreover, the physical properties of a matrix, e.g., pH, proton affinity and peak wavelength absorbance, directly affect the observed analyte sensitivity.[62] 2,5-Dihydroxybenzoic acid (DHB) is the most commonly used MALDI matrix that offers adequate sensitivity for various analyte classes in positive ion mode detection, while 9-Aminoacridine (9AA) has been more often used for the detection of low molecular weight compounds in negative ion mode and 1,5-Diaminonaphthalene (DAN) has been shown to provide high sensitivity for many lipid classes in both positive and negative ion modes.[63] A comprehensive review of commonly employed MALDI matrices in MALDI MSI of lipids could be found in the two studies of Leopold et al.[64,65]

The ionization process starts by irradiating the co-crystallized sample with a pulsating UV laser of a short wavelength. Two laser types have been predominantly used in MALDI MSI; namely, N_2 lasers with a wavelength of 337 nm and, the more recent, Nd:YAG lasers with a wavelength of 355 nm.[66] The matrix absorbs the delivered laser energy leading to a phase change, in which neutral and ionized matrix molecules, matrix clusters and ionized biomolecules move into the gas phase. While in gas phase, ions such as H^+, Na^+ and K^+ are transferred between the matrix and the analyte leading to the formation of analyte ions, or "adducts".[67] The generated cations could then be measured in positive ion mode detection. Likewise, negative ions could also be created by abstracting H^+ from the analyte or through fragmentation during ionization, which could then be measured in negative ion mode detection.[64] Several models have been proposed to explain this process such as the gas-phase photoionization and the lucky survivor models.[54,68] However, ionization pathways, in-source fragmentation and cluster formations are still not completely understood and are open fields for investigation.[16,69]

Charged matrix molecules and biomolecules are then passed to mass analyzers where these could be measured based on their *m/z* property. Several types of mass analyzers exist, e.g., TOF, ion mobility spectrometry (IMS) and Fourier transform ion cyclotron resonance (FTICR) mass spectrometers.[70] The basic principle of MALDI TOF mass analyzers is depicted in **Figure 1.1**. In such systems, charged ions are accelerated towards a detector within an electric field inside a vacuum tube. Once the ions pass through a charged grid, they move freely in a field-free space, known as the drift zone, where the separation of the ions according to their *m/z* is achieved. The ions with lower mass reach the detector faster. The use of a reflector instead of a linear TOF mass analyzer can further enhance peak resolution by extending the flight trajectory. The *m/z* value of an ion is then determined by measuring the
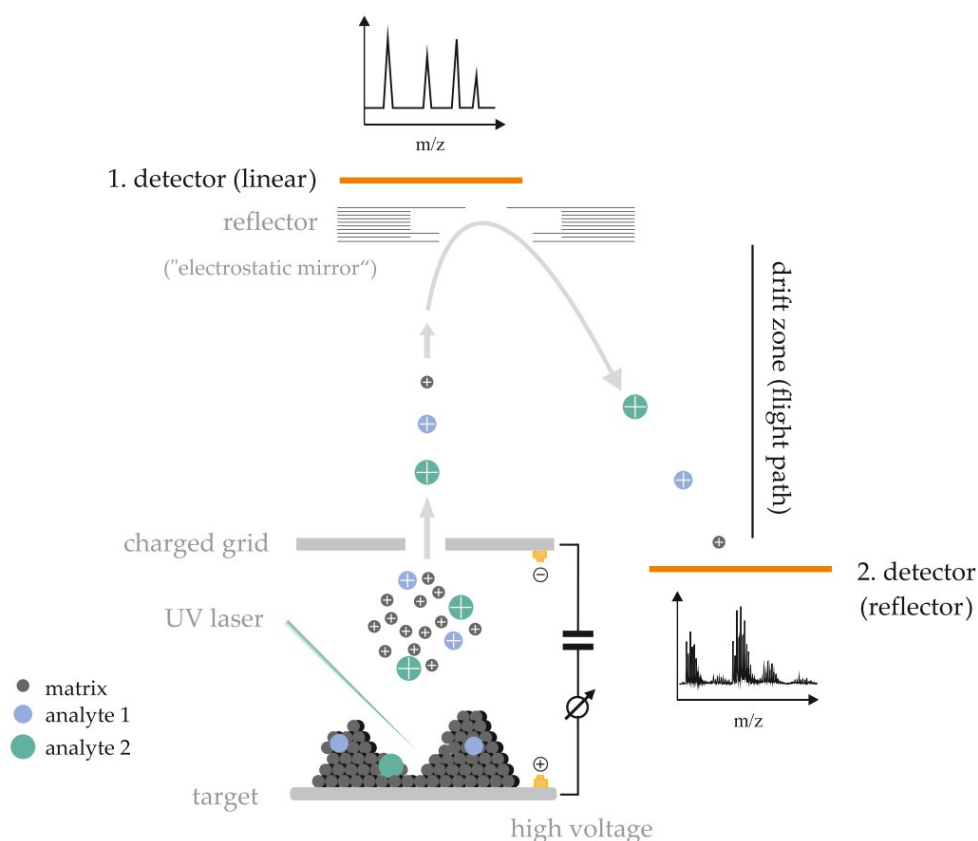
FIGURE 1.1: The basic principle of matrix-assisted laser desorption/ionization time-of-flight (MALDI-TOF) process occurring in the mass spectrometer for positive ionization. The mass resolving power can be improved by further extending the flight path using an electrostatic mirror (reflector). Reproduced from Leopold et al.[64] under the conditions of the Creative Commons Attribution (CC BY) license (http://creativecommons.org/licenses/by/4.0/).

time it takes for that ion to traverse the distance from source to detector, i.e. time-of-flight.[64] Modern TOF mass analyzers offer high acquisition speeds, high sensitivity and moderate mass resolving power (10-50k). In IMS-MS, an additional "filtration step" is introduced between the ion source and the mass analyzer (which is typically a TOF mass analyzer) where ions are separated based on their mobility through a buffer gas in a millisecond timescale inside an ion mobility drift tube.[71] A similar ion mobility concept called trapped ion mobility spectrometry (TIMS) propels ions via a gas flow and an electrical field, acting against the ion-flow, stops them from moving beyond a position defined by the ion's mobility.[71]

Fourier Transform-based mass analyzers such as the FTICR mass spectrometers determine ion's *m/z* based on the cyclotron frequency of the ions in a fixed magnetic field. The basic principle of FTICR mass analyzers is depicted in **Figure 1.2**. In such systems, the mass analyzer is an ion cyclotron resonance (ICR) cell situated in the center of a superconducting magnet. Within the ICR cell, the homogeneous magnetic field induces a circular motion in the trapped ion packets with a cyclotron frequency which is inversely proportional to the ion mass. These ion packets are then resonantly

FIGURE 1.2: The basic principle of data acquisition with Fourier transform ion cyclotron resonance (FTICR) mass spectrometers. Reproduced from van Agthoven et al.[72] under the conditions of the Creative Commons Attribution (CC BY) license (http://creativecommons.org/licenses/by/4.0/).
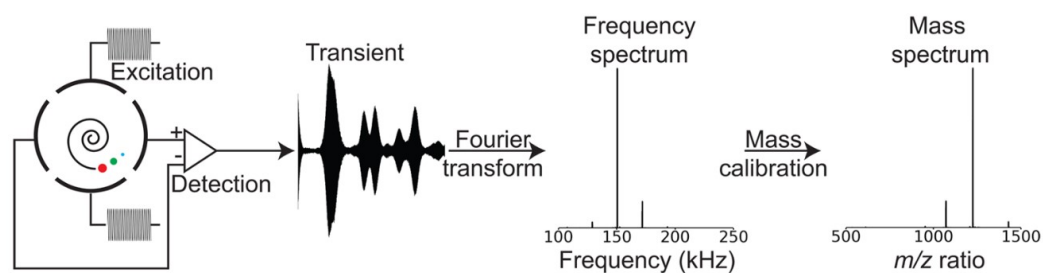
excited with a radio-frequency voltage applied to the excitation plates causing them to form coherent packet formations. Fourier transformation of the transient leads to a frequency spectrum showing peaks at the frequencies of the ions. The mass spectrum is obtained by converting the cyclotron frequencies into *m/z* values.[72] These analyzers offer high sensitivity and ultra-high mass resolving power (> 1.5M at *m/z* 400) but with slower acquisition rates.[70,73]

The mass resolving power of a mass spectrometer could be regarded as the primary characteristic when choosing the right modality for a certain MSI-based application. For instance, to properly distinguish isobaric compounds inherent to the complexity of biological samples, a high resolving power at full-width at half-maximum (R_{FWHM} > 300k at *m/z* 400) is required in the absence of an upstream separation method (such as ion mobility).[74] The theoretical modeling of the mass resolving power is challenging and is different for the different mass spectrometer types. Marshall et al.[75] reported that for FTICR mass spectrometers R_{FWHM} inversely scales with m, where m is the ion mass. On the other hand, the theoretical formulation of R_{FWHM} for TOF mass spectrometers is completely different and is relatively constant across the mass range.[76] For a more detailed description, please see **section 3.3** in **Chapter 3**.

1.2 Mass Spectrometry Imaging Data

The data acquisition principle of MALDI MSI is depicted in **Figure 1.3**. A matrix-coated tissue section mounted on a conductive glass slide is irradiated by a UV-laser applied in a raster-like scanning. Although a high lateral (spatial) resolution MALDI-MSI reaching down to 1.4 µm per pixel (i.e. sub-cellular scale) has been previously reported[77], typically MALDI MSI experiments employ a lateral resolution ranging from 200 µm down to 20 µm.[2] The resulting three-dimensional dataset is represented by a so-called datacube with spatial *x,y*-coordinates and a mass-to-charge ratio (*m/z*) depth coordinate representing the molecular information encoded into spectra of intensities, such that for every *x,y*-position (pixel) a mass spectrum is recorded and
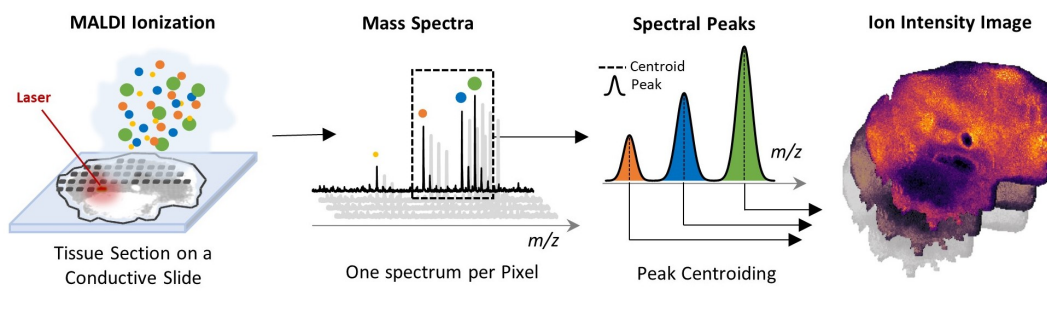
FIGURE 1.3: MALDI MSI data acquisition. A tissue section mounted on a conductive slide is coated with a MALDI matrix and rastered with an ionizing laser beam. This results in hyperspectral imaging data with each pixel location encoding the detected ionized molecular content at that laser spot. Afterwards, the recorded mass spectra are centroided and binned. An ion intensity image represents relative intensities of the ion across all pixels.

for every *m/z* an *m/z*-specific ion intensity image is rendered which highlights the spatial distribution of the molecule underlying that particular *m/z*.[16]

MSI data of tissues is typically memory-demanding sparse hyperspectral imaging data. Its dimensionality (i.e. number of *m/z* bins) depends on the analyzer and is usually in the order of 10^3 for TOF analyzers, 10^4 for QTOF analyzers, and over 10^4 for Fourier transformation-based analyzers.[16] Most vendors of mass spectrometers often include centroiding in their measurement platforms, which reduces data size and facilitates data storage and handling especially for ultra-high-resolving power analyzers such as FTICR or Orbitrap mass spectrometers. Spectral centroiding (i.e. peak picking) is a process of converting a continuous spectral peak (also called profile data) corresponding to an ion to a centroid *m/z* value with an associated intensity, typically defined as the area under the peak or its maximum (see **Figure 1.3**).[16] For most measurement platforms and software packages, centroiding is based on SNR≥3, i.e. only peaks whose intensity is higher than 3 times the calculated noise level are retained. Historically, this seems to come from the IUPAC guidelines[78] for defining the limit of detection for quantifying trace elements using analytical methods which is normally set to $\mu + 3\sigma$, where μ and σ are the mean and standard deviation of the signal of the blank (i.e. detector noise). This allows for a confidence level of >99% that a detected signal above that threshold is not a random event (three-sigma rule).

For any molecule-of-interest (MOI), an ion image can be generated to inspect its spatial distribution within tissue morphology. Ion images, i.e. false color renderings of *m/z* intervals of interest, are generated typically by summing up all observed (centroided or profile) ion intensities, e.g., a peak-of-interest (POI), with identical weights (i.e. uniform mass-window weighting) within a user-defined mass-range around a certain theoretical *m/z* value representing the MOI (**Figure 1.4**).[79,80]

Owing to its sparsity and complexity, MSI data often undergoes certain data "cleaning" and pre-processing procedures depending on the acquisition platform and application. These may include intensity normalization, baseline subtraction,
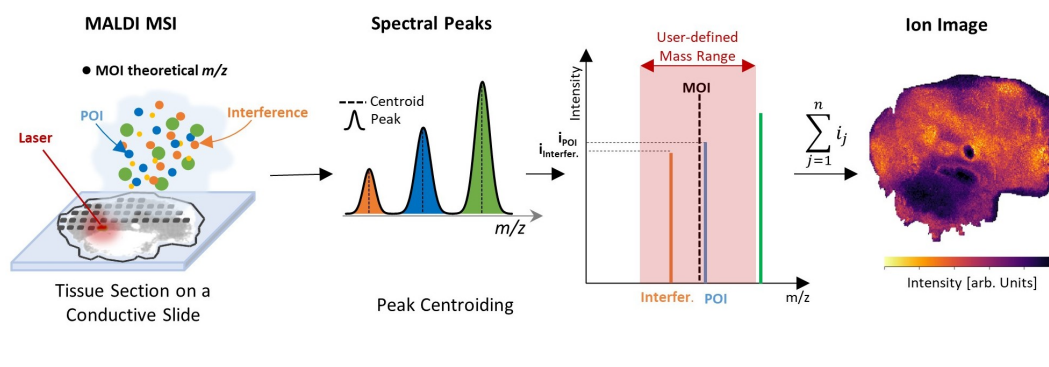
FIGURE 1.4: Ion image generation in MSI. Typically, an ion image is generated by summing up (with identical weights) all observed ion intensities, e.g., a peak-of-interest (POI; blue circle and line) within a user-defined mass-range (red area) around the a certain theoretical *m/z* value representing a molecule-of-interest (MOI; black circle and dashed line). If set too-high, the user-defined mass-range could contain a background peak (orange) which might interfere with the detected POI signal.

smoothing, peak detection (centroiding), peak alignment or binning.[23,39] For targeted applications, i.e. imaging for a specific MOI like a drug, the analysis and interpretation of MSI data often include ion image generation and visualization as described above.[9–12] However, MSI has also been used in untargeted imaging applications where the correlation and colocalization of biomolecule ensembles is of interest, e.g., multivariate inspection of spectral similarities across tissues or multivariate classification for classifying tissues or spectra according to a specific property or test. Applied untargeted analysis on MSI data could be broadly categorized into two main categories: on one hand, unsupervised multivariate analysis where spatial segmentation methods such as *k*-means clustering[81], spatially-aware clustering[82] and spatial shrunken centroids[83] and dimensionality reduction techniques such as principal component analysis (PCA)[84], non-negative matrix factorization (NNMF)[85], probabilistic latent semantic analysis (pLSA)[86] or t-distributed stochastic neighbor embedding (t-SNE)[87] are used to deduce tissue morphological similarities.[24] On the other hand, supervised multivariate analysis where spectra or tissues are labeled based on a specific (e.g., clinically) relevant attribute and fed into classification models to establish classifiers that can distinguish spectra or tissues based on their molecular content.[28,88–91]

Several open source tools and packages[20–22,92,93] as well as stand-alone software[47,48] and computational platforms[23,94] have been developed for MSI data that provide researchers and bioinformaticians with valuable methods for MSI data handling, cleaning and pre-processing. Most notably, *Cardinal*[18], *MALDIquant*[17] and *rMSI*[19] R packages have been widely adopted in the MSI community. The unified imzML data format[34], proposed in 2012, has been instrumental in streamlining data analysis pipelines for MSI data. Based on the mass spectrometry data standard mzML[95], imzML enhanced exchangeability of MSI data and analysis tools of different MSI vendors and research labs.

1.3 Reproducibility and Batch Effects

It is well known that the quality and information content of MALDI MSI data strongly depends on numerous factors related to the preparation and acquisition processes. Sample preparation, ion suppression, homogeneity of matrix application, spatial resolution, analyte delocalization, and the availability of community-wide standardized protocols have been identified as primary factors affecting reproducibility of MSI experiments.[40,96] More often than not, MALDI MSI experiments also suffer from technical variability which includes signal intensity variations, mass inaccuracies, chemical and instrumental noise, as well as loss of data integrity during data conversion processes.[37,39]

As MALDI MSI is increasingly applied in large-scale clinical and pharmacological studies where cohorts of tissues are analyzed, the collective effect of the above factors result in what has been recently called batch effects.[40,97] Batch effects are systemic sources of technical variability affecting MSI data of tissue cohorts measured in batches which could be categorized into different levels, e.g., day-to-day (time factor), location and operator. While the previously mentioned categories are common to most analytical techniques, some are specific to MSI which include pixel-to-pixel, section-to-section and slide-to-slide batch effects.[40]

Pixel-to-pixel batch effects mainly arise at the sample preparation step. Since MALDI-MSI requires the application of a MALDI matrix, inhomogeneous matrix application and crystallization leads to spatially varying matrix-related analyte suppression.[37] Spatial differences in tissue chemical properties and biological content also affects the extraction and ionization efficiency of ions resulting in regional ion suppression effects which were found to be pronounced in MALDI-based ionization.[98] Systematic biases in data acquisition can also lead to increased pixel-to-pixel batch effects such as continuous decrease in detector sensitivity, gradual evaporation of matrices during long acquisitions or accumulation of residual material in the ion source.[40,99] Moreover, uneven sample topology and stage tilt can lead to pixel-to-pixel mass shifts, i.e., variations of the *m/z* of the same ion(s), which degrades mass resolution and mass accuracy in MSI data.[100] Differences in tissue topology can also cause spatially-dependent variations in the laser focus, fluence and ablation spot size resulting in inhomogeneous pixel-to-pixel ionization throughout the sample.[101]

Section-to-Section batch effects have similar causes as for the pixel-to-pixel case. Here, tissue sections at different locations on the measurement slide might receive a lower/higher exposure to laser irradiation and/or matrix application, but also differences in tissue section thickness[102] as well as differences in tissue processing[103] and storage[104] may lead to systematic variations on a section-to-section basis. However, slide-to-slide variability can be considered the highest source of variation for any MSI measurement acquired within a single location (lab) since not only pixel-to-pixel and section-to-section variations accumulate, but this might also be significantly

compounded by differences in sample preparation and time factors.[103] These accumulated effects can reach to a point where true biological response is completely masked, especially in the biomarker discovery applications where the outcome is extremely sensitive to disturbances in ion intensities.[40]

Addressing the challenge of batch effects and technical variability has been the subject of many studies in the recent years. Site-to-site MSI experiments reproducibility has been thoroughly investigated by comparing results obtained from imaging clinical tissue samples collected at different facilities and measured at different sites with a standard protocol.[31] Computational and statistical scores have been proposed to compare standard sample preparation protocols for processing formaline-fixed, paraffin-embedded human biopsy tissues prior to MSI.[32] Hardware improvements have been introduced to MALDI-MSI where modified optics can correct for coarse height differences on-the-fly[101] and a new hardware configuration can perform MALDI-based imaging of tissues in atmospheric pressure conditions[77]. Cost-effective open-source hardware has been developed for matrix deposition for MALDI MSI-based experiments that allows for development and sharing of matrix deposition and sample preparation protocols across labs.[58,105]

Quality control procedures has been continuously introduced into the MSI domain. For instance, Gustaffson et al.[106] formulated reporting standards specifically suited for MSI experiments which try to capture and standardize accurate reporting of both experiments and the resulting data. Fractional factorial design has been employed to optimize standard operating procedures for sample preparation[107], matrix deposition[108] and MALDI MSI acquisition parameters[109]. Condina et al.[110] went on to suggest the use of egg white as an external control for peptide and N-glycan MALDI-MSI to monitor detector performance and sample preparation throughout the experiment. On the other hand, Palmer et al.[80] created a gold-standard set using collective expert judgments of 80 MSI experts to rate the relative quality between 52 pairs of ion images from MALDI-TOF-MSI data of rat brain coronal sections, which was then used to evaluate image-based computational quality measures including local coefficient of variation, local signal-to-noise ratio and spatial chaos[111], among others. Other tools and platforms for quality control have been proposed which can screen for low quality spectra in MALDI MSI data[22], provide an overview of mass accuracy across the tissue sample[23] and establish unified and transparent MSI data processing pipelines based on FAIR (findable, accessible, interoperable, and reusable) data sharing principles[33].

Systematic mass misalignment has been observed early on in MALDI MSI data which could arise from i) uneven sample topography, ii) limits in the precision of the ion detector and iii) differences in the ions' initial velocities at the onset of the MALDI ionization process.[35,100] Spectral alignment and mass recalibration methods have been proposed as a remedy in which the chemical noise background observed in MALDI peptide imaging is used as a reference for recalibration[35] or, in a more

recent study, a data-dependent internal recalibration is used based on endogenous lipids and metabolites that are identified across a set of biologically similar tissues and are used as internal calibrants.[36]

Finally, the ion intensities observed in MALDI MSI data are known to be sensitive to the various forms of batch effects described above. Common methods for MSI data normalization typically involve computing a scalar, e.g., spectrum total ion count (TIC) or root mean squared (RMS), to be used as a normalization factor for each single spectrum.[37,39] Veselkov et al.[94,112] proposed a normalization method based on median fold change (MFC), which better suits inter-sample tissue comparisons. More recently, Boskamp et al.[38] reported a cross-normalization technique based on computing spectral intensity profiles that capture the statistical distribution of spectral intensities as a function of mass and then transforming spectral intensities to make their statistical distributions more similar. This cross-normalization method was evaluated in inter-lab and cross-protocol scenarios showing promising results.[38]

1.4 Quantification in Mass Spectrometry Imaging

MSI is now being used more frequently in pharmaceutical studies to measure tissue-drug content. Until recently, MALDI MSI was referred to be a semi-quantitative technology and has been predominantly used for the spatial assessment of compounds' presence in tissues and their relative change in concentrations across samples.[16,41,42] Quantitative information can still be extracted with the right conditions, processing, and software, though the degree of accuracy must be carefully monitored and rigorously examined. Tissue heterogeneity, ion suppression and ionization efficiency, sample topography, batch effects (see **section 1.3**) and other factors are all regarded as significant challenges in this field.[3]

A number of studies have made an effort to bridge this gap by testing quantification protocols based on MALDI MSI and demonstrated that MALDI MSI can produce quantification results with a high level of concordance with liquid chromatography-mass spectrometry (LC-MS), which is considered the benchmark for quantification in tissues.[43] Signal normalization against a stable isotope-labeled version of the MOI (e.g. drug) or a structurally similar compound to the MOI as an internal standards (IS) has been essential in elevating the reliability of MALDI MSI-based quantification. Deuterated versions of the MOI were frequently used by mixing the IS with the matrix solution and homogeneously spraying over the slide prior to sectioning or over the tissue sections after sectioning. The IS can then be used to correct for the MOI signal intensity (calculated as MOI intensity/IS intensity) pixel by pixel across tissue sections.[44,46] To account for inherent tissue heterogeneity and inhomogeneous ion suppression, Hamm et al.[45] proposed the use of tissue extinction coefficient (TEC) when quantifying olanzapine and propranolol in rat and mouse whole body sections by MALDI-MSI. In this method, a homogeneous amount of a compound mixed with

the matrix is sprayed over the tissue section and, once measured, TEC is calculated for every tissue morphology part by dividing the average intensity of the compound on tissue by the average intensity of the compound on a glass slide. The regional TEC values can then be used as a normalization factor.[45]

Setting up analyte calibration curves is an important step for obtaining quantification. Based on spotted dilution series of the MOI, calibration curves are calculated which can be used for back-calculating MOI concentrations or amounts from detected MSI signal levels in tissues.[43] To limit the impact of slide-to-slide batch effects, researchers have adopted a same-slide on-tissue spotting technique where MOI dilution spots are applied on the same or separate "control" sections adjacent to the tissue under study and measured within the same imaging run. This "control" can be a serial section of the tissue under study, but researchers have also used other controls such as liver tissue which is known to be homogeneous. Researchers have also created techniques where the standards are spiked into tissue homogenates to boost the homogeneity of the areas where the standards are spotted. These homogenates are put into a mold and are then frozen, sectioned, and positioned next to the imaged section.[113,114] Developing computational methods specifically suiting spatial quantification via MSI is an active area of research and development. Davoli et al. have contributed a comprehensive review focusing on the field of spatial localization and quantification of drugs in human tissues via MSI in clinical pharmacology.[115]

1.5 Mass Spectrometry Imaging in Cancer Research

Recent developments in analytical techniques, collectively known as "omics", significantly improved our understanding of cellular metabolism. These techniques provide valuable insights into metabolic profiles of healthy, as well as tumor tissues. MALDI MSI employs soft ionization for the extraction and analysis of endogenous biomolecules without destroying the sample, which allows for combining molecular imaging with simultaneous histological evaluations for studying numerous different cancer types in many different studies including brain, breast, lung, ovarian, prostate and gastrointestinal cancers.[1,2]

One of the main areas where MALDI MSI is applied is tissue samples classification. For instance, molecular MS profiles of tissues have been used in distinguishing colorectal tumor from normal tissue[88], discriminating breast from pancreatic cancer metastasis in formalin-fixed paraffin-embedded (FFPE) tissues[116], classification of epithelial ovarian cancer[117], histo-molecular differentiation of renal cancer subtypes[118] and discrimination of renal oncocytoma from renal cell cancer subtypes and normal kidney tissues.[119] MALDI MSI has also been used to uncover clinically relevant mass signatures that correlate with colorectal cancer status, grade and survival in large-scale tissue microarrays.[120]

Owing to its spatial imaging capabilities, MALDI MSI has been also applied to uncover intratumoral heterogeneity, a well-known factor in tumor resistance to treatment in gastric and breast carcinoma.[121] It has also found application in uncovering molecular mechanisms concerning tumor microenvironment, immunosupression and metabolic activity.[14,15]

Lastly, targeted measurement of anti-cancer drugs and their metabolites with MALDI MSI has been previously reported, which allowed for the investigation of pharmacokinetics and pharmacodynamics of drugs in tumor and surrounding tissues, making it possible to gain insight into the penetration of treatment drugs into their target tumor tissues.[115,122]

In this work, gastrointestinal stromal tumor (GIST), isocitrate dehydrogenase-wild type (IDH-WT) glioblastoma (GB) and IDH-mutant (IDH-MUT) and -WT glioma tissue samples were used to showcase the proposed computational methods described in **Chapter 3**. The following two sections provide a brief description of these tumor types.

1.5.1 Gastrointestinal Stromal Tumor (GIST)

GIST is a type of mesenchymal tumor that arises in the gastrointestinal tract, primarily in stomach (60%) and small intestine (30%) but also as a metastatic tumor elsewhere in the abdominal cavity, as well as in liver, but rarely in lungs and distant peripheral sites. It is considered a rare disease estimated to occur with a frequency of 14-20 per million.[123] GISTs are thought to arise from the interstitial cells of Cajal and are characterized by the expression of the KIT protein (CD117), a transmembrane receptor tyrosine kinase that plays a key role in cell proliferation and survival. Mutations in the KIT gene are present in the majority of GISTs and result in constitutive activation of the KIT protein, leading to uncontrolled cell growth and proliferation.[124]

The standard treatment for GISTs is surgical resection when feasible, with the goal of achieving complete resection of the tumor. In patients with high-risk or metastatic disease, treatment with tyrosine kinase inhibitors (TKIs) such as imatinib, sunitinib, and regorafenib has been shown to be effective in controlling tumor growth and improving overall survival. Imatinib is also considered for adjuvant treatment in order to minimize the risk of tumor resurgence. However, GISTs are prone to imatinib resistance, which is mainly attributed to secondary somatic mutations in the receptor tyrosine kinases KIT, the gene product of the protooncogene c-kit, or the platelet-derived growth factor receptor alpha (PDGFRA). For this reason, the genetic characterization of GIST is important as it denotes the effectiveness of targeted drug therapies.[125]

MALDI MSI analysis of GIST samples have been previously reported where multiple workflows for dewaxing, antigen retrieval and on-slide digestion of formalin-fixed and paraffin-embedded (FFPE) GIST tissue samples have been compared using

proposed MSI-based computational and statistical scores.[32] Another study used GIST tissue samples to evaluate a novel multimodal acquisition guidance system where upstream tissue segmentation using Fourier transform infrared (FTIR) microscopy was used to guide downstream high resolution MALDI MSI acquisition.[81]

1.5.2 Glioma

Glioma is the most common type of primary brain tumor in humans. The exact cellular origin of glioma is unknown with recent studies suggesting that astrocytes, oligodendrocyte progenitor cells, and neural stem cells could all serve as the cell of origin. GB is its most aggressive form of glioma (WHO grade IV)[126] which is usually rapidly fatal, with a short median overall survival rate of 12–15 months only. While lower-grade gliomas (WHO grade II and III gliomas)[126] appear less aggressive at the time of diagnosis, they eventually progress into the malignant phase within 5–10 years.[127] The standard treatment, if feasible, is gross total resection, followed by radiotherapy and administration of Temozolamide, a chemotherapy drug. Temozolamide is an alkylating agent that is more toxic to cancer cells due to inhibition of tumor cell DNA replication.[127,128]

IDH-WT gliomas lack mutations in the IDH type-1 or type-2 genes. Until recently, GB was classified into two subtypes: IDH-WT and IDH-MUT, with IDH-WT representing the majority (approximately 90%) of GB cases.[128,129] The most recent WHO classification of central nervous system tumors, reclassified IDH-MUT GB into IDH-MUT astrocytoma (WHO grade 4).[126,130] The main purpose of introducing this change was to clarify the prognosis of the diagnosis; patients with this morphology and lacking mutations in IDH have a worse overall prognosis compared to other tumors with similar morphology but with those mutations. This change also emphasized that this tumor entry is specific to the adult population commonly found in elderly patients.[131]

The identification of molecular subtypes, including IDH-WT and IDH-MUT gliomas, has provided important insights into the genetic and molecular characteristics of these tumors.[13,128] Recently published landmark studies in this area have laid ground for uncovering GB's molecular and cellular landscapes aligning individual histologic features with genomic alterations and gene expression patterns[132], established a comprehensive approach for the DNA methylation-based classification of central nervous system tumors across all entities and age groups[133] and uncovered immunosuppressive alterations of tryptophan metabolism in GB linking that to Aryl hydrocarbon receptor activation driven by tryptophan-catabolic enzymes.[134]

MALDI MSI has been previously used to probe the complex and heterogeneous histological environment of GB. Researchers were able to discriminate neovascularization from necrosis via MALDI MSI, an important factor in differentiating GM from anaplastic astrocytoma.[135] In a spatially-resolved MALDI-based multi-omics study,

researchers uncovered evidence of tumor-host interdependence, which results in spatially exclusive adaptive transcriptional programs.[136] Other studies involving MALDI MSI uncovered heterogeneity of tryptophan catabolism across GB tissues[137] and provided further insight into the altered metabolic landscape of IDH-MUT gliomas by profiling the distribution of metabolites at high anatomical spatial resolution.[14] This multi-omics setup together with MALDI MSI has been successfully used to investigate transcriptional alterations, metabolic and lipidomic adaptation and alterations of tumor cells, which can aid in suggesting therapeutic targets and evaluating treatment effects.[138]

Chapter 2

Aims

2.1 Motivation

The fundamental concept in mass spectrometry imaging (MSI) data processing, the conversion of raw data into ion images for visualization, spatial interpretation and molecular analysis, has not changed since the inception of the technology. Ion images, i.e. false color renderings of mass-to-charge ratio (*m/z*) intervals of interest, are used as the fundamental investigation tool in MSI for conveying the spatial distribution of molecules-of-interest (MOIs, e.g. metabolites, drugs, lipids or proteins) within biological tissues often compared to external histopathology annotations. Ion images are also used as a gold-standard for validating the outcomes of computational and machine learning methods in biomarker discovery applications in MSI.[1,87,139] However, the generated ion images can be prone to technical artifacts, user input- and user perception-bias.[40,79] For instance, in a pharmaceutical study, an incorrectly assigned mass-window width by the end-user for rendering ion images of a certain drug, which if set too high, could include interfering noise and other interfering background signals. Current procedures for rendering ion images from raw MSI data typically do not include built-in methods that account for mass accuracy and instrument- and measurement-dependent mass resolving power. Another even more drastic source of bias originates in user's visual perception and interpretation of the MOI's spatial distribution and penetration into tissue sub-compartments, a judgment that is usually based on user's perception of intensity differences within the image. The color-coding of these intensities is also a source of bias as it was shown that different color-coding schemes could result in differing interpretation of MOIs' spatial distributions.[79] Filtering, cross-normalization and collective judgement approaches have been shown to improve the outcome of ion image interpretation, but they do not offer a definitive solution.[37,38,80,140]

Moreover, it is not uncommon in MSI studies to encounter experiments that perform comparison of drug or metabolite distribution in test- versus reference tissues, e.g., those dosed with drugs or carrying mutations versus controls.[13,141] Here, again, ion images are used to visually compare color-coded intensity distribution of MOIs in both test and reference tissues put side-by-side in a single image plane.

Unfortunately, this procedure is affected by the same pitfalls described above for the single ion image. To remedy this qualitative comparison approach, scientists typically resort to pooling signal intensities of the generated ion images to generate box/violin-plots and perform statistical significance testing. This approach, however, completely disregards the spatial dimension of the MSI experiment, making it impossible to trace the tissue morphology where the molecule (e.g. drug) has a statistically significant difference.

Furthermore, simultaneous mapping of metabolite ensembles within a single ion image is lacking. In such situations, scientists typically resolves to encoding signal intensities of MOIs using the RGB (red, green and blue) color model thus creating a composite RGB ion images in the process.[9,79] This procedure, however, can only visualize three MOIs at a time. Methods for spatial probing of tissue characteristics such as ion milieu, lipid saturation, or even the distribution of entire lipid classes relative to tissue morphology could be of importance for understanding tissue-local microenvironments, computing spatial quantitative MSI scores (e.g., local energy score) and probe entire molecular pathways as required for translational applications.

2.2   Objectives

This work introduces the concept of spatial probabilistic mapping in MSI as a solution to the known limitations of ion images when it comes to spatial visualization and interpretation of MOIs' distribution in tissue samples via MSI. It proposes a computational framework, *moleculaR*, that uses user-independent assignment of *m/z* intervals for capturing MOIs based on the device- and measurement-dependent mass resolving power and Gaussian-weighting of observed peaks-of-interest (POIs) for improved reliability of metabolite/lipid/drug signals in MSI. Instead of relying on a subjective qualitative judgment of the end-user concerning the observed spatial distribution of an MOI within a tissue sample, *moleculaR* proposes molecular probabilistic maps (MPMs) which apply pixel-wise spatial significance testing of MOI intensities against a complete spatial randomness (CSR) model inferred from the signal intensities of that particular MOI. The *moleculaR* framework also allows for spatial statistical comparisons of different tissues (cross-tissue MPMs, or CT-MPMs) and for collective projections of metabolite ensembles onto a single tissue plane, followed by computation of collective projection probabilistic maps (CPPMs). Ultimately, computed "hotspot" and "coldspot" spatial contours provide user-independent and probabilistic localization of tissue areas where an MOI has a statistically significant non-random relative spatial abundance or deficiency, respectively.

Furthermore, this work attempts to further investigate quantitative spatial mapping of drugs in tissue sections by performing tissue-drug content quantification on an entire tissue cohort of 56 specimens of tumor and corresponding non-tumor samples measured in triplicates on time-of-flight- (TOF)- and Fourier transform ion

cyclotron resonance (FTICR)-MALDI-MSI modalities comparing their results to the gold-standard ultra-high performance liquid chromatography electrospray-ionization quadrupole time-of-flight mass spectrometry (UHPLC-ESI-QTOF-MS). A generalized nonlinear calibration model is proposed as a replacement for the traditional linear model that could better model drug-intensity response in the presence of batch effects. Finally, an attempt is made to link cross-tissue molecular probabilistic maps to drug quantification where tissue-drug content is estimated by iterative comparison with single on-tissue drug dilution spots without the need for constructing calibration curves.

The remainder of this dissertation is organized into a materials and methods chapter where tissue samples, measurement techniques and methods implementations are thoroughly explained, a results chapter outlining the results obtained from implementing the proposed methods and demonstrating the outcomes on different tissue showcases and finally discussion and summary chapters.

Chapter 3

Materials and Methods

This chapter describes methods used in this work spanning both the proposed *moleculaR* computational framework (based on the published study Abu Sammour et al.[142]; **sections 3.3-3.12**) as well as the quantitative spatial mapping of imatinib (based on the published study Abu Sammour et al.[143]; **section 3.13**). The chapter is sub-divided into 13 sections: 1) Tissues and matrix-assisted laser desorption ionization mass spectrometry imaging (MALDI-MSI) measurements, 2) Data pre-processing, 3-12) Probabilistic spatial mapping of molecules in tissues via MSI and 13) Regression models and quantification.

3.1 Tissues and MALDI MSI Measurements

3.1.1 Gastrointestinal Stromal Tumor (GIST) Tissue Samples

A total of 56 human Gastrointestinal Stromal Tumor (GIST) and corresponding normal (non-tumor) tissue samples were used in this work to investigate drug quantification with MALDI-MSI. Tissue samples were surgically removed from 27 patients after obtaining their informed consent and approval by Medical Ethics Committee II of the Medical Faculty Mannheim of Heidelberg University (2012-289N-MA; 2015-868R-MA; 2017-806R-MA) and was carried out in accordance with guidelines and regulations.

As part of their treatment plan, all patients received a daily dosage of 400-800 mg of imatinib orally including the day prior to the surgical intervention. Since the elimination half-life of imatinib is approximately 16-18 hours[144], the investigated tissue specimens were assumed to have a steady state drug status at the point of surgery. After removal, tissues were snap-frozen and stored at -80° C in a biobank. Clinical treatment, surgical removal and storage took place under the supervision of Prof. Dr. Peter Hohenberger at the Division of Surgical Oncology and Thoracic Surgery, University Medical Center Mannheim of Heidelberg University. For all tissue samples, histology, mitotic activity and immunohistochemistry in addition to KIT and PDGFRA gene mutations were assessed by Prof. Dr. Alexander Marx at the Institute of Pathology of University Medical Center Mannheim of Heidelberg

University. **Supplementary Table 8.1** provides an overview of the clinical metadata of the tissue samples.

To establish drug calibration curves for quantification, porcine liver tissues were used which were supplied by the local slaughterhouse and immediately snap-frozen at -80° C. Each GIST sample was then sectioned in triplicate with each replicate comprising several 8 μm-thick sections to allow for a multi-modal investigation based on time-of-flight MALDI-MSI (MALDI-TOF-MSI), Fourier transform ion cyclotron resonance MALDI-MSI (MALDI-FTICR-MSI), ultra-high performance liquid chromatography electrospray-ionization quadrupole time-of-flight mass spectrometry (UHPLC-ESI-QTOF-MS), Fourier transform infrared (FTIR) microscopy[81] and hematoxylin and eaosin (H&E) histological staining. For MALDI-TOF- and MALDI-FTICR-MSI, each target slide contained duplicated spots of an imatinib dilution series (25, 12.5, 6.25, 3.125, 1.56, 0.78 pmol and a blank control spot) spotted onto porcine liver tissue which is mounted adjacent to the GIST tissues under investigation (see **Supplementary Figure 8.3**).

Before following on with MALDI-TOF- and -FTICR imaging, deuterated imatinib (imatinib-D8) was sprayed onto the slide to be used as an internal standard (IS) for normalization after which 2,5-Dihydroxybenzoic acid (DHB) MALDI matrix was sprayed. MALDI-TOF-MSI tissue measurement was performed on an UltrafleXtreme MS device (Bruker Daltonics) while high-resolving-power MALDI-FTICR-MSI was acquired on a SolariX 7T XR FTICR MS (Bruker Daltonics). All MSI measurements were recorded in positive-ion mode with a 200 and 50 μm raster width for the imatinib dilution series part and GIST tissues, respectively. Tissue handling, FTIR microscopy, MALDI-MSI acquisition and UHPLC-ESI-QTOF-MS were conducted by C. Marsching, A. Geisel, K. Erich, S. Schulz, C. Ramallo Guevara and J-H Rabe at the center of Mass Spectrometry and Optical Spectroscopy (CeMOS). Detailed information can be found in the corresponding published study Abu Sammour et al.[143]

3.1.2 Isocitrate Dehydrogenase-wild type (IDH-WT) Glioblastoma (GB) Tissue Samples

One human isocitrate dehydrogenase-wilt type (IDH-WT) glioblastoma (GB) tissue sample and its replicate were used to develop and showcase the spatial probabilistic methods described in **sections 3.6-3.9**. Patients, who had been treated at the Heidelberg University Hospital, gave informed consent prior to inclusion to exploratory molecular analysis including but not limited to MALDI-MSI. The research was conducted in concordance with the declaration of Helsinki and was approved by the ethics committee at Heidelberg University, Germany (applications S-130/2022 and AFmu-207/2017). Clinical treatment of patients and tissue storage after surgical removal took place under the supervision of Prof. Dr. Wolfgang Wick and Dr. Tobias Kessler at the Department of Neurology and National Center for Tumor Diseases, Heidelberg University Hospital. H&E histological annotation was conducted by

Prof. Dr. Andreas von Deimling at the Department of Neuropathology, Heidelberg University Hospital.

Frozen GB tissue was cryosectioned with 10 µm thickness and mounted on conductive indium-tin-oxide (ITO) slides. 1,5-diaminonaphthalene (DAN) MALDI matrix was sprayed onto the target slide. High-resolution MALDI-FTICR-MSI measurements were acquired on a Solarix 7T XR (Bruker Daltonics) in negative- and positive-ion modes (same spot) with a 50 µm lateral spatial resolution and mass-to-charge ratio (*m/z*) 100-1200 range. Profile (continuous; see **section 1.2**) MSI data was saved with a data reduction factor of 97% in addition to centroided mass spectra (SQLite peaks list) which were generated during acquisition. The reduced profile data was then used to randomly sample a single spectrum for the estimation of the full-width at half-maximum (FWHM) model (see **section 3.3**) while centroided data was used for the subsequent analysis. Tissue handling, and MALDI-MSI acquisition were conducted by C. Marsching and C. Ramallo Guevara at the center of mass spectrometry and optical spectroscopy (CeMOS). Detailed information can be found in the corresponding study Abu Sammour et al.[142]

3.1.3 Glioma Tissue Samples

Five sets of human control, IDH-WT and IDH-mutant (IDH-MUT) high-grade glioma tissue samples were previously collected from adult patients undergoing brain surgery after informed consent. Patient sample collection was carried out at the Freiburg University Hospital under the ethics protocol 472/15. Clinical treatment of patients and tissue storage and handling were coordinated by Dr. Mirco Friedrich and Prof. Dr. Michael Platten from the Clinical Cooperation Unit Neuroimmunology and Brain Tumor Immunology, German Cancer Research Center (DKFZ) in Heidelberg, Germany and their associates[13]. For the MALDI-FTICR-MSI measurements, frozen tissue sections were mounted on conductive ITO glass slides such that every slide would contain one set of three glioma tissue sections: control, IDH-WT and IDH-MUT. These slides were spray-coated with 1,5-DAN MALDI matrix using an HTX TM-Sprayer (HTX Technologies) and high-resolution MALDI-FTICR-MSI data was acquired on a 7T SolariX XR (Bruker Daltonics) in negative-ion mode within a mass range of *m/z* 100-1200 at 50 µm lateral spatial resolution. Spectra were acquired using 1 million transient data points (FID 0.4893s) with an online calibration using an internal lock mass of *m/z* 157.076025. Further detailed description of the sample collection processes is to be found in the corresponding study of Friedrich et al.[13] Only one slide, namely "set1" described in Friedrich et al.[13] was showcased in this work.

Profile (continuous; see **section 1.2**) MSI data was saved with a data reduction factor of 97% in addition to centroided mass spectra (SQLite peaks list) which were generated during acquisition. The reduced profile data was then used to randomly sample a single spectrum for the estimation of the FWHM model (see **section 3.3**)

while centroided data was used for the subsequent analysis. Tissue handling, and MALDI-MSI acquisition were conducted by C. Ramallo Guevara at the center of Mass Spectrometry and Optical Spectroscopy (CeMOS). Detailed information on the acquisition parameters and tissue handling can be found in the corresponding published study of Friedrich et al.[13]

3.1.4   Mouse Brain Tissue Samples

Fresh-frozen mouse brains of female wilt-type C57BL/6N mice, sacrificed at 12 weeks of age for the purpose of breeding control, were obtained from the German Cancer Research Center (DKFZ). Tissues were sliced at 10 µm thickness, mounted on conductive ITO slides and sprayed-coated with 4-phenyl-α-cyanocinnamic acid amide (PhCCAA) matrix. This resulted in eight sagittal mouse brain tissue serial sections each mounted on a conductive ITO slide.

MALDI-FTICR-MSI was performed on the first six sections as described in **section 3.1.2** but with 20 µm lateral resolution in the mass range between *m/z* 100-3000 in negative ion mode. Trapped ion mobility spectrometry time-of-flight (timsTOF) MALDI-MSI data of one tissue section was obtained on a timsTOF fleX (Bruker Daltonics) also in negative ion mode in the mass range of *m/z* 600-1800. Finally, an additional MALDI-TOF-MSI measurement was obtained for the last section on a Rapiflex MALDI-TOF MS (Bruker Daltonics) with the same ion mode and mass range.

Tissue handling and MALDI-MSI acquisition were conducted by C. Marsching at the center of mass spectrometry and optical spectroscopy (CeMOS). Detailed information on measurements and tissue handling can be found in the corresponding study Abu Sammour et al.[142]. Additionally, previously published publicly available MALDI-TOF-MSI of the APP NL-G-F Alzheimer's disease mouse model[145] was re-used in this work (**Figure 4.9de**).

3.2   Data Pre-processing

3.2.1   Gastrointestinal Stromal Tumor (GIST) MALDI-MSI Data

The imatinib quantification study[143] comprised a total of 48 MALDI-TOF-MSI and three MALDI-FTICR-MSI measurements, which were all exported into the open imzML format[34] using FlexImaging software (v. 4.1; Bruker Daltonics). Each measurement slide contained duplicated spots of an imatinib dilution series (25, 12.5, 6.25, 3.125, 1.56, 0.78 pmol and a blank control spot) spotted onto porcine liver tissue which is mounted adjacent to the GIST tissues under investigation (see **Supplementary Figure 8.3**).

A mass-binning rate of 120,000 bins per spectrum was used during conversion for the continuous (i.e. profile) MALDI-TOF-MSI data while an in-house conversion

tool was used to directly convert the centroided SQLite peaks list of MALDI-FTICR-MSI data directly into a processed (i.e. centroided) imzML. *MALDIquant* and and *MALDIquantForeign* R packages[17] were used to import imzML data into R[146]. All subsequent analysis and visualization of MSI data was carried out via *MALDIquant*, *ggplot2* and *fmsb* R packages which are all publicly accessible. The sprayed IS, imatinib-D8, was used to normalize all mass spectra to the maximum peak intensity over the mass-window range *m/z* 502.32 ± 100 ppm and ± 10 ppm for MALDI-TOF-MSI and MALDI-FTICR-MSI, respectively.

3.2.2 IDH-WT Glioblastoma (GB) MALDI-MSI Data

This dataset, described in **section 3.1.2**, comprised two inter-slide measurements of one IDH-WT GB tissue and its serial section (see **Figure 4.9** and **Supplementary Figure 8.1**) as described in the corresponding study Abu Sammour et al.[142]. Centroided MALDI-FTICR-MSI measurement data, described in **section 3.2.2**, were converted into an imzML format[34] via an in-house tool directly from the SQLite peaks list data. The centroided imzML data was imported into R (v. 4.0.2)[146] via the *MALDIquantForeign* and subsequently analyzed with *MALDIquant* packages[17].

To estimate the FWHM model as a function of *m/z*-axis (see **section 3.3**), one randomly chosen pixel representing a continuous (profile) mass spectrum was exported as a CSV file via FlexImaging software (v. 5.0; Bruker Daltonics). FWHM values were estimated for all peaks and plotted against the *m/z*-axis which were then used to model a continuous relationship of FWHM as a function of *m/z*-axis by running a locally-estimated scatter-plot smoothing (LOESS) as described in **section 3.3** (see also **Figure 4.2**). To remove spurious random peaks in the centroided MALDI-MSI data, peaks that occurred in less than 1% of all pixels were filtered out.

Peak binning was curried out via *MALDIquant*[17]; the observed peak masses of all pixels of the MALDI-MSI measurement were grouped and sorted into a single vector and the difference between each neighboring pair was computed. Then iterative bisecting was applied on the mass vector, each time at the largest difference, until all peaks within each bin fulfilled the criterion $|m_{ij} - \bar{m}_j|/\bar{m}_j < (\Delta m/m)$; where m_{ij} the mass of the *i*-th peak at the *j*-th bin, $\bar{m}_j$ is the mean mass of all peaks present in the *j*-th bin (bin center; the new peak position) and $\Delta m/m$ is the specified tolerance for maximal relative peak deviation of peak positions to be considered as identical which, for this work, was set to 12 ppm ($= \Delta m/m$; $\Delta m =$ FWHM at *m/z* 400 $\approx$ 0.0048 Da; $m =$ *m/z* 400). Since the focus of this study was on the lipidome, *m/z* 400 was chosen.

Binned MALDI-MSI data (negative- and positive-ion modes) was then exported back into imzML format via *MALDIquantForeign* in order to apply data-driven pixel-wise mass recalibration based on endogenous biological signals[36] after which it was uploaded into the METASPACE annotation platform (https://metaspace2020.eu)[147] to conduct lipid identification against the SwissLipids database[148]. The resulting

identifications were then fetched as CSV files and only verified (i.e. annotated) lipids were then considered as molecules-of-interest (MOIs) for the molecular probabilistic maps (MPMs) and collective projection probabilistic maps (CPPMs).

To transform the histological annotations of the corresponding H&E images into the MALDI-MSI coordinates, semi-automatic multi-modal image registration was applied between the optical MSI image, which is acquired prior to MALDI-MSI measurement, and the corresponding H&E images. The Semi-automatic multi-modal image registration was carried out by J. Cordes using the previously published M2aia tool[149] as described in detail in Abu Sammour et al.[142]

3.2.3 IDH-MUT and -WT Glioma MALDI-MSI Data

This dataset comprised one MALDI-FTICR-MSI measurement (one slide) of a sets of three Glioma tissue sections: control, IDH-WT and IDH-MUT as described in **section 3.1.3**. Only IDH-WT and IDH-MUT glioma sections were used for this work in the context of cross-tissue molecular probabilistic maps (CT-MPMs). The corresponding centroided MALDI-FTICR-MSI measurement data was converted into an imzML format via an in-house tool directly from the SQLite peaks list data. The centroided imzML[34] data was imported into R (v. 4.0.2)[146] via *MALDIquantForeign* and subsequently analyzed with *MALDIquant* packages.[17]

To avoid including non-tissue measurement regions (due to tissue tears, folds and cuts), matrix-only regions were identified based on pixel total ion count (TIC) and filtered out by employing unimodal histogram thresholding.[150] The rest of the pre-processing was similar to the one described in **section 3.2.2** except for the binning tolerance which was set to 6 ppm ($= \Delta m / m$; $\Delta m =$ FWHM at m/z 200 $\approx$ 0.0012 Da; $m = m/z$ 200) to accommodate the mass range of the MOI, Tryptophan, at m/z 203.0815. The search mass-window used for identifying Tryptophan signal was inferred from fitted FWHM vs m/z-axis curve as described in **section 3.3**.

3.2.4 Mouse Brain MALDI-MSI Data

This cohort comprised six MALDI-FTICR-MSI, one MALDI-timsTOF-MSI and one MALDI-TOF-MSI data of sagittal mouse brain tissue serial sections. The MALDI-FTICR-MSI of the mouse brain tissue was pre-processed similar to the MALDI-FTICR-MSI of the GB tissue described in **section 3.2.2**. The centroided MALDI-timsTOF-MSI mouse brain data was converted into an imzML format via an in-house tool directly from the SQLite peaks list data. The centroided imzML[34] data was imported into R (v. 4.0.2)[146] via *MALDIquantForeign* and subsequently analyzed with *MALDIquant* packages.[17]

FWHM model fitting was performed on a randomly chosen profile spectrum and peak binning was performed via *MALDIquant* as described in **section 3.2.2**. The profile MALDI-TOF-MSI mouse brain data was pre-processed as described in **section**

3.2.2 but without applying IS normalization as no IS was sprayed during sample preparation. All pre-processed centroided MALDI-MSI data was then exported into a centroided (processed) imzML format and uploaded into the METASPACE annotation platform (https://metaspace2020.eu)[147] to conduct lipid annotation against the SwissLipids database.[148]

3.3 Full-Width at Half-Maximum (FWHM) Model Fitting

Rendering ion images of MOIs always entails the selection of an appropriate mass-search-window where that MOI signal is to be found. In order to achieve a user-independent and modality-, measurement- and data-specific assignment of this mass-window width, a mass resolving power-dependent estimation could be thought of as a suitable and unbiased property to specify the mass-window width at a given *m/z*. However, theoretical modeling of the mass resolving power is challenging and is different for the different mass spectrometer types. Marshall et al.[75] reported that for FTICR mass spectrometers whose mass resolving power* is $R_{FWHM} = m/\Delta m_{50\%}$, the FWHM $\Delta m_{50\%}$ of a mass spectrum peak at an ion mass *m* could be calculated by the following relationship[75]

$$\Delta m_{50\%} = \frac{7.589 m^2}{q\, B\, T_{FID}} \tag{3.1}$$

where q is the ion charge, B is the magnetic field strength at the center of the trap of the mass spectrometer and T_{FID} is the free-induction-decay time. This state is referred to as the low-pressure limit, since ion-neutral collisions inside the trap are neglected. However, if ion-neutral as well as ion-ion collisions are considered, $\Delta m_{50\%}$ can be described by[75]

$$\Delta m_{50\%} = \frac{2\sqrt{3}\, m^2}{q\, B\, \tau} \tag{3.2}$$

where, τ is the damping constant of the radial ion motion. **Equations 3.1 and 3.2** show that peaks' FWHM $\Delta m_{50\%}$ for FTICR mass spectrometers scales with m^2.**

On the other hand, the theoretical formulation of mass resolving power for TOF mass spectrometers is completely different[76] and, therefore, an empirical method for estimating mass resolving power from data independent of the measurement device would be more suitable. This was achieved by plotting all individual peaks' (SNR ≤ 3) FWHM as a function of *m/z* and then fitting a locally-estimated scatter-plot

---

*The terms mass resolution and mass resolving power have been often used interchangeably in literature. To avoid ambiguity, the recommendation of Murray et al.[151] has been adopted throughout this dissertation.

The literature review underlying this paragraph as well as **Equations 3.1 and 3.2 was contributed by S. Schmidt as mentioned in the author contributions section in the cited study Abu Sammour et al.[142]

smoothing (LOESS) curve that would approximate FWHM at any given *m/z*-value and therefore provide an estimate for the mass resolving power at any given *m/z*. Since the proposed method deals mainly with centroided MSI data, the peaks FWHM values are calculated from the provided randomly chosen profile spectrum corresponding to the MSI data under investigation.

When a FWHM model is fitted, for any given *m/z* MOI, the estimated FWHM could be used to infer the corresponding standard deviation σ_w of a hypothetical Gaussian that could be used to represent the theoretical MOI peak shape and, hence, its extent[35,48], which is governed by $FWHM = 2\sqrt{2\,ln2}\,\sigma_w$. This enables data-driven calculation of the mass-search-window width taken as $m_{MOI} \pm 3\sigma_w$ (i.e. the span of the erected Gaussian-window; m_{MOI} is the *m/z* value at MOI) independent of the user, measurement device and measurement parameters while also taking into account the mass resolving power at that mass range.

3.4 Gaussian Mass-Window Weighting

As described in **section 3.3**, the main rational of fitting a data-driven FWHM model as a function of *m/z* is to implement a user-independent estimation of a device-, measurement- and mass range-appropriate mass-search-window for rendering MOI ion images. However, the proposed method also allows for the use of a Gaussian mass-window weighting scheme instead of the classical and more common method of uniform mass-window weighting (see **section 1.2**). For any MOI, considering ion mode and expected adduct formations, its theoretical monoisotopic mass, m_{MOI}, is computed or taken from a curated database. For this *m/z*, the expected data-dependent FWHM and σ_w of a Gaussian envelope centered at *m/z* m_{MOI} are determined as described in **section 3.3**. This Gaussian envelope, after scaling to [0,1] range, is then used as an intensity-weighting function for any detected peaks-of-interest (POIs) which could occur within the mass-search-window $m_{MOI} \pm 3\sigma_w$ (i.e. the span of the Gaussian) such that the MOI pixel intensity MOI_{pixel} for every pixel could be estimated by $\Sigma_{j=1}^{p} w_j\, i_j$ where p is the number of peaks observed within $m_{MOI} \pm 3\sigma_w$, and w_j is the corresponding Gaussian weight at the *j*-th peak with intensity i_j. This type of weighting is expected to reduce the impact of proximal background signals on the estimation of MOI_{pixel}.

3.5 Spatial Point Pattern (SPP) Representation of MSI Data

A spatial point pattern (SPP) is a dataset representing spatial locations of points within a given spatial area or window. A point, in this context, could generally represent any event or observation generated by a certain spatial process within a spatial area or window, e.g., locations of tress in a forest, locations of volcanoes on the global map or car accidents or crime incidents within a certain city.[152]

MSI data is commonly represented by raster images made up of a uniform grid of pixels which represent the laser shots positions (see **section 1.2**). Generally speaking, the difference between SPP and raster image representations could be described as the difference between vector- and raster-based graphics; they are equivalent representations of the same spatial distribution, but each provides a unique set of tools and methods that are tailored to the specific nature of each representation. In this work, switching to an SPP representation for MSI data is dictated by the need for generating complete spatial randomness (CSR) SPP models which would describe the spatial null hypothesis (absence of spatial structures) of MOI SPPs as described in **section 3.6**. MSI ion images of a certain MOI are raster images with a uniform spatial grid, but creating a corresponding CSR model within the same spatial domain (i.e. on a spatial grid) would directly violate the randomness criterion of such models. Therefore, in order to facilitate the direct and homogeneous comparison between MOI and a corresponding CSR model, MOI spatial intensities must be converted into an SPP representation.

Once MOI's intensities are computed according to the Gaussian mass-window weighting method described in **section 3.4**, these intensities are then represented by marked (i.e. intensity-weighted) points within an SPP of MOI signals, SPP_{MOI}, whose locations are the MSI-pixel x, y-coordinates distributed in a spatial 2D contour Φ_{tissue} representing the tissue section with a spatial point density Λ, which equals the number of points per unit area, i.e., the average spatial density of all points n within Φ_{tissue} or n / A_{tissue} where A_{tissue} is the total area of Φ_{tissue}. The *spatstat* framework[152] has been used extensively throughout this work for analysis and manipulation of SPP-encoded MSI data.

3.6 Molecular Probabilistic Maps (MPMs)

The aforementioned MOI SPPs, or SPP_{MOI}, are then used to computationally deduce molecular probabilistic maps (MPMs) which provide a user-independent spatial evaluation of the MOI's distribution. First, a complete spatial randomness (CSR) model CSR_{MOI} is generated within the same tissue window Φ_{tissue} which is used to represent a sample of random events to be considered as an intrinsic control or a spatial null hypothesis specific to the MOI under study. Previously published CSR generating models primarily dealt with unmarked (unweighted) SPPs which only considered points locations[153,154]. In MSI data, however, each point must carry an intensity value (representing pixel signal intensity) in addition to the x, y-coordinate and, therefore, CSR_{MOI} must model randomness in spatial locations as well as in signal intensities in an unbiased way. This criterion has been achieved in this work by randomly permuting SPP_{MOI} marked points, which basically has the effect of spatial reshuffling of SPP_{MOI} points, until they assume a homogeneous spatial Poisson process[152] with equal spatial point density Λ, thus effectively dissolving any spatial clustering or autocorrelation of signals.

Next, to capture MOI's spatial trend, kernel density estimation (KDE) is applied on both ends (SPP_{MOI} and its corresponding CSR_{MOI}) via an isotropic (since no specific "direction" is assumed for MOI) bivariate Gaussian kernel[155] (also see **section 3.8**) which are then sum-normalized to compute weighted spatial density functions $\rho_{MOI}(x,y)$ and $\rho_{CSR}(x,y)$, respectively. Let $f_{MOI}(k)$ and $f_{CSR}(k)$ denote the density functions of intensities k obtained from the resulting $\rho_{MOI}(x,y)$ and $\rho_{CSR}(x,y)$, respectively. As a consequence of the central limit theorem, and as a convenient byproduct of applying KDE on CSR_{MOI}, the intensity distribution $f_{CSR}(k)$ converges towards a normal distribution as the bandwidth increases, which in practice can already be observed for low bandwidth values. This does not necessarily apply to $f_{MOI}(k)$ (see **Figure 4.12**). Hence

$$f_{CSR}(k) \cong \frac{1}{\sigma_{CSR}\sqrt{2\,\pi}}\, e^{-\frac{1}{2}\left(\frac{k-\mu_{CSR}}{\sigma_{CSR}}\right)^2} \tag{3.3}$$

where μ_{CSR} and σ_{CSR} are the mean and standard deviation of $\rho_{CSR}(x,y)$. To identify areas with higher likelihood of showing a significant relative spatial abundance of MOI when compared to a random distribution (so-called MOI hotspot; i.e. non-random spatial accumulations of MOI intensities) and, on the other hand, areas which have a higher likelihood of showing a significant relative spatial deficiency of MOI (so-called MOI coldspot; i.e. non-random spatial depletion of MOI intensities), the lower and upper tail p-values are computed for every pixel intensity in $\rho_{MOI}(x,y)$ against the null distribution $f_{CSR}(k)$ resulting in two spatial maps of lower and upper tail p-values $P_{lwr}(x,y)$ and $P_{upr}(x,y)$, respectively.

Next, to account for the inherent multiple testing problem, Benjamini-Hochberg p-value correction is applied resulting in $P^*_{lwr}(x,y)$ and $P^*_{upr}(x,y)$ (see **Figure 4.8**). Then null-hypothesis significance testing is carried out by comparing each corrected p-value in $P^*_{lwr}(x,y)$ and $P^*_{upr}(x,y)$ against a significance level of $\alpha = 0.05$. Locations that reject the null-hypothesis are declared to belong to either an MPM hotspot (x_{hs}, y_{hs}) or coldspot (x_{cs}, y_{cs}) if

$$\begin{aligned} (x_{hs}, y_{hs}) &\in \{x,y : P^*_{upr}(x_{hs}, y_{hs}) \leq \alpha\} \\ (x_{cs}, y_{cs}) &\in \{x,y : P^*_{lwr}(x_{cs}, y_{cs}) \leq \alpha\} \end{aligned} \tag{3.4}$$

The MOI's molecular probabilistic map, MPM_{MOI} is then defined as a composite representation of MOI spatial density of Gaussian weighted intensities (**section 3.4**), with MOI hotspots and/or coldspots superimposed as polygonal contours identifying areas of MOI significant abundance and deficiency, respectively.

3.7 Cross-tissue molecular Probabilistic Maps (CT-MPMs)

Ion intensity distributions of metabolites or drugs are compared between test and reference tissues, e.g. those dosed with a drug or carrying certain mutations versus controls, in two steps: First, areas of significant relative spatial abundance/deficiency are computed in the test tissue (testing against the spatial null hypothesis; MPM method described above) as described in the preceding **section 3.6**. Then the signal intensities of the reference tissue are used to infer a non-parametric (distribution-free) empirical cumulative distribution function (eCDF) which acts as an estimator of the underlying cumulative distribution function. All MOI intensities of the test tissue are then tested against it (i.e. the inferred eCDF) in order to find the likelihood of them (i.e. signal intensities of the test tissue) being drawn from the signal distribution of the reference tissue. More precisely, the lower and upper tail p-values are computed for every MOI intensity in SPP_{MOI} of the test tissue against the inferred eCDF of the reference tissue and Benjamini-Hochberg correction is applied to account for the inherent multiple testing problem. Similar to the "within-tissue" MPM method described in the preceding section, the p-value threshold beyond which the null hypothesis is rejected is set to $\alpha = 0.05$. Finally, test tissue intensities which reject both the spatial and test-vs-reference intensity distributions null hypotheses are designated as having significant cross-tissue relative spatial abundance/deficiency. In other words, pixel locations of these intensities could be described as areas of the test tissue which exhibit a statistically significant non-random spatial MOI abundance/deficiency pattern and contain intensities that are unlikely to belong to the distribution of MOI intensities of the reference tissue.

3.8 Kernel Density Estimation (KDE) Bandwidth

KDE is a nonparametric technique commonly used for the estimation of the underlying probability density functions (a.k.a. density estimation) based on observed data points[156]. KDE is a key step in the MPM workflow: i) It captures the overall spatial trend of the MOIs' intensities and ii) it forces f_{CSR} to converge to a normal distribution (see **section 3.6**). This, however, makes MPMs sensitive to the chosen kernel bandwidth h_{KDE}. To prevent spatial over-smoothing, this work introduced a method for KDE bandwidth estimation which takes into account the inherent spatial autocorrelation of MSI measurements[157].

This has been achieved by applying KDE smoothing iteratively with h_{KDE} varying from 1 to 10 (pixels; multiples of $50\,\mu m$ in this work) in 0.5 increments, during each iteration the global Moran's I statistic, a measure of spatial autocorrelation, is determined (via the *raster* package; first order Queen's case adjacency with unit weights). The optimal h_{KDE} is then determined by finding the point of maximum curvature, i.e. the "knee" point, via the *Kneedle* method[158] in the Moran's I vs h_{KDE}

plot. This is the point, after which an increase in h_{KDE} does not result in a considerable increase in the spatial autocorrelation of the smoothed density image.

In other words, the KDE bandwidth at which the Moran's I statistic's rate of change abruptly falls, is the scale, at which it is expected that random pixel fluctuations are smoothed away and important spatial structures/features/patterns start dominating the spatial landscape.

3.9   Collective Projections Probability Maps (CPPMs)

This work further extends the concept of MPM to cover situations where there is an interest in investigating the collective distribution of a custom group of metabolites that could share a certain similarity (ex. lipid classes).

Given a set of target MOIs $C \in \{MOI_1, MOI_2, \ldots, MOI_m\}$, which in this work are queried from the SwissLipids database (https://www.swisslipids.org)[148] and verified against the POI-MOI matching platform METASPACE (https://metaspace2020.eu)[147], for each single MOI_i an SPP representation SPP_i is calculated as described in **sections 3.4-3.5**. Next, all individual SPP_i are projected into the same tissue plane Φ_{tissue} resulting in an SPP for the collective projection, SPP_C.

Since SPP representations do not restrict the number or location of points in the point pattern, a single SPP can hold any number of points coming from any number of MOIs. Since POI-MOI matching usually reports a group of candidate molecules for a single POI (at a given FDR, metabolite database and mass resolving power), mapping MOIs to POIs could result in duplicated representations of POIs within CPPMs. This problem is mitigated by filtering out duplicated counts of the same *m/z* value by incorporating only the intensities of unique masses present in SPP_C. Moreover, if two MOIs of the MOI set *C* overlap due to insufficient resolving power of the mass spectrometer at *m/z* MOI, the Gaussian mass-window weighting compensates for this, provided that the two MOIs are at least partly resolved (See **Figures 4.5**, **4.6** and **4.7** exemplifying resolved, partially resolved and unresolved MOIs, respectively).

Intensity z-score normalization (i.e. standardization) is then applied on the intensities of each individual SPP_i within SPP_C by subtracting its (i.e. SPP_i) intensities mean and dividing by the standard deviation. This type of transformation aims to equalize the variance of measured MOI intensities by setting the mean intensity of each MOI equal to zero, thereby adjusting for differences in the offset between MOIs with high and low intensity ranges, while, at the same time, setting the standard deviation of intensities equal to one[159]. This is done to (at least partially) compensate for the inherent heteroscedasticity and possible differences in ionization efficiency between the individual MOI_is. Then CSR_C is created and subsequently KDE is applied to both SPP_C and CSR_C , in order to compute MPM_C as described in **section 3.6**, i.e. the resulting collective projection probabilistic map CPPM is equivalent to MPM_C.

The naming distinction is only made to emphasize that CPPMs are based on the visualization of multiple MOIs at a time.

3.10   Spatial Arithmetic Expressions

The proposed method also allows for basic arithmetic operations on MOIs' SPPs which could be useful in situations when a ratio of two MOIs is desired or when a more complex composite score is of interest. This could be achieved, first, by converting the set of input SPP_{MOI}s into corresponding pixel-based images with equal pixel grids. Afterwards the spatial expression is evaluated on a pixel-by-pixel basis. Calculation artifacts such as division by zero (i.e. absence of a peak in that pixel) are computationally dropped during the conversion back to SPP, while low values in the denominator (representing detector baseline or very low peak intensities) are not expected because *moleculaR* works mainly with centroided (SNR $\geq$ 3) MSI data. The resulting raster image is then converted back to an SPP whose points are carrying the respective computed pixel intensities. This SPP is then fed into the MPM framework as described in **section 3.6**. No arithmetic operations are applied on the hotspot/coldspot contours.

3.11   Synthetic Data Generation

In order to validate the proposed methods, a ground-truth SPP data was simulated based on four pre-defined spatial patterns of simulated foregrounds representing high MOI abundance: i) Single central circle of radius 25 length units (**Figure 4.14a**), ii) five equidistantly placed circles of 10 length units radius (**Figure 4.14b**), iii) a ring-like structure with 30 and 20 length units for outer and inner radii, respectively (**Figure 4.14c**) and iv) a dominant central circle of 20 length units radius with four adjacent smaller ones of 5 length units radius each (**Figure 4.14d**).

Each foreground pattern was placed within a square window of 100 length units denoting the background. Points were distributed within foreground and background areas according to a homogeneous spatial Poisson point process with spatial point densities Λ of 0.4 and 0.3 points per unit area for foreground and background, respectively. Points' intensity values (marks) were sampled from above and below the upper quartile (i.e. Q3) of the empirical intensities of i) a MALDI-FTICR-MSI measurement of a human IDH-WT GB tissue sample (**section 3.1.2**; **Figure 4.9a**) at *m/z* 544.3009 ([PE(20:1)+Na]$^+$; FDR $\leq$ 0.2) or ii) a MALDI-TOF-MSI measurement of a human gastrointestinal stromal tumor (GIST) tissue sample (**section 3.1.1**; **Figure 4.32e**) at *m/z* 494.2662 (imatinib [M+H]$^+$) for the simulated foreground and background areas, respectively.

The difference in spatial point densities and marked intensities accounts for the increased signal intensities and spatial density of peak signals, which is normally

observed for areas of high relative abundance of an MOI (i.e. high spatial autocorrelation) which indicate a probable biological process spatially localized within a given tissue morphology.

The evaluation proceeded by testing the ability of MPMs to localize the simulated foreground correctly and identify points exhibiting significant relative spatial abundance visually and by computing Dice similarity coefficient (DSC) values between the foreground areas and estimated MPM hotspots (see **Figure 4.14**). Moreover, the simulated ground-truth was also used for validating the proposed KDE bandwidth estimation method (**section 3.8**), by iteratively estimating MPM for every simulated SPP type using incrementally assigned KDE Gaussian bandwidth h_{KDE}, which was varied from values of 0 to 10 length units in 0.1 incremental steps. During each iteration, DSC was computed between the estimated hotspot contour and the ground-truth foreground used for generating the simulated SPP.

3.12   Artificially Added Noise

To further test the proposed methods for stability and robustness against noise sources commonly observed in MALDI MSI, raw data was artificially "contaminated" with different noise types (see **Figure 4.18**): i) random Gaussian noise, ii) presence of abnormally high-intensity peak artifacts ("intensity artifacts"), and iii) added overlapping peaks at an arbitrary $2\sigma_w$ distance away from *m/z* MOI ("interference").

For added Gaussian noise, intensities were sampled from a Gaussian distribution $f_{Gaussian}$ with $\mu_{noise} = \mu_{MOI}$ and $\sigma_{noise} = \sigma_{MOI}$ and added to all pixels of the MSI data, where μ_{noise} and σ_{noise} are the mean and standard deviation of $f_{Gaussian}$ and μ_{MOI} and σ_{MOI} are the mean and standard deviation of the MOI intensity distribution f_{MOI}. Moreover, MPMs were tested against a Gaussian noise source with varying $\sigma_{noise} = \sigma_k$ ($k = 0 \ldots 10$), where $\sigma_0 = \sqrt{\mu_{MOI}}$ and $\sigma_k = k\,\sigma_{MOI}$ for $k = 1 \ldots 10$. For $k = 0$, the resulting noise is similar to Poisson noise with $\lambda_{Poisson} = \mu_{MOI} \gg 1000$ (see **Figure 4.20**).

The same computational experiment was repeated, this time spiking sampled noise in the vicinity of *m/z* MOI (point **iii** above) at *m/z* MOI + $2\sigma_w$, where σ_w is the standard deviation of the Gaussian envelope inferred from fitted FWHM vs *m/z*-axis curve as described in **section 3.4**. For added intensity artifacts (point **ii** above), noise intensities were sampled from a uniform rectangular distribution whose range far exceeded the range of the MOI intensity distribution f_{MOI}. These were added to $n = 10$ random pixels of the MSI data, but also, for an extended evaluation, with a varying number of intensity artifacts n (up to $n = 5000$; $\approx 20\%$ of the total tissue pixels) randomly placed within the tissue window (see **section 4.4.6**).

An additional evaluation was performed by comparing MOIs' hotspots of raw data and its artificially contaminated counterpart for 142 MOIs (identified with FDR $\leq$

0.2 in positive ion mode against the SwissLipids[148] database) of a MALDI-FTICR-MSI measurement of the human IDH-WT GB tissue section described in **section 3.1.2**, each time computing DSC values of MPM-based hotspots of raw and contaminated MOIs (**Figure 4.19**). The higher the DSC value for a particular artificial noise contamination, the lower the proposed method is impacted by that type of artificial noise.

3.13 Regression Models and Quantification

The imatinib quantification study[143] comprised a total of 48 MALDI-TOF-MSI and three MALDI-FTICR-MSI measurements (slides) each containing duplicated spots of an imatinib dilution series (25, 12.5, 6.25, 3.125, 1.56, 0.78 pmol and a blank control spot) spotted onto porcine liver tissue which is mounted adjacent to the GIST tissues (see **Supplementary Figure 8.3**) for constructing intra-measurement linear and nonlinear drug calibration curves as proposed in the published study Abu Sammour et al.[143] and described in the following two sections.

3.13.1 Linear Calibration Model

Linear calibration curves, which are predominantly used for quantification MALDI-MSI studies[78,160], has been fitted to the imatinib dilution for every measurement slide. Here, linear regression has been performed to assess the linear relation between imatinib signal intensity y (arb. units; normalized to IS) and amount of spotted Imatinib x (pmol) such that

$$y = a\,x + b \tag{3.5}$$

Where a is the slope and b is the y-intercept. To express the limit of detection (LOD), let y_{Limit} denote the smallest detectable signal intensity and y_{Blank} and σ_{Blank} are the mean and the standard deviation of the signal intensity in the blank (control) measurement area, respectively. Assuming a normal distribution of the detector noise signal it can be stated that

$$y_{Limit} = \bar{y}_{Blank} + k\,\sigma_{Blank} \tag{3.6}$$

Where k is a factor normally equal to 3 for a confidence level >99.7% i.e. the smallest reliably detectable drug signal is $k = 3$ standard deviations above the mean signal, all measured within the blank (control) measurement area. **Equation 3.5** can be re-written to reflect LOD

$$y_{Limit} = a\,x_{Limit} + \bar{y}_{Blank} \tag{3.7}$$

Which could be substituted into **Equation 3.6** to yield

$$x_{Limit} = \frac{k \, \sigma_{Blank}}{a} \tag{3.8}$$

Where x_{Limit} = LOD for $k = 3$ and x_{Limit} = the limit of quantification (LOQ) for $k = 10$.[78,160] In other words, LOD and LOQ for a linear regression model can be expressed (here, in the unit of pmol) conveniently by the standard deviation of the signal of interest in the blank (i.e. detector baseline) and the slope of the fitted model. Moreover, for centroided (peak-picked) MALDI-MSI data where the background detector noise is normally eliminated during pre-processing, LOD and LOQ could still be estimated since σ_{Blank} can also be approximated by the standard error of the y-intercept in the fitted linear model.

To limit the effect of heteroscedasticity on the regression model, which is normally observed in MALDI-MSI[37,39,161], a weighted linear regression has been performed such that each calibration point (representing the mean intensity of the drug signal within the respective dilution area) was down weighted by its pixel-wise variance within that area.

3.13.2 Generalized Nonlinear Calibration Model

Although linear calibration curves are the norm in quantitative MALDI MSI as discussed in the previous section, a nonlinear behavior of the Imatinib dilution series which closely resembles a power-function response was observed in all measured MALDI-TOF-MSI and MALDI-FTICR-MSI GIST datasets (see **section 4.5**. To accommodate this observation, a nonlinear regression was performed by fitting a power function as a calibration curve in the form of

$$y = a \, x^b + c \tag{3.9}$$

Where a, b and c are constants, c was added to represent the superimposed detector noise (background signal when the drug signal is absent). Note that as $b \to 1$, the model's response approaches linearity and the above equation reduces to an equation of a line. To quantify the LOD and LOQ, **Equation 3.9** can be re-written as follows

$$y_{Limit} = a \, x_{Limit}^b + \bar{y}_{Blank} \tag{3.10}$$

Rearranging the above equation and plugging **Equation 3.6** into it yields

$$x_{Limit} = \left(\frac{k \, \sigma_{Blank}}{a}\right)^{1/b} \tag{3.11}$$

Where x_{Limit} = LOD for $k = 3$ and x_{Limit} = LOQ for $k = 10$.[78,160] Therefore, similar to the linear model, the LOD and LOQ for the nonlinear fit can be conveniently

expressed as a function of the standard deviation of the signal of interest in the blank measurement area (i.e. detector baseline) and the coefficients of the fitted model *a* and *b*.

Moreover, and similar to the linear case, for centroided (peak-picked) MALDI-MSI data where the background detector noise is normally eliminated during pre-processing, σ_{Blank} can be approximated by the standard error of coefficient *c* derived from the nonlinear model fit. The nonlinear regression was also weighted by the inverse of the variance of each calibration point to limit the impact of the signal heteroscedasticity[37,39,161] on the fitted model.

Chapter 4

Results

This chapter outlines the results obtained from implementing the methods discussed in the preceding chapter demonstrating the outcomes on different tissue showcases. The chapter is sub-divided into five sections: 1) The *moleculaR* package, 2) data-driven modeling of mass spectrum peaks as a function of mass-to-charge ratio (*m/z*), 3) Gaussian versus uniform mass-window weighting, 4) probabilistic spatial mapping of molecules in tissues via mass spectrometry imaging (MSI) and 5) quantitative spatial mapping of imatinib in gastrointestinal stromal tumor (GIST) tissue samples. **Sections 4.2-4.4** are based on the proposed *moleculaR* framework[142] while **section 4.5** is based on the study Abu Sammour et al.[143]

4.1   The *moleculaR* Package

The computational framework, *moleculaR*, has been made available for the scientific community as an open-source R package deposited on Github (https://github.com/CeMOS-Mannheim/moleculaR). All methods described in **sections 3.3-3.12** have been implemented in R and provided to the end-user in a well-documented structure. Additional helping functions have also been provided for importing MSI data, basic pre-processing, simulation, conversion to spatial point pattern (SPP) and sparse matrix representations and visualization of the results. As of this writing, the *moleculaR* package constitutes 40 functions and methods and >3000 lines of code.

moleculaR comes pre-loaded with an example data of the glioblastoma (GB) tissue sample (**section 3.1.2**) and is capable of importing metabolite annotation results from the METASPACE annotation engine (https://metaspace2020.eu)[147] to compute FDR-verified moleculaR probabilistic maps (MPMs) and collective projection probabilistic maps (CPPMs). *moleculaR* also provides a graphical user interface* developed using the *shiny* framework in R which can be run locally or hosted remotely on a server. Code vignettes are also provided as part of the package to illustrate its basic functionality, one such vignette is illustrated in **section 8.3** in the Appendix. Data used in this work is available for download (https://metaspace2020.eu/ project/abusammour-2022) in the imzML[34] data format.

---

*The graphical user interface based on *shiny* was developed with contribution from J. L. Cairns

4.2 Data-driven Modeling of Mass Spectrum Peaks

Rendering ion images of molecules-of-interest (MOIs) in MSI always entails the selection of an appropriate mass-search window where that MOI signal is to be found.[79] In order to achieve a user-independent and modality-, measurement- and data-specific assignment of this mass-window width, the measurement-specific mass resolving power, R_{FWHM}, was chosen as a suitable and unbiased property to define the extent of the mass-window width for any given MOI. However, mass resolving power theoretical modeling is different depending on the mass spectrometer technology (see **section 3.3**). This has called for an empirical estimation of this property by plotting the full-width at half-maximum (FWHM), or $\Delta m_{50\%}$, values for individual mass peaks, whose signal-to-noise ratio (SNR) ≥ 3, as a function of ion mass m and then fitting a locally-estimated scatter-plot smoothing (LOESS) curve that would approximate FWHM at any given m/z-value and therefore provide an estimate for the mass resolving power at any given mass range since $R_{FWHM} = m / \Delta m_{50\%}$.

Figure 4.1 demonstrates FWHM modeling as a function of ion m/z for Fourier transform ion cyclotron resonance (FTICR; Solarix, Bruker Daltonics), time-of-flight (TOF; rapifleX, Bruker Daltonics) and Trapped ion mobility spectrometry time-of-flight (timsTOF; timsTOFflex, Bruker Daltonics) matrix-assisted laser desorption ionization (MALDI) MSI devices. For each case, peaks of 100 randomly sampled spectra were used to construct the FWHM vs ion m/z plot (black points in **Figure 4.1**). Despite the clearly observed fluctuations of the detected FWHM values along the y-axis, it can be seen that for the MALDI-FTICR-MSI case, the fitted FWHM model closely follows the FWHM theoretical expectation (**Equation 3.2**) for the mass spectrometer. For time-of-flight-based mass spectrometers (**Figure 4.1bc**), the fitted FWHM model deviates somewhat from the expected linear (i.e. constant) behavior[76] but not significantly when compared to the case of FTICR in **Figure 4.1a**.

moleculaR is designed to work with centroided MSI data (i.e. not profile, retaining only m/z values and corresponding signal intensities of the detected/observed peaks in any given spectrum; see **section 1.2**). Since peaks' FWHM values cannot be computed for centroided data, this information has to be supplied externally in the form of a profile spectrum randomly chosen from the same MSI measurement data. To test if one randomly chosen spectrum could be representative of the entire MSI measurement data to correctly model the inherent FWHM as a function of the m/z-axis, a comparison has been performed between FWHM models generated based on one and 100 randomly chosen spectra of a Glioblastoma (GB) tissue MALDI-FTICR-MSI measurement in both positive and negative ion modes (total of four measurements; **Figure 4.2**). The results illustrate that a single spectrum could indeed be enough to generate a FWHM model for an entire MSI measurement. Also, when all four fitted models are superimposed, it can be seen in **Figure 4.2c** that the chosen ion mode has rather no influence on the FWHM model outcome, which is theoretically

expected (see **section 3.3**). Moreover, six arbitrary peaks taken from the sampled positive and negative ion mode spectra were compared, such that the corresponding FWHM values were manually measured by the vendor software and estimated based on the fitted FWHM curves (**Figure 4.2d**). The differences observed ranged between 0.0001 Da and 0.0021 Da for the lower and higher mass range, respectively.
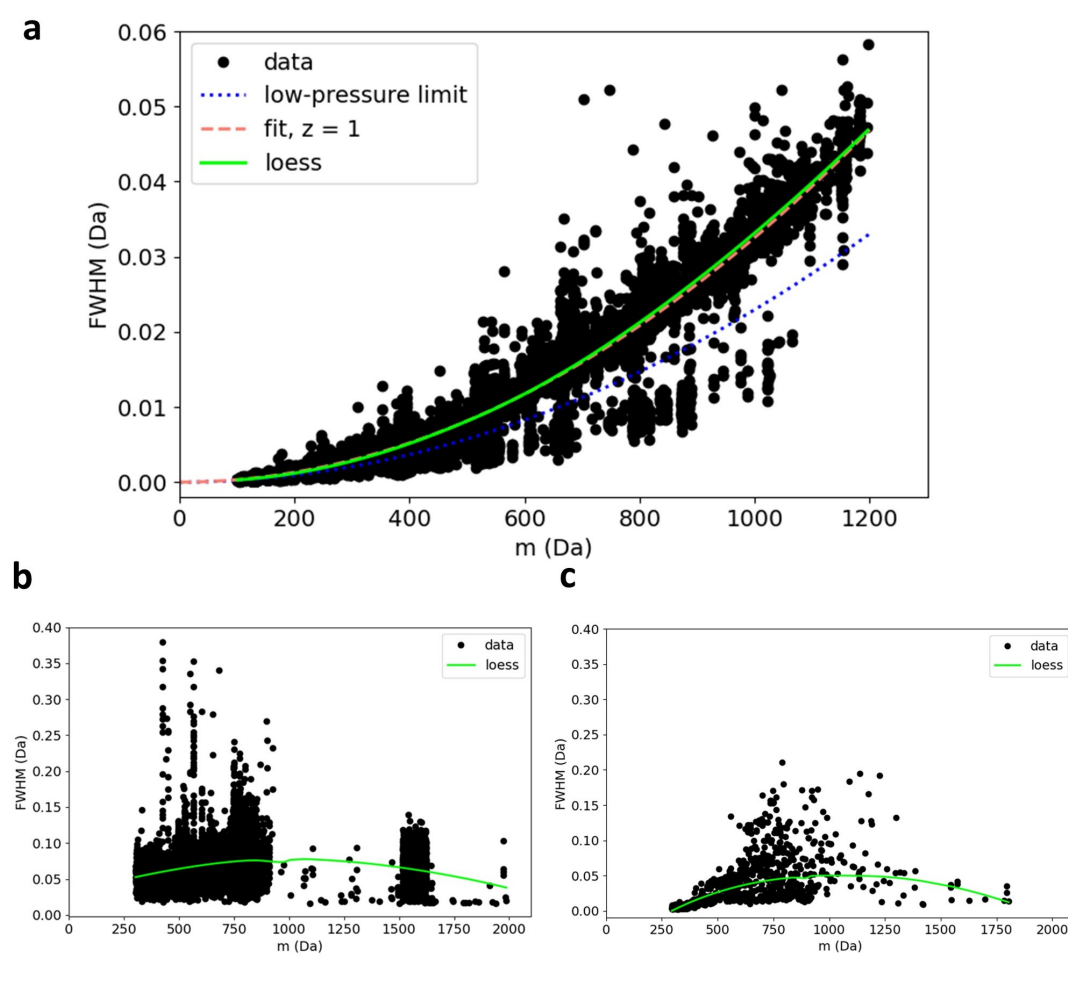

FIGURE 4.1: Comparison of fitted full-width at half-maximum (FWHM) curves as a function of ion mass for a) FTICR, b) rapifleX TOF and 3) timsTOFflex MALDI MSI devices. For every case, 100 randomly chosen mass spectra were evaluated for the FWHM curve via locally estimated scatter-plot smoothing (LOESS; green curve). Panel **a** shows a comparison between the calculated theoretical FWHM vs mass relationship excluding ion collisions (low-pressure limit; dashed blue curve; **Equation 3.1**) and including ion collisions (dashed pink curve; **Equation 3.2**; z is the ion charge) on one hand, and the empirical FWHM vs m/z based on the estimated FWHM values (solid green curve; LOESS) for the MALDI-FTICR-MSI data. The estimated FWHM model based on empirical data closely follows the FWHM theoretical expectation for the mass spectrometer. Figure was adapted from Abu Sammour et al.[142] with partial contribution from S. Schmidt and with permission from Springer Nature.
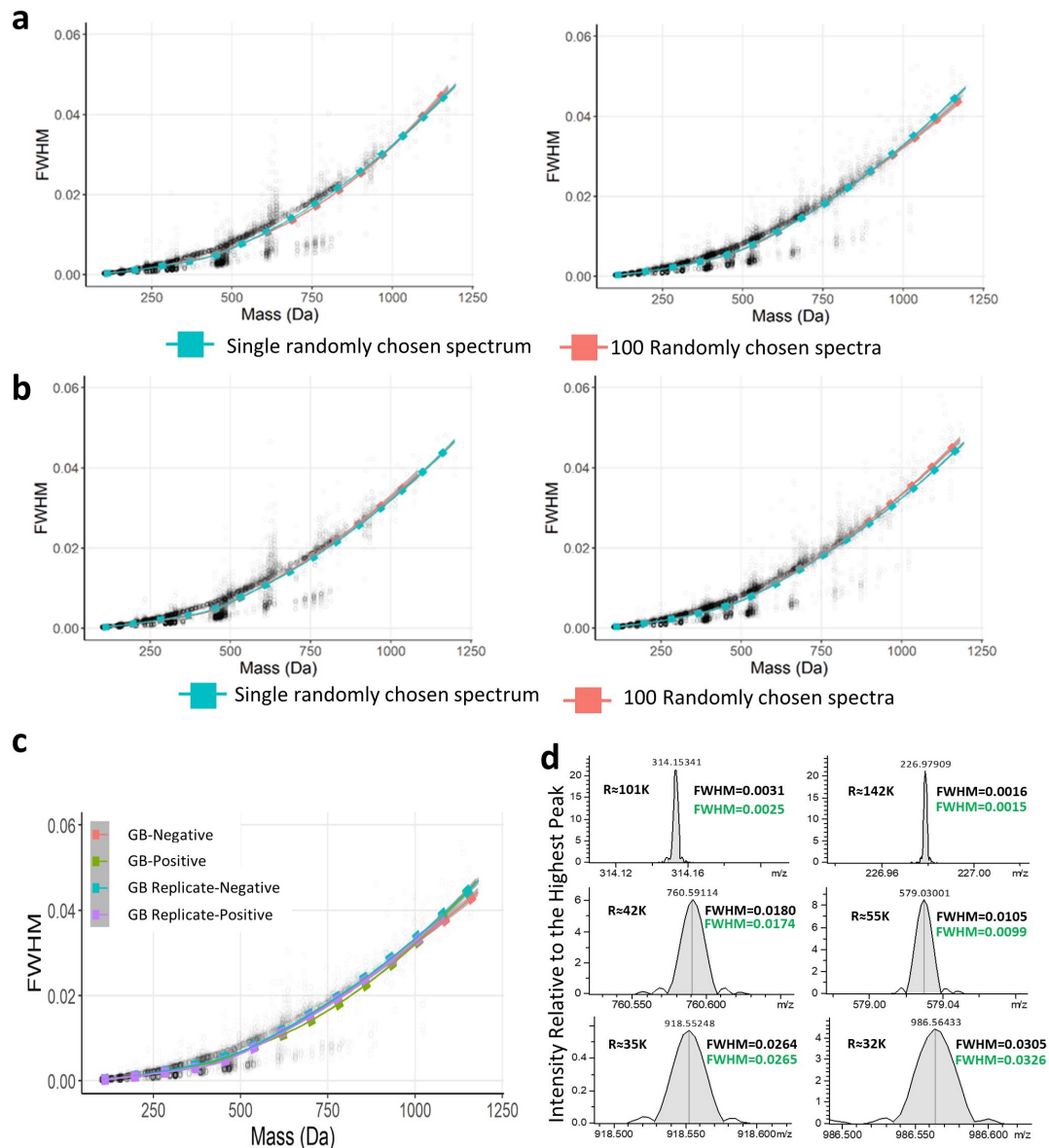
FIGURE 4.2: Modeling FWHM as a function of *m/z* for MALDI-FTICR-MSI data for the human Isocitrate Dehydrogenase-Wild Type (IDH-WT) glioblastoma (GB) tissue section and its serial section as a technical replicate (**section 3.1.2**; **Figure 4.9a**). **a)** locally-estimated scatter-plot smoothing (LOESS) curves were fit to FWHM vs *m/z* data points for this GB tissue data based on a single versus 100 randomly chosen spectra for the positive ion- (left panel) and negative ion (right panel) modes. **b)** Same as **a** but created for the GB tissue replicate data. **c)** **a** and **b** superimposed showing similar behavior of FWHM fitted curves for data that has been measured with the same measurement parameters. **d)** Six arbitrary peaks taken from the sampled positive ion (left column) and negative ion (right column) mode spectra in **c**. The corresponding FWHM values (black) are displayed as provided by the vendor software (DataAnalysis version 5.3; Bruker Daltonics) and as estimated based on the fitted FWHM curves (green). Figure was adapted from Abu Sammour et al.[142] with partial contribution from S. A. Mohammed and with permission from Springer Nature.

4.3 Gaussian vs Uniform Mass-window Weighting

The preceding section described the empirical modeling of FWHM as function of *m/z* for any given MALDI-MSI data that could be used to estimate peaks' FWHM values (and hence the mass resolving power) at any given *m/z* value. This is then used to calculate the mass-window width needed for rendering MOI ion intensity images in a user-independent and device-, measurement- and mass range-appropriate way. This has been achieved by exploiting the direct relation between the FWHM and the standard deviation σ_w of a hypothetical Gaussian that could be used to represent the theoretical MOI peak shape and, hence, its extent[35,48], which is governed by FWHM $= 2\sqrt{2\,ln2}\,\sigma_w$ (see **section 3.3**). This enables data-driven calculation of the mass-search-window width taken as $m_{MOI} \pm 3\sigma_w$ (i.e. the span of the erected Gaussian-window; m_{MOI} is the MOI's *m/z* value).

The described Gaussian envelope helps not only in determining the extent of the MOI- and peaks' FWHM-specific mass-window but also provides a convenient framework for down-weighting proximal interfering signals in the vicinity of *m/z* MOI (**Figure 4.3**). This is achieved by assigning corresponding Gaussian weights for all peaks-of-interest (POIs; i.e. observed peak signals within the estimated mass-window; see **section 1.2**) such that, the further the measured *m/z* (= POI or interference in **Figure 4.3**) from the theoretical *m/z* (= MOI; dashed black line in **Figure 4.3**), the lower the weight it receives in the final ion representation.
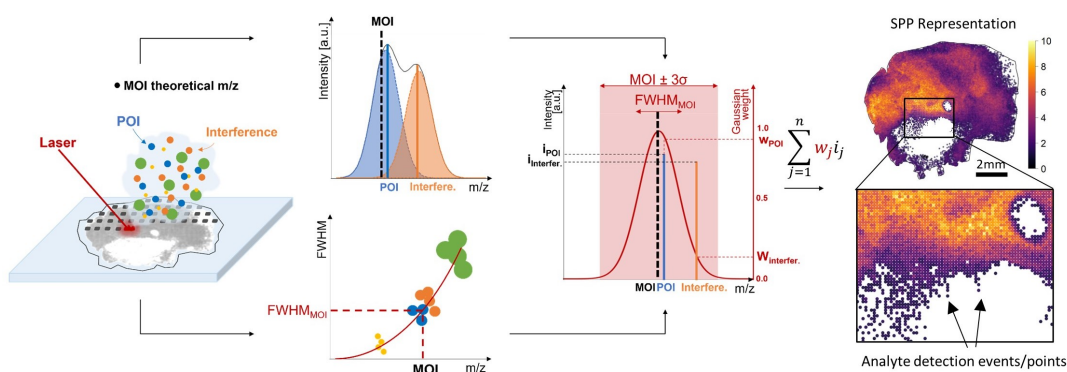

FIGURE 4.3: Data-dependent Gaussian weighting of ion intensities and transformation into a spatial point pattern (SPP) representation of a molecule-of-interest (MOI). Full-width at half-maximum (FWHM) values are computed for all peaks of a randomly chosen full profile mass spectrum and curve-fitted to model FWHM as a function of *m/z*. For any *m/z* MOI (dashed black line), a Gaussian envelope is computed whose standard deviation σ_w is inferred from the estimated FWHM at *m/z* MOI. All observed peaks (peak-of-interest, i.e. POI: solid blue line; interference: solid orange line), which fall within the span of the calculated Gaussian envelop centered at *m/z* MOI, are Gaussian-weighted, thereby down-weighting proximal interfering signals. Figure was adapted from Abu Sammour et al.[142] with partial contribution from M. Rittel and with permission from Springer Nature.

To explore the effects of Gaussian mass-window weighting, MALDI-FTICR-MSI data of an Isocitrate Dehydrogenase-Wild Type (IDH-WT) glioblastoma (GB) sample (**section 3.1.2**) was artificially "contaminated" with a random Gaussian noise source by computationally spiking in an interfering signal at successive mass intervals (multiples of σ_w) away from an example MOI, PE(20:1)[M+Na]$^+$ (**Figure 4.4**). Pixel-wise mean squared error (MSE) between raw data image and the artificially contaminated version was computed at increasing *m/z* distances measured away from *m/z* MOI for both, uniform and Gaussian mass-window weighting within the extent of the estimated mass-window (**Figure 4.4b**). Not surprisingly, Gaussian mass-window
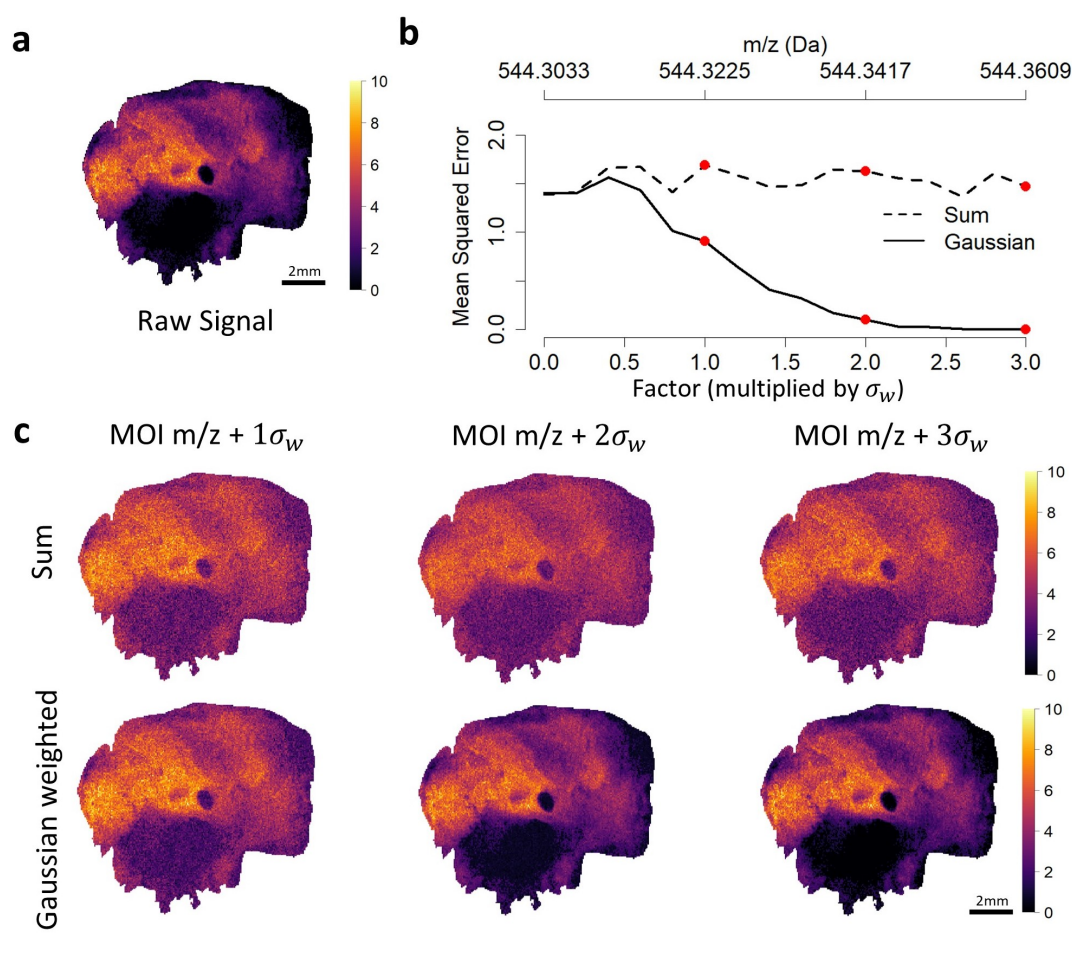

FIGURE 4.4: The effect of Gaussian mass-window weighting on an exemplary molecule-of-interest (MOI), PE(20:1)+Na$^+$ (monoisotopic *m/z* 544.3009; FDR $\leq$ 0.2), „contaminated" with an artificial noise source (see **Figure 4.18ab**; interference type spiked at a close proximity of *m/z* MOI). **a)** Raw ion image of *m/z* 544.3009 of an MALDI-FTICR-MSI Isocitrate Dehydrogenase-Wild Type (IDH-WT) glioblastoma (GB) data (estimated FWHM = 0.0082; corresponding to σ_w = 0.0193). **b)** Pixel-wise mean squared error (MSE) between raw data image in **a** and artificially contaminated data image computed for increasing *m/z* distances measured in multiples of σ_w away from *m/z* MOI (MOI + Factor$\times\sigma_w$). Compared to the standard uniform mass window weighting (indicated as "sum"; dashed line in **b**), Gaussian mass-window weighting method handles interference noise (modeling proximal background signals) more effectively, which is also optically evident in the lower panel of **c**. Figure was adapted from Abu Sammour et al.[142] with permission from Springer Nature.

weighting was more effective in removing interference noise (modeling proximal background signals), as indicated by the computed MSE (**Figure 4.4b**) and by visual inspection (**Figure 4.4c**).

To further validate this approach, two adjacent MOIs*, phosphatidylserine PS(40:6) [M-H]$^-$ (*m/z* 834.5290) and C20:0 sulfatide (3'-sulfo) GalCer(38:1) [M-H]$^-$ (*m/z* 834.5770) were visualized in adjacent sagittal mouse brain sections (see **section 3.1.4**) for a cross-platform comparison using FTICR (**Figure 4.5**), timsTOF (**Figure 4.6**) and TOF (**Figure 4.7**) MALDI-MSI data. Here, for the MALDI-FTICR-MSI case shown in **Figure 4.5**, at a calculated mass resolving power of 45k corresponding to a $3\sigma_w$ of 0.0237 Da, a clear separation for both uniform and Gaussian mass-window weighting was expected. However, due to the presence of Fourier transform-specific artifacts, formally known as side lobes[162], the position of the upper side lobe signal of *m/z* 834.5290 (MOI1) was directly at the lower edge of the estimated (from data) mass-window of *m/z* 834.5770 (MOI2). This can be clearly observed in the centroided overview sum spectrum in lower panel of **Figure 4.5**. In uniform mass-window weighting, all observed POI are equally weighted and, therefore, the mentioned artifact directly interferes with the rendered ion intensity image of *m/z* 834.5770 (MOI2) resulting in a homogeneous intensity distribution for *m/z* 834.5770 (MOI2) throughout the tissue section ("sum"; **Figure 4.5**). The Gaussian mass-window weighting, on the other hand, successfully down-weights this interference, as indicated by the distinguishable intensity images for both MOIs.

For the case of MALDI-timsTOF-MSI of **Figure 4.6**, uniform mass-window weighting was ineffective in distinguishing the above two MOIs. The centroided overview sum spectrum in lower panel of **Figure 4.6** shows a clear overlap between the data-estimated mass-windows due to the lower mass resolving power ($\approx$ 15k at that mass range) compared to the case of MALDI-FTICR-MSI above. Despite this, Gaussian mass-window weighting was able to down-play the effects of proximal interfering peaks for both MOIs producing distinctive ion intensity images in accordance with the result obtained from MALDI-FTICR-MSI.

On the other hand, both POI weighting methods failed to differentiate between both MOIs for the MALDI-TOF-MSI case of **Figure 4.7** owing to the sub-standard mass resolving power of just about 5,000 for that particular measurement which resulted in almost a complete overlap between of the data-estimated mass-windows as seen in the centroided overview sum spectrum in lower panel of **Figure 4.7**.

---

*The presence of these two MOIs was first noted and reported by J.L. Cairns
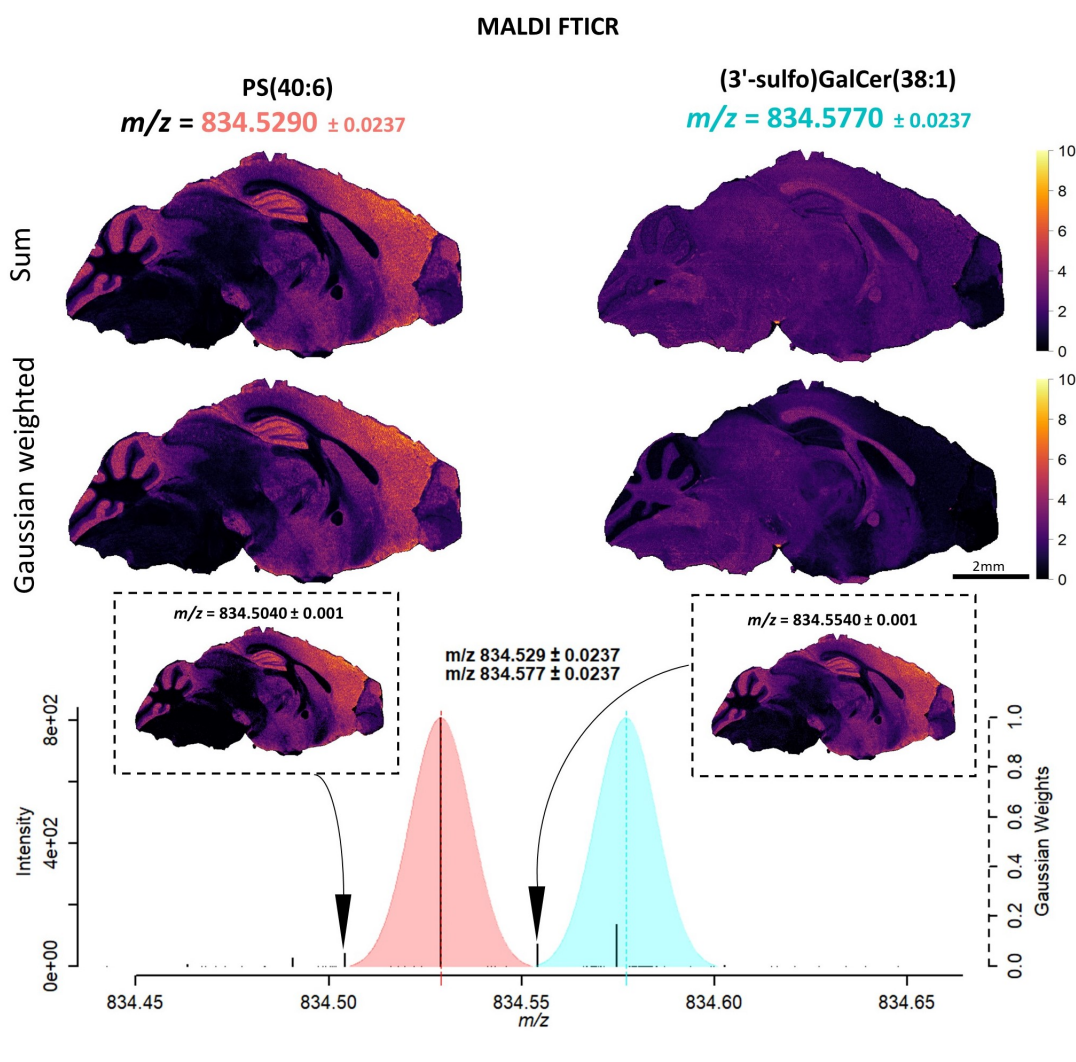
FIGURE 4.5: Comparison of Gaussian and uniform mass-window weighting shown on MALDI-FTICR-MSI data. Gaussian mass-window weighting (at *m/z* 834.5290, FWHM = 0.0186; σ_w = 0.0079; $3\sigma_w$ = 0.0237; mass resolving power ≈45k) of exemplary molecules-of-interest (MOIs), phosphatidylserine PS(40:6) [M-H]$^-$ (MOI1; *m/z* 834.5290; FDR ≤ 0.05; light red) and C20:0 Sulfatide (3'-sulfo) GalCer(38:1)[M-H]$^-$ (MOI2; *m/z* 834.5770; FDR ≤ 0.10; turquoise) shown for a sagittal mouse brain MALDI-FTICR-MSI data (**section 3.1.4**). The mass spectrum in the lower panel shows a centroided overview sum spectrum generated by summing up all peak intensities throughout the entire measurement. The color-coded Gaussians represent Gaussian mass-window weighting envelopes for the above mentioned MOIs (red dotted line for MOI1 and turquoise dotted line for MOI2). The mass window width is inferred from the mass resolving power at the respective MOI and taken as the calculated *m/z* MOI ± $3\sigma_w$ (i.e. the span of each Gaussian envelope width of the colored areas of each MOI individually) for both uniform mass-window weighting ("sum"; upper row) and Gaussian mass-window weighting (middle row). Note the two side lobe peaks[162] (black arrows) of MOI1 with the one at *m/z* 834.5540 falling within the calculated mass window of MOI2. This interfering peak results in a homogeneous intensity distribution for MOI2 throughout the tissue section based on uniform window weighting ("sum"), while the Gaussian–weighted method successfully down-weights this interference, as indicated by the distinguishable intensity images for both MOIs. Figure was adapted from Abu Sammour et al.[142] with permission from Springer Nature. The presence of MOI1 and MOI2 was first noted and reported by J.L. Cairns.
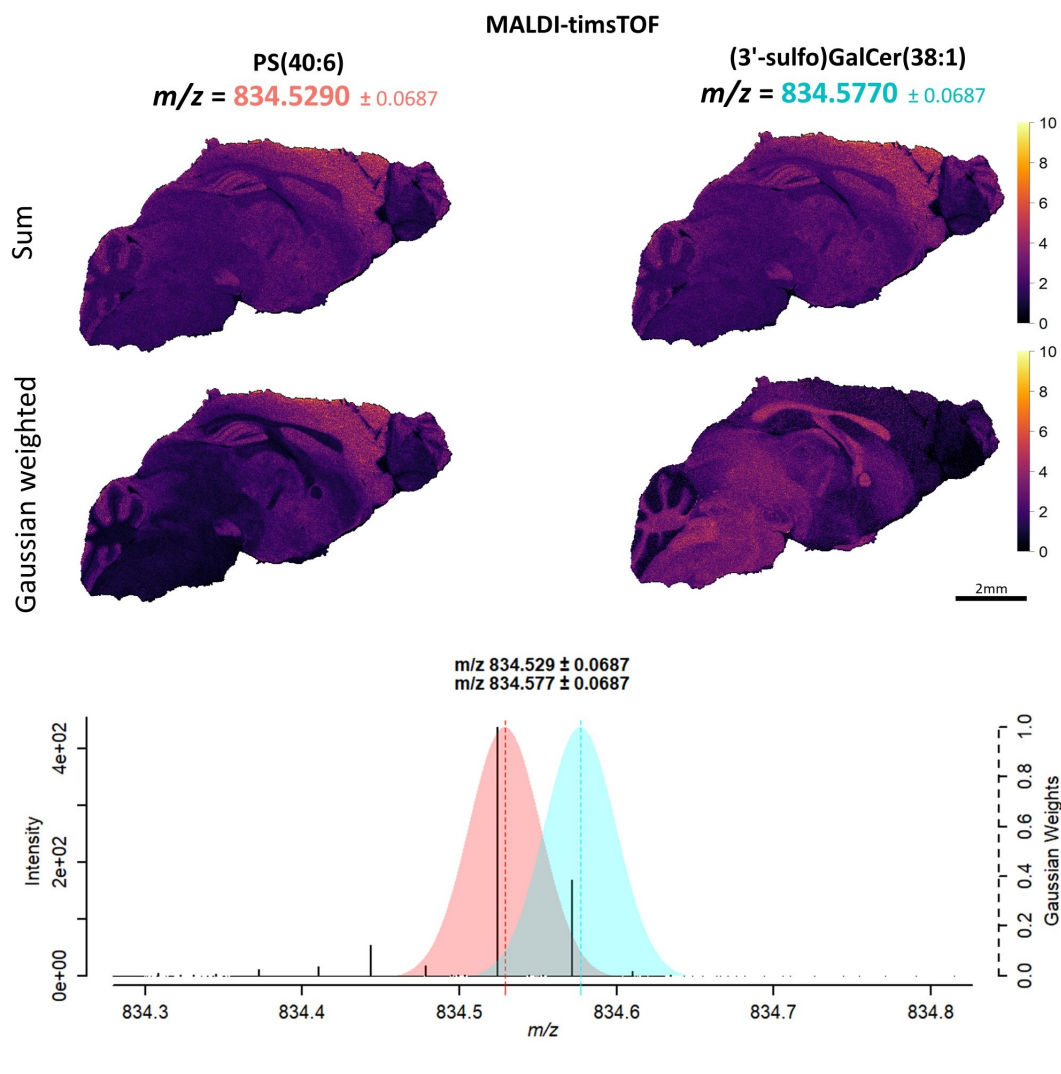
FIGURE 4.6: Comparison of Gaussian and uniform mass-window weighting shown on MALDI-timsTOF-MSI data. Gaussian mass-window weighting (at *m/z* 834.5290, FWHM = 0.0539; $\sigma_w = 0.0229$; $3\sigma_w = 0.0687$; mass resolving power ≈15k) of exemplary molecules-of-interest (MOIs), phosphatidylserine PS(40:6)[M-H]$^-$ (MOI1; *m/z* 834.5290; FDR ≤ 0.05; light red) and C20:0 Sulfatide (3'-sulfo) GalCer(38:1)[M-H]$^-$ (MOI2; *m/z* 834.5770; FDR ≤ 0.10; turquoise) shown for a sagittal mouse brain MALDI-timsTOF-MSI data. The mass spectrum in the lower panel shows a centroided overview sum spectrum generated by summing up all peak intensities throughout the entire dataset. The color-coded Gaussians represent Gaussian mass-window weighting envelopes for the above mentioned MOIs (red dotted line for MOI1 and turquoise dotted line for MOI2). The mass window width is inferred from the mass resolving power at the respective MOI and taken as the calculated *m/z* MOI ± $3\sigma_w$ (i.e. the span of each Gaussian envelope width of the colored areas of each MOI individually) for both uniform mass-window weighting ("sum"; upper row) and Gaussian mass-window weighting (middle row). The results indicate that Gaussian-weighting is able to down-play the effects of proximal interfering peaks. Figure was adapted from Abu Sammour et al. [142] with permission from Springer Nature. The presence of MOI1 and MOI2 was first noted and reported by J.L. Cairns.
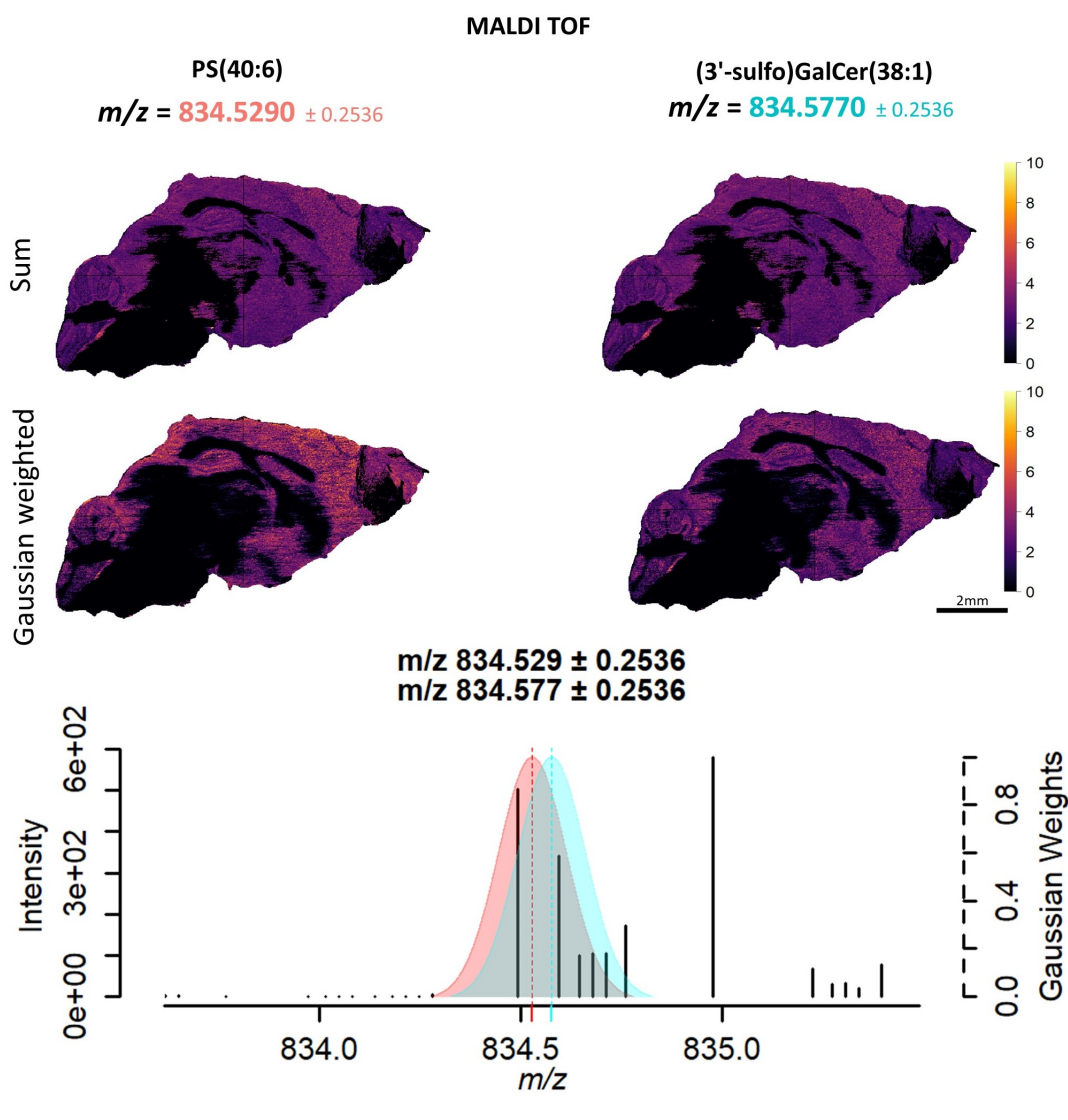
FIGURE 4.7: Comparison of Gaussian and uniform mass-window weighting shown on MALDI-TOF-MSI data. Gaussian mass-window weighting (at *m/z* 834.5290, FWHM = 0.1991; σ_w = 0.0845; $3\sigma_w$ = 0.2536; mass resolving power $\approx$5k) of exemplary molecules-of-interest (MOIs), phosphatidylserine PS(40:6)[M-H]$^-$ (MOI1; *m/z* 834.5290; FDR $\leq$ 0.05; light red) and C20:0 Sulfatide (3'-sulfo) GalCer(38:1)[M-H]$^-$ (MOI2; *m/z* 834.5770; FDR $\leq$ 0.10; turquoise) shown for sub-standard (used on purpose) sagittal mouse brain MALDI-TOF-MSI data. The mass spectrum in the lower panel shows a centroided overview sum spectrum generated by summing up all peak intensities throughout the entire dataset. The color-coded Gaussians represent Gaussian mass-window weighting envelopes for the above mentioned MOIs (red dotted line for MOI1 and turquoise dotted line for MOI2). The mass window width is inferred from the mass resolving power at the respective MOI and taken as the calculated *m/z* MOI $\pm 3\sigma_w$ (i.e. the span of each Gaussian envelope width of the colored areas of each MOI individually) for both uniform mass-window weighting ("sum"; upper row) and Gaussian mass-window weighting (middle row). The mass resolving power of this measurement was insufficient for distinguishing the mentioned MOIs as was possible with MALDI-FTICR-MSI (**Figure 4.5**) and MALDI-timsTOF-MSI (**Figure 4.6**). Figure was adapted from Abu Sammour et al.[142] with permission from Springer Nature. The presence of MOI1 and MOI2 was first noted and reported by J.L. Cairns.

4.4 Probabilistic Spatial Mapping of Biomolecules in MSI

This work proposes an alternative way of studying the spatial distribution of MOIs in a tissue samples and is based on the corresponding study of Abu Sammour et al.[142] The preceding two sections showed how the the proposed *moleculaR* framework introduces i) user-independent rendering of ion intensities where the mass-window is estimated based on the mass-resolving power of the mass spectrometer (**section 4.2**) and ii) a new mass-window weighting scheme which down-plays interfering background signals (**section 4.3**). More importantly, this work proposes a user-independent spatial interpretation of the distribution of MOI's signal relative to the tissue morphology via spatial probabilistic mapping. In the following subsections, an attempt is made to visually explain, evaluate, showcase and validate the methods described in **sections 3.6-3.12** of **Chapter 3**.

4.4.1 Molecular Probabilistic Maps (MPMs)

The main idea of this approach is to compare the MOI's spatial distribution against a complete spatial randomness (CSR) model to find areas which exhibit statistically significant non-random spatial patterns of MOI intensities independent of how an end-user may perceive its (i.e. MOI's) spatial relative abundance or deficiency.

The creation of the CSR model requires a gridless representation of the centroided MSI data, because creating an MOI-based CSR model within the same spatial domain (i.e. on a spatial grid) would directly violate the randomness criterion of such models (see **section 3.5** for details). To achieve this, MOI pixel intensities (centroided; SNR ≥ 3) are converted into a spatial point pattern (SPP) representation[152] as follows: Once MOI's pixel intensities are computed according to the Gaussian mass-window weighting method (**section 4.3**), these pixels are then represented by marked data points (i.e. data points carrying ion intensities) within an SPP of MOI signals. The locations of these data points are the MSI-pixels x, y-coordinates placed in a spatial 2D contour representing the tissue section as shown in the rightmost tissue illustration of **Figure 4.3** and **Figure 4.8a**.

Next, to create the CSR model corresponding to a given MOI, random spatial permutation (i.e. spatial "reshuffling") is applied to the data points of the MOI's SPP, until they assume a homogeneous spatial Poisson process[152], which is then used as the spatial null distribution for significance testing (**Figure 4.8a**). As a consequence of applying kernel density estimations (KDE) via an isotropic Gaussian on both sides (see **section 4.4.4**), the sample distribution of the intensities, $f_{CSR}(k)$ in **Figure 4.8a**, derived from the CSR spatial density image, is expected and observed to converge towards a normal distribution (see **section 4.4.4**). This then forms the basis for a pixel intensity-wise significance testing based on the CSR null distribution to isolate intensities of MOI's density image that are unlikely to occur if generated by a random spatial process. **Figure 4.8b** provides an illustration of this process: For each pixel

intensity value in the MOI's spatial density function, $\rho_{MOI}(x,y)$, a lower- and upper-tail p-values are computed based on the null distribution $f_{CSR}(k)$ resulting in two spatial maps of lower and upper tail p-values $P_{lwr}(x,y)$ and $P_{upr}(x,y)$ in **Figure 4.8b**, respectively. These p-values are then Benjamini-Hochberg-corrected. Spatial null-hypothesis significance testing is carried out against a significance level α of 0.05.

Consequently, MPM hotspot and coldspot contours are defined as locations where the null-hypothesis is rejected for the upper- or lower-tail corrected p-values, thus
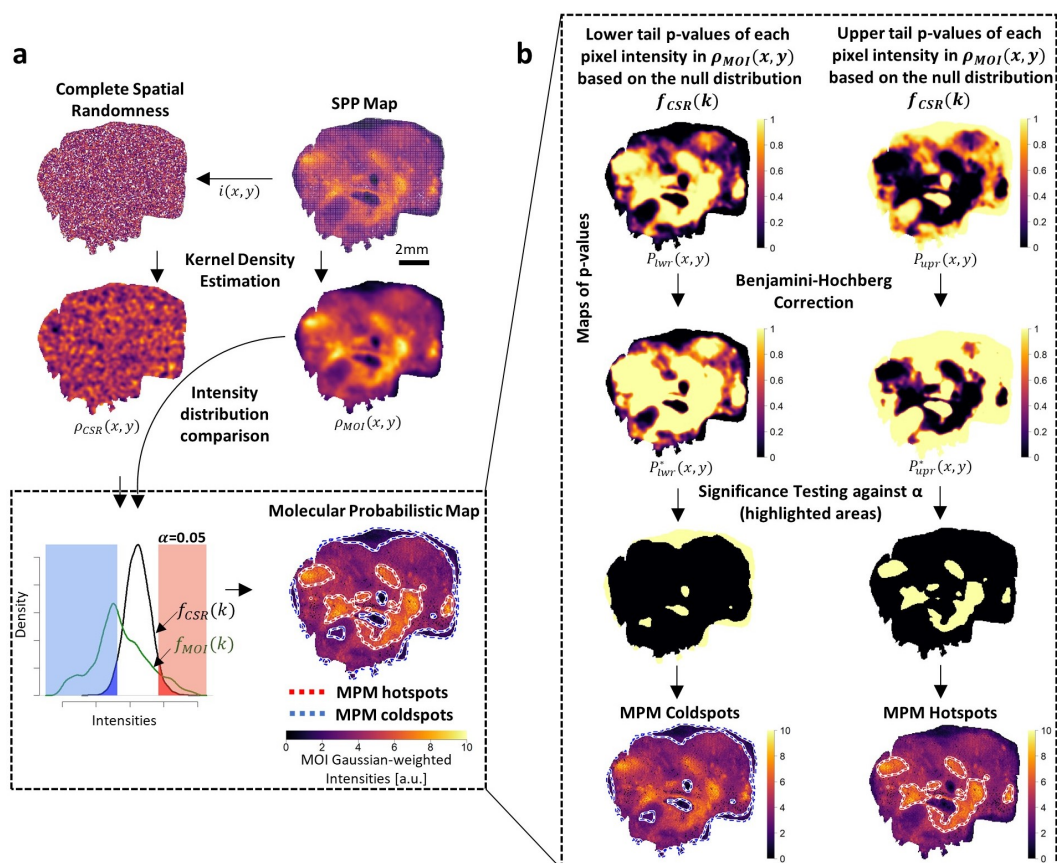

FIGURE 4.8: Molecular Probabilistic Map (MPM) computational workflow. **a)** A corresponding complete spatial randomness (CSR) model is created for each molecule-of-interest's (MOI; here SM(d36:4)[M+H]$^+$; FDR $\leq$ 0.10; FTICR MSI) spatial point pattern (SPP) with equal spatial point density. Kernel density estimation (KDE) is applied for both, thus resulting in weighted spatial density functions, $\rho_{MOI}(x,y)$ and $\rho_{CSR}(x,y)$. The intensity distribution function $f_{CSR}(k)$, which converges to a normal distribution (**Figure 4.12**), then serves as the null distribution against which the pixel intensities of $\rho_{MOI}(x,y)$ are tested. **b)** For each pixel intensity value in $\rho_{MOI}(x,y)$ lower and upper tail p-values are computed based on the null distribution $f_{CSR}(k)$ resulting in two spatial maps of lower and upper tail p-values $P_{lwr}(x,y)$ and $P_{upr}(x,y)$, respectively. These p-values are then Benjamini-Hochberg corrected and null-hypothesis significance testing is carried out against a significance level α of 0.05. MPM hotspots (red/white contours) and coldspots (blue/white contours) are accordingly defined as locations where the null-hypothesis is rejected for the upper or lower tail corrected p-values, respectively. Figure was adapted from Abu Sammour et al. [142] with permission from Springer Nature.

signifying areas of significant MOI relative spatial abundance or deficiency, respectively (**Figure 4.8**). MPMs are therefore composite representations of MOI's spatial distribution on a raster grid with data-dependent Gaussian weighted intensities and superimposed hotspot and/or coldspot contours indicating areas of statistically significant non-random spatial patterns of MOI intensities.

Spatial probabilistic mapping can be used to outline MOIs' significant relative spatial abundance or deficiency relative to vital tumor regions as inferred from a neuropathologist's annotation. To demonstrate this, two example MOIs, sphingomyelin SM(d36:4)[M+H]$^+$ (*m/z* 725.5592; FDR $\leq$ 0.10) and the phosphatidylserine PS(36:1)[M-H]$^-$ (*m/z* 788.5447; FDR $\leq$ 0.05), have been visualized in an neurooncology example of a fresh-frozen tissue section of an IDH-WT GB (**Figure 4.9ab**). In the typical interrogation procedure employed in MSI, based on his own visual perception of the intensity values, an end-user will roughly judge whether the shown MOIs had a relatively higher (or lower) spatial abundance in the viable tumor area of the GB sample in **Figure 4.9b** (green mesh). MPMs, on the other hand, provide MOI hotspot designations based on a probabilistic model indicating that PS(36:1)[M-H]$^-$ but not SM(d36:4)[M+H]$^+$, had higher relative spatial abundance in the viable tumor (and surrounding) area, as indicated by the respective MPM hotspot contours. Contrary to PS(36:1)[M-H]$^-$, the method showed a coldspot for SM(d36:4)[M+H]$^+$ in the viable tumor region indicating statistically significant relative spatial deficiency (**Figure 4.9b**).

Since the analytical ground-truth for the above mentioned metabolites in the GB example were unknown, MPM has been applied on another example for which MOI distributions had previously been published. As depicted in **Figure 4.9c**, applied on a MALDI-FTICR-MSI data of a sagittal mouse brain section, MPM of C24:1 sulfatide ((3'-sulfo)GalCer(d42:2)[M-H]$^-$; *m/z* 888.6240), previously reported to be present in the midbrain and white matter regions[163], revealed MPM hotspot contours that coincided well with these regions as referenced by the Allen mouse brain atlas[164] (purple regions **Figure 4.9c**; Allen Reference Atlas – Mouse Brain [brain atlas]. Available from atlas.brain-map.org).

moleculaR's MPM workflow was also applied on a more difficult scenario of a MALDI-TOF-MSI measurement of a brain tissue sample of an Alzheimer's disease mouse model. Here a comparison was conducted between MPMs and the previously reported *PlaquePicker*[145] for their ability to detect sparsely distributed fine-structured amyloid peptide $A\beta_{1-38}$ (*m/z* 4060.5) plaques. Out of the box, MPM hotspots (red/white contours of **Figure 4.9d**) were able to localize pockets of $A\beta_{1-38}$ plaques referenced by *PlaquePicker* (pixels highlighted in red in **Figure 4.9d**). One notable distinction was that the generated MPM disregarded subsets of single-pixels assumed to be plaques by *PlaquePicker*. This could be attributed to the fact that, unlike *PlaquePicker*, which strictly relies on image-global intensity thresholding, MPMs also
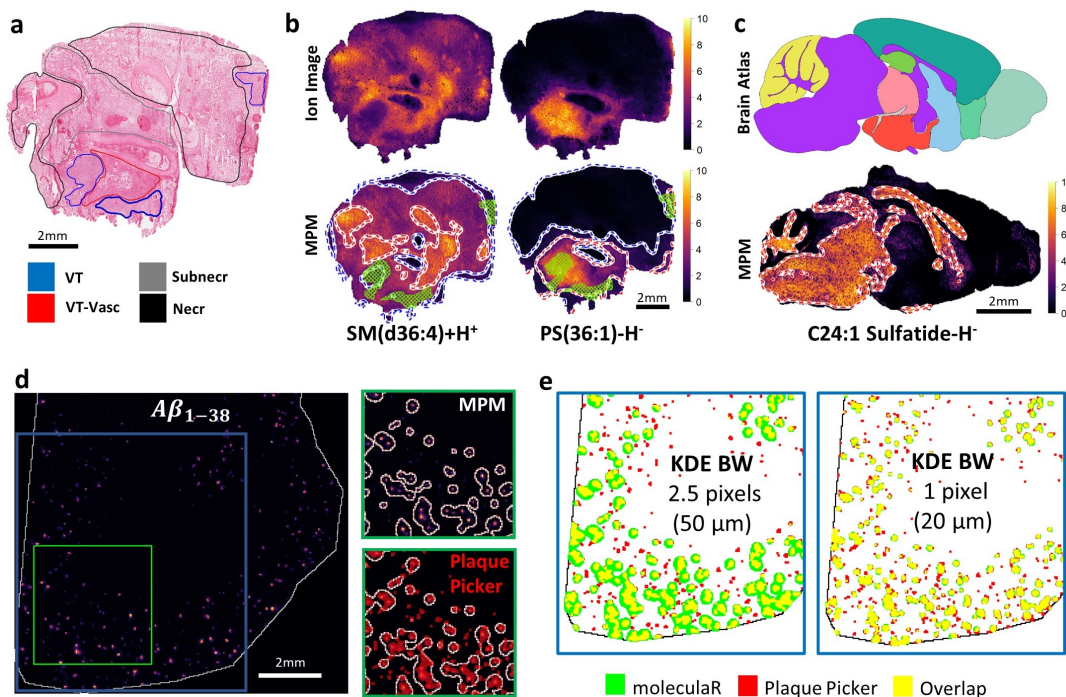
FIGURE 4.9: Molecular probabilistic Maps (MPM) for spatial probabilistic mapping of MOI hotspot and coldspot contours indicating areas of increased and decreased, respectively, MOI relative spatial abundance in tissue. **a)** Hematoxylin and eosin (H&E)-stained human glioblastoma (GB) tissue section annotated by an expert neuropathologist (VT: vital tumor; VT-Vasc: vascularized vital tumor; Subnecr: pre-necrotic; Necr: necrotic). **b)** Comparison of MALDI-FTICR-MSI ion images and corresponding MPM hotspot (red/white) and coldspot (blue/white) contours of SM(d36:4)$[M+H]^+$ and PS(36:1)$[M-H]^-$ (FDR $\leq$ 0.10; FTICR MSI) relative to VT regions (green mesh). **c)** MPM of *m/z* 888.6240 (C24:1 Sulfatide $[M-H]^-$; FTICR MSI), previously reported to be present in midbrain and white matter (fiber tracts) regions[163], in a sagittal mouse brain section. Hotspot contours correctly outline these regions, as referenced by purple areas in a brain atlas example (adapted from the Allen Reference Atlas - Mouse Brain; atlas.brain-map.org).[164] **d)** MPM of amyloid peptide $A\beta_{1-38}$ (*m/z* 4060.5; MALDI-TOF-MSI) in plaques in an Alzheimer's disease mouse model.[145] MPM hotspot contours localized pockets of $A\beta_{1-38}$-containing amyloid plaques, as referenced by the previously reported *PlaquePicker* method[145] (pixels highlighted in red). **e)** moleculaR enables the custom assignment of KDE bandwidth based on a theoretical size consideration. Out-of-the-box moleculaR (green spots) used data-inferred KDE bandwidth of 2.5 pixels (equivalent to 50 µm; left panel and also part **d**). MPMs correctly identified pockets of $A\beta_{1-38}$ plaques declared as such by *PlaquePicker* (red spots), but tends to not identify small, single-pixel-sized ones (left panel). Since $A\beta_{1-38}$ plaques are known to vary in shape and size, the KDE bandwidth was assigned to a single pixel length, corresponding to the smallest possible scale of 20 µm (i.e. the spatial resolution limit of the measurement) or 400 µm^2 pixel area. The resulting hotspot contours provide a more precise overlap (yellow) to the spots declared as $A\beta_{1-38}$ plaques by *PlaquePicker*. Figure was adapted from Abu Sammour et al.[142] with permission from Springer Nature. Part **c**, upper panel was contributed by M. Rittel.

take into account the spatial co-dependence of analyte signals which could be an important criteria for filtering out spurious outlier single-pixel signals.

Furthermore, MPMs also allows for manual fine-tuning of the KDE bandwidth (see **section 4.4.4**) against an orthogonal (e.g., Optical) method or inferred from what is theoretically expected for the object being imaged (ex. minimum theoretical

plaque diameter or mean diameter of single cells imaged in a single cell MSI data experiment). This his been tested on the amyloid plaques example above and shown in **Figure 4.9e**. When the KDE bandwidth value is adjusted to a single pixel length, corresponding to the smallest possible scale of 20 µm (i.e. the spatial resolution limit of the measurement) or 400 µm^2 pixel area, the resulting hotspot contours provide a more precise overlap (yellow areas in **Figure 4.9e**) to the spots declared as $A\beta_{1-38}$ plaques by *PlaquePicker*.

4.4.2 Cross-tissue Molecular Probabilistic Maps (CT-MPMs)

In MSI studies, it is not uncommon to encounter experiments that perform comparison of drug or metabolite distribution in test- versus reference tissues, e.g., those dosed with drugs or versus controls. Here, the proposed cross-tissue molecular probabilistic maps (CT-MPM) enables spatial statistical testing where normally only pooled signal intensities are used for statistical comparisons (e.g., box/violin-plots of **Figure 4.10b**) that disregard the spatial localization of MOIs under study (see **section 3.7**).

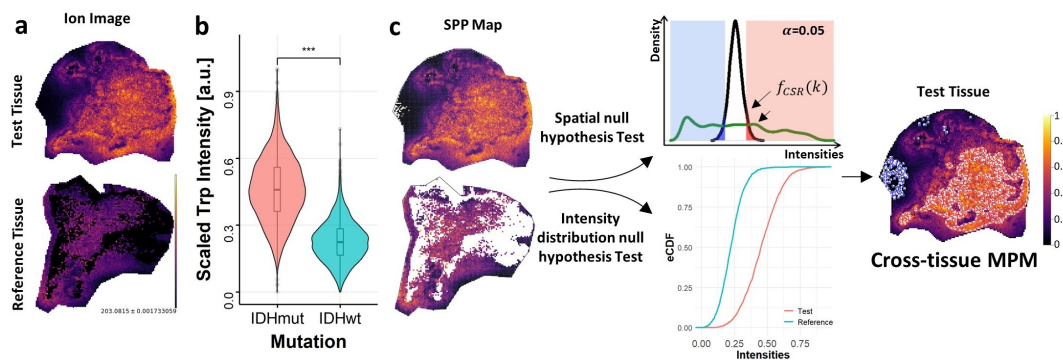The proposed CT-MPM workflow has been tested on previously published data

FIGURE 4.10: Cross-tissue molecular probabilistic maps (CT-MPMs) enable spatially-aware cross-tissue comparison of tryptophan [Trp-H]$^+$ in isocitrate dehydrogenase-mutant (IDH-MUT) (test tissue) with IDH-wild type (IDH-WT) glioma (reference tissue). **a)** Ion images of test and reference tissue samples showing the spatial distribution and intensity of tryptophan. **b)** Pooled signal intensities of tryptophan in the test and reference tissue samples are used to create a box/violin-plot which indicates significantly higher tryptophan levels in IDH-MUT- compared to IDH-WT glioma. This common practice, however, does not convey any statistical information on where the tryptophan signal had significantly higher accumulation relative to the test tissue morphology ($^{***}P < 0.001$; two-sided Wilcoxon rank sum test). **c)** CT-MPM enables spatial statistical testing of tryptophan localizing areas of significant cross-tissue relative spatial abundance. This is achieved by first finding hotspots/coldspots, i.e. areas of significant relative spatial abundance/deficiency as in **Figure 4.8**. Then all pixel intensities of the test tissue (here, IDH-MUT glioma) are tested against the empirical cumulative distribution function (eCDF) inferred from the pixel intensities of the reference tissue (here, IDH-WT glioma). Test tissue intensities which reject both the spatial null (= MOI is spatially randomly distributed) and Test-vs-Reference intensity distributions null hypotheses are designated as having significant cross-tissue relative abundance/deficiency. Figure was adapted from Abu Sammour et al.[142] with permission from Springer Nature.

of immunosuppression-associated tryptophan (Trp) in IDH-mutant (IDH-MUT) compared to IDH-WT glioma.[13] This was achieved by first finding areas of MOI's (= [Trp-H]$^-$; *m/z* 203.0815) significant relative spatial abundance/deficiency (i.e. testing against the spatial null hypothesis to find MOI hotspots/coldspots) as shown in **Figure 4.8**. Then the (distribution-free) empirical cumulative distribution function (eCDF) is inferred from the signal intensities of the reference tissue (IDH-WT glioma; tissue sample at the bottom of **Figure 4.10ac**) and all signal intensities of the test tissue (IDH-MUT glioma; tissue sample at the top of **Figure 4.10ac**) are tested against it in order to find the likelihood of them (i.e. signal intensities of the test tissue) being drawn from the signal distribution of the reference tissue (**Figure 4.10c**). The p-value threshold, beyond which the null hypothesis is rejected, is set to a significance level $\alpha = 0.05$ and Benjamini-Hochberg correction is applied to account for the inherent multiple testing problem. Only test tissue intensities, which reject both the spatial, and intensity sample distributions null hypotheses are designated as having significant cross-tissue relative abundance/deficiency (hotspot/coldspot contours of **Figure 4.10c**). The observed results demonstrated that the test tissue pixel intensities of Trp which were marked by hotspot contours are not homogeneously distributed across the tissue section. In other words, not all parts of the test tissue (IDH-MUT glioma) contained significantly higher Trp intensities compared to the reference tissue (IDH-WT glioma). This observation highlights the utility of CT-MPMs in cross-tissue spatial analysis, especially for comparing heterogeneous tissue samples.

4.4.3   Collective Projections Probabilistic Maps (CPPMs)

The previous sections discussed probabilistic mapping of metabolites/drugs from a single molecule perspective. The proposed framework *moleculaR* also proposes data-integrating probabilistic maps of larger metabolite (or other biomolecules) sets or ensembles, typically assembled based on MSI scientists' research interests (see **section 3.9**). MSI data for every metabolite in a molecular ensemble is transformed to its respective SPP representation, and then all of these SPPs are collectively projected into a single image space which is then followed by spatial probabilistic mapping using the proposed MPM workflow (**section 4.4.1**), hence the name: collective projections probabilistic maps (CPPMs; **Figure 4.11a**).

This computational framework permits spatial evaluation of composite numeric scores obtained by applying basic arithmetic operations on spatial point patterns of multiple MOIs (see **section 3.10**). For instance, **Figure 4.11b** illustrates how the SPPs of nucleotides [ATP-H]$^-$, [ADP-H]$^-$ and [AMP-H]$^-$ (upper row of **Figure 4.11b**) can be combined together to generate MPMs of their signal distribution, individually relative to their sum (bottom row of **Figure 4.11b**). Even more complex scores could be achieved such as the adenylate energy charge[14] (([ATP-H]$^-$ + $\frac{1}{2}$ [ADP-H]$^-$)/([ATP-H]$^-$ + [ADP-H]$^-$ + [AMP-H]$^-$); top right of **Figure 4.11b**), an index used commonly to indicate the energy status of biological cells by providing a score of the degree of
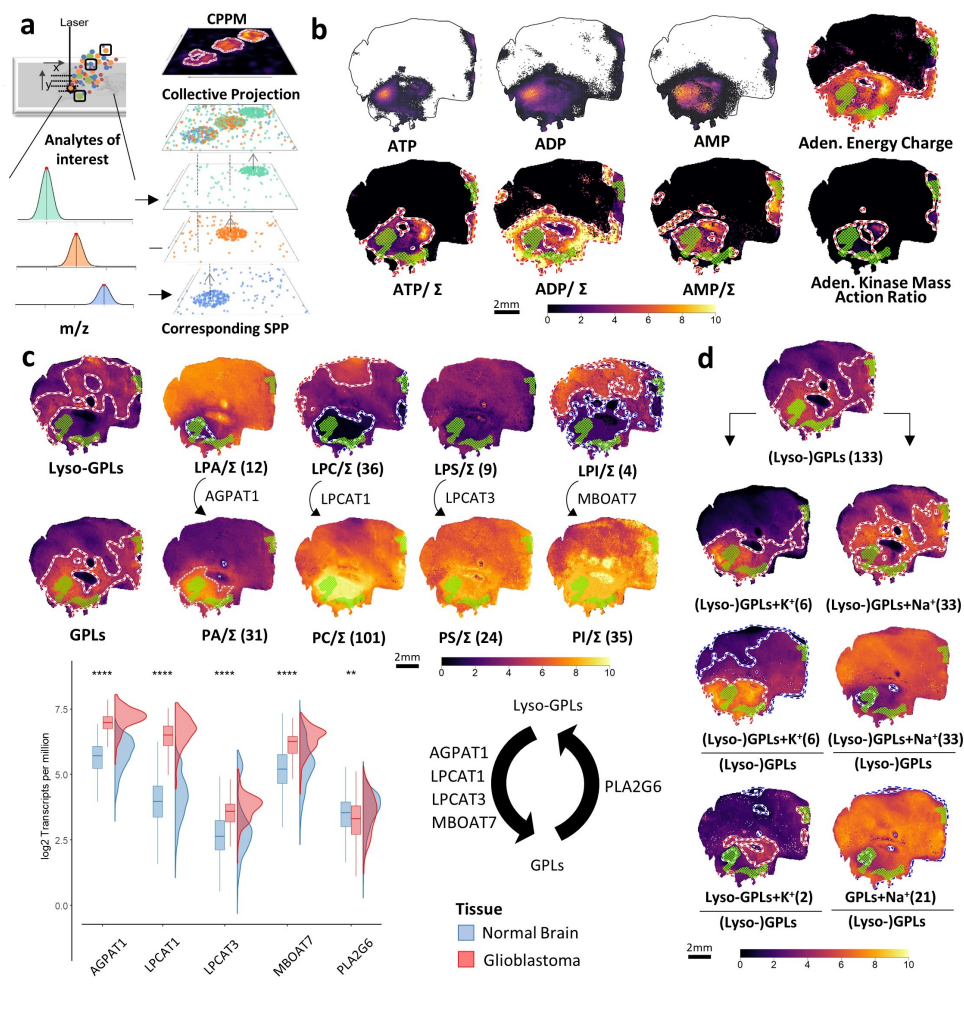
FIGURE 4.11: Collective projection probabilistic maps (CPPMs) of metabolite ensembles for visualization and interpretation of scores for energy metabolism, of glycerophospholipid (GPL) remodeling pathways, or of ion milieu. **a)** Spatial point patterns (SPPs) for a user-chosen ensemble of molecules-of-interest (MOIs) are collectively projected onto the same tissue plane. A molecular probabilistic map (MPM; as described in **Figure 4.8**) is then computed for this ensemble of SPPs. **b)** CPPMs enable basic arithmetic manipulations on SPPs of multiple MOIs such as the nucleotides $[ATP-H]^-$, $[ADP-H]^-$ and $[AMP-H]^-$ (FDR $\leq$ 0.2; upper row), e.g., normalization against the sum of these nucleotides (bottom row; Σ = $[ATP-H]^-$ + $[ADP-H]^-$ + $[AMP-H]^-$). CPPMs also allow for hotspot and coldspot contours for complex spatial quantitative scores such as adenylate energy charge[14,165] and adenylate kinase mass action ratio[166]. Green mesh indicates co-registered vital tumor regions (**Figure 4.9a**). **c)** CPPMs enable spatial investigation of GPL remodeling (Lands' cycle) in glioblastoma (GB) by visualizing lipid classes (FDR $\leq$ 0.5) on the same tissue plane. Upper panel: CPPMs of all lyso-GPLs and single classes (LPC, LPE, LPS, LPI; top row) compared to all GPLs and GPL classes (PC, PE, PS, PI; bottom row). Lyso- and non-lyso-GPL pairs are normalized to their sum (ex. for LPC and PC, Σ represents the sum of LPCs and PCs). Lower panel: Rainfall plots of the expression levels of selected Lands' cycle enzymes in normal brain (blue; GTEx data) and GB (red; TCGA data) both represented as log2 transcripts per million (two-sided Wilcoxon rank-sum test, ** P < 0.01, **** P < 0.0001). Numbers in parenthesis = METASPACE-verified[147] at FDR $\leq$ 0.2. **d)** Analysis of the tissue's alkali ion milieu. Top: CPPMs for all (lyso-)GPLs (= lyso-GPLs + GPLs; FDR$\leq$0.5). Left column from top: 1. CPPM of all potassium adducts of (Lyso-)GPLs, 2. of all potassium adducts of (Lyso-)GPLs relative to sum of all (lyso-)GPL adducts, and 3. CPPM of all potassium adducts of only lyso-GPLs relative to the overall sum of all (Lyso-)GPL adducts. Right column: As left column but showing sodium adducts. Figure was adapted from Abu Sammour et al.[142] with permission from Springer Nature. Part **c**, lower panel was contributed by A. Sadik.

the strictly regulated phosphorylation of the ATP-ADP-AMP system.[165] Moreover, adenylate kinase mass action ratio[166], also known as the adenylate kinase equilibrium constant[167], can also be computed as $[ATP-H]^- [AMP-H]^-/([ADP-H]^-)^2$ (bottom right of **Figure 4.11b**). This score reflects the relative concentrations of the adenine nucleotides and their effect on the reversible reaction ATP+AMP $\rightleftharpoons$ 2ADP.[168] Within the limits of error propagation (see **section 5.7**), such complex scores could be used to infer tissue's metabolic states relative to tissue morphology.

CPPMs also allow for the study of Lands cycle, a process of phospholipid remodeling in which the acyl chains of phospholipids are modified by deacylation and reacylation reactions resulting in new phospholipids with different acyl chain compositions.[169] CPPMs of all detected glycerophospholipids (GPLs) and their lyso-glycerophospholipids (lyso-GPLs) counterpart have been examined in the IDH-WT GB example described above as shown in **Figure 4.11c**. An enrichment of GPLs and concomitant depletion of lyso-GPLs was observed in the viable tumor of the IDH-WT GB tissue sample of **Figure 4.11c** and its serial section shown in **Supplementary Figure 8.1c**. The same could be said for the individual lipid classes of PC, PA, PS but less so of PI and their corresponding lyso-GPL cleavage products, LPC, LPA, LPS and LPI. Retrospective transcript expression profiling of Lands cycle enzymes revealed overexpression of various acyltransferase genes (*LPCAT1*, *AGPAT1*, *LPCAT3*, *MBOAT7*) in GB compared to normal brain tissue that support the CPPM-based assessment (**Figure 4.11c**).

Another set of examples that illustrates the type of analyses that CPPMs enable, examines the ion milieu makeup in cancer tissue by targeting potassium or sodium adducts of detected lipids in a tissue sample. As observed in **Figure 4.11d**, the CPPM of potassium adducts of all (lyso-)GPLs (i.e. GPLs plus lyso-GPLs) revealed their higher abundance in vital tumor and surrounding areas, whereas the CPPM of projected sodium adducts was more pronounced in necrotic tissue. Furthermore, repeating these computations but normalized by their sum (i.e. by all (lyso-)GPLs), further supported the above observation in addition to showing significant relative spatial deficiency (coldspot) in vital tumor for the projected sodium adducts of (lyso-)GPLs.

4.4.4 KDE Bandwidth Estimation Validation

KDE is a key step in the MPM workflow: i) It captures the overall spatial trend of the MOIs' intensities; ii) it forces f_{CSR} to converge to a normal distribution and, iii) being a low-pass filter, its application results in the desired by-product of smoothing technical variations and noise fluctuations when estimating hotspots/coldspots which has in turn a positive outcome on the method's tolerance to pixel-to-pixel batch effects, and section-to-section/slide-to-slide batch effects[40] (see **section 4.4.6**).

To test point **ii** above, namely the convergence of f_{CSR} (i.e. the sample distribution of intensities k of the weighted spatial density $\rho_{CSR}(x, y)$ as shown in **Figure 4.8a**) to a normal distribution as previously described in **section 4.4.1**, $f_{MOI}(k)$ and corresponding $f_{CSR}(k)$ were plotted for three arbitrary lipids detected in the IDH-WT GB tissue sample shown in **Figure 4.12**. When varying the KDE bandwidth, it can be observed, that while $f_{MOI}(k)$ does not necessarily converge onto a normal distribution for the range of bandwidths under consideration, as a consequence of the central limit theorem, the corresponding intensity distribution $f_{CSR}(k)$ approximates a normal distribution as the bandwidth increases, which could already be observed at smaller bandwidth values.
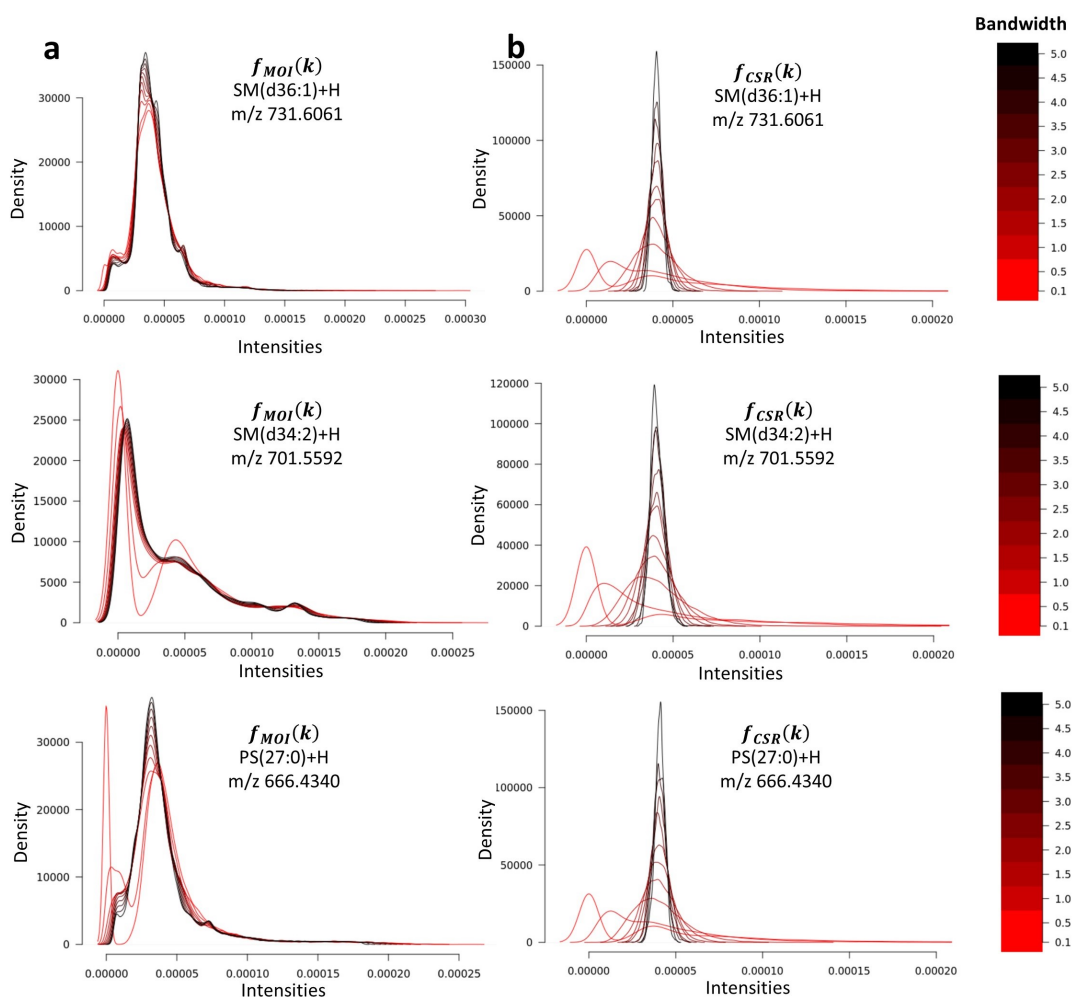

FIGURE 4.12: Intensity distributions $f_{MOI}(k)$ (first column) and $f_{CSR}(k)$ (second column) corresponding to the 2D spatial densities of the MOI, $\rho_{MOI}(x, y)$, and of the complete spatial randomness (CSR) model, $\rho_{CSR}(x, y)$, respectively, of three arbitrary *m/z* that putatively correspond to the indicated lipids (rows). While $f_{MOI}(k)$ does not necessarily converge onto a normal distribution for the range of bandwidths under consideration (first column), as a consequence of the central limit theorem, the corresponding intensity distribution $f_{CSR}(k)$ approximates a normal distribution as the bandwidth increases, even for smaller bandwidth values (second column). Figure was adapted from Abu Sammour et al.[142] with permission from Springer Nature.

Estimating an optimal data-dependent KDE scale (bandwidth) is of high importance, which, on its own, is a well-known challenge.[170] This is because MPMs are sensitive to the chosen kernel bandwidth h_{KDE} (see **section 3.8**). To prevent spatial over-smoothing, which is associated with high bandwidth numbers, this work proposes a method for KDE bandwidth estimation which takes into account the MOI's spatial autocorrelation[157] estimated over a scale-space representation[171] of the MOI intensity image. More precisely, the bandwidth h_{KDE} is varied iteratively and during each iteration the global Moran's I statistic, a measure of spatial autocorrelation, is determined. The optimal h_{KDE} is then determined by finding the point of maximum curvature, i.e. the "knee" point in the Moran's I vs h_{KDE} plot as shown in **Figure 4.13**.
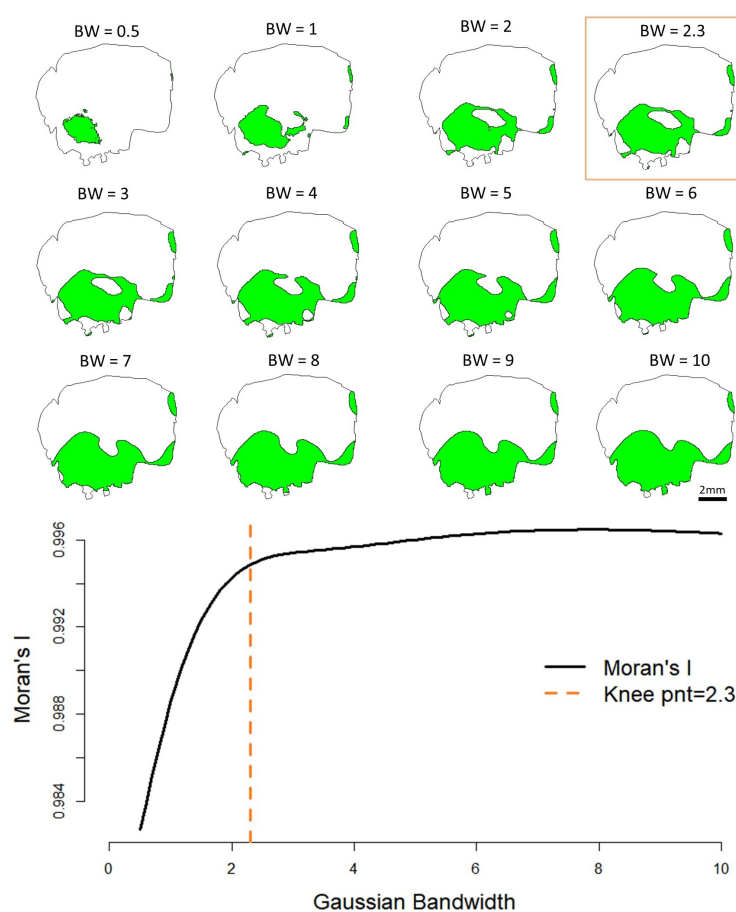

FIGURE 4.13: Bandwidth estimation for the kernel density estimation (KDE) procedure as part of the molecular probabilistic map (MPM) workflow (**Figure 4.8a**) evaluated for putative PS(36:1)[M-H]$^-$ at *m/z* 788.5447 (**Figure 4.9b**). The KDE bandwidth h_{KDE} is varied iteratively from values of 1 to 10 (i.e., pixels; multiples of $50\,\mu m$ for this measurement) in 0.5 incremental steps. During each iteration KDE is applied, and the Moran's I statistic, a measure of autocorrelation, is determined. The optimal h_{KDE} is then determined by finding the point in the Moran's I vs bandwidth h_{KDE} plot, at which the spatial autocorrelation levels-off, i.e. after which an increase in h_{KDE} does not result in a considerable increase in the spatial autocorrelation of the smoothed density image. This "knee" point is estimated via the *kneedle* method[158]. Figure was adapted from Abu Sammour et al.[142] with permission from Springer Nature.

This is the point, after which an increase in h_{KDE} does not result in a considerable increase in the spatial autocorrelation of the smoothed density image and at which it is expected that random pixel fluctuations are smoothed away while important spatial structures/features/patterns start dominating the spatial landscape.

To validate the proposed method described above, SPP data was simulated based on four different spatial patterns of ground-truths (see **section 4.4.5** for a detailed description). As depicted in **Figure 4.14**, MPM was applied iteratively for every simulated SPP type with step-wise assignments for the KDE bandwidth h_{KDE}, which
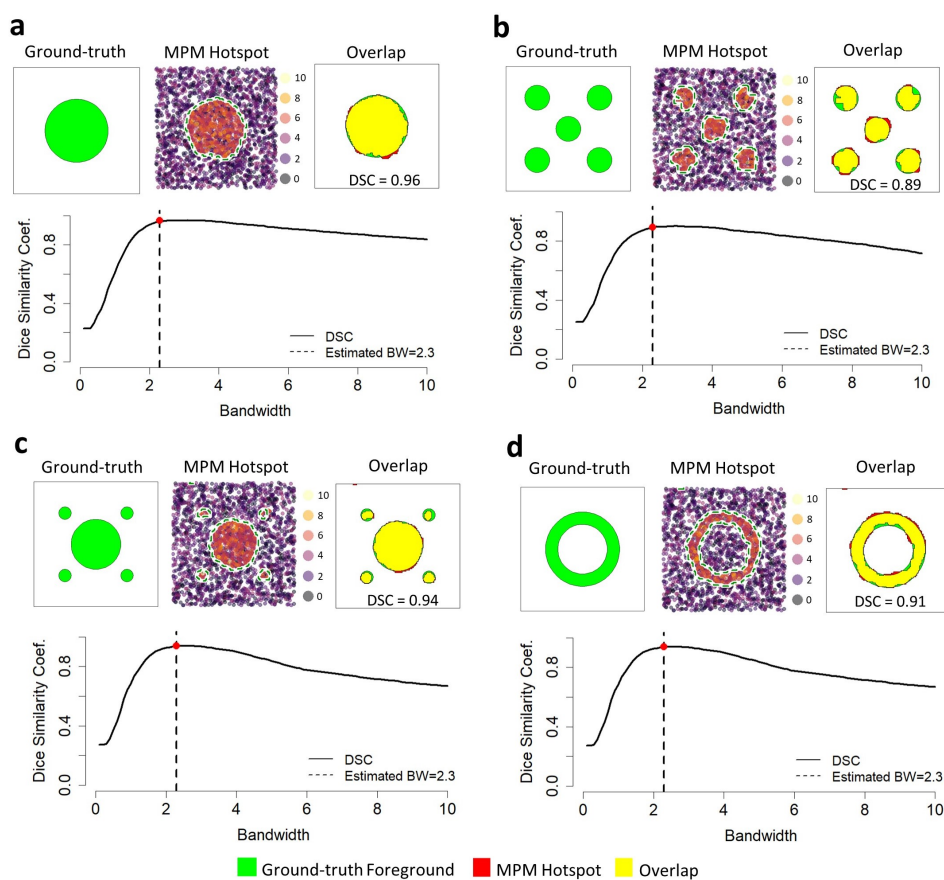

FIGURE 4.14: Use of simulated data (see **section 4.4.5**) for evaluating the proposed kernel density estimation (KDE) bandwidth estimation method (**section 3.8**; **Figure 4.13**) as part of the molecular probabilistic map (MPM) workflow. For each simulated spatial point pattern (SPP) in **a**, **b**, **c**, and **d**, MPM was estimated with the KDE bandwidth estimation method shown in **Figure 4.13** and the Dice similarity coefficient (DSC) was computed between the calculated hotspot contour (red) and the ground-truth shape (green) based on which the simulated SPP was created. DSCs of all simulation types showed high degree of overlap (yellow) at 0.96, 0.89, 0.94 and 0.91 for **a**, **b**, **c**, and **d**, respectively. Moreover, MPM was iteratively estimated for every simulated SPP type using an assigned KDE bandwidth h_{KDE}, which was varied from values of 0 to 10 length units in 0.1 incremental steps. During each iteration, DSC was computed between the estimated hotspot contour and the ground-truth shape used for generating the simulated SPP. The resulting curves suggest that the proposed KDE bandwidth estimation method of MPM coincides with the highest (i.e. optimum) DSC for all simulated SPPs. Figure was adapted from Abu Sammour et al.[142] with permission from Springer Nature.

was varied from values of 0 to 10 length units in 0.1 incremental steps. During each iteration, DSC was computed between the estimated hotspot contour and the foreground shape (representing high MOI abundance) of the ground-truth used for generating the simulated SPP. It can be observed from the Dice similarity coefficient (DSC) vs Bandwidth curves that the estimated KDE bandwidth (based on the proposed method described above) coincides with the highest (i.e. optimum) DSC for all simulated SPPs (shown as vertical dashed line in **Figure 4.14**). Additionally, DSCs of all simulated SPPs showed high degree of overlap (yellow areas in **Figure 4.14**) of more than 89%.

4.4.5   Assessment of *moleculaR*'s Performance on Simulated Data

In order to test the validity of the proposed MPM workflow, a computational method for generating artificial data that mimics a hypothetical analyte distribution according to a predefined spatial ground-truth has been attempted. Uniform Poisson SPPs of four different patterns of ground-truth were simulated as described in **section 3.11** and shown in **Figures 4.14-4.15**: i) Single central circle of radius 25 length units, ii) five equidistantly placed circles of 10 length units radius, iii) a ring-like structure with 30 and 20 length units for outer and inner radii, respectively and iv) a dominant central circle of 20 length units radius with four adjacent smaller ones of 5 length units radius each. Each of these patterns, representing heightened MOI presence (i.e. foreground), was placed within a square window of 100 length units denoting the background. Their Intensity values were sampled from above and below the upper quartile (i.e. Q3) of the empirical intensities of a MALDI-FTICR-MSI measurement of IDH-WT GB tissue sample (**Figure 4.9ab**) at *m/z* 544.3009 (PE(20:1)[M+Na]$^{+}$; FDR $\leq$ 0.2) for foreground and background, respectively.

When applying the MPM workflow on each of the simulated SPPs, MPM hotspots were able to reliably localize all foregrounds (green contours in the SPP plots in **Figures 4.14-4.15**) and identify points exhibiting significant relative spatial abundance (green points on density and surface plots in **Figure 4.15**). Moreover, as described in the preceding section, high degree of overlap between the detected hotspots and respective foreground shapes was observed as judged by the high DSC score of more than 0.89 (**Figure 4.14**).

It is important to note, that the simulated SPP of **Figure 4.15d** was specifically created to test whether larger foregrounds (i.e. large areas of high MOI abundance) would obstruct smaller ones by having too much weight in the resulting SPP. For this purpose, the foregrounds have been arranged into a central bigger circle of 20 length units radius and four adjacent smaller circles of 5 length units. Despite the big difference in foreground circle areas (smaller circles are 16 times smaller than the central one), MPM was able to correctly localize all four smaller local hotspots (**Figure 4.15d**) with high overlap between the estimated MPM hotspots and foreground shape indicated by a high DSC of 0.94 (**Figure 4.14c**).

Since SNR of MALDI-FTICR data is commonly high, and typically better than MALDI-TOF instruments, the same test above has been repeated on a more challenging case based on MALDI-TOF data. The MPM workflow was tested on simulated SPPs based on the same ground-truth patterns described above, this time sampling intensities from above and below the upper quartile of the empirical intensities of a MALDI-TOF-MSI measurement of a human gastrointestinal stromal tumor (GIST)
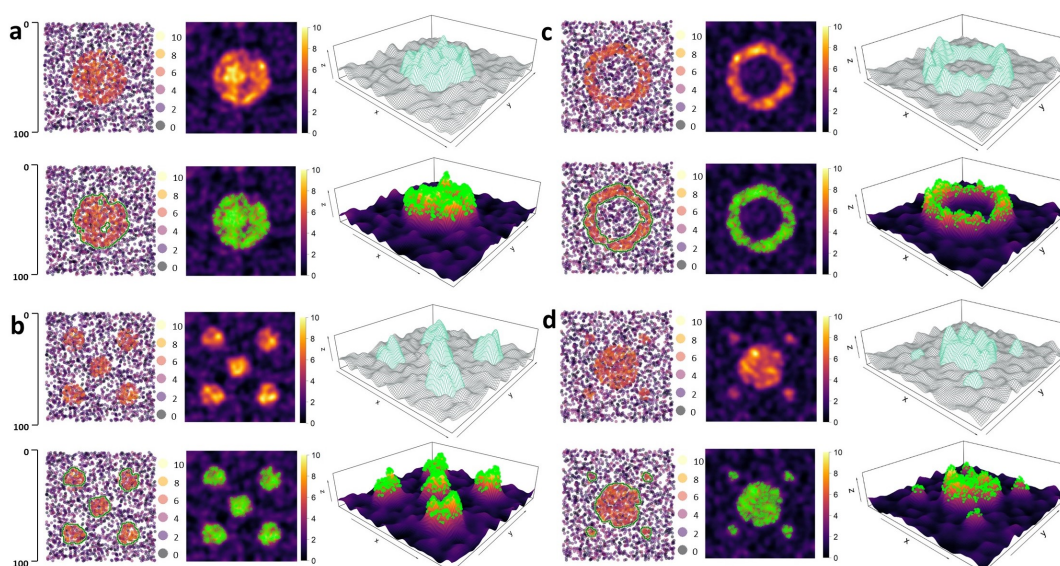

FIGURE 4.15: Molecular probabilistic maps (MPMs) correctly assign significant relative spatial abundance in simulated data. **a)** Synthetic homogeneous Poisson spatial point pattern (SPP) simulating an MOI spatial ground-truth with a circular central foreground of radius 25 length units embedded in a non-hotspot background (top-left; also see ground-truth in **Figure 4.14**). Intensity values were sampled from above and below the upper quartile (i.e. Q3) of the empirical intensities of a MALDI-FTICR-MSI measurement of a human isocitrate dehydrogenase-wild type (IDH-WT) glioblastoma (GB) tissue sample (**Figure 4.9a**) at m/z 544.3009 (PE(20:1)[M+Na]$^+$; FDR $\leq$ 0.2) for the foreground and background areas, respectively (foreground n$\approx$570 with spatial point density of $\approx$0.4 points per unit area; back¬ground n$\approx$1970 with spatial point density of $\approx$0.3 points per unit area; mean signal intensity of foreground/mean signal intensity background $\approx$2.3). The corresponding spatial density image (top row; middle) and 3D surface plots (top row; right) are shown. MPM contours were able to localize the simulated foreground correctly (green contours; bottom row; left) and identify points exhibiting significant relative spatial abundance (green points; bottom row; middle and right). **b)** Simulated SPP for an MOI spatial ground-truth similar to a with five identical circular foregrounds of 10 length units radius (foreground n$\approx$470; background n$\approx$1950; same spatial point density as in **a**; mean signal intensity of foregrounds/mean signal intensity background $\approx$2.3). MPM contours were able to localize and identify hotspot points in all foreground areas. **c)** Simulated spatial point pattern (SPP) showing a ring-like foreground with 30 and 20 length units for outer and inner radii, respectively (foreground n$\approx$520; background n$\approx$1950; same spatial point density as in a; mean signal intensity of foreground/mean signal intensity background $\approx$2.3). **d)** Simulated SPP with a central circle of 20 length units radius and four adjacent smaller circles of 5 length units radius as foregrounds (central circle area/peripheral circle area = 16; hotspot n $\approx$430; background n$\approx$1950; same spatial point density as in **a**; mean signal intensity of foregrounds/mean signal intensity background $\approx$2.3). Figure was adapted from Abu Sammour et al.[142] with permission from Springer Nature.

tissue sample (**Figure 4.32cde**) at 494.2662 m/z (imatinib $[M+H]^+$; SNR $\geq$ 3) for foreground and background, respectively. The MPM method was able to correctly identify points exhibiting significant relative spatial abundance within the simulated foreground (green points on density and surface plots in **Figure 4.16**).

Validation via simulated data was also attempted for CT-MPMs. As outlined in **section 3.7** and shown in **section 4.4.2**, CT-MPMs identify areas of the test tissue, which exhibit a statistically significant non-random spatial MOI abundance/deficiency pattern and contain intensities that are unlikely to belong to the distribution of MOI intensities in the reference tissue. To validate this cross-tissue variant of the MPM method, four cases of test and reference SPPs were simulated as depicted in **Figure 4.17**. In case (**a**) it is expected that both the spatial and test-vs-reference intensity

FIGURE 4.16: Molecular Probabilistic Maps (MPMs) correctly assign significant relative spatial abundance/deficiency in simulated data. For all four spatial ground-truths shown in **Figure 4.15**, intensity values were sampled from above and below the upper quartile of the empirical intensities of a MALDI-TOF-MSI measurement of a human gastrointestinal stromal tumor (GIST) tissue sample (**Figure 4.32e**) at *m/z* 494.2662 (imatinib $[M+H]^+$; SNR $\geq$ 3) for the ground-truth foreground (representing MOI high abundance) and background areas, respectively. Spatial parameters of the simulated SPPs were similar to the ones described in **Figure 4.15**.The MPM method was able to identify points exhibiting significant relative spatial abundance (green points on density and surface plots) in accordance with the corresponding ground-truth. Figure was adapted from Abu Sammour et al. [142] with permission from Springer Nature.
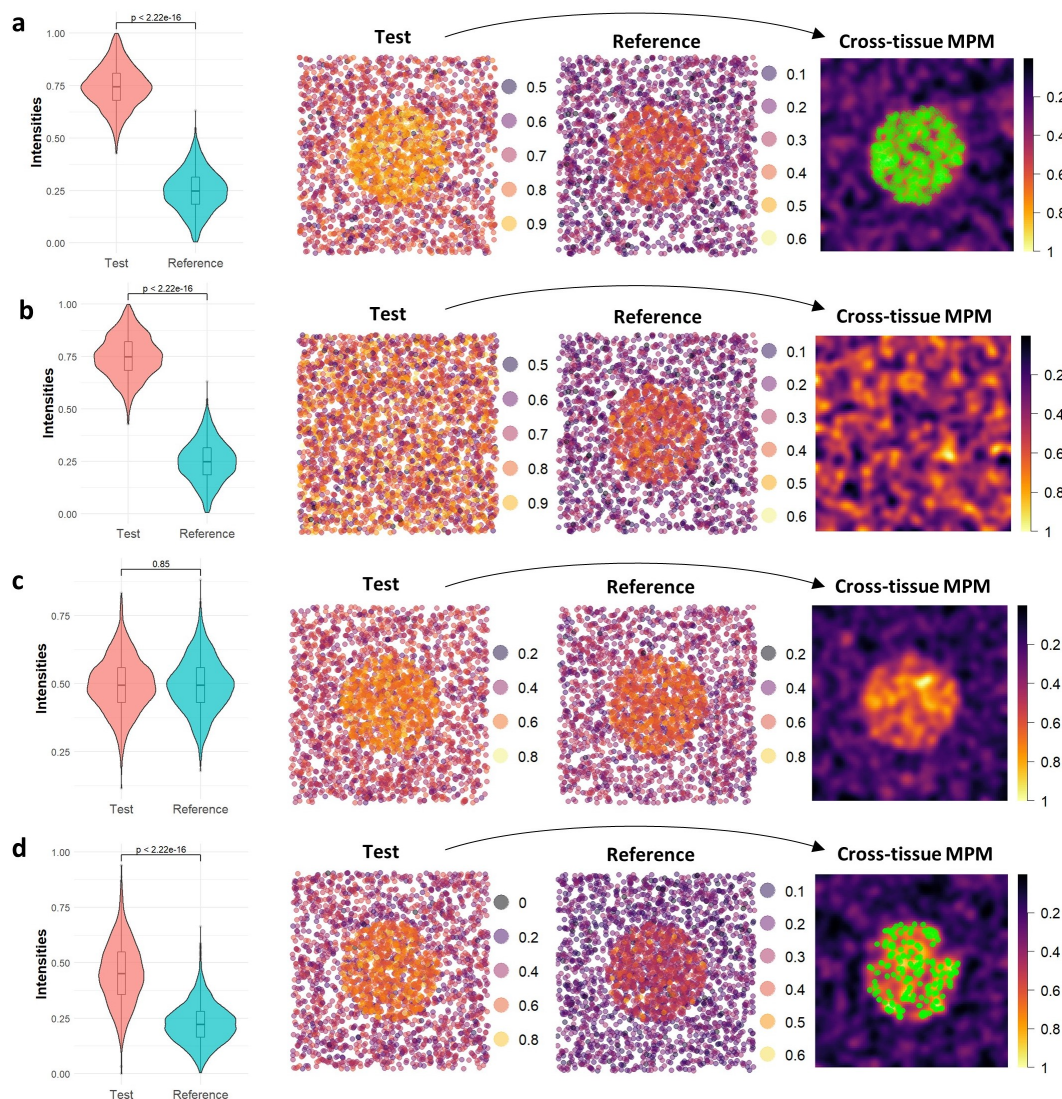
FIGURE 4.17: Validation test of cross-tissue molecular probabilistic maps (CT-MPMs) based on a simulated spatial point patterns (SPP) in "Test" versus "Reference" datasets. A simulated ground-truth foreground (a spatial circular structure; see **Figure 4.14a**) in the "Test" -SPP is either present (**a**, **c**, **d**) or absent (**b**). Moreover, a statistically significant difference between the simulated MOI intensities of "Test"- and "Reference"-SPPs is either present (**a**, **b**, **d**) or absent (**c**). "Test" and "Reference" SPP intensities in **a** and **b** were drawn from normal distributions with μ of 0.75 and 0.25 (σ = 0.1 for both), respectively. In **c**, they were drawn from the same normal distribution with μ = 0.5 and σ = 0.1, and in **d** from the empirical intensities of a MALDI-FTICR-MSI measurement of isocitrate dehydrogenase-mutant (IDH-mut) ("Test") and IDH-wild type (WT) ("Reference") human glioma tissue sample (**Figure 4.10a**) at m/z 203.0815 ([Trp-H]$^-$). Simulated SPPs were generated as described in **Figure 4.15**. "Test" SPP points' intensities, for which both the spatial null hypothesis (i.e. MOI intensities follow a complete spatial randomness model) and the Test-vs-Reference intensity distributions null hypothesis are rejected, are labeled with green points for having significant cross-tissue relative abundance (right-most panels of **a** and **d**). Despite the statistically significant difference in MOI intensity distributions in **b**, no significant cross-tissue relative abundance was detected in the corresponding "Test" SPP, because it did not exhibit a spatial pattern (i.e. it consequently did not reject the spatial null hypothesis). On the other hand, despite the clear presence of a non-random spatial pattern in **c**, no significant cross-tissue relative abundance was detected because MOI intensities of the "Test" and "Reference" SPPs were drawn from the same intensity distribution. Figure was adapted from Abu Sammour et al.[142] with permission from Springer Nature.

distributions null hypotheses are rejected, since a simulated spatial structure of high MOI abundance (foreground) is present and intensity values are sampled from different normal distributions (**Figure 4.17a**). In case (**b**) the spatial null hypothesis is accepted, but the intensity distribution null hypothesis is rejected, because no simulated high-MOI area is present but intensity values are again sampled from different normal distributions (**Figure 4.17b**). In case (**c**) the spatial null hypothesis is rejected while the intensity distributions null hypothesis is accepted, since a simulated high-MOI area is present, but here intensity values are sampled from the same normal distribution (**Figure 4.17c**). Finally, in case (**d**) it is expected that both the spatial and test-vs-reference intensity distributions null hypotheses are rejected, since a simulated foreground is present and intensity values were sampled from the empirical intensities of a MALDI-FTICR-MSI measurement of IDH-MUT ("Test") and IDH-WT ("Reference") human glioma tissue sample (see box/violin-plots of **Figure 4.10b**) at *m/z* 203.0815 (**Figure 4.17d**). The results demonstrated that the generated CT-MPMs on simulated data, in accordance with experiment expectations, correctly identified only the first and last cases to include areas of significant cross-tissue relative spatial abundance (**Figure 4.17**).

4.4.6 Assessment of *moleculaR*'s Robustness against Superimposed Noise

MALDI-MSI data is not devoid of noise and signal interference which are caused by various factors accompanying the data generation process.[40] Since this is the case, any proposed new workflow must also possess at least some degree of resilience against commonly encountered technical variability. To address this important point, the robustness of the proposed molecular probabilistic mapping against various types of artificially added noise was systematically investigated.

Three different noise types have been added to the data; on one hand, artificial Gaussian and interference noise types and, on the other, artificial intensity artifacts (**Figure 4.18ab**). The intensities of both artificial Gaussian and interference noise types are sampled from a Gaussian distribution whose mean and standard deviation are equal to those of the intensities of the raw MOI signal. The difference between the two is that the former was randomly spiked exactly at the *m/z* MOI while the latter at an arbitrary distance of $2\sigma_w$ away from *m/z* MOI to represent an interfering signal (hence the name, artificial interference noise; σ_w is the standard deviation of the Gaussian weighting envelop as described in **section 3.4**). On the other hand, the intensities of the artificial intensity artifacts type were sampled from a uniform rectangular distribution whose range exceeds the range MOI's signal intensities to represent random (and typically few) single pixels of extremely high intensities (relative to the mean signal intensity of the measurement) in MSI measurements. These are thought to arise from tissue gaps (ex. tears), inhomogeneous matrix crystal spatial distribution, ion source contamination or abrupt chemical inhomogeneities.

Sphingomyelin SM(d34:2)[M+H]$^+$ (*m/z* 701.5592; FDR $\leq$ 0.1) was chosen as a test MOI for evaluating the effect of the above mentioned noise source on its raw signal and the resulting MPMs each time comparing the result to the current benchmark, i.e. the classical ion images (see **section 3.3**). MPMs were rather robust against different types of computationally added noise. As shown in **Figure 4.18c**, despite the degraded visual quality of artificially "contaminated" data, MPMs were able to identify areas of significant metabolite spatial relative abundance. This is evidenced by the high degree of overlap (yellow areas in **Figure 4.18c**) for all noise types between estimated MPM hotspot contours of raw (green areas in **Figure 4.18c**) and artificially "contaminated" data (red areas in **Figure 4.18c**), as judged by their respective DSC scores of 0.85, 0.97 and 0.98 for artificially added Gaussian noise, intensity artifacts or interference peaks placed in the *m/z* proximity of the MOI, respectively.

The testing procedure described above has been expanded to include 142 different MOIs detected in the same GB tissue sample (positive ion mode; all METASPACE-verified[147] based on the SwissLipids[148] database at FDR $\leq$ 0.2). The results observed in **Figure 4.19** revealed median DSC scores of 0.91, 0.98 and 0.98 for these three types of added noise, respectively.

The performance of the proposed method was further tested against superimposed artificial noise by varying the standard deviation of the sampled Gaussian noise relative to the standard deviation of the raw signal of an example MOI sphingomyelin SM(d34:2)[M+H]$^+$ (**Figure 4.20**). Starting with a rather low noise dispersion resembling that of a Poisson noise (see **section 3.12**), the standard deviation of the spiked noise was varied all the way up to 10 times the standard deviation of the raw MOI signal. At each iteration two similarity scores were calculated namely; DSC between the MPM hotspot contours of raw and noise-contaminated MOI data as a performance indicator for MPM and the normalized cross correlation (NCC) as a performance indicator for the visual image similarity between raw and noise-contaminated ion images (**Figure 4.20b**). The results indicated that the proposed method was able to withstand Gaussian noise sources up to 4 times the standard deviation of the raw MOI signal retaining hotspot overlap of above 0.75 DSC, all this while observing noticeable visual image degradation (**Figure 4.20c**).

A similar computational experiment was repeated this time resembling the artificial interference noise (**Figure 4.18ab**) with sampled noise spiked in the vicinity of the same MOI, sphingomyelin SM(d34:2)[M+H]$^+$, at an arbitrary distance of $2\sigma_w$ away) of *m/z* MOI. Again the standard deviation of the sampled Gaussian noise was varied relative to the standard deviation of the raw MOI signal starting with a low noise dispersion resembling that of a Poisson noise all the way up to 10 times the standard deviation of the raw MOI signal as demonstrated in **Figure 4.21**. Owing to the proposed Gaussian mass-window weighting, MPM hotspot contours are able to withstand artificial interference noise (spiked at *m/z* MOI + $2\sigma_w$) with σ_{noise} up to 10

times σ_{MOI} retaining hotspot contours overlap of 0.91 DSC, all this while observing clear visual degradation of the corresponding ion images which is also mirrored in their computed NCC relative to the raw ion image.

Finally, a similar computational experiment has been repeated with the last type of artificial noise contamination namely, artificial intensity artifacts. Intensity artifacts were added iteratively according to the scheme in **Figure 4.18ab** to the peak signal of sphingomyelin SM(d34:2)[M+H]$^+$, each time varying the number of intensity artifacts n (up to $n = 5000$; $\approx 20\%$ of the total tissue pixels) randomly placed within the tissue window (**Figure 4.22**). At each iteration the DSC score was computed between the estimated MPM hotspot contours of the raw and artificially contaminated data
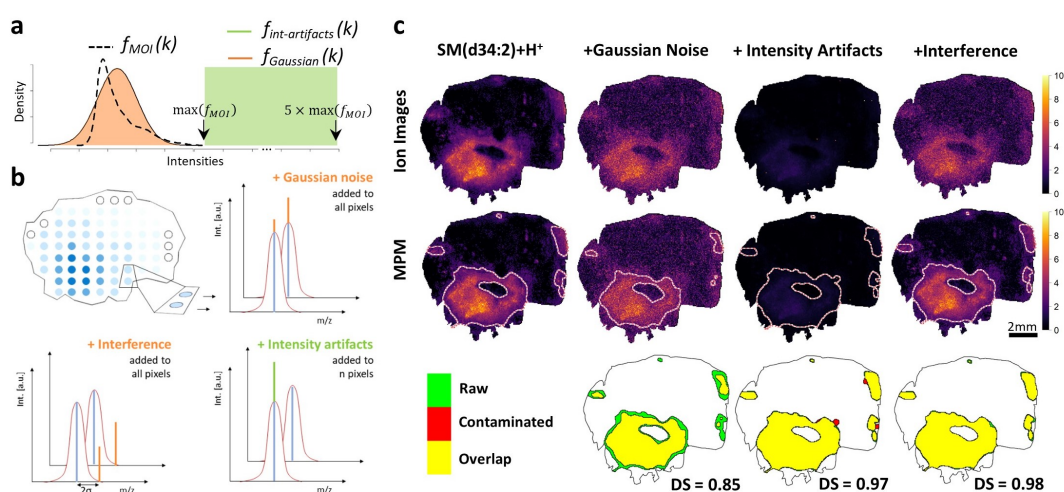
FIGURE 4.18: Molecular probabilistic maps (MPMs) are robust against various forms of artificially added noise. **a)** Schematic representation of ion intensity sample distributions of a typical molecule-of-interest (MOI) ($f_{MOI}(k)$; dashed black curve) and of the corresponding Gaussian distribution ($f_{Gaussian}(k)$; orange) from which artificial Gaussian noise and artificial interference noise were sampled. Mean and standard deviation of $f_{Gaussian}(k)$ are equal to those of $f_{MOI}(k)$. $f_{int-artifacts}(k)$ is a uniform rectangular distribution whose range exceeds the range of $f_{MOI}(k)$ (see dotted x-axis). **b)** Artificial Gaussian noise is sampled from $f_{Gaussian}(k)$ and is added to all pixels to the raw signal of m/z MOI present in each pixel. Artificial interference noise is also sampled from $f_{Gaussian}(k)$ but is added to all pixels arbitrarily at m/z MOI + $2\sigma_w$ where σ_w is the standard deviation of the Gaussian weighting envelop (see **section 3.4** and **Figure 4.3**). The latter is a function of the mass resolving power at m/z MOI (see **section 3.3**). Artificial intensity artifact noise is sampled from $f_{int-artifacts}(k)$ and is added to $n = 10$ randomly selected pixels at m/z MOI. **c)** MPMs (middle row) but not ion images (upper row) of exemplary sphingomyelin SM(d34:2)[M+H]$^+$ (m/z 701.5592; FDR ≤ 0.1) are robust against various forms of artificially added noise and signal artifacts: artificial Gaussian noise (second column), artificial intensity artifacts i.e. presence of abnormally-high-intensity peaks (third column) and artificial interference noise added $2\sigma_w$ away from m/z MOI (fourth column). Despite the degraded visual quality of artificially contaminated data, MPMs are able to identify areas of significant metabolite spatial relative abundance. This is demonstrated by the high degree of overlap (yellow) for all noise types between estimated MPM hotspot contours of raw (green) and artificially contaminated data (red), as judged by their Dice similarity coefficient (DSC). Figure was adapted from Abu Sammour et al.[142] with permission from Springer Nature.

while also computing the NCC similarity metric between the raw and artificially contaminated ion images (**Figure 4.22b**). MPM hotspot contours were able to withstand added single-pixel intensity artifacts of $n = 450$ randomly placed within the tissue window reliably delineating the correct hotspot area and retaining hotspot contours overlap of 0.78 DSC, all this while observing clear visual degradation of the corresponding ion images relative to the raw ion image which is also mirrored in their computed NCC which falls below the 0.5 mark for the same n (**Figure 4.22bc**).
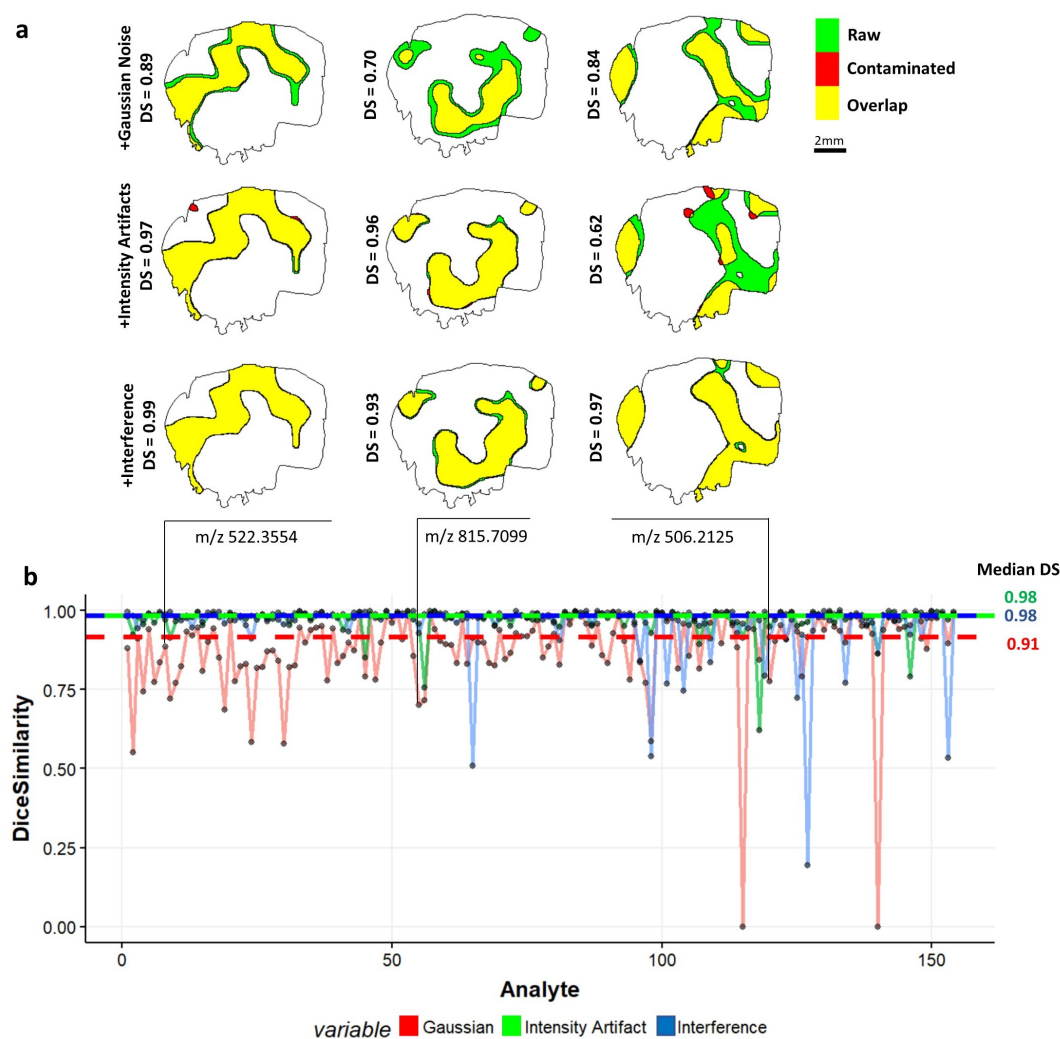
FIGURE 4.19: Dice similarity coefficients (DSC) computed for MOI estimated hotspot contours between raw data and artificially contaminated (with different types of noise) data of 142 MPMs of MOIs identified in METASPACE[147] with FDR $\leq$ 0.2 in positive ion mode. Noise was artificially added according to the three noise types presented in **Figure 4.18**; artificial Gaussian noise added to MOI (first row of **a**; red curve in **b**), presence of abnormally high-intensity peak artifacts (second row of **a**; green curve in **b**) and artificial interfering noise occurring within the span of the theoretical Gaussian envelop specific for MOI ($2\sigma_w$ away from m/z MOI; third row of **a**; blue curve in **b**). Median DSC values were 0.91 (dashed red line), 0.98 (dashed green line) and 0.98 (dashed blue line) for Gaussian noise, intensity artifacts and interference, respectively. Figure was adapted from Abu Sammour et al.[142] with permission from Springer Nature.
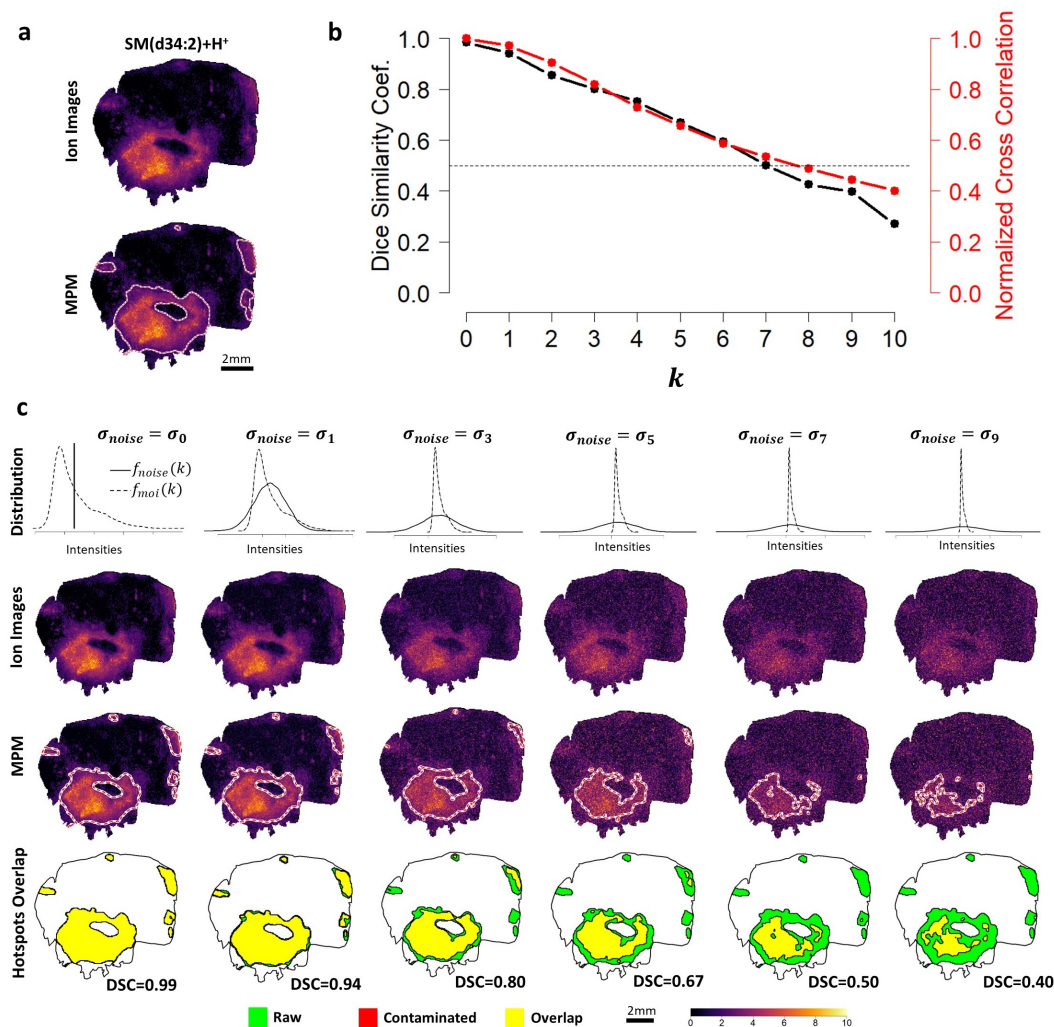
FIGURE 4.20: Evaluating the robustness of molecular probabilistic maps (MPMs) against artificially added Gaussian noise spiked at m/z of a molecule-of-interest (MOI). **a)** Ion image and MPM of an example MOI, sphingomyelin SM(d34:2)[M+H]$^+$ (FDR $\leq$ 0.1). **b)** Gaussian noise was added iteratively according to the scheme in **Figure 4.18** to the peak signal of **a** with varying $\sigma_{noise} = \sigma_k$ ($k = 0 \ldots 10$), where $\sigma_0 = \sqrt{\mu_{MOI}}$ and $\sigma_k = k\sigma_{MOI}$ for $k = 1 \ldots 10$ and σ_{MOI} and μ_{MOI} are the standard deviation and mean of the signal intensities of MOI. Note that for $k = 0$, the resulting noise is similar to Poisson noise with $\lambda_{Poisson} = \mu_{MOI} \gg 1000$. At each iteration the Dice similarity coefficient (DSC) was computed between the estimated MPM hotspot contour of the raw and artificially contaminated data (black solid curve) while also computing the normalized cross correlation (NCC) similarity metric between the raw and artificially contaminated images (red solid curve). **c)** Visual illustrations of MOI signal intensity distribution $f_{MOI}(k)$ relative to the added noise distribution $f_{noise}(k)$ at each noise iteration (first row), corresponding ion images (second row), calculated MPM hotspot contours (third row) and hotspot contours overlap between raw and artificially contaminated data (bottom row). MPM hotspot contours are able to withstand Gaussian noise with σ_{noise} up to 4 times σ_{MOI} retaining hotspot contours overlap of above 0.75 DSC, all this while observing clear visual degradation of the corresponding ion images which is also mirrored in their computed NCC relative to the raw ion image. Figure was adapted from Abu Sammour et al.[142] with permission from Springer Nature.
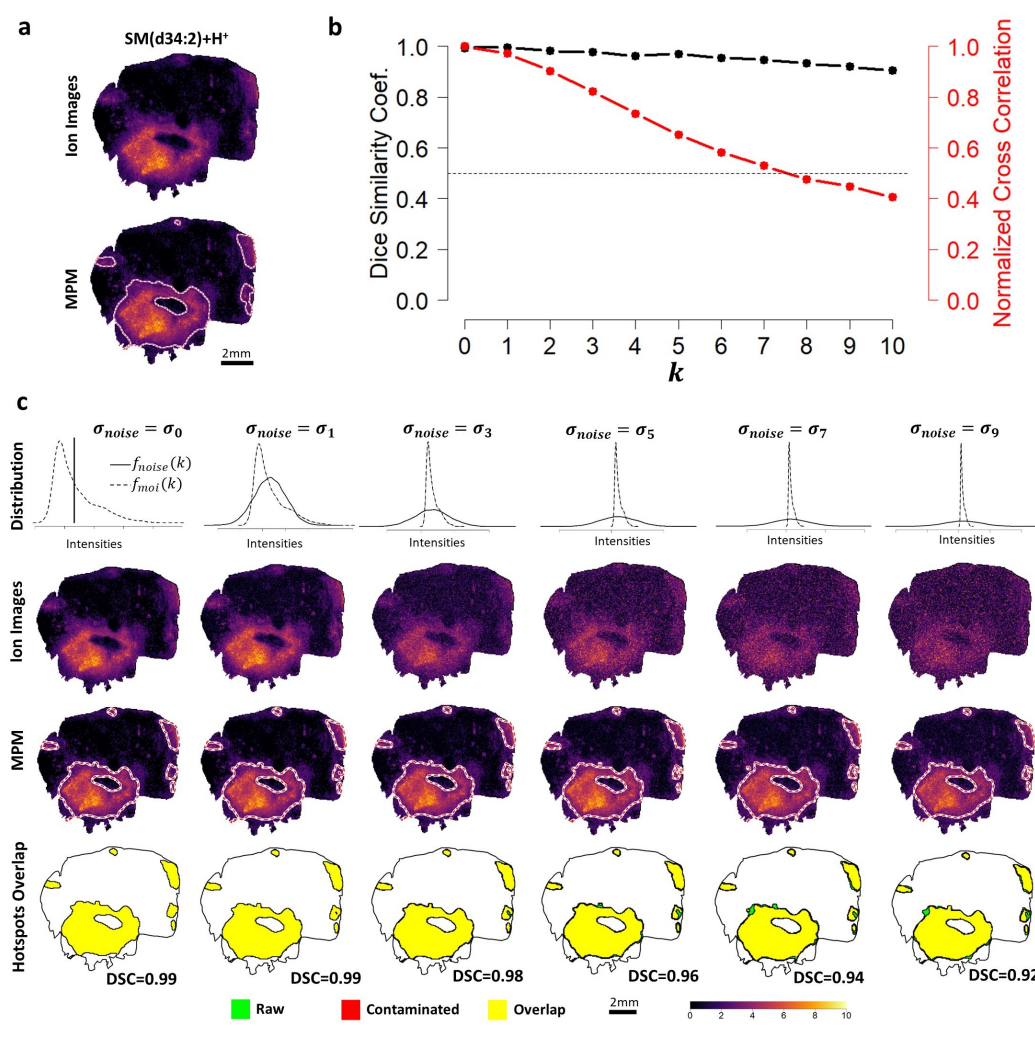
FIGURE 4.21: Evaluating the robustness of molecular probabilistic maps (MPMs) against artificially added interference noise spiked in the vicinity (i.e. $2\sigma_w$ away) of *m/z* of a molecule-of-interest (MOI). **a)** Ion image and MPM of an example MOI, sphingomyelin SM(d34:2)[M+H]$^+$ (FDR $\leq$ 0.1). **b)** Artificial interference noise was added iteratively according to the scheme in **Figure 4.18** at $2\sigma_w$ away from the peak signal of **a** (i.e. at *m/z* MOI + $2\sigma_w$; σ_w is the standard deviation of the Gaussian weighting envelop) with varying $\sigma_{noise} = \sigma_k$ ($k = 0 \ldots 10$), where $\sigma_0 = \sqrt{\mu_{MOI}}$ and $\sigma_k = k\sigma_{MOI}$ for $k = 1 \ldots 10$ and σ_{MOI} and μ_{MOI} are the standard deviation and mean of the signal intensities of MOI. Note that for $k = 0$, the resulting noise is similar to Poisson noise with $\lambda_{Poisson} = \mu_{MOI} \gg 1000$. At each iteration the Dice similarity coefficient (DSC) was computed between the estimated MPM hotspot contours of the raw and artificially contaminated data (black solid curve) while also computing the normalized cross correlation (NCC) similarity metric between the raw and artificially contaminated ion images (red solid curve). **c)** Visual illustrations of MOI signal intensity distribution $f_{MOI}(k)$ relative to the added noise distribution $f_{noise}(k)$ at each noise iteration (first row), corresponding ion images (second row), calculated MPM hotspot contours (third row) and hotspot contours overlap between raw and artificially contaminated data (fourth row). As a consequence of Gaussian mass-window weighting, MPM hotspot contours are able to withstand artificial interference noise (spiked at *m/z* MOI + $2\sigma_w$) with σ_{noise} up to 10 times σ_{MOI} retaining hotspot contours overlap of 0.91 DSC, all this while observing clear visual degradation of the corresponding ion images which is also mirrored in their computed NCC relative to the raw ion image. Figure was adapted from Abu Sammour et al.[142] with permission from Springer Nature.
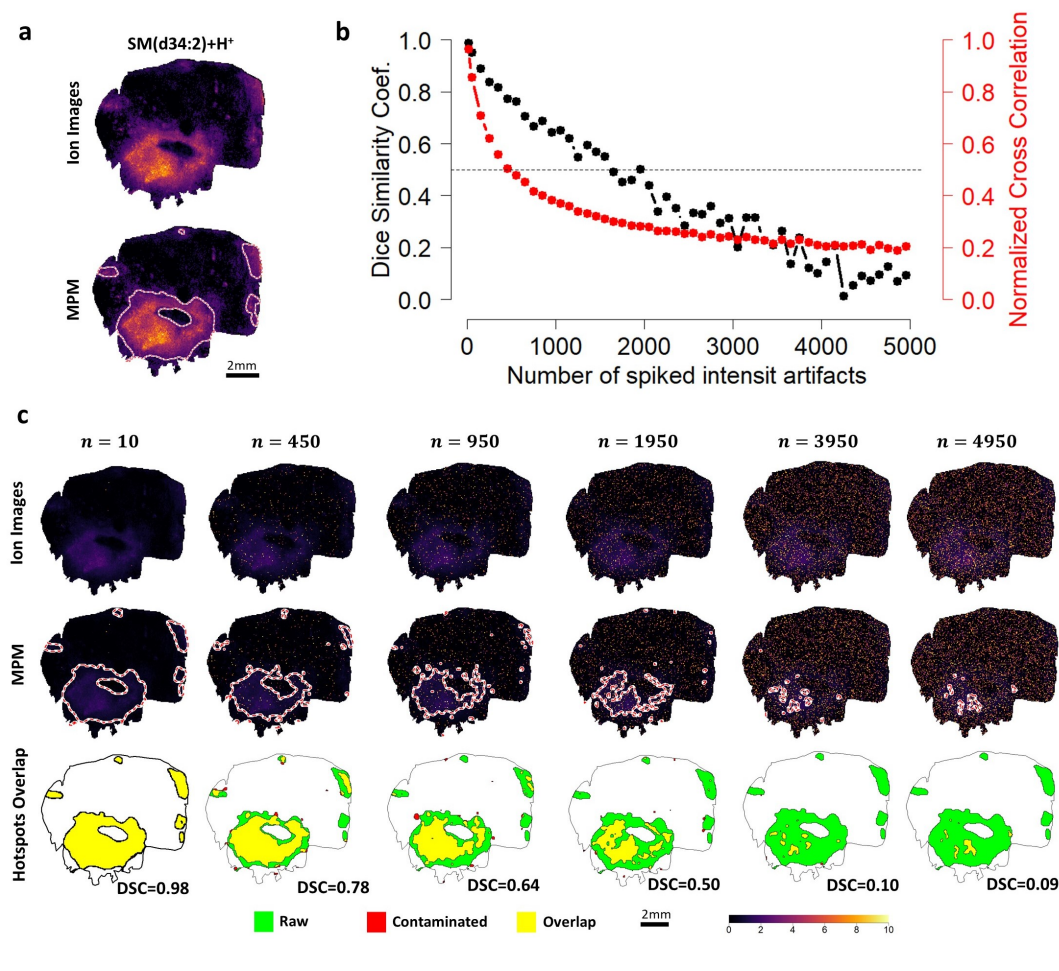
FIGURE 4.22: Evaluating the robustness of MPM against artificially added intensity artifacts spiked at *m/z* of a molecule-of-interest (MOI). **a)** Ion image and MPM of an example MOI, sphingomyelin SM(d34:2)[M+H]$^+$ (FDR $\leq$ 0.1). **b)** Intensity artifacts were added iteratively according to the scheme in **Figure 4.18ab** to the peak signal of **a**, with a varying number of intensity artifacts *n* (up to *n* = 5000; $\approx$ 20% of the total tissue pixels) randomly placed within the tissue window. At each iteration the Dice similarity coefficient (DSC) was computed between the estimated MPM hotspot contour of the raw and artificially contaminated data (black solid curve) while also computing the normalized cross correlation (NCC) similarity metric between the raw and artificially contaminated images (red solid curve). **c)** Visual illustrations of noise-contaminated ion images (first row), calculated MPM hotspot contours (second row) and hotspot contours overlap between raw and artificially contaminated data (bottom row). MPM hotspot contours are still able to withstand added single-pixel intensity artifacts of *n* = 450 randomly placed within the tissue window reliably delineating the correct hotspot area and retaining hotspot contours overlap of 0.78 DSC, all this while observing clear visual degradation of the corresponding ion images relative to the raw ion image which is also mirrored in their computed NCC (red curve in b) which falls below the 0.5 mark (dashed horizontal line in **b**) for the same *n*. Figure was adapted from Abu Sammour et al.[142] with permission from Springer Nature.

4.4.7 Assessment of *moleculaR*'s Stability against Random Permutations

As previously shown in **section 4.4.1**, the MPM approach relies on a CSR model against which the the MOI's spatial distribution is compared to find areas which exhibit statistically significant non-random spatial patterns of MOI intensities independent of how an end-user may perceive its (i.e. MOI's) spatial relative abundance or deficiency.

Since each MOI-specific CSR model is unique for every MPM evaluation, it was important to test the impact of the stochastic nature of the CSR model on the stability of the generated MPM hotspot/coldspot contours. For this purpose, the MPM evaluation for an example MOI, PE(20:1)[M+Na]$^+$ at *m/z* 544.3009 (MALDI-FTICR-MSI data of the IDH-WT GB tissue sample shown in **Figure 4.9a**), was repeated 100
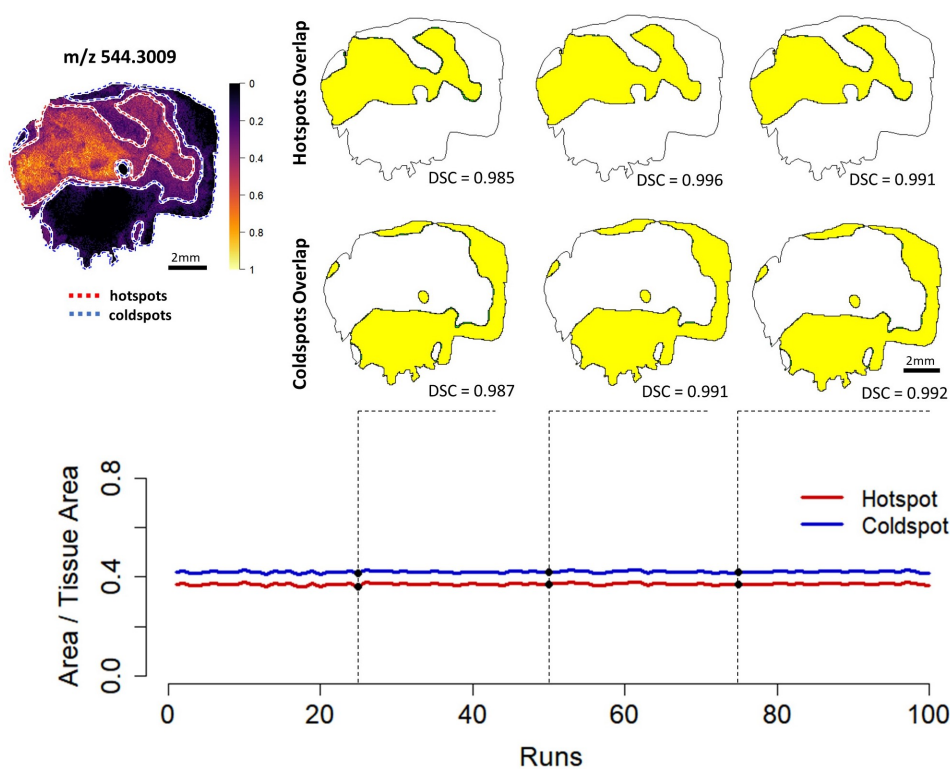
FIGURE 4.23: Stability of molecular probabilistic maps (MPMs) for 100 permutations of the generated complete spatial randomness (CSR) model. MPM was re-computed 100 times for the example MOI, PE(20:1)[M+Na]$^+$ (*m/z* 544.3009; FDR $\leq$ 0.2) of the isocitrate dehydrogenase-wild type (IDH-WT) glioblastoma (GB) tissue section of **Figure 4.9a**, each time generating a different random permutation of the CSR model. For each iteration, the area of the MOI's MPM hotspot (red curve) and coldspot (blue curve) contours relative to the total tissue area was computed. The overlap (yellow) between the hotspot and coldspot contour of the 25th, 50th and 75th iterations relative to the hotspot and coldspot areas of the 1st iteration are shown as examples. Relative areas' mean and standard deviation were 0.3234 and 0.0045 for hotspot contours, respectively, and 0.3771 and 0.0036 for coldspot contours, respectively. DSCs mean and standard deviation between hotspot and coldspot contour areas of each run relative to that of the first run were 0.9883 and 0.0069, respectively, for hotspot contours and 0.9914 and 0.0046 for coldspot contours, respectively. Figure was adapted from Abu Sammour et al. [142] with permission from Springer Nature.

times, each time with a different CSR permutation as shown in **Figure 4.23**. The results demonstrated that the estimated hotspot and coldspot areas relative to the total tissue area were stable across all iterations, with mean overlap DSCs of 0.988 and 0.991 between the hotspot and coldspot areas, respectively, for each of the 100 iterations
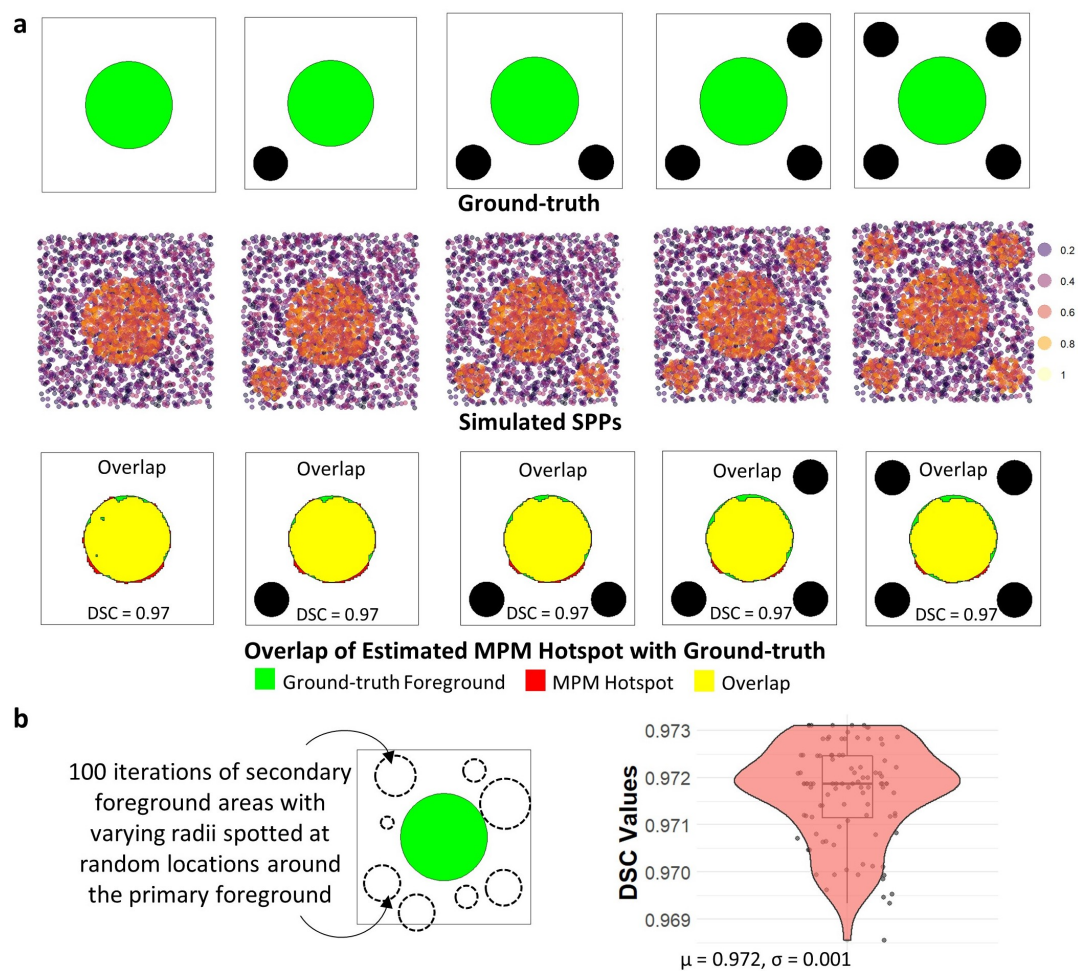

FIGURE 4.24: Stability testing of molecular probabilistic maps (MPMs) of an MOI ground truth area (central green filled circle) using simulated data. Here, areas of high-intensity points (black filled circles) were cumulatively (**a**) or iteratively (**b**) added to a ground-truth. A simulated spatial point pattern (SPP) was created based on the ground-truth of **Figure 4.14a** and as described in **Figure 4.15a**. **a)** Secondary areas containing high-intensity points (black filled circles) were cumulatively added to an MOI ground truth containing a central area (green filled circles; upper row). At each step, an MPM was computed for the entire simulated SPP (i.e. central plus added secondary areas), but the Dice similarity coefficient (DSC) was calculated between the green area and its computed MPM hotspot only (i.e. the spotted secondary black areas where excluded from the DSC computation). The MPM hotspot contours of the central green area were unaffected by the cumulative addition of points/areas of high intensity. **b)** Additionally, 100 random ground-truths were created, each time spotting one secondary area (dashed circles) with a randomly chosen radius and position around the central area (green filled circle). At each iteration, MPM and DSC values were computed as described in **a**. Similar to **a**, the computed MPM hotspot contours of the central area were rather unaffected, as indicted by the low variance of the computed DSC values ($\mu = 0.972$, $\sigma = 0.001$). Figure was adapted from Abu Sammour et al.[142] with permission from Springer Nature.

relative to that of the first iteration. The standard deviations of the computed DSCs was below 0.01 which is also evident by the limited fluctuation of the red and blue curves of **Figure 4.23** representing the computed areas of MOI's MPM hotspots and coldspots relative to the total tissue area.

The impact of cumulatively or iteratively spiking complete areas of high-intensity points into a simulated SPP on the hotspot contours was also considered. For cumulative addition case, secondary high-intensity areas (black filled circles in **Figure 4.24a**) were step-wise added to a simulated SPP containing one central circular foreground (green filled circles in **Figure 4.24a**) and the overlap between the estimated MPM hotspot and foreground was computed solely based on the central circle, which remained rather unaffected (**Figure 4.24a**). Additionally, 100 secondary high-intensity foreground areas with varying radii were spotted iteratively at varying positions randomly assigned around the primary foreground area (**Figure 4.24b**). At each iteration, MPM and DSC values were computed as in the previous step. Similarly, the estimated hotspot contours of the main simulated hotspot were rather not affected as indicted by the box/violin-plot of the computed DSC values.

4.4.8   Assessment of *moleculaR*'s Robustness against Batch Effects

MALDI-MSI data generation is known to be affected by systematic sources of technical variation, the so-called batch effects. Batch effects can occur at different levels; sample preparation and measurement-specific pixel-to-pixel, tissue section-to-section and measurement slide-to-slide batch effects.[40] Since these batch effects are largely unavoidable, it was important to evaluate the performance of MPMs when sources of technical variation are present in the MSI data.

To (partially) compensate for pixel-to-pixel batch effects in MALDI-MSI data, typically intensity normalization techniques are applied.[40] Therefore, comparing the resulting MPM of a given raw MOI data to the MPM of its (i.e. MOI's) intensity-normalized version would in principle provide insight on how MPMs change with different levels of pixel-to-pixel variations. To this end, using the MALDI-FTICR-MSI data of the IDH-WT GB tissue section along with its serial section, MPMs have been generated for three example lipids shown in **Figure 4.25**. MPMs were tested based on three different versions of each MOI; raw data (without intensity normalization), total-ion-count (TIC) normalization and root mean squared (RMS) normalization. MPM hotspot and coldspot contours show good agreement irrespective of the normalization type or the lack thereof, which could also be seen for the IDH-WT GB serial section of **Supplementary Figure 8.2**.

To test how MPMs compare in inter-sample and inter-measurement scenarios (representing section-to-section and slide-to-slide batch effects, respectively), MPMs of the same example MOIs mentioned above have been compared in two serial sections of the IDH-WT GB tissue (**Figure 4.26**) based on raw (without normalization)
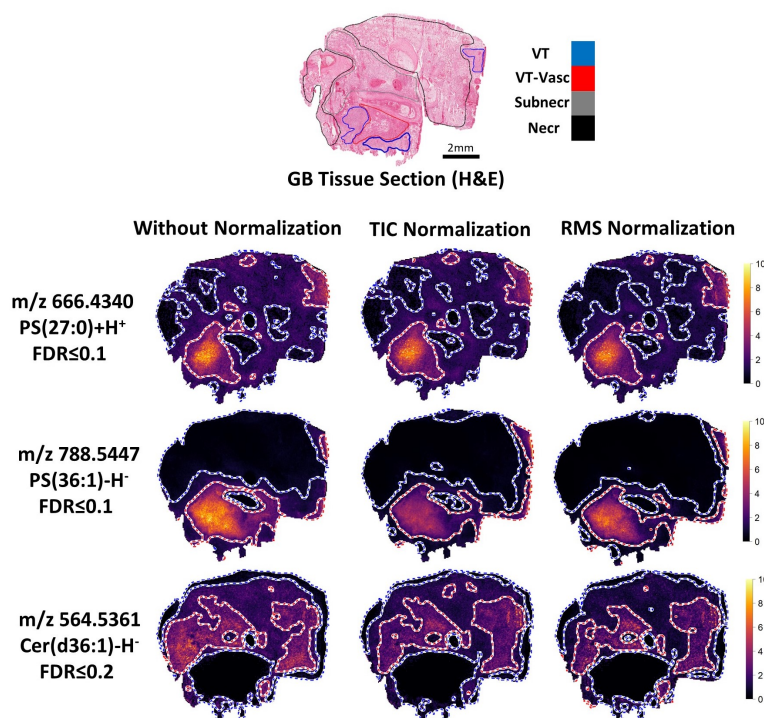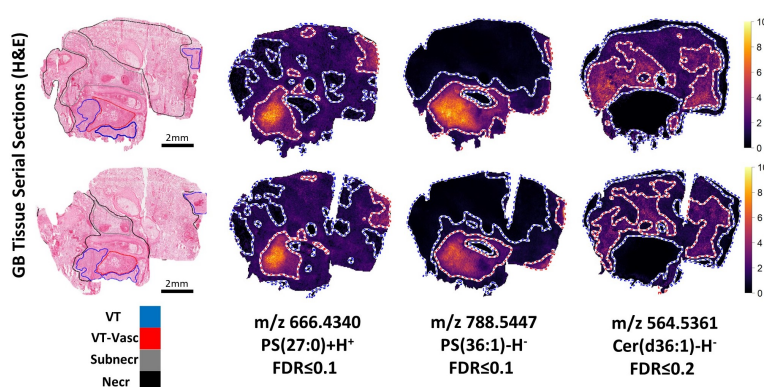
FIGURE 4.25: Comparison of the resulting molecular probabilistic maps (MPMs) of three exemplary lipids shown on the isocitrate dehydrogenase-wild type (IDH-WT) glioblastoma (GB) tissue section measured with MALDI-FTICR-MSI based on raw data (without intensity normalization), total-ion-count (TIC) and root mean squared (RMS) normalization. MPM hotspot/coldspot contours show good agreement irrespective of the normalization type or the lack thereof as also shown for the serial section of **Supplementary Figure 8.2**. The intensity range has been rescaled for every image independently to the range 0 to 10 arb. units. Figure was adapted from Abu Sammour et al.[142] with permission from Springer Nature.

FIGURE 4.26: Comparison of the resulting molecular probabilistic maps (MPMs) of three exemplary lipids shown on two IDH-WT glioblastoma (GB) tissue technical replicates analyzed by MALDI-FTICR-MSI on separate slides (i.e., separate measurement runs) based on raw data (without intensity normalization). MPMs show good agreement across both tissue replicates referenced by the similar localization for the MOIs' hotspots/coldspots. The intensity range has been re-scaled to the range 0 to 10 arb. units independently for every shown MPM. Figure was adapted from Abu Sammour et al.[142] with permission from Springer Nature.
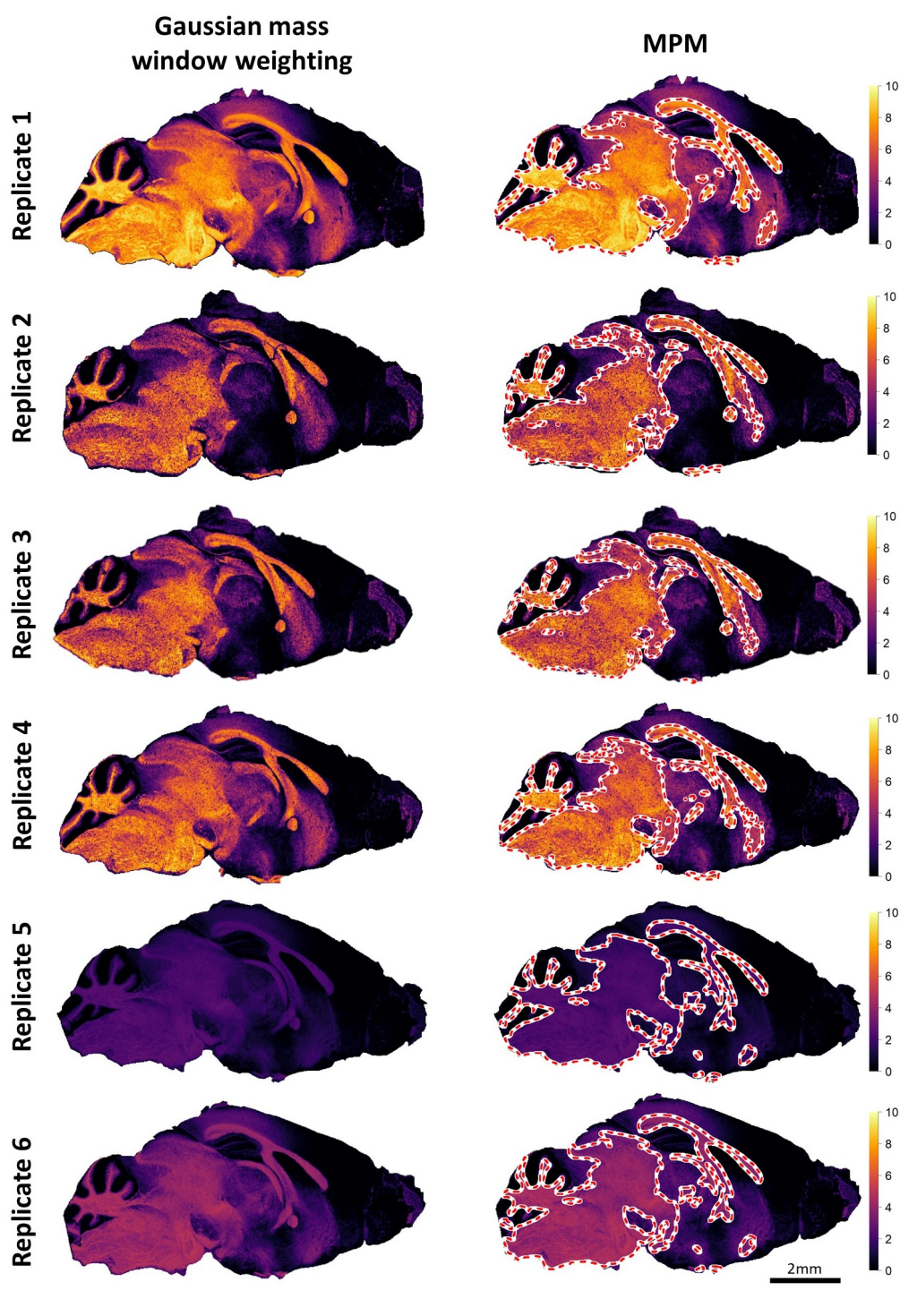
FIGURE 4.27: Gaussian mass-window weighted intensity images and the corresponding molecular probabilistic maps (MPMs) of a molecule-of-interest (MOI), (3'-sulfo)GalCer(d42:2)[M-H]$^-$ (*m/z* 888.6240; FDR $\leq$ 0.05) shown on MALDI-FTICR-MSI datasets of six serial sections of sagittal mouse brain tissue measured on different slides (measurement runs). Despite the striking differences in (total-ion-count (TIC)-normalized) ion intensities across the tissue replicates, MPM hotspot contours show high similarity in their spatial localization highlighting white matter and mid brain regions. Note that the intensity range has been re-scaled to the range 0 to 10 arb. units independently for every shown MPM. Figure was adapted from Abu Sammour et al.[142] with permission from Springer Nature.

MALDI-FTICR-MSI data. The corresponding MPMs showed good agreement across both tissue replicates referenced by the similar localization for the MOIs' hotspots and coldspots. Moreover, the MOI (3'-sulfo)GalCer(d42:2)[M-H]$^-$, mentioned in **Figure 4.9c**, has been used to generate MPMs for MALDI-FTICR-MSI datasets of six serial sections of sagittal mouse brain tissue measured on different slides (i.e. inter-sample and inter-measurement case). **Figure 4.27** illustrates that despite the striking differences in (TIC-normalized) ion intensities across the tissue replicates, MPM hotspot contours show high similarity in their spatial localization highlighting white matter and mid brain regions.

4.5 Quantitative Spatial Mapping of Imatinib in Tissues

The preceding **section 4.4** demonstrated how spatial probabilistic mapping of any given MOI can help in the spatial analysis and interpretation of MOI's signal distribution in a given tissue sample independent from user's own judgment and despite the presence of various technical variability sources. This section attempts to investigate the applicability of the cross-tissue probabilistic spatial mapping concept in quantitative spatial mapping of drugs in tissue sections by utilizing the capabilities of CT-MPMs. First, a generalized nonlinear calibration model based on drug dilution series is proposed as a replacement for the traditional linear model that takes into account the inherent measurement nonlinearities characteristic to MALDI-MSI data. It's applicability is then tested in a clinical pharmacology setup by MALDI-MSI-based tissue-drug content quantification of an entire cohort of tumor tissues in a clinical pharmacology setup. Finally, an attempt is made to derive spatial relative quantification based on cross-tissue spatial probabilistic mapping. The results described in this section are based on the corresponding study of Abu Sammour et al.[143] and on the methods described in **sections 3.1.1, 3.2.1** and **3.13** of **Chapter 3**.

4.5.1 Calibration Curves and Quantification of Imatinib

The aim of this work was the quantitative spatial mapping of imatinib, a tyrosine kinase inhibitor (TKI), in 56 resection specimens of tumor and surrounding non-tumor tissues from 27 patients with biopsy-proven GIST (see **section 1.5.1**) who received imatinib as first line treatment but presented with refractory disease. GIST tissue specimens were distributed across 48 measurement slides each containing several tumor and surrounding non-tumor tissues alongside with an imatinib dilution series spotted onto a porcine liver tissue as shown in **Supplementary Figure 8.3** (see **section 3.1.1**).

To perform imatinib quantification, a calibration curve has to be fitted to its dilution series. In this work, an imatinib dilution series of 25, 12.5, 6.25, 3.125, 1.56, 0.78 pmol and a blank control were spotted on a porcine liver. **Figure 4.28a** shows a MALDI-TOF-MSI data of an imatinib dilution series of a given sample shown

as surface and imatinib peak detection plots where green pixels indicate imatinib detection at SNR ≥ 3. Typically the end-user manually encircles tissue regions to be included in the computation of calibration curves. In contrast, to avoid signal dilution by areas/pixels that do not carry the signal of interest, this work proposes a computational definition of drug-bearing areas where only pixels where the drug is detected with SNR ≥ 3 are taken into account.

It can be seen from **Figure 4.28a** that the lower the drug concentration spotted, the
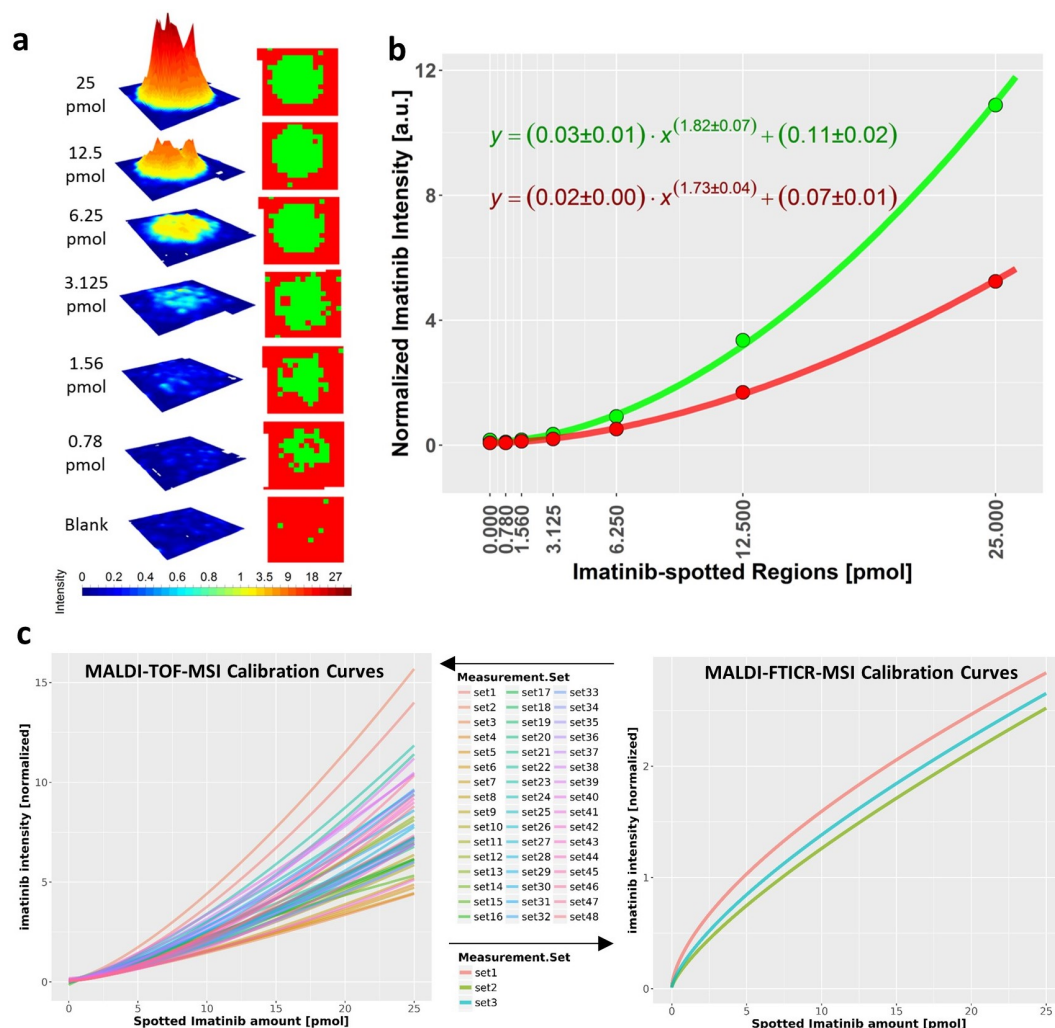

FIGURE 4.28: Imatinib calibration curves based on dilution series deviate from linearity. **a)** Imatinib ion intensity surface plot (left column) and imatinib peak detection plot (right column; green pixels indicate imatinib detection at SNR ≥ 3) based on a dilution series for one of the MALDI-TOF-MSI quantification datasets. **b)** Fitted nonlinear calibration curves based on drug-bearing pixels (i.e. pixels where imatinib peak was detected at SNR ≥ 3; green curve) and user-defined areas (i.e. visually defined measurement areas; red curve) for a chosen MALDI-TOF-MSI dilution series data. Solid circles represent the mean drug intensity of pixels depending on the method used. **c)** Nonlinearity response observed in all (left panel) 48 and (right panel) 3 calibration curves obtained for MALDI-TOF-MSI and MALDI-FTICR-MSI quantification measurement sets, respectively. Figure was adapted from Abu Sammour et al. [143] with permission from Springer Nature.

more the outlines of drug-spotted areas diverge from the expected circular shape and
the more spatially heterogeneous the signal is. Moreover, this signal heterogeneity,
which leads to signal dilution by pixels not bearing the drug signal, could have
a substantial effect on the down-stream drug normalized intensity vs. dilution
amount as shown by the fitted nonlinear curves in **Figure 4.28b**. The described signal
heterogeneity can also take place at the tissue where the drug is to be quantified,
especially for heterogeneous tumor tissues where the drug is observed to be sparsely
distributed (see **Figure 4.30c**).

More importantly, all drug dilution series measured either with MALDI-TOF-
MSI (*n*=48) or MALDI-FTICR-MSI (*n*=3) deviated from linearity (**Figure 4.28c**). This
deviation is observed to resemble a power function, $y = ax^b + c$ (**Equation 3.9**), where
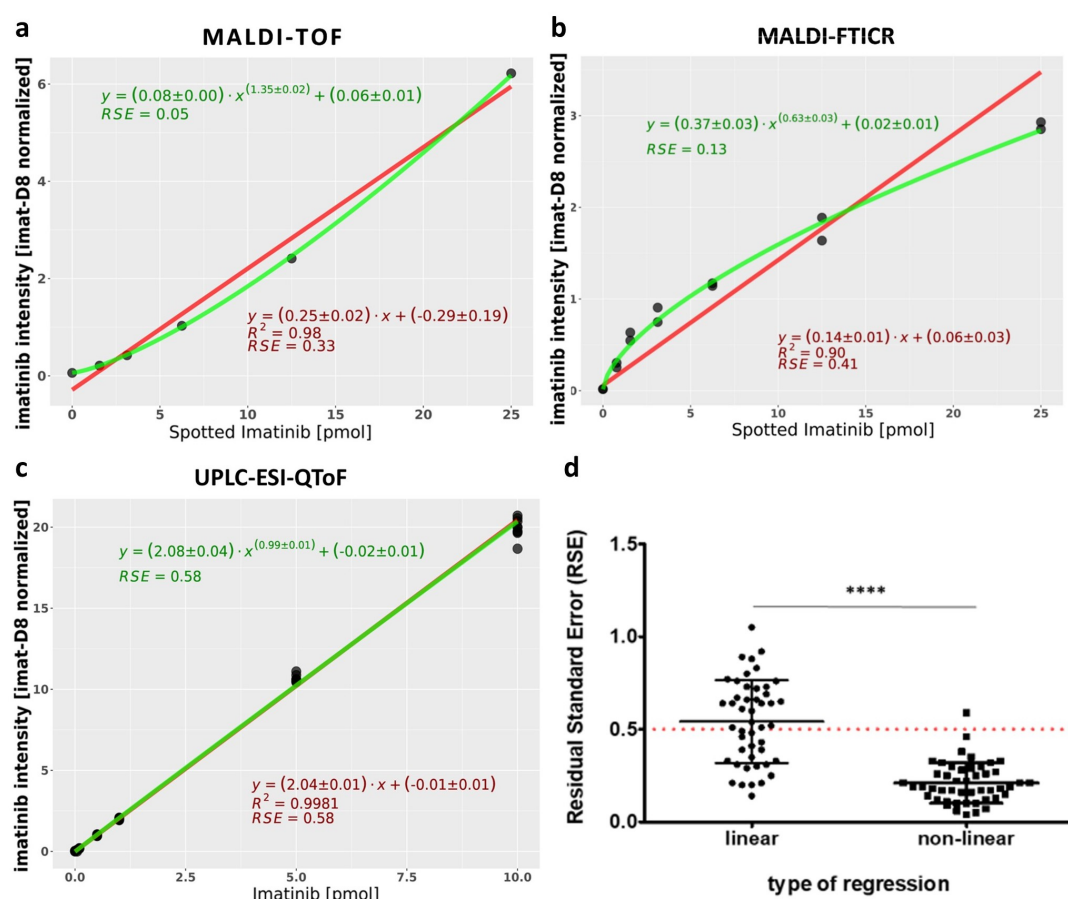a, b and c are constants and c was added to represent the superimposed detector

FIGURE 4.29: Generalized nonlinear compared to linear regression models for calibration in
MSI. Imatinib calibration curves for a sample dataset by linear (red) and generalized nonlinear
regression (green) for **a)** MALDI-TOF-MSI, **b)** MALDI-FTICR-MSI and **c)** UHPLC-ESI-QTOF-
MS. Grey circles represent the mean intensity of the imatinib-containing pixels within a
dilution series area. **d)** Residual standard error (RSE) computed for linear and generalized
nonlinear calibration curves of the 48 MALDI-TOF-MSI measurements (**Figure 4.28c**). Figure
was adapted from Abu Sammour et al.[143] with permission from Springer Nature. Part **d** was
contributed by C. Marsching.

noise (see **section 3.13.2**).

To test the proposed generalized nonlinear calibration fit proposed in this work (see **section 3.13.2**), both linear and nonlinear calibration curve fitting has been performed for a sample dataset measured by MALDI-TOF-MSI, MALDI-FTICR-MSI and the gold-standard UHPLC-ESI-QTOF-MSI. It can be observed in **Figure 4.29ab** that the generalized nonlinear calibration provided a better fit indicated by the 6- and 3- fold better residual standard error (RSE) for MALDI-TOF-MSI and MALDI-FTICR-MSI, respectively. Moreover, RSE for the nonlinear fits was significantly lower (****$P < 0.0001$; $n = 48$) compared to linear case (**Figure 4.29d**). Interestingly, for the exponent b in all nonlinear fits, it was consistently observed that $b \geq 1$ and $0 < b < 1$ for TOF- and FTICR-MALDI-MSI, respectively, as also observed in the sample dataset of **Figure 4.29ab**. Lastly, the linear and nonlinear fits were nearly identical for UHPLC-ESI-QTOF-MS calibration resulting in an identical RSE which indicates a true linear response of the system (**Figure 4.29c**).

4.5.2   Quantitative Analysis of Imatinib Content in GIST

The generalized nonlinear calibration model described in the preceding section has been used evaluate the mean imatinib content in normal and tumor tissue sections (in pmol/section) based on MALDI-MSI compared to the gold-standard, i.e. linear calibration model based on UHPLC-ESI-QTOF-MS, for the entire GIST cohort. The mean imatinib signal intensity in MALDI-MSI data was calculated solely from imatinib-containing pixels (SNR $\geq$ 3 for *m/z* 494.26).

As illustrated in **Figure 4.30ab**, most tissue sections with imatinib levels above the limit of quantification (LOQ) for both MS methods corresponded to normal liver tissue. This higher but sparse accumulation of imatinib in normal liver tissue can also be observed in the tissue overview of **Supplementary Figure 8.4** and **Figure 4.30c**. In these cases, imatinib quantified by MALDI-TOF-MSI displayed acceptable correlation with results from the one based on UHPLC-ESI-QTOF-MS. However, MALDI-TOF-MSI tended to underestimate imatinib content. Nevertheless, 78% of all samples, in which imatinib could be quantified, were inside a window of a 2-fold difference (grey area in **Figure 4.30d**). MALDI-FTICR-MSI matched the UHPLC-ESI-QTOF-MS results even more closely (**Figure 4.30e**) where 87% of all samples that reached the MALDI-FTICR-MSI measurement round were within a 2-fold difference relative to UHPLC-ESI-QTOF-MS.

4.5.3   Limited Imatinib Uptake in Metastatic GIST

Since imatinib is the standard first line treatment for GIST, the aim of this work was to investigate imatinib's tumor penetration capability in human GIST samples. For this purpose and as described in the preceding sections, the GIST tissue cohort was imaged with MALDI-TOF-MSI ($n = 27$; in triplicates when enough tissue was available)
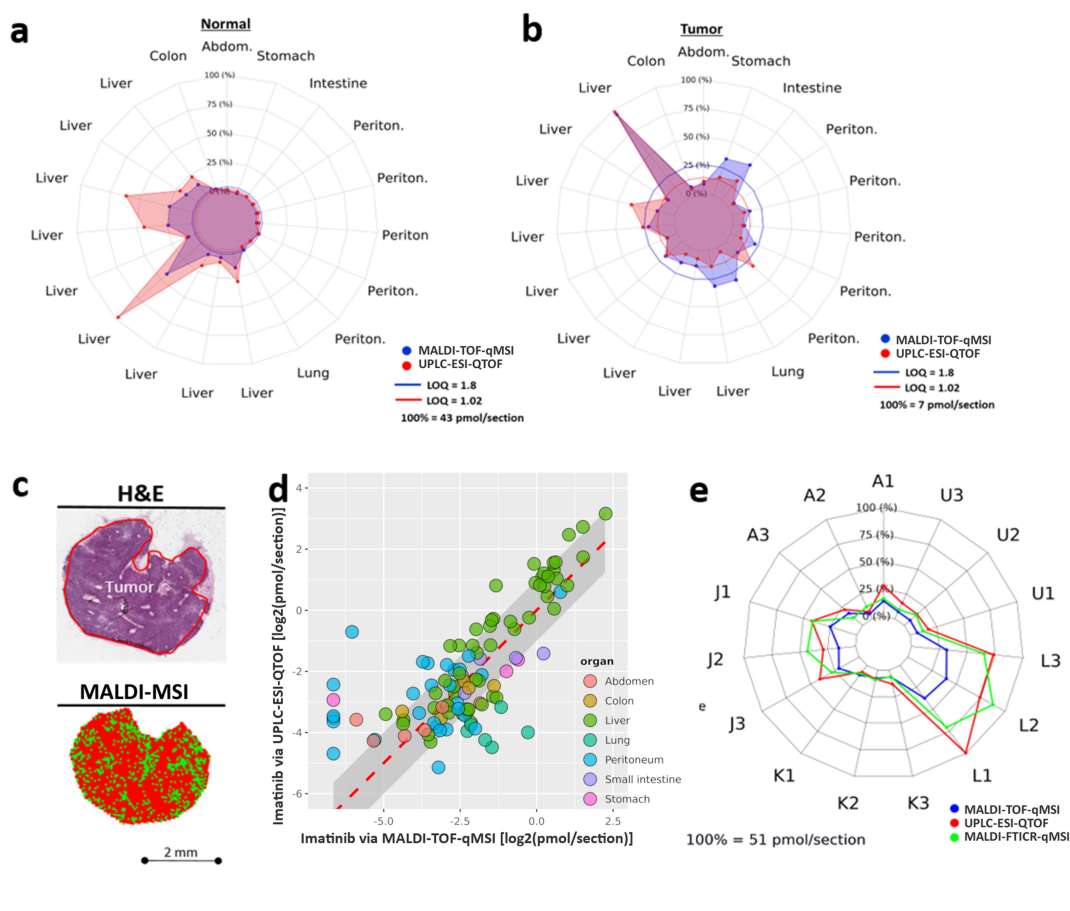
FIGURE 4.30: Comparison MALDI-TOF-MSI and UHPLC-ESI-QTOF-MS quantification of imatinib in gastrointestinal stromal tumor (GIST) for **a)** the surrounding normal and **b)** tumor tissues. **c)** A liver metastasis tissue sample showing imatinib detection in MALDI-TOF-MSI (bottom; green pixels) and corresponding hematoxylin and eosin (H&E)-stained image (top). **d)** A correlation plot showing MALDI-TOF-MSI on the *x*-axis and UHPLC-ESI-QTOF-MS on the *y*-axis, both log2-scaled. The dashed red line represents an identity line (1:1 line) with the log2 fold change of 1 represented by the grey area around it. **e)** Comparison of MALDI-TOF-MSI, UHPLC-ESI-QTOF-MS and MALDI-FTICR-MSI imatinib quantification for five (replicated three times each) unaffected liver samples. Figure was adapted from Abu Sammour et al.[143] with permission from Springer Nature

for spatial quantitative mapping of imatinib and subsequently with UHPLC-ESI-QTOF-MS (n =18; in triplicates when enough tissue was available) for validation (see **Supplementary Figures 8.3 and 8.4** and previous **section 4.5.2**). Follow-up histopathological examination suggested that 26 of the tumor tissue replicates examined contained only slight traces of regressive tumor areas with fibrosis and necrotic tissue throughout. They were, therefore, omitted from analysis.

Quantification of imatinib (pmol/section) in tumor tissue sections and their corresponding non-tumor (normal) control tissues by MALDI-TOF-MSI revealed that despite continuous administration of the prescribed dosage of imatinib until surgery (see **Supplementary Table 8.1**), in most tumor sections (48 of 60 sections; 80%, in MALDI-TOF-MSI and 31 of 44; 70%, in UHPLC-ESI-QTOF-MS), imatinib content was below LOQ regardless of its type (i.e. primary tumor or metastasis) and mutation
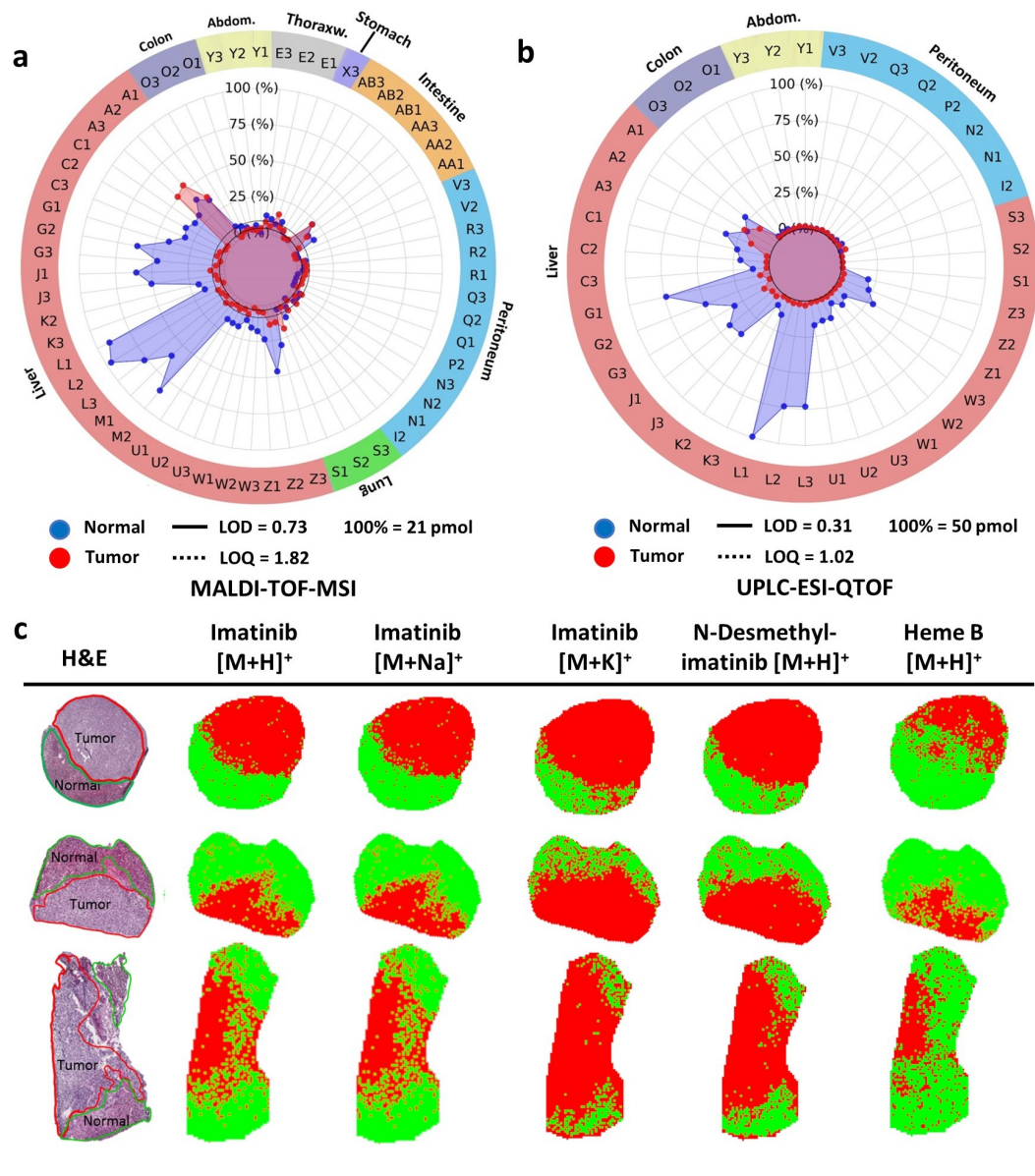
FIGURE 4.31: Liver metastases of gastrointestinal stromal tumor (GIST) is observed to have limited uptake of imatinib independent of mutation status. **a)** Imatinib content in pmol per tissue section in MALDI-TOF-MSI data for 23 GIST ("Tumor"; red) and corresponding non-tumor ("Normal"; blue) tissue specimens using nonlinear calibration model ($n = 3$ per tissue specimen when available). **b)** Imatinib content in pmol per section in UHPLC-ESI-QTOF data for 18 GIST ("Tumor"; red) and corresponding non-tumor ("Normal"; blue) tissue specimens using linear calibration ($n = 3$ per tissue specimen when available). **c)** Three sample A replicates containing both "Normal" and "Tumor" tissue based on histopathological re-examination (left column). For verification, three different imatinib ionization states where visualized, namely; protonated ($[M+H]^+$), sodiated ($[M+Na]^+$) and potassiated ($[M+K]^+$). Additionally, N-desmethylimatinib, a known metabolite of imatinib[172], and Heme B, a proven MALDI-MSI vasculature marker,[173] were visualized. Signal absence and detection (at SNR $\geq$ 3) are encoded by red and green pixels, respectively. Figure was adapted from Abu Sammour et al.[143] with permission from Springer Nature.

status (**Figure 4.31ab**). In comparison, for the corresponding non-tumor (normal) tissue sections, 40 of 83 sections (48%) and 23 of 54 sections (43%) contained imatinib amounts below LOQ for MALDI-TOF-MSI and UHPLC-ESI-QTOF-MS, respectively. **Figure 4.31ab** also shows that imatinib levels were higher in normal liver tissues compared to the others. Furthermore, the orally administered imatinib showed low uptake and/or retention in metastatic GIST in liver despite the high accumulation of the drug in the surrounding normal liver tissue (**Figure 4.31ab**).

One noticeable exception to the observation mentioned above is sample A, which showed comparable amounts of imatinib present in both normal and metastatic GIST tissues observed in both MALDI-TOF-MSI and UHPLC-ESI-QTOF-MS measurements as shown in **Figure 4.31ab**. Upon histopathological re-examination, all three replicates of sample A were found to contain both normal hepatic and metastatic GIST tissues as can be seen in **Figure 4.31c**. Here, the spatially-resolved MALDI-TOF-MSI shows that the imatinib signal (SNR $\geq$ 3) was mainly accumulated in the non-tumor regions of the tissue sections for all three replicates (**Figure 4.31c**). Visualizing ion intensities for the sodium and potassium adducts of imatinib provides further evidence of this observation by showing that the absence of the targeted drug is not caused by differential tissue-dependent adduct formations. Additionally, to rule out the possibility that the drug has been completely metabolized within tumor areas, N-desmethylimatinib (*m/z* 480.25), a known metabolite of imatinib,[172] was visualized as demonstrated in **Figure 4.31c**. It can be seen that the signal of N-desmethylimatinib (SNR $\geq$ 3) showed clear co-localization with imatinib mainly accumulating in normal liver tissue. Lastly, the Heme B signal (*m/z* 616.17), a proven MALDI-MSI marker of vasculature[173] has been also visualized, which showed decreased signal intensity within the tumor core when compared with the surrounding hepatic tissue as seen in **Figure 4.31c**.

4.5.4 Imatinib Tissue-content Estimation via Cross-tissue Molecular Probabilistic Maps (CT-MPM)

Previously, in **section 4.4.2**, it has been shown how cross-tissue probabilistic mapping can be used to perform signal distribution comparison of a given metabolite in test- versus reference tissues providing spatially-aware localization and per pixel statistical significance testing. While the preceding **sections 4.5.1-4.5.3** have shown the results of imatinib quantification using drug calibration curves based on drug dilution series, the proposed CT-MPMs could also be used to provide discrete estimation of tissue-drug content by comparing the signal intensities of the drug in the test tissue to its intensities in the drug dilution spots.

Figure 4.32 demonstrates how CT-MPMs can be used to spatially localize areas of significant cross-tissue relative spatial abundance of imatinib in GIST tissue sample A when compared against a series of imatinib dilution spots in MALDI-TOF-MSI data. For validation, tissue-drug content quantification has been performed via calibration

curves fitted to the imatinib dilution series as described in the preceding sections. For MALDI-TOF-MSI, the nonlinear model has been used (**Figure 4.32ab**) while for UHPLC-ESI-QTOF-MS a linear calibration curve has been fitted separately.

The calculated mean imatinib content in sample A was 7.78 pmol (95% CI 7.28, 8.46 pmol) and 7.81 pmol (95% CI 7.63, 7.99 pmol) based on MALDI-TOF-MSI and UHPLC-ESI-QTOF-MS quantification, respectively. Consecutive comparison of the imatinib-tissue content against four imatinib dilution spots (3.125, 6.25, 12.5 and 25 pmol) showed a gradual decrease in the number of pixel-intensities (zero at 25 pmol) that were detected as significant cross-tissue relative spatial abundance of imatinib (hotspot contours of **Figure 4.32f-i**). The cross-tissue test carried out against the imatinib dilution spot of 6.25 pmol, i.e. the closest to the reported mean imatinib-tissue content by both measurement methods, showed that the distributions of drug signal intensities for both test (=sample A tissue) and reference (= 6.25 pmol dilution spot) are not significantly different as evidenced by the high p-value (two-sided Wilcoxon rank sum test). Moreover, this comparison revealed that the areas in the normal tissue part with significant cross-tissue relative spatial abundance of imatinib (hotspot contours of **Figure 4.32g**) were spatially sparse and coincided with the high-intensity pixels in the imatinib intensity image of **Figure 4.32e**. More importantly, clear spatial heterogeneity in imatinib-tissue content has been observed with some pixels showing much higher levels than the reported mean per tissue as evidenced by the few hotspots in **Figure 4.32h** indicating imatinib amounts above 12.5 pmol, which is much higher than the mean imatinib content estimated based on calibration curves (7.78 pmol and 7.81 pmol based on MALDI-TOF-MSI and UHPLC-ESI-QTOF-MS quantification, respectively).
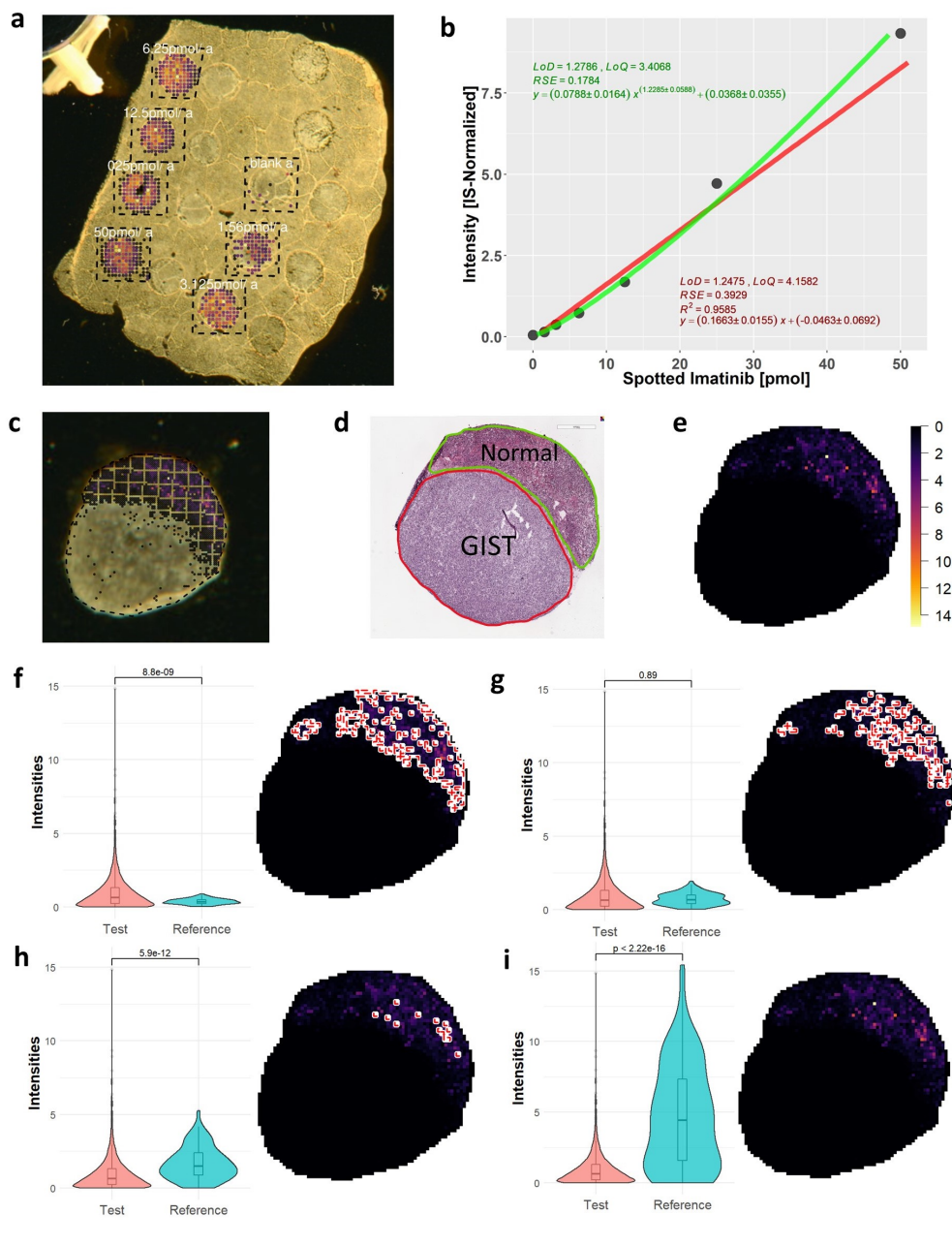
FIGURE 4.32: The cross-tissue molecular probabilistic map (CT-MPM) workflow was used to spatially localize areas of significant cross-tissue relative abundance of imatinib in a gastrointestinal stromal tumor (GIST) tissue sample when compared against a series of imatinib dilution spots in MALDI-TOF-MSI data. **a)** Optical image of a porcine tissue section where the imatinib dilution series (25, 12.5, 6.25, 3.125, 1.56, 0.78 pmol and a blank control) was spotted. MALDI-TOF-MSI measurement regions are indicated by dashed polygons. MALDI-TOF-MSI pixels with imatinib signal (SNR $\geq$ 3; m/z 494.2662; $[M+H]^+$) are superimposed. **b)** Generalized nonlinear (green) and linear (red) regression models fitted to the imatinib dilution series in **a**. **c)** Optical image of a metastatic GIST tissue sample with superimposed MALDI-TOF-MSI pixels with imatinib signal (SNR $\geq$ 3). **d)** Histopathology-annotated hematoxylin and eosin (H&E) image of the resected GIST tissue **c** showing both tumor (red) and non-tumor (normal; green) tissue. **e)** An intensity image of imatinib in the GIST tissue sample **c**. Mean imatinib content in the sample tissue was found to be 7.78 pmol (95% CI 7.28, 8.46 pmol) and 7.81 pmol (95% CI 7.63, 7.99 pmol) based on MALDI-TOF-MSI and UHPLC-ESI-QTOF-MS quantification, respectively. Panels **f-e** illustrate CT-MPMs computed for the tissue sample in **c** compared against imatinib dilution series spots of 3.125 (**f**), 6.25 (**g**), 12.5 (**h**) and 25 pmol (**i**), respectively. CT-MPMs are able to spatially localize tissue areas with significant cross-tissue relative abundance of imatinib, which mainly concentrate in the non-tumor tissue part. Figure was adapted from Abu Sammour et al.[142] with permission from Springer Nature

Chapter 5

Discussion

This chapter provides a discussion on the proposed methods (**Chapter 3**) and their resulting outcomes, which were demonstrated in **Chapter 4**. This is followed by a discussion on methods limitations and ended with a conclusion.

5.1 Mass Resolving Power and Mass Peaks' FWHM

The term resolution is a key concept in mass spectrometry, which describes the ability to resolve mass spectrum intensity peaks. Mass resolution and mass resolving power are two terms that have been often interchangeably used to refer to the ability of a mass spectrometer to separate intensity peaks that are close together in a mass spectrum. Over the years, the international union for pure and applied chemistry (IUPAC) and the American society for mass spectrometry have recommended similar definitions of mass resolution and mass resolving power, leading to confusion about the proper use of these terms.[151] To avoid ambiguity, the recommendation of Murray et al.[151] has been adopted throughout this dissertation in which the use of mass resolving power rather than mass resolution as a quantitative measure is encouraged and, for this work, is given by $R_{FWHM} = m/\Delta m_{50\%}$, where m is the ion mass and $\Delta m_{50\%}$ is obtained from the peak's full-width at half-maximum (FWHM).

Together with spatial resolution, sensitivity and acquisition speed, the mass resolving power of a mass spectrometer could be regarded as the primary characteristics when choosing the right modality for a certain MSI-based application.[10] The theoretical modeling of the mass resolving power and mass peaks' FWHM is challenging and is different for the different mass spectrometer types. Marshall et al.[75] reported that for Fourier transform ion cyclotron resonance (FTICR) mass spectrometers, mass peaks' FWHM scales with m^2 and is, therefore, a nonlinear function of the ion mass m (see **Equations 3.1** and **3.2** in **section 3.3**). On the other hand, the theoretical formulation of mass peaks' FWHM as a function of mass range for TOF mass spectrometers is completely different and is relatively constant across the mass range.[76]

In this work, an empirical method for estimating mass peaks' FWHM from data has been developed, which is central for rendering ion intensity images as will be

discussed in the following section. This was achieved by plotting all FWHM values of individual mass spectrum peaks (whose signal-to-noise ration, SNR, is ≥ 3) as a function of mass-to-charge ratio (*m/z*) and then fitting a locally-estimated scatterplot smoothing (LOESS) curve that would approximate FWHM at any given *m/z* value and therefore provide an estimate for the mass resolving power at any given mass range. The results of this fitting has been demonstrated in **Figure 4.1** for three different mass spectrometers: FTICR (Solarix, Bruker Daltonics), time-of-flight (TOF; rapifleX, Bruker Daltonics) and trapped ion mobility spectrometry time-of-flight (timsTOF; timsTOFflex, Bruker Daltonics) matrix-assisted laser desorption ionization mass spectrometry imaging (MALDI-MSI) devices. Considerable fluctuations of the detected FWHM values along the *y*-axis has been observed, which could be attributed to the overlap of adjacent peaks, partially resolved isotopes, space charge effects or side lobes.[162] Despite this, the fitted FWHM model for the MALDI-FTICR-MSI case closely followed the FWHM theoretical expectation (**Equation 3.2**) for the mass spectrometer, which could be explained by the smoothing characteristic of the LOESS model that seemed to compensate for FWHM fluctuations by smoothing out deviations. For time-of-flight-based mass spectrometers (**Figure 4.1bc**), the fitted FWHM model deviates somewhat from the expected linear (i.e. constant) behavior[76] but not significantly when compared to the case of FTICR.

The proposed methods are designed to work with centroided MSI data (i.e. processed – not profile, retaining only *m/z* values and corresponding signal intensities of the detected/observed peaks in any given spectrum; see **section 1.2**). Since peaks' FWHM values cannot be computed for centroided data, this information has to be supplied externally in the form of a profile spectrum randomly chosen and externally provided by the end-user from the same MSI data. To test if one randomly chosen spectrum could be representative of the entire MSI measurement data, a comparison has been performed between FWHM models generated based on one and 100 randomly chosen spectra of a glioblastoma (GB) tissue MALDI-FTICR-MSI measurement in both positive and negative ion modes (**Figure 4.2**). The results illustrate that a single spectrum could indeed be enough to generate a FWHM model for an entire MSI measurement. The location that the chosen full profile spectrum is taken from seems irrelevant. The same can be said for the identities of the peaks present in it. This could be explained by the fact that for any MSI measurement, the sample is measured with the same measurement parameters, and therefore resolving power as a function of *m/z* is expected to be similar across the tissue while deviations in the measured FWHM values are handled by the smoothing capabilities of the LOESS model as described above. However, relying on one single spectrum for this estimation could be seen as a downside of this approach since a user might (randomly) select a corrupt spectrum (a spectrum that only contains noise). To address this possibility, *molecular* allows for employing more than one profile spectrum for FWHM model fitting.

5.2 Capturing the Molecule-of-interest

Ion images, i.e. false color renderings of *m/z* intervals of interest, are used as the fundamental investigation tool in MSI for conveying the spatial distribution of molecules-of-interest (MOIs, e.g. metabolites, drugs, lipids or proteins) within biological tissues often compared to external histopathology annotations. The conversion of raw data into ion images for visualization, spatial interpretation and molecular analysis, has not changed since the inception of the technology and normally does not include built-in methods that account for mass accuracy and instrument- and measurement-dependent mass resolving power.

Ion images are typically generated by summing up all observed (centroided or profile) ion intensities with identical weights (i.e. uniform mass-window weighting) within a user-defined mass-range around a certain theoretical *m/z* value representing the MOI (see **section 1.2**).[79,80] In other words, rendering ion images of MOIs always entails the selection of an appropriate mass-search-window where that MOI signal is to be found. This, however, could be a source of bias. For instance, in a targeted drug-uptake study, an incorrectly assigned mass-window width by the end-user for rendering ion images of a certain drug, which if set too high, could include interfering noise and other interfering background signals.

In this work, an attempt was made to develop a data-driven user-independent method for estimating an appropriate width for the mass-search-window at a given *m/z* MOI based on the mass resolving power of the mass spectrometer. After estimating an empirical FWHM model as described in the preceding section, for any given *m/z* MOI, the model could be used to infer the corresponding standard deviation σ_w of a hypothetical Gaussian that could be used to represent the theoretical MOI peak shape and, hence, its extent[35,48], which is governed by $\text{FWHM} = 2\sqrt{2\,ln2}\,\sigma_w$. This enables data-driven calculation of the mass-search-window width taken as $m_{MOI} \pm 3\sigma_w$ (i.e. the span of the erected Gaussian-window; m_{MOI} is the *m/z* value of the MOI) independent of the user, measurement device and measurement parameters while also taking into account the mass resolving power at that mass range.

The described Gaussian envelope helps not only in determining the extent of the MOI mass-window but also provides a convenient framework for down-weighting proximal interfering signals in the vicinity of *m/z* MOI (see **Figure 4.3**). This is achieved by assigning corresponding Gaussian weights for all observed peaks-of-interest (POIs; i.e. observed peak signals within the estimated mass-window) such that, the further the measured *m/z* POI from the theoretical *m/z*, the lower the weight it receives in the final ion representation. The effectiveness of the Gaussian mass-window weighting was demonstrated against the typical uniform mass-window weighting by i) artificially "contaminating" the raw data of a MALDI-FTICR-MSI measurement of an isocitrate dehydrogenase-wild type (IDH-WT) GB sample with a random Gaussian noise source at successive mass intervals (multiples of σ_w) away

from an example MOI and by ii) visualizing two adjacent MOIs in sagittal mouse brain sections measured on FTICR- (**Figure 4.5**), timsTOF- (**Figure 4.6**) and MALDI-TOF- (**Figure 4.7**) MSI modalities in a cross-platform setup (see **section 4.3**). The results illustrated that Gaussian mass-window weighting was more effective in removing interference noise and observed peaks (weather artificial, real or caused by artifacts) which (partially) overlap with the MOI signal. It should be noted, however, that a complete overlap of POI signals cannot be remedied, not even by Gaussian mass-window weighting as in the shown case of MALDI-TOF-MSI (**Figure 4.7**).

In all presented cases, the uniform mass-window weighting, typically used for ion image generation, struggled in separating the showcased signals. It could be argued, that an experienced end-user would typically further refine the used mass-window width by inspecting mean spectra and would therefore arrive to results similar to the ones obtained by the Gaussian mass-window weighting. This, however, would make the entire process heavily user-dependent which would undoubtedly cast a shadow over the inter-operator reproducibility of ion images and their rendering. In this regard, the proposed Gaussian mass-window weighting avoids this user dependence and can be considered as a step in the right direction.

5.3 Molecular Probabilistic Maps (MPMs) vs. Ion Images

In MSI, ion images, i.e. false color renderings of *m/z* intervals, remain the gold-standard for the visualization and spatial interpretation of MOIs in any given sample. Typically ion images are generated by integrating (with equal weights) ion intensities of all peaks present in a user-defined mass-window centered at the *m/z* MOI.[79] This work proposes a computational framework, *moleculaR*, that suggests an alternative way for studying the spatial distribution of MOIs in tissue samples. In the previous two sections, a discussion has been provided on the proposed user-independent rendering of ion intensities where the mass-window is estimated based on the mass-resolving power of the mass spectrometer (**section 5.1**) and the filtration of interfering background signals through the Gaussian mass-window weighting (**section 5.2**). But more importantly, the primary aim of this work is to propose a user-independent spatial interpretation of the distribution of MOI's signal relative to the tissue morphology via spatial probabilistic mapping.

The central idea in this spatial probabilistic analysis concept is the comparison between MOI's detected spatial distribution within a tissue sample against a complete spatial randomness (CSR) model created out of the same MOI's signals. This spatial comparison scans for tissue areas that exhibit statistically significant non-random spatial patterns of MOI intensities independent of how an end-user may perceive its spatial accumulation or deficiency. Previously published CSR generating models primarily dealt with unmarked (unweighted) spatial point patterns (SPPs) which only considered points locations.[153,154] In particular, Kather et al.[153] proposed a

similar concept for detecting angiogenic hotspots in immunostained histological whole-slide images. After computational extraction of blood vessels locations by image segmentation, a corresponding CSR model was used as a spatial control. In MSI data, however, each point must carry an intensity value (representing pixel signal intensity and indicating MOI local abundance in tissue) in addition to the x, y-coordinate. Therefore, the corresponding CSR map must model randomness in spatial locations as well as in signal intensities in an unbiased way. This has been achieved by randomly permuting intensity-marked points, which basically has the effect of spatial reshuffling of MSI pixels, until they assume a homogeneous spatial Poisson process[152], thus effectively dissolving any spatial clustering or autocorrelation of signals. Another approach involving hotspot identification in marked (i.e. signal intensity weighted) SPPs of spatial transcriptomics data has been reported by Edsgärd et al.[174] In their approach, the x, y-positions of marked points remained stationary while the signal intensities (expression level) were randomly reassigned repeatedly, up to 1000 times, to establish a per-point null distribution based on the resampling of the mark distribution. This approach, however, has relatively high computational complexity as all possible point pairs for every permutation need to be assessed. This hinders its application in MALDI-MSI experiments, which typically employ higher spatial resolutions (20-50 µm in this work), yielding much larger numbers of spatial points, compared to the spatial resolution of 200 µm reported in the above study.

While MOI signals spatial representation inherit the discretized and gridded nature of the MSI data (see **section 1.2**), creating a CSR model on a spatial grid would directly violate such models' randomness criterion. As a result, MOI pixel intensities are mapped into an SPP representation (see **section 3.5** for details) in order to facilitate a direct and homogeneous comparison between the MOI and the corresponding CSR model. It is important to note, however, that the final MPM is represented not as an SPP but as a gridded image with hotspots and/or coldspots superimposed as polygonal contours. This was chosen because, for the end-user, who is used for working with gridded MSI data, a visualization based on SPPs would be very unfamiliar and thus might cause unnecessary confusion.

The MOI-specific CSR model is generated by random permutations of the MOI's SPP data points. This means that the generated CSR model is unique for every MPM evaluation, which, consequently, has a direct effect on the resulting hotspot/coldspot contours. For this purpose, computational experiments involving real and simulated data has been carried out to test the impact of the stochastic nature of the CSR model on the stability of the generated MPM hotspot/coldspot contours (see **section 4.4.7**). The results indicated that MPMs are rather robust against such permutation tests. This could be explained by the smoothing effect of the kernel density estimation (KDE) step at the heart of the MPM method, in which, fluctuations in the resulting CSR are relatively smoothed out.

The beneficial effect of the KDE step, which is internally performed with each

MPM evaluation, does not seem to stop here. MPMs have been extensively tested against three types of superimposed artificial noise sources showing remarkable resilience and stability (see **section 4.4.6**). Even when the intensity of the added artificial noise is increased (by increasing its standard deviation σ_{noise}; see **Figures 4.20-4.21**), the resulting MPMs are able to withstand noise with σ_{noise} up to 4 and 10 times σ_{MOI} (i.e. the standard deviation of the raw MOI signal) for artificially added Gaussian and interference noise, respectively. Such noise levels are much higher than the previously reported and typically expected Poisson noise inherent to MSI data.[175] Moreover, MPMs were also shown to be robust against spiking intensity artifacts showing resilience to up to an unlikely $n = 450$ randomly placed high intensity artifacts (see **Figure 4.22**). It is important to note that in all artificial noise "contamination" experiments, obvious visual degradation and high dissimilarity between raw and artificially contaminated data was observed in the corresponding "classical" ion images. This could be explained by the fact that MPMs employ i) Gaussian mass-window weighting which might be able to tune down interfering peaks proximal to the *m/z* MOI that may obstruct ion images and ii) the KDE step, which is expected to conveniently reduce technical variations and noise fluctuations during the process of hotspot/coldspot estimation.

MALDI-MSI data generation is known to be affected by systematic sources of technical variation, the so-called batch effects. Batch effects can occur at different levels: sample preparation and measurement-specific pixel-to-pixel, tissue section-to-section and measurement slide-to-slide batch effects (see **section 1.3** in **Chapter 2**).[40] Since these batch effects are largely unavoidable, it was important to evaluate the performance of MPMs when sources of technical variation are present in the MSI data. Here, MPMs were shown to be largely stable in experimental setups where pixel-to-pixel, section-to-section and slide-to-slide batch effects are involved (see **section 4.4.8**).

Following the discussion above, it can be seen that the application of KDE within the MPM framework has three main advantages: i) it captures the overall spatial trend of the MOI's intensities, ii) it forces spatial null distribution ($f_{CSR}(k)$ in **Figure 4.8b**; see **section 4.4.1**) to converge to a normal distribution (see **Figure 4.12**) and, being a low-pass filter, iii) it has the often-desired outcome of smoothing technical variations and noise fluctuations during the process of hotspot/coldspot estimation which has in turn a positive outcome on the method's tolerance to pixel-to-pixel, section-to-section and slide-to-slide batch effects (see **section 4.4.8**). However, KDE application requires estimating an optimal data-dependent smoothing scale (i.e. kernel bandwidth) which, on its own, is a well-known challenge.[170] Smoothing SPPs with high KDE bandwidths while generating MPMs has the potential adverse effect of overlooking fine, small or sparse spatial structures which leads to their exclusion from being characterized as hotspots/coldspots. To address this issue, a data-driven mechanism for KDE bandwidth estimation has been proposed in this work based

on spatial autocorrelation that prevents spatial over-smoothing (see **sections 3.8** and **4.4.4**).

Spatial autocorrelation measures the degree of spatial co-dependency of observations (pixels or points) existing in a defined neighborhood size within a spatial window.[157] The idea behind this step-wise evaluation of autocorrelation as a function of smoothing comes from scale-space theory in computer vision, where an image is represented by a one-parameter (i.e. the smoothing scale) family of smoothed images.[171] The proposed KDE bandwidth estimation method is based on the hypothesis that, in a Moran's I vs smoothing bandwidth plot, the point at which Moran's I statistic rate of change abruptly falls, is the scale at which exactly those random pixel fluctuations or small variations are reduced or smoothed away and important spatial structures/features/patterns start dominating the spatial landscape. This hypothesis seems to hold true when MPMs were tested against various types of artificially added noise as discussed above. It is, nevertheless, important to define the spatial scale of such small variations. Here, it is known from scale space theory, that when convolving a Gaussian kernel with an image, only image structures much smaller than the scale parameter (i.e. the bandwidth of the Gaussian kernel; see **section 4.4.4**) will be largely smoothed away in the process.[171] Considering that the computed KDE bandwidth values for all cases shown in this work were between 2 and 2.6 pixels, structures that could be smoothed away and, as a result, overlooked by MPMs are thus smaller than 2 pixels. Moreover, structures with cross-sections smaller than this but with high intensity (indicating high SNR or MOI abundance) will largely resist this smoothing and would still be seen as hotspots. The test case of the APP NL-G-F Alzheimer's disease mouse model brain (see **Figure 4.9d**) measured in linear mode MALDI-TOF-MSI (at low SNR) provides a clear example; sparsely distributed and fine amyloid plaques $A\beta_{1-38}$ (*m/z* 4060.5) were detected as hotspots. In this example, however, the generated MPM disregarded subsets of single-pixels assumed to be plaques by the previously published *PlaquePicker*[145] specifically designed to do this task. This could be attributed to the fact that, unlike *PlaquePicker*, which strictly relies on image-global intensity thresholding, MPMs also take into account the spatial co-dependence of MOI signals which could be an important criteria for filtering out spurious outlier single-pixel signals. Whether the single-pixel signals labeled as plaques by *PlaquePicker* but disregarded by MPMs are in fact $A\beta_{1-38}$ plaques would have to be a subject for additional experimentation with orthogonal methods. Nonetheless, *moleculaR* also allows for the manual fine-tuning of the KDE bandwidth, which can be fine-tuned against an orthogonal (e.g. optical) method or simply inferred from what is theoretically expected for the object being imaged (see **Figure 4.9d**).

Several showcases have been provided where the MPM method has been applied on MALDI MSI data generated by different mass spectrometers including FTICR-, timsTOF- and TOF-MALDI-MSI devices (see **section 4.4.1**) as well as on simulated

data based on empirical intensities derived from actual MALDI-MSI data (see **section 4.4.5**). In all demonstration cases, MPMs were benchmarked against the typical interrogation procedure employed in MSI: on the one hand, an end-user's visual perception of intensity values, who is judging roughly whether an MOI had a relatively higher spatial abundance in a certain tissue morphology. On the other hand, MPMs, which provide MOI hotspot/coldspot designations of non-random spatial patterns based on a statistical model. For example, as illustrated in **Figure 4.9**, looking at ion images, the researcher would be relying on their subjective perspective based on visual differentiation of color-coded intensities to describe and localize MOI accumulation while MPMs clearly outline MOI hotspots and coldspots relative to the tissue morphology without leaving any room for the end-user's personal opinion. Simulation-based experiments mimicking ground-truth have also shown that MPMs were able to reliably localize all simulated high-MOI areas and identify points exhibiting significant relative spatial abundance (see **section 4.4.5**).

Different probabilistic analysis concepts have been previously applied on MSI data. Hanselmann et al.[86] applied probabilistic latent semantic analysis (pLSA) for unsupervised dimensionality reduction of MSI data and used Akaike information criterion (AIC) for data-driven estimation of the number of components of the pLSA model. Bemis et al.[83] proposed spatial shrunken centroids, a probabilistic segmentation method, for segmentation of MSI data into newly discovered homogeneous segments of similar molecular content. Pamler et al.[147] were the first to introduce false discovery rate (FDR)-controlled metabolite annotation to the MSI field. In that setup, the FDR, an important statistical measure for the quantification of annotation quality, is defined as the ratio of false positives to the total number of annotations. These three concepts are, however, different in scope and aims from the probabilistic spatial mapping introduced in this work. For instance, pLSA and spatial shrunken centroids are multivariate analysis techniques that are designed to discover tissue morphological similarities based on the entire molecular content present in each pixel of the MSI data. Similarly, the FDR-based metabolite annotation approach attempts to solve an entirely different problem with the help of target–decoy-based FDR-estimation the goal of which is to test if a detected and observed POI (i.e. MS peak) is the sought-after MOI (i.e. the actual molecule). In contrast, the proposed spatial probabilistic mapping applies a probabilistic concept in order to spatially localize non-random patterns of detected MOI signals in order to assist the user in spatial interpretation.

Perhaps the closest concept to the proposed MPMs is the measure of spatial chaos[111], a score that has been introduced to i) automatically select spatially structured ion images in MSI data and ii) has been reused later as a computational measure of ion image quality, which was tested against a curated set of ion images based on collective expert judgments[80], and iii) as part of the FDR-based annotation engine described above to quantify the likelihood of the presence of a metabolite with a

given sum formula in the MSI data[147]. The difference here, is that the measure of spatial chaos tries to test if an ion image exhibits a non-random pattern or not. In contrast, *moleculaR* provides the added benefit of spatially localizing non-random patterns within ion intensity images. Furthermore, the measure of chaos returns a value between 0 and 1, which is high for spatially structured images and low for noisy images and does not provide a definitive data-driven threshold to separate noisy from structured images. In contrast, MOI hotspot/coldspot contours computed by *moleculaR* are based on pixel-wise statistical significance testing against a spatial null distribution derived from a CSR model with a p-value threshold set to a significance level $\alpha = 0.05$, Benjamini-Hochberg corrected. Moreover, similar to the measure of spatial chaos, MPMs can also be used for automated screening for spatially structured ion signals in MSI data such that the absence of detected hotspot/coldspot contours would indicate POI signals resembling random noise.

5.4 Cross-tissue Molecular probabilistic maps (CT-MPMs)

CT-MPMs are valuable in scenarios where it is necessary to compare the distribution of metabolite or drug signals between test and reference tissues. This is particularly relevant in cases where drugs are administered or specific mutations are present. CT-MPMs allow for cross-tissue spatial statistical testing, unlike traditional statistical comparisons that solely focus on signal intensities which are pooled together and represented by box/violin plots (e.g. see **Figure 4.10**), which do not account for the spatial localization of the MOI under study. CT-MPMs not only determine the presence of hotspots/coldspots in the test tissue, but also evaluate whether and where the intensity distribution in the test tissue differs significantly from that in the reference tissue (see **section 4.4.2**). In other words, CT-MPMs identify the pixel locations in the test tissue that carry intensities that are unlikely to belong to the distribution of reference tissue pixel intensities and exhibit a non-random spatial pattern which makes CT-MPMs even stricter than MPMs.

CT-MPMs have been showcased on a previously published data involving IDH-mutant (IDH-MUT) and IDH-WT glioma samples measured in MALDI-FTICR-MSI.[13] The advantage of using CT-MPMs can clearly be seen where instead of only reporting box/violin plots of the tryptophan signal intensity, one can also get a visual illustration of the spatial tissue-context in the test tissue (IDH-MUT glioma) sample where the tryptophan signal has significantly higher relative spatial abundance when compared to the reference tissue (IDH-WT) sample (see **Figure 4.10**). The true spatial distribution (i.e. the ground-truth) of the tryptophan signal cannot be inferred and therefore CT-MPMs had to be validated using other means. This has been accomplished by utilizing the developed SPP simulation methods described previously (see **section 4.4.5**). In that experimental setup, the generated CT-MPMs on simulated data correctly identified only the case in which a simulated spatial structure of high-MOI

abundance was present and intensity values were sampled from different normal distributions (shown in **Figure 4.17a**).

It must be noted that, as is the case with classical drug/metabolite intensity distribution testing of Test-vs-Reference tissues, which is commonly encountered in the MSI literature, it is important to ensure that the signal intensities of both test and reference tissues are comparable. This requires observing appropriate experimental design, which deliberately minimizes technical variation (e.g., placing them on the same slide to be measured in a single measurement)[40] and/or by relying on robust intensity normalization methods.[37–39,94]

5.5 Collective Projection Probabilistic Maps (CPPMs)

Typically ion images are used to encode signal intensities of a single MOI at a time. For simultaneous visualization of multiple MOIs, researchers sometimes resolve to the RGB (red, green and blue) color model where a single MOI map is assigned to a single color channel thus creating a composite RGB ion images in the process.[9,79] This procedure, however, can only visualize few MOIs at a time. The proposed framework, *moleculaR*, provides researchers with the ability to visualize not only one molecular entity at a time or per color-channel but also a custom list of biomedically relevant MOIs if needed. This list depends on their research question. For example, the researcher might want to investigate the collective intensity of a subset of saturated lipids within a certain lipid class and correlate its signal accumulation to the tissue-local microenvironment. More importantly, these collective visualizations can take full advantage of the probabilistic mapping methodology discussed in the preceding sections.

As an example, CPPMs were used to study all glycerophospholipids (GPLs) and lyso-glycerophospholipids (lyso-GPLs) in the two IDH-WT GB serial sections (**Figure 4.11** and **Supplementary Figure 8.1**) in an attempt to investigate phospholipid remodeling (Lands cycle) across the GB tissue morphology. In this process, acyl chains of phospholipids are modified by deacylation and reacylation reactions resulting in new phospholipids with different acyl chain compositions thereby affecting their impact on biological processes.[169]. Here, CPPMs of all lyso-GPLs and single classes (LPC, LPE, LPS, LPI) compared to all GPLs and single GPL classes (PC, PE, PS, PI) suggested enrichment of GPLs and depletion of lyso-GPLs in viable tumor regions (see **Figure 4.11c**). This observation was supported by retrospective transcript expression profiling of Lands cycle enzymes which showed overexpression of various acyltransferase genes (*LPCAT1, AGPAT1, LPCAT3, MBOAT7*) in GB compared to normal brain tissue but less changes in *PLA2G6* expression. Previous studies reported the implication of acyltransferases in cancer progression and drug resistance, for instance, *AGPAT* isoforms overexpression has been shown to correlate with increased risk of tumor

development or aggressiveness of several tumors types[176] while upregulation of *LPCAT1* has been observed in multiple tumors.[177]

In another assessment, CPPMs of potassium and sodium adducts of lipids across lipid classes detected in the same GB tissue sections suggested that potassium adducts of all (lyso-)GPLs (i.e. GPLs and lyso-GPLs together) were more abundant in vital tumor and surrounding areas while sodium adducts were more pronounced in necrotic tissue showing significant relative spatial deficiency (coldspot) in vital tumor (see **Figure 4.11d**). This observation agrees with previously published data where highly abundant Na^+-adducts colocalized with necrotic tissue in xenografts of five different tumor cell lines.[139] Deen et al. have also previously shown that sodium magnetic resonance imaging (MRI) can serve as an indicator of tumor cellularity *in vivo* based on the fact that the sodium-potassium pump maintains high overall intracellular potassium and low sodium concentrations in viable cells and higher cellularity corresponds to a lower tissue sodium concentration.[178]

This computational framework further enables spatial evaluation of composite numeric scores obtained by applying basic arithmetic operations on SPPs of multiple MOIs in different ways. This has been showcased with the adenine nucleotides [ATP-H]⁻, [ADP-H]⁻ and [AMP-H]⁻, which were visualized individually and relative to their collective sum, as well as in more complex scores such as the adenylate energy charge, an index used commonly to indicate the energy status of biological cells by providing a score of the degree of the strictly regulated phosphorylation of the ATP-ADP-AMP system.[165] The observed results suggest that areas of high adenylate energy charge overlap with tissue regions annotated as viable tumor. Previously, Fack et al.[14] reported higher energy charge score of patient-derived xenografts in IDH-WT glioma when compared to IDH-MUT and control (normal) brain tissue and suggested that the energy charge score correlates with tumor proliferation and aggressiveness. Additionally, Torata et al.[179] also observed higher energy charge score in breast carcinoma when compared to normal tissue in a MALDI-MSI-based experiment comprising a cohort of 119 samples. Likewise, adenylate kinase mass action ratio[166], also known as the adenylate kinase equilibrium constant[167], can also be computed. This score reflects the relative concentrations of the adenine nucleotides and their effect on the reversible reaction ATP+AMP ⇌ 2ADP, which is catalyzed by adenylate kinase, a phosphotransferase enzyme; a high mass action ratio means that the reaction is biased towards production of ADP from ATP and AMP, while a low mass action ratio means that it is biased towards the reverse reaction.[168]

Taken together, the showcased examples suggest that CPPMs of molecular ensembles in MSI may provide insights into spatially resolved pathophysiology or can be potentially used to localize viable tumor areas with high cellularity in highly heterogeneous tissue samples without the need for external histopathological annotation which would not be possible by single molecule ion images or MPMs not involving collective projections. It must be noted, however, that the above observations will

obviously require extensive follow-up studies with larger sample cohorts, before clinically valid statements can be made.

5.6 Drug Quantification in the Presence of Batch Effects

In this work an attempt was made to further investigate quantitative spatial mapping of drugs in tissue sections by performing tissue-drug content quantification on an entire tissue cohort of 56 specimens of gastrointestinal stromal tumor (GIST) and corresponding non-tumor samples. Sample measurements were conducted in triplicates on TOF- and FTICR-MALDI-MSI modalities comparing their results to the gold-standard ultra-high performance liquid chromatography electrospray-ionization quadrupole time-of-flight mass spectrometry (UHPLC-ESI-QTOF-MS). The study aimed at improving computational calibration in MALDI-TOF-MSI and to cast light onto the effectiveness of uptake (or lack of export or tissue metabolism) of the therapeutic tyrosine kinase inhibitor (TKI), imatinib, into GIST tissue.

All slides, on which tissue sections were mounted for MALDI-MSI measurements, featured an imatinib dilution series spotted onto porcine liver tissue and spray-coated with deuterated imatinib-D8 for calibration and normalization. It has been observed that all drug dilution series signal intensity responses measured either with MALDI-TOF-MSI ($n = 48$) or MALDI-FTICR-MSI ($n = 3$) deviated from linearity (see **Figure 4.28**). A similar behavior has already been reported by Pirman and co-workers, and was attributed to the matrix-to-analyte ratio such that increasing the matrix spray-coating time resulted in an increased deviation from linearity of the intensity response.[46] Moreover, the complex MALDI process, non-uniform tissue-ion suppression resulting in pixel-to-pixel batch effects, interference from matrix background signals, and different ion detection/counting technologies are all factors that could contribute to the observed nonlinear response.[96] While it is typical for MALDI-TOF and -FTICR-MSI drug quantification investigations to employ linear calibration for drug dilution series, this linearity may not always be guaranteed, particularly in the case of scarce and heterogeneous tissue samples even when the matrix-to-analyte ratios have been optimized.[45] This is especially the case for clinical samples which are obtained from different individuals and typically contain different amounts of the target analyte. Hence, in this work, it was hypothesized that a nonlinear calibration may better model the system's response and can be generally more applicable, especially in clinical pharmacology. Moreover, when comparing the typical linear and nonlinear calibration curves for UHPLC-ESI-QTOF-MS calibration, both fits were nearly identical with the *b* exponent converging to unity (see **Equation 3.9** and **Figure 4.29c**), indicating a true linear response for UHPLC-ESI-QTOF-MS. This highlights the generalizability and the ability of the proposed calibration method to not only model the calibration curves of analytes but also convey a quantitative assessment of its deviation from linearity.

Interestingly, a very recent study went as far as to suggest a deep learning-based regression model for predicting chlordecone, a carcinogenic pesticide, in mouse liver tissue via MALDI-TOF-MSI to account for the inherent signal variability.[180] Dewez et al.[50] have also observed substantial heterogeneity in ion suppression across a tissue sample while conducting quantification of an endogenous peptide of histone H4 by MALDI-MSI. They proposed a novel multi-labeling approach where a mixture of isotopically labeled internal standards (ISs), each at a different concentration, is applied to the sample, thus making it possible to create per-pixel internal calibration curves that account for local ionization differences. One challenge of such a method is that the matrix-to-analyte ratio described above can quickly become a limiting factor for the number of data points used for constructing per-pixel calibration curves since spraying additional concentration layers of ISs can increase this ratio and could cause an increased deviation from linearity of the intensity response.

Despite the known challenges of batch effects, quantitative MALDI-MSI provides the crucial benefit of spatial mapping of drug distribution over UHPLC-ESI-QTOF-MS-based quantification. This spatial aspect, and together with overlaid histopathological tissue annotations, enable colocalization analysis of drugs and their metabolites plus other relevant biomolecules within different tissue morphologies. A clear example of this has been shown with one GIST sample (sample A) and its three replicates, whose histopathological assessment and MALDI-MSI measurements showed obvious heterogeneity containing both normal liver and metastatic GIST tissue (see **Figure 4.31c**). Here, MALDI-MSI was instrumental in deducing that the apparent similar levels of imatinib in normal and tumor tissue as seen by UHPLC-ESI-QTOF-MS were caused by the presence of unknown fractions of non-tumor tissue in the tumor sample.

In order to achieve efficacy, drugs that target cancer must be able to penetrate tissue sufficiently. In this work, the ability of imatinib to penetrate tumors in samples of human GIST was investigated. The results showed that despite the drug being present at high levels above the limit of quantification (LOQ) in the normal liver tissue surrounding the metastatic GIST, the orally administered imatinib showed limited uptake or retention in metastatic GIST, independent of mutation status, with amounts below LOQ. A subsequent spatially-resolved analysis by MALDI-MSI revealed that the drug apparently was unable to penetrate into the metastatic tumor despite high concentrations within the surrounding liver tissue. Additionally, ion intensity maps of sodium and potassium adducts of imatinib as well as its metabolite, N-desmethylimatinib, revealed that the lack of imatinib within metastatic GIST in liver was not due to differential tissue-dependent adduct formations or to the possibility of it being completely metabolized within the tumor tissue. Reasons for such discrepancy between imatinib amount in normal hepatic and metastatic GIST could be attributed to characteristics common to solid tumors such as poorly organized vasculature, increased interstitial fluid caused by the lack of functional

lymphatics and/or inflammation and abnormal structures of the extracellular matrix.[181] However, it has been previously reported that tumor vascularity decreases in GIST metastases after treatment with imatinib.[182] Imaging of Heme B, a proven MALDI-MSI marker of vasculature[173], supported these results suggesting lower vasculature within the tumor core when compared with the surrounding hepatic tissue. The findings of this study on the lack of drug penetration into tumor tissue also supports previous MALDI-MSI-based drug studies involving different cell line-based and patient-derived xenograft models.[183–185]

Finally, the proposed spatial probabilistic mapping discussed in the previous sections was combined with the MALDI-MSI-based spatial quantitative mapping of drug signals based on dilution series (see **section 4.5.4**). Here, CT-MPMs were generated to spatially localize areas of significant cross-tissue relative spatial abundance of imatinib in the GIST tissue sample A (test tissue) when compared against a series of imatinib dilution spots (reference tissue) in MALDI-TOF-MSI data. Consecutive cross-tissue comparisons revealed high spatial heterogeneity in drug-tissue content with some pixels showing much higher levels than the reported mean per tissue as evidenced by the detected cross-tissue hotspots restricted spatially to small parts of the tissue section (e.g. few hotspots in **Figure 4.32h** indicating imatinib amounts above 12.5 pmol while the mean imatinib content based in calibration curves was 7.78 pmol and 7.81 pmol based on MALDI-TOF-MSI and UHPLC-ESI-QTOF-MS quantification, respectively). These findings illustrate how the probabilistic spatial mapping through CT-MPMs could potentially be used to spatially investigate tissue drug content against single spots of therapeutic or toxic drug concentration spotted alongside the tissue section without the need for preparing drug dilution series and drug calibration curves, thereby, saving effort and time and reducing the impact of batch effects on the outcome.

5.7 Methods Limitations

This work presented a computational framework, *moleculaR*, which proposes a user-independent MALDI-MSI-based spatial interpretation of the distribution of single MOIs and MOI ensembles relative to the tissue morphology via spatial probabilistic mapping. As in the case of ion images, *moleculaR* does its calculations based on ion signal intensities generated by the MALDI ionization processes, which inevitably adds technical variability to biology-related variability.[40] *moleculaR* should not be considered as an MSI data denoising method, because it was not primarily designed to detect and filter out technical variability. Despite the internal mechanisms of Gaussian mass-window weighting and KDE smoothing, both of which are expected to reduce the impact of signal uncertainty on the hotspot/coldspot contours, each ion intensity image will still contain an unknown amount of non-biological technical variability. This aspect is even more pronounced in situations where arithmetic operations are applied to individual SPPs of MOIs whose uncertainty could be carried on to the

composite image representation through error propagation. In particular, division of variables may be prone to uncertainty amplification.

The effectiveness of the proposed Gaussian mass-window weighting, which serves as a protection against possible proximal background signals by down-weighting them relative to *m/z* MOI, has been demonstrated on real data as well as in artificial setups (see **section 5.2**). It, however, does not protect against mis-calibrated/misaligned MSI data. In such situations, it is strongly advised to utilize data-adaptive MSI recalibration methods.[36] On the other hand, the reliance of the Gaussian mass-window weighting on the estimated FWHM model, which, itself, is based on a single spectrum provided externally by the end-user could also be seen as a downside of this approach since the end-user might accidentally select a corrupt spectrum (a spectrum that only contains noise). To address this possibility, *moleculaR* allows for employing more than one profile spectrum for FWHM model fitting.

Another important workflow, that might be sensitive in particular to slide-to-slide batch effects, is the CT-MPM approach. Here, as in the commonly encountered drug/metabolite intensity distribution testing of test-vs-reference tissues, it is important to ensure that the signal intensities of both test and reference tissues are comparable. This requires observing appropriate experimental design, which deliberately minimizes technical variation (ex. placing them on the same slide to be measured in a single measurement)[40] and/or by relying on robust intensity normalization methods.[37–39,94] This also applies to the discussed idea of CT-MPM-based quantitative spatial mapping.

The beneficial effects of the KDE step, which is internally performed with each MPM evaluation, has been discussed in **section 5.3**. However, KDE application requires estimating an optimal data-dependent smoothing scale (bandwidth) which, on its own, is a well-known challenge.[170] To resolve this issue, this work has proposed a data-driven mechanism for KDE bandwidth estimation based on spatial autocorrelation[157] that prevents spatial over-smoothing (see **section 3.8**). This method has been validated on real as well as simulated data (see **section 4.4.4**). However, the dependence of the resulting MPM hotspots/coldspots on the KDE bandwidth might still be seen as a limitation to the proposed method resulting in an uncertainty that would require a MALDI-MSI-based phantom sample with controlled molecular content to quantify, which, unfortunately, has not yet been developed within the MSI community.

It is important to note that *moleculaR* does not provide a framework for testing if a detected and observed POI (i.e. MS peak) is the sought-after MOI (i.e. the actual molecule). Analogous to "classical" ion images, it rather permits the end-user to analyze and visualize single MOIs or MOI ensembles that he/she is interested in. Whether the intensity distribution observed is, in fact, the desired MOI (drug, metabolite, etc.) is a question that must be validated by orthogonal analytical approaches

such as MS/MS fragmentation or ion mobility MS and/or accurate mass and sum formula determination at very high resolving power. Throughout this work, the METASPACE annotation engine[147] (https:// metaspace2020.eu), has been used for POI-MOI matching based on the SwissLipids[148] database and the false discovery rate (FDR) has been reported when possible. False positive matching is unavoidable. If a false positive POI-MOI match (through an external method) may occur for an interfering peak that is observed in a close proximity of the theoretical *m/z* MOI which also happen to have a degree of spatial autocorrelation (i.e. possesses a spatial pattern), then *moleculaR* will provide an MPM that shows hotspots/coldspots for that particular POI. It is important to note, however, that ion images, which are still the current norm in studying spatial distribution of MOIs in MSI, will also fail in this case. More importantly, for all reported results involving MPMs and, in particular, CPPMs, an unknown degree of uncertainty is present caused by in-source fragmentation and modification of lipids that might happen during the MALDI ionization process.[63,186]

This work further investigated quantitative spatial mapping of drugs in tissue sections by performing nonlinear calibration-based tissue-drug content quantification on an entire tissue cohort of GIST specimens on TOF- and FTICR-MALDI-MSI modalities comparing their results to the gold-standard UHPLC-ESI-QTOF-MS. Here, due to the limited tissue availability and since all measurements were conducted in triplicates, some samples were completely used up before reaching the next round of measurements with UHPLC-ESI-QTOF-MS and MALDI-FTICR-MSI. This has negatively impacted quantification comparisons across these three modalities. It must also be stated that, while MALDI-TOF- and -FTICR-MSI have historically been compared to UHPLC-MS as the definitive method for quantification, it is important to exercise caution when performing such validation. This is because MALDI-MSI provides quantification on a pixel-by-pixel basis of a very thin tissue surface layer[187], whereas UHPLC-MS quantifies the drug within a tissue volume. In the case of MALDI-MSI, due to its proximity to the applied matrix, the spray-coated IS as well as on-tissue spotted drug within the dilution series might exhibit different mass transfer kinetics into the MALDI matrix when compared to endogenous analytes in the cellular environment.[50,51] This and other previously reported factors affecting MALDI-MSI-based quantification, such as the various types of batch effects[40], may add to the uncertainty in drug-tissue quantification, despite the promising results reported in this work and in previous studies.

5.8 Conclusion

This work introduces a computational framework, *moleculaR*, which proposes the concept of spatial probabilistic mapping in MSI as a solution to the known limitations of ion images when it comes to spatial visualization and interpretation of MOIs' distribution in tissue samples via MSI. It provides user-independent solutions for the

conversion of raw data into ion intensity images; namely, data-driven FWHM modeling for the calculation of the mass-search window, Gaussian mass-window weighting for improved signal reliability, user-independent spatial interpretation of the distribution of single MOIs and MOI ensembles based spatial probabilistic mapping through MPMs and CPPMs as well as CT-MPMs for the cross-tissue spatially-aware comparison of metabolite or drug signals distribution between test and reference tissues.

The different parts of the framework have been tested and validated on MALDI-MSI data measured with different mass spectrometers including ultra-high-resolution MALDI-FTICR, high-resolution MALDI-timsTOF and MALDI-TOF mass spectrometers featuring different tissue samples; namely, human IDH-WT GB, human IDH-WT and -MUT glioma, human GIST, wild-type mouse brain, porcine liver and APP NL-G-F Alzheimer's disease mouse tissue samples. Moreover, simulation-based experiments mimicking MALDI-MSI ground-truth have also been developed and utilized to test the proposed workflows.

The observed results suggest that *moleculaR* is equally applicable for ultra-high-resolution MSI like magnetic resonance mass spectrometry (MRMS), for high-resolution instruments like MALDI-timsTOF or for MALDI-TOF mass spectrometers. The applicability of the proposed methods is also expected to include other types of mass spectrometry imaging data, which, however, requires follow-up testing. Furthermore, the results suggest that the proposed spatial probabilistic mapping represented by MPMs, CPPMs and CT-MPMs shall replace or complement ion images for the spatial analysis of MOI because of its valuable benefit of enabling localization of significant relative spatial abundance or deficiency of MOIs. *moleculaR* has been released as an open-source R package (https:// github.com/CeMOS-Mannheim/moleculaR) complementing leading MSI-bioinformatics packages and the results depicted and discussed in this work have been made available to the scientific community.[142]

In this work an attempt was also made to further investigate the applicability of the cross-tissue probabilistic spatial mapping concept in quantitative spatial mapping of drugs in tissue sections. A generalized nonlinear calibration model based on drug dilution series was proposed as a replacement for the traditional linear model that takes into account the inherent measurement nonlinearities characteristic to MALDI-MSI data. It's applicability was then tested in a clinical pharmacology setup by MALDI-MSI-based tissue-drug content quantification of an entire cohort of tumor tissue samples. The findings illustrated emphasize the significant potential of MALDI-MSI as a technique for investigating the spatial distribution of targeted drugs in oncology. This methodology could be further transferred to other clinical drugs beyond the example of imatinib presented in this work. In particular, MALDI-MSI could serve as a complementary method to evaluate the pharmacokinetics of drugs and their metabolites in tissue specimens post-surgery, providing insight into drug

uptake and tissue penetration efficiency and their impact on treatment resistance. Furthermore, the combination of spatial probabilistic and quantitative mapping through the use of CT-MPMs could potentially be used to spatially investigate tissue drug content and predict therapeutic sensitivity of diseased tissues. Findings presented and discussed in this work have been made available to the scientific community.[143]

Chapter 6

Summary

Ion images, i.e. false color renderings of mass-to-charge ratio (*m/z*) intervals of interest, are used as the fundamental investigation tool in mass spectrometry imaging (MSI) for conveying the spatial distribution of molecules-of-interest (MOIs, e.g., metabolites, drugs, lipids or proteins) within biological tissues that are often compared to external histopathology annotations. Ion images are also used as a gold-standard for validating the outcomes of computational and machine learning methods in biomarker discovery applications in MSI.[1,87,139] However, the conversion of raw MSI data into ion images for visualization, spatial interpretation and molecular analysis has not changed since the inception of the technology. Moreover, the generated ion images can be prone to technical artifacts, user input- and user perception-bias.[40,79]

The aim of this work was to address the known limitations of ion images when it comes to spatial visualization and interpretation of MOIs' distribution in tissue samples with MSI. The proposed solution is a computational framework, *moleculaR*, that employs a user-independent assignment of *m/z* intervals for capturing MOIs based on the device- and measurement-dependent mass resolving power along with Gaussian-weighting of observed peaks-of-interest (POIs) for improved reliability of metabolite/lipid/drug signals in MSI. Instead of relying on the subjective qualitative judgment of the end-user concerning the observed spatial distribution of an MOI within a tissue sample, *moleculaR* proposes molecular probabilistic maps (MPMs), which apply pixel-wise spatial significance testing of MOI intensities against a complete spatial randomness (CSR) model inferred from the signal intensities of that same MOI. *moleculaR* also allows for spatial statistical comparisons of different tissues (cross-tissue MPMs or CT-MPMs) and for collective projections of metabolite ensembles onto a single tissue plane, followed by computation of collective projection probabilistic maps (CPPMs). Ultimately, computed "hotspot" and "coldspot" spatial contours provide user-independent and probabilistic localization of tissue areas where an MOI has a statistically significant non-random relative spatial abundance or deficiency, respectively.

The different parts of the framework have been tested and validated on matrix-assisted laser desorption ionization (MALDI) MSI data measured with different mass

spectrometers including ultra-high-resolution Fourier transform ion cyclotron resonance (FTICR), high-resolution trapped ion mobility spectrometry time-of-flight (timsTOF) and TOF mass spectrometers, featuring different tissue samples and simulation-based experiments mimicking MALDI-MSI ground-truth, which have been developed and utilized to test the proposed workflows. The observed results indicated the cross-platform applicability of *moleculaR*. Furthermore, the results suggest that the proposed spatial probabilistic mapping represented by MPMs, CPPMs and CT-MPMs shall replace or complement ion images for the spatial analysis of MOIs because of its valuable benefit of enabling localization of significant relative spatial abundance/deficiency of MOI signal intensities. *moleculaR* has been released as an open-source R package complementing leading MSI-bioinformatics packages and the results depicted and discussed in this work have been made available to the scientific community.[142]

Furthermore, this work attempted to investigate quantitative spatial mapping of drugs in a tissue sections. Here, a generalized nonlinear calibration model based on drug dilution series was proposed as a replacement for the traditional linear model that takes into account the inherent measurement nonlinearities characteristic to MALDI-MSI data. It's applicability was then tested in a clinical pharmacology setup by performing tissue-drug content quantification on an entire tissue cohort of gastrointestinal stromal tumor (GIST) specimens on TOF- and FTICR-MALDI-MSI modalities, comparing their results to the gold-standard ultra-high performance liquid chromatography electrospray-ionization quadrupole time-of-flight mass spectrometry (UHPLC-ESI-QTOF-MS). The findings revealed striking inefficiency in imatinib penetration into GIST liver metastases. This was despite the abundant imatinib levels beyond the limit of quantification (LOQ) observed within the corresponding healthy liver tissues surrounding the metastatic GIST, thus providing evidence for secondary drug resistance independent of mutation status. This emphasizes the significant potential of MALDI-MSI as a technique for investigating the spatial distribution of targeted drugs in oncology. In particular, MALDI-MSI could serve as a complementary method to evaluate the pharmacokinetics of drugs and their metabolites in resected specimens post-surgery, shedding light on the role of drug uptake and tissue penetration efficiency in treatment resistance. The results depicted and discussed have been made available to the scientific community.[143]

Finally, an attempt was made to combine the proposed spatial probabilistic mapping with the MALDI-MSI-based spatial quantitative mapping of drug signals in tissues. The results suggest that the probabilistic spatial mapping through CT-MPMs could potentially be used to spatially investigate tissue drug content, e.g., against single spots of therapeutic or toxic drug concentration spotted alongside the tissue section, without the need for preparing drug dilution series and drug calibration curves, thereby, saving effort and time and reducing the impact of batch effects on the outcome.

Bibliography

1. Schöne C, Höfler H, Walch A: MALDI imaging mass spectrometry in cancer research: combining proteomic profiling and histological evaluation. *Clinical biochemistry* 46: 539–545, 2013

2. Aichler M, Walch A: MALDI Imaging mass spectrometry: current frontiers and perspectives in pathology research and practice. *Laboratory investigation; a journal of technical methods and pathology* 95: 422–431, 2015

3. Buchberger AR, DeLaney K, Johnson J, Li L: Mass Spectrometry Imaging: A Review of Emerging Advancements and Future Insights. *Analytical chemistry* 90: 240–265, 2018

4. Chaurand P: Imaging mass spectrometry of thin tissue sections: a decade of collective efforts. *Journal of proteomics* 75: 4883–4892, 2012

5. Gusev AI, Vasseur OJ, Proctor A, Sharkey AG, Hercules DM: Imaging of thin-layer chromatograms using matrix-assisted laser desorption/ionization mass spectrometry. *Analytical chemistry* 67: 4565–4570, 1995

6. Caprioli RM, Farmer TB, Gile J: Molecular imaging of biological samples: localization of peptides and proteins using MALDI-TOF MS. *Analytical chemistry* 69: 4751–4760, 1997

7. Stoeckli M, Chaurand P, Hallahan DE, Caprioli RM: Imaging mass spectrometry: a new technology for the analysis of protein expression in mammalian tissues. *Nature medicine* 7: 493–496, 2001

8. Ščupáková K, Balluff B, Tressler C, Adelaja T, Heeren RMA, Glunde K, Ertaylan G: Cellular resolution in clinical MALDI mass spectrometry imaging: the latest advancements and current challenges. *Clinical chemistry and laboratory medicine* 58: 914–929, 2020

9. Hinsenkamp I, Schulz S, Roscher M, Suhr AM, Meyer B, Munteanu B, Fuchser J, Schoenberg SO, Ebert MPA, Wängler B, Hopf C, Burgermeister E: Inhibition of Rho-Associated Kinase 1/2 Attenuates Tumor Growth in Murine Gastric Cancer. *Neoplasia (New York, N.Y.)* 18: 500–511, 2016

10. Schulz S, Becker M, Groseclose MR, Schadt S, Hopf C: Advanced MALDI mass spectrometry imaging in pharmaceutical research and drug development. *Current opinion in biotechnology* 55: 51–59, 2019

11. Swales JG, Hamm G, Clench MR, Goodwin RJ: Mass spectrometry imaging and its application in pharmaceutical research and development: A concise review. *International Journal of Mass Spectrometry* 437: 99–112, 2019

12. Fülöp A, Sammour DA, Erich K, von Gerichten J, van Hoogevest P, Sandhoff R, Hopf C: Molecular imaging of brain localization of liposomes in mice using MALDI mass spectrometry. *Scientific reports* 6: 33791, 2016

13. Friedrich M, Sankowski R, Bunse L, Kilian M, Green E, Ramallo Guevara C, Pusch S, Poschet G, Sanghvi K, Hahn M, Bunse T, Münch P, Gegner HM, Sonner JK, von Landenberg A, Cichon F, Aslan K, Trobisch T, Schirmer L, Abu-Sammour D, Kessler T, Ratliff M, Schrimpf D, Sahm F, Hopf C, Heiland DH, Schnell O, Beck J, Böttcher C, Fernandez-Zapata C, Priller J, Heiland S, Gutcher I, Quintana FJ, von Deimling A, Wick W, Prinz M, Platten M: Tryptophan metabolism drives dynamic immunosuppressive myeloid states in IDH-mutant gliomas. *Nature cancer* 2: 723–740, 2021

14. Fack F, Tardito S, Hochart G, Oudin A, Zheng L, Fritah S, Golebiewska A, Nazarov PV, Bernard A, Hau AC, Keunen O, Leenders W, Lund-Johansen M, Stauber J, Gottlieb E, Bjerkvig R, Niclou SP: Altered metabolic landscape in IDH-mutant gliomas affects phospholipid, energy, and oxidative stress pathways. *EMBO molecular medicine* 9: 1681–1695, 2017

15. Sun C, Li T, Song X, Huang L, Zang Q, Xu J, Bi N, Jiao G, Hao Y, Chen Y, Zhang R, Luo Z, Li X, Wang L, Wang Z, Song Y, He J, Abliz Z: Spatially resolved metabolomics to discover tumor-associated metabolic alterations. *Proceedings of the National Academy of Sciences of the United States of America* 116: 52–57, 2019

16. Alexandrov T: Spatial Metabolomics and Imaging Mass Spectrometry in the Age of Artificial Intelligence. *Annual review of biomedical data science* 3: 61–87, 2020

17. Gibb S, Strimmer K: MALDIquant: a versatile R package for the analysis of mass spectrometry data. *Bioinformatics (Oxford, England)* 28: 2270–2271, 2012

18. Bemis KD, Harry A, Eberlin LS, Ferreira C, van de Ven SM, Mallick P, Stolowitz M, Vitek O: Cardinal: an R package for statistical analysis of mass spectrometry-based imaging experiments. *Bioinformatics (Oxford, England)* 31: 2418–2420, 2015

19. Ràfols P, Torres S, Ramírez N, Del Castillo E, Yanes O, Brezmes J, Correig X: rMSI: an R package for MS imaging data handling and visualization. *Bioinformatics (Oxford, England)* 33: 2427–2428, 2017

20. Inglese P, Correia G, Takats Z, Nicholson JK, Glen RC: SPUTNIK: an R package for filtering of spatially related peaks in mass spectrometry imaging data. *Bioinformatics (Oxford, England)* 35: 178–180, 2019

21. Janda M, Seah BKB, Jakob D, Beckmann J, Geier B, Liebeke M: Determination of Abundant Metabolite Matrix Adducts Illuminates the Dark Metabolome of MALDI-Mass Spectrometry Imaging Datasets. *Analytical chemistry* 93: 8399–8407, 2021

22. Palarea-Albaladejo J, Mclean K, Wright F, Smith DGE: MALDIrppa: quality control and robust analysis for mass spectrometry data. *Bioinformatics (Oxford, England)* 34: 522–523, 2018

23. Föll MC, Moritz L, Wollmann T, Stillger MN, Vockert N, Werner M, Bronsert P, Rohr K, Grüning BA, Schilling O: Accessible and reproducible mass spectrometry imaging data analysis in Galaxy. *GigaScience* 8, 2019

24. Verbeeck N, Caprioli RM, van de Plas R: Unsupervised machine learning for exploratory data analysis in imaging mass spectrometry. *Mass spectrometry reviews* 39: 245–291, 2020

25. Thomas SA, Race AM, Steven RT, Gilmore IS, Bunch J: Dimensionality reduction of mass spectrometry imaging data using autoencoders. In: 2016 IEEE Symposium Series on Computational Intelligence (SSCI), 1–7, IEEE, 2016

26. Abdelmoula WM, Lopez BGC, Randall EC, Kapur T, Sarkaria JN, White FM, Agar JN, Wells WM, Agar NYR: Peak learning of mass spectrometry imaging data using artificial neural networks. *Nature communications* 12: 5544, 2021

27. Seddiki K, Saudemont P, Precioso F, Ogrinc N, Wisztorski M, Salzet M, Fournier I, Droit A: Cumulative learning enables convolutional neural network representations for small mass spectrometry data classification. *Nature communications* 11: 5595, 2020

28. Guo D, Föll MC, Volkmann V, Enderle-Ammour K, Bronsert P, Schilling O, Vitek O: Deep multiple instance learning classifies subtissue locations in mass spectrometry images from tissue-level annotations. *Bioinformatics (Oxford, England)* 36: i300–i308, 2020

29. Baker M: 1,500 scientists lift the lid on reproducibility. *Nature* 533: 452–454, 2016

30. Fanelli D: Opinion: Is science really facing a reproducibility crisis, and do we need it to? *Proceedings of the National Academy of Sciences of the United States of America* 115: 2628–2631, 2018

31. Ly A, Longuespée R, Casadonte R, Wandernoth P, Schwamborn K, Bollwein C, Marsching C, Kriegsmann K, Hopf C, Weichert W, Kriegsmann J, Schirmacher P, Kriegsmann M, Deininger SO: Site-to-Site Reproducibility and Spatial Resolution

in MALDI-MSI of Peptides from Formalin-Fixed Paraffin-Embedded Samples. *Proteomics. Clinical applications* 13: e1800029, 2019

32. Erich K, Sammour DA, Marx A, Hopf C: Scores for standardization of on-tissue digestion of formalin-fixed paraffin-embedded tissue in MALDI-MS imaging. *Biochimica et biophysica acta. Proteins and proteomics* 1865: 907–915, 2017

33. Föll MC, Volkmann V, Enderle-Ammour K, Timme S, Wilhelm K, Guo D, Vitek O, Bronsert P, Schilling O: Moving translational mass spectrometry imaging towards transparent and reproducible data analyses: a case study of an urothelial cancer cohort analyzed in the Galaxy framework. *Clinical proteomics* 19: 8, 2022

34. Schramm T, Hester Z, Klinkert I, Both JP, Heeren RMA, Brunelle A, Laprévote O, Desbenoit N, Robbe MF, Stoeckli M, Spengler B, Römpp A: imzML–a common data format for the flexible exchange and processing of mass spectrometry imaging data. *Journal of proteomics* 75: 5106–5110, 2012

35. Boskamp T, Lachmund D, Casadonte R, Hauberg-Lotte L, Kobarg JH, Kriegsmann J, Maass P: Using the Chemical Noise Background in MALDI Mass Spectrometry Imaging for Mass Alignment and Calibration. *Analytical chemistry* 92: 1301–1308, 2020

36. La Rocca R, Kune C, Tiquet M, Stuart L, Eppe G, Alexandrov T, de Pauw E, Quinton L: Adaptive Pixel Mass Recalibration for Mass Spectrometry Imaging Based on Locally Endogenous Biological Signals. *Analytical chemistry* 93: 4066–4074, 2021

37. Deininger SO, Cornett DS, Paape R, Becker M, Pineau C, Rauser S, Walch A, Wolski E: Normalization in MALDI-TOF imaging datasets of proteins: practical considerations. *Analytical and bioanalytical chemistry* 401: 167–181, 2011

38. Boskamp T, Casadonte R, Hauberg-Lotte L, Deininger S, Kriegsmann J, Maass P: Cross-Normalization of MALDI Mass Spectrometry Imaging Data Improves Site-to-Site Reproducibility. *Analytical chemistry* 93: 10584–10592, 2021

39. Fonville JM, Carter C, Cloarec O, Nicholson JK, Lindon JC, Bunch J, Holmes E: Robust data processing and normalization strategy for MALDI mass spectrometric imaging. *Analytical chemistry* 84: 1310–1319, 2012

40. Balluff B, Hopf C, Porta Siegel T, Grabsch HI, Heeren RMA: Batch Effects in MALDI Mass Spectrometry Imaging. *Journal of the American Society for Mass Spectrometry* 32: 628–635, 2021

41. Unsihuay D, Mesa Sanchez D, Laskin J: Quantitative Mass Spectrometry Imaging of Biological Systems. *Annual review of physical chemistry* 72: 307–329, 2021

42. Rzagalinski I, Volmer DA: Quantification of low molecular weight compounds by MALDI imaging mass spectrometry - A tutorial review. *Biochimica et biophysica acta. Proteins and proteomics* 1865: 726–739, 2017

43. Swales JG, Dexter A, Hamm G, Nilsson A, Strittmatter N, Michopoulos F, Hardy C, Morentin-Gutierrez P, Mellor M, Andren PE, Clench MR, Bunch J, Critchlow SE, Goodwin RJA: Quantitation of Endogenous Metabolites in Mouse Tumors Using Mass-Spectrometry Imaging. *Analytical chemistry* 90: 6051–6058, 2018

44. Chumbley CW, Reyzer ML, Allen JL, Marriner GA, Via LE, Barry CE, Caprioli RM: Absolute Quantitative MALDI Imaging Mass Spectrometry: A Case of Rifampicin in Liver Tissues. *Analytical chemistry* 88: 2392–2398, 2016

45. Hamm G, Bonnel D, Legouffe R, Pamelard F, Delbos JM, Bouzom F, Stauber J: Quantitative mass spectrometry imaging of propranolol and olanzapine using tissue extinction calculation as normalization factor. *Journal of proteomics* 75: 4952–4961, 2012

46. Pirman DA, Reich RF, Kiss A, Heeren RMA, Yost RA: Quantitative MALDI tandem mass spectrometric imaging of cocaine from brain tissue with a deuterated internal standard. *Analytical chemistry* 85: 1081–1089, 2013

47. Robichaud G, Garrard KP, Barry JA, Muddiman DC: MSiReader: an open-source interface to view and analyze high resolving power MS imaging files on Matlab platform. *Journal of the American Society for Mass Spectrometry* 24: 718–721, 2013

48. Källback P, Nilsson A, Shariatgorji M, Andrén PE: msIQuant–Quantitation Software for Mass Spectrometry Imaging Enabling Fast Access, Visualization, and Analysis of Large Data Sets. *Analytical chemistry* 88: 4346–4353, 2016

49. Zhao C, Cai Z: Three-dimensional quantitative mass spectrometry imaging in complex system: From subcellular to whole organism. *Mass spectrometry reviews* 41: 469–487, 2022

50. Dewez F, de Pauw E, Heeren RMA, Balluff B: Multilabel Per-Pixel Quantitation in Mass Spectrometry Imaging. *Analytical chemistry* 93: 1393–1400, 2021

51. Wu Q, Rubakhin SS, Sweedler JV: Quantitative Imprint Mass Spectrometry Imaging of Endogenous Ceramides in Rat Brain Tissue with Kinetic Calibration. *Analytical chemistry* 92: 6613–6621, 2020

52. Granborg JR, Handler AM, Janfelt C: Mass spectrometry imaging in drug distribution and drug metabolism studies – Principles, applications and perspectives. *TrAC Trends in Analytical Chemistry* 146: 116482, 2022

53. Takáts Z, Wiseman JM, Gologan B, Cooks RG: Mass spectrometry sampling under ambient conditions with desorption electrospray ionization. *Science (New York, N.Y.)* 306: 471–473, 2004

54. Karas M, Krüger R: Ion formation in MALDI: the cluster ionization mechanism. *Chemical reviews* 103: 427–440, 2003

55. Anderton CR, Chu RK, Tolić N, Creissen A, Paša-Tolić L: Utilizing a Robotic Sprayer for High Lateral and Mass Resolution MALDI FT-ICR MSI of Microbial Cultures. *Journal of the American Society for Mass Spectrometry* 27: 556–559, 2016

56. Hankin JA, Barkley RM, Murphy RC: Sublimation as a method of matrix application for mass spectrometric imaging. *Journal of the American Society for Mass Spectrometry* 18: 1646–1652, 2007

57. Baluya DL, Garrett TJ, Yost RA: Automated MALDI matrix deposition method with inkjet printing for imaging mass spectrometry. *Analytical chemistry* 79: 6862–6867, 2007

58. Tucker LH, Conde-González A, Cobice D, Hamm GR, Goodwin RJA, Campbell CJ, Clarke DJ, Mackay CL: MALDI Matrix Application Utilizing a Modified 3D Printer for Accessible High Resolution Mass Spectrometry Imaging. *Analytical chemistry* 90: 8742–8749, 2018

59. Fülöp A, Porada MB, Marsching C, Blott H, Meyer B, Tambe S, Sandhoff R, Junker HD, Hopf C: 4-Phenyl-a-cyanocinnamic acid amide: screening for a negative ion matrix for MALDI-MS imaging of multiple lipid classes. *Analytical chemistry* 85: 9156–9163, 2013

60. Gemperline E, Rawson S, Li L: Optimization and comparison of multiple MALDI matrix application methods for small molecule mass spectrometric imaging. *Analytical chemistry* 86: 10030–10035, 2014

61. Engel KM, Prabutzki P, Leopold J, Nimptsch A, Lemmnitzer K, Vos DRN, Hopf C, Schiller J: A new update of MALDI-TOF mass spectrometry in lipid research. *Progress in lipid research* 86: 101145, 2022

62. Zhou Q, Fülöp A, Hopf C: Recent developments of novel matrices and on-tissue chemical derivatization reagents for MALDI-MSI. *Analytical and bioanalytical chemistry* 413: 2599–2617, 2021

63. Perry WJ, Patterson NH, Prentice BM, Neumann EK, Caprioli RM, Spraggins JM: Uncovering matrix effects on lipid analyses in MALDI imaging mass spectrometry experiments. *Journal of mass spectrometry : JMS* 55: e4491, 2020

64. Leopold J, Popkova Y, Engel KM, Schiller J: Recent Developments of Useful MALDI Matrices for the Mass Spectrometric Characterization of Lipids. *Biomolecules* 8, 2018

65. Leopold J, Prabutzki P, Engel KM, Schiller J: A Five-Year Update on Matrix Compounds for MALDI-MS Analysis of Lipids. *Biomolecules* 13: 546, 2023

66. Dreisewerd K: Recent methodological advances in MALDI mass spectrometry. *Analytical and bioanalytical chemistry* 406: 2261–2278, 2014

67. Knochenmuss R, Zenobi R: MALDI ionization: the role of in-plume processes. *Chemical reviews* 103: 441–452, 2003

68. Zenobi R, Knochenmuss R: Ion formation in MALDI mass spectrometry. *Mass Spectrometry Reviews* 17: 337–366, 1998

69. Hu C, Luo W, Xu J, Han X: RECOGNITION AND AVOIDANCE OF ION SOURCE-GENERATED ARTIFACTS IN LIPIDOMICS ANALYSIS. *Mass spectrometry reviews* 41: 15–31, 2022

70. Trim PJ, Snel MF: Small molecule MALDI MS imaging: Current technologies and future challenges. *Methods (San Diego, Calif.)* 104: 127–141, 2016

71. May JC, McLean JA: Ion mobility-mass spectrometry: time-dispersive instrumentation. *Analytical chemistry* 87: 1422–1436, 2015

72. van Agthoven MA, Lam YPY, O'Connor PB, Rolando C, Delsuc MA: Two-dimensional mass spectrometry: new perspectives for tandem mass spectrometry. *European biophysics journal : EBJ* 48: 213–229, 2019

73. Bowman AP, Blakney GT, Hendrickson CL, Ellis SR, Heeren RMA, Smith DF: Ultra-High Mass Resolving Power, Mass Accuracy, and Dynamic Range MALDI Mass Spectrometry Imaging by 21-T FT-ICR MS. *Analytical chemistry* 92: 3133–3142, 2020

74. Tiquet M, La Rocca R, Kirnbauer S, Zoratto S, van Kruining D, Quinton L, Eppe G, Martinez-Martinez P, Marchetti-Deschmann M, de Pauw E, Far J: FT-ICR Mass Spectrometry Imaging at Extreme Mass Resolving Power Using a Dynamically Harmonized ICR Cell with 1w or 2w Detection. *Analytical chemistry* 94: 9316–9326, 2022

75. Marshall AG, Hendrickson CL, Jackson GS: Fourier transform ion cyclotron resonance mass spectrometry: A primer. *Mass Spectrometry Reviews* 17: 1–35, 1998

76. Boesl U: Time-of-flight mass spectrometry: Introduction to the basics. *Mass spectrometry reviews* 36: 86–109, 2017

77. Kompauer M, Heiles S, Spengler B: Autofocusing MALDI mass spectrometry imaging of tissue sections and 3D chemical topography of nonflat surfaces. *Nature methods* 14: 1156–1158, 2017

78. Long GL, Winefordner JD: Limit of Detection A Closer Look at the IUPAC Definition. *Analytical chemistry* 55: 712A–724A, 1983

79. Race AM, Bunch J: Optimisation of colour schemes to accurately display mass spectrometry imaging data based on human colour perception. *Analytical and bioanalytical chemistry* 407: 2047–2054, 2015

80. Palmer A, Ovchinnikova E, Thuné M, Lavigne R, Guével B, Dyatlov A, Vitek O, Pineau C, Borén M, Alexandrov T: Using collective expert judgements to evaluate quality measures of mass spectrometry images. *Bioinformatics (Oxford, England)* 31: i375–84, 2015

81. Rabe JH, A Sammour D, Schulz S, Munteanu B, Ott M, Ochs K, Hohenberger P, Marx A, Platten M, Opitz CA, Ory DS, Hopf C: Fourier Transform Infrared Microscopy Enables Guidance of Automated Mass Spectrometry Imaging to Predefined Tissue Morphologies. *Scientific reports* 8: 313, 2018

82. Alexandrov T, Kobarg JH: Efficient spatial segmentation of large imaging mass spectrometry datasets with spatially aware clustering. *Bioinformatics (Oxford, England)* 27: i230–8, 2011

83. Bemis KD, Harry A, Eberlin LS, Ferreira CR, van de Ven SM, Mallick P, Stolowitz M, Vitek O: Probabilistic Segmentation of Mass Spectrometry (MS) Images Helps Select Important Ions and Characterize Confidence in the Resulting Segments. *Molecular & cellular proteomics : MCP* 15: 1761–1772, 2016

84. Race AM, Steven RT, Palmer AD, Styles IB, Bunch J: Memory efficient principal component analysis for the dimensionality reduction of large mass spectrometry imaging data sets. *Analytical chemistry* 85: 3071–3078, 2013

85. Boskamp T, Lachmund D, Oetjen J, Cordero Hernandez Y, Trede D, Maass P, Casadonte R, Kriegsmann J, Warth A, Dienemann H, Weichert W, Kriegsmann M: A new classification method for MALDI imaging mass spectrometry data acquired on formalin-fixed paraffin-embedded tissue samples. *Biochimica et biophysica acta. Proteins and proteomics* 1865: 916–926, 2017

86. Hanselmann M, Kirchner M, Renard BY, Amstalden ER, Glunde K, Heeren RMA, Hamprecht FA: Concise representation of mass spectrometry images by probabilistic latent semantic analysis. *Analytical chemistry* 80: 9649–9658, 2008

87. Abdelmoula WM, Balluff B, Englert S, Dijkstra J, Reinders MJT, Walch A, Mc-Donnell LA, Lelieveldt BPF: Data-driven identification of prognostic tumor subpopulations using spatially mapped t-SNE of mass spectrometry imaging data. *Proceedings of the National Academy of Sciences of the United States of America* 113: 12244–12249, 2016

88. Mittal P, Condina MR, Klingler-Hoffmann M, Kaur G, Oehler MK, Sieber OM, Palmieri M, Kommoss S, Brucker S, McDonnell MD, Hoffmann P: Cancer Tissue Classification Using Supervised Machine Learning Applied to MALDI Mass Spectrometry Imaging. *Cancers* 13, 2021

89. Leuschner J, Schmidt M, Fernsel P, Lachmund D, Boskamp T, Maass P: Supervised non-negative matrix factorization methods for MALDI imaging applications. *Bioinformatics (Oxford, England)* 35: 1940–1947, 2019

90. Deininger SO, Bollwein C, Casadonte R, Wandernoth P, Gonçalves JPL, Kriegsmann K, Kriegsmann M, Boskamp T, Kriegsmann J, Weichert W, Schirmacher P, Ly A, Schwamborn K: Multicenter Evaluation of Tissue Classification by Matrix-Assisted Laser Desorption/Ionization Mass Spectrometry Imaging. *Analytical chemistry* 94: 8194–8201, 2022

91. Behrmann J, Etmann C, Boskamp T, Casadonte R, Kriegsmann J, Maaß P: Deep learning for tumor classification in imaging mass spectrometry. *Bioinformatics (Oxford, England)* 34: 1215–1223, 2018

92. Bond NJ, Koulman A, Griffin JL, Hall Z: massPix: an R package for annotation and interpretation of mass spectrometry imaging data for lipidomics. *Metabolomics : Official journal of the Metabolomic Society* 13: 128, 2017

93. Łącki MK, Startek MP, Brehmer S, Distler U, Tenzer S: OpenTIMS, TimsPy, and TimsR: Open and Easy Access to timsTOF Raw Data. *Journal of proteome research* 20: 2122–2129, 2021

94. Veselkov K, Sleeman J, Claude E, Vissers JPC, Galea D, Mroz A, Laponogov I, Towers M, Tonge R, Mirnezami R, Takats Z, Nicholson JK, Langridge JI: BASIS: High-performance bioinformatics platform for processing of large-scale mass spectrometry imaging data in chemically augmented histology. *Scientific reports* 8: 4053, 2018

95. Martens L, Chambers M, Sturm M, Kessner D, Levander F, Shofstahl J, Tang WH, Römpp A, Neumann S, Pizarro AD, Montecchi-Palazzi L, Tasman N, Coleman M, Reisinger F, Souda P, Hermjakob H, Binz PA, Deutsch EW: mzML–a community standard for mass spectrometry data. *Molecular & cellular proteomics : MCP* 10: R110.000133, 2011

96. Heeren RMA, Smith DF, Stauber J, Kükrer-Kaletas B, MacAleese L: Imaging mass spectrometry: hype or hope? *Journal of the American Society for Mass Spectrometry* 20: 1006–1014, 2009

97. Goh WWB, Wang W, Wong L: Why Batch Effects Matter in Omics Data, and How to Avoid Them. *Trends in biotechnology* 35: 498–507, 2017

98. Taylor AJ, Dexter A, Bunch J: Exploring Ion Suppression in Mass Spectrometry Imaging of a Heterogeneous Tissue. *Analytical chemistry* 90: 5637–5645, 2018

99. Jackson SN, Muller L, Roux A, Oktem B, Moskovets E, Doroshenko VM, Woods AS: AP-MALDI Mass Spectrometry Imaging of Gangliosides Using 2,6-Dihydroxyacetophenone. *Journal of the American Society for Mass Spectrometry* 29: 1463–1472, 2018

100. McCann A, Rappe S, La Rocca R, Tiquet M, Quinton L, Eppe G, Far J, de Pauw E, Kune C: Mass shift in mass spectrometry imaging: comprehensive analysis and practical corrective workflow. *Analytical and bioanalytical chemistry* 413: 2831–2844, 2021

101. Kompauer M, Heiles S, Spengler B: Atmospheric pressure MALDI mass spectrometry imaging of tissues and cells at 1.4-mm lateral resolution. *Nature methods* 14: 90–96, 2017

102. Longuespée R, Kriegsmann K, Cremer M, Zgorzelski C, Casadonte R, Kazdal D, Kriegsmann J, Weichert W, Schwamborn K, Fresnais M, Schirmacher P, Kriegsmann M: In MALDI-Mass Spectrometry Imaging on Formalin-Fixed Paraffin-Embedded Tissue Specimen Section Thickness Significantly Influences m/z Peak Intensity. *Proteomics. Clinical applications* 13: e1800074, 2019

103. Goodwin RJA: Sample preparation for mass spectrometry imaging: small mistakes can lead to big consequences. *Journal of proteomics* 75: 4893–4911, 2012

104. Lukowski JK, Pamreddy A, Velickovic D, Zhang G, Pasa-Tolic L, Alexandrov T, Sharma K, Anderton CR: Storage Conditions of Human Kidney Tissue Sections Affect Spatial Lipidomics Analysis Reproducibility. *Journal of the American Society for Mass Spectrometry* 31: 2538–2546, 2020

105. Stoeckli M, Staab D: Reproducible Matrix Deposition for MALDI MSI Based on Open-Source Software and Hardware. *Journal of the American Society for Mass Spectrometry* 26: 911–914, 2015

106. Gustafsson OJR, Winderbaum LJ, Condina MR, Boughton BA, Hamilton BR, Undheim EAB, Becker M, Hoffmann P: Balancing sufficiency and impact in reporting standards for mass spectrometry imaging experiments. *GigaScience* 7, 2018

107. Oetjen J, Lachmund D, Palmer A, Alexandrov T, Becker M, Boskamp T, Maass P: An approach to optimize sample preparation for MALDI imaging MS of FFPE sections using fractional factorial design of experiments. *Analytical and bioanalytical chemistry* 408: 6729–6740, 2016

108. Tressler C, Tilley S, Yang E, Donohue C, Barton E, Creissen A, Glunde K: Factorial Design to Optimize Matrix Spraying Parameters for MALDI Mass Spectrometry Imaging. *Journal of the American Society for Mass Spectrometry* 32: 2728–2737, 2021

109. Ferey J, Marguet F, Laquerrière A, Marret S, Schmitz-Afonso I, Bekri S, Afonso C, Tebani A: A new optimization strategy for MALDI FTICR MS tissue analysis for untargeted metabolomics using experimental design and data modeling. *Analytical and bioanalytical chemistry* 411: 3891–3903, 2019

110. Condina MR, Mittal P, Briggs MT, Oehler MK, Klingler-Hoffmann M, Hoffmann P: Egg White as a Quality Control in Matrix-Assisted Laser Desorption/Ionization Mass Spectrometry Imaging (MALDI-MSI). *Analytical chemistry* 91: 14846–14853, 2019

111. Alexandrov T, Bartels A: Testing for presence of known and unknown molecules in imaging mass spectrometry. *Bioinformatics (Oxford, England)* 29: 2335–2342, 2013

112. Veselkov KA, Vingara LK, Masson P, Robinette SL, Want E, Li JV, Barton RH, Boursier-Neyret C, Walther B, Ebbels TM, Pelczer I, Holmes E, Lindon JC, Nicholson JK: Optimized preprocessing of ultra-performance liquid chromatography/mass spectrometry urinary metabolic profiles for improved information recovery. *Analytical chemistry* 83: 5864–5872, 2011

113. Groseclose MR, Castellino S: A mimetic tissue model for the quantification of drug distributions by MALDI imaging mass spectrometry. *Analytical chemistry* 85: 10099–10106, 2013

114. Hansen HT, Janfelt C: Aspects of Quantitation in Mass Spectrometry Imaging Investigated on Cryo-Sections of Spiked Tissue Homogenates. *Analytical chemistry* 88: 11513–11520, 2016

115. Davoli E, Zucchetti M, Matteo C, Ubezio P, D'Incalci M, Morosi L: THE SPACE DIMENSION AT THE MICRO LEVEL: MASS SPECTROMETRY IMAGING OF DRUGS IN TISSUES. *Mass spectrometry reviews* 40: 201–214, 2021

116. Casadonte R, Kriegsmann M, Zweynert F, Friedrich K, Baretton G, Otto M, Deininger SO, Paape R, Belau E, Suckau D, Aust D, Pilarsky C, Kriegsmann J: Imaging mass spectrometry to discriminate breast from pancreatic cancer metastasis in formalin-fixed paraffin-embedded tissues. *Proteomics* 14: 956–964, 2014

117. Klein O, Kanter F, Kulbe H, Jank P, Denkert C, Nebrich G, Schmitt WD, Wu Z, Kunze CA, Sehouli J, Darb-Esfahani S, Braicu I, Lellmann J, Thiele H, Taube ET: MALDI-Imaging for Classification of Epithelial Ovarian Cancer Histotypes from a Tissue Microarray Using Machine Learning Methods. *Proteomics. Clinical applications* 13: e1700181, 2019

118. Möginger U, Marcussen N, Jensen ON: Histo-molecular differentiation of renal cancer subtypes by mass spectrometry imaging and rapid proteome profiling of formalin-fixed paraffin-embedded tumor tissue sections. *Oncotarget* 11: 3998–4015, 2020

119. Zhang J, Li SQ, Lin JQ, Yu W, Eberlin LS: Mass Spectrometry Imaging Enables Discrimination of Renal Oncocytoma from Renal Cell Cancer Subtypes and Normal Kidney Tissues. *Cancer Research* 80: 689–698, 2020

120. Hinsch A, Buchholz M, Odinga S, Borkowski C, Koop C, Izbicki JR, Wurlitzer M, Krech T, Wilczak W, Steurer S, Jacobsen F, Burandt EC, Stahl P, Simon R, Sauter G, Schlüter H: MALDI imaging mass spectrometry reveals multiple clinically relevant masses in colorectal cancer using large-scale tissue microarrays. *Journal of Mass Spectrometry* 52: 165–173, 2017

121. Balluff B, Frese CK, Maier SK, Schöne C, Kuster B, Schmitt M, Aubele M, Höfler H, Deelder AM, Heck A JR, Hogendoorn PCW, Morreau J, Maarten Altelaar af , Walch A, McDonnell LA: De novo discovery of phenotypic intratumour heterogeneity using imaging mass spectrometry. *The Journal of Pathology* 235: 3–13, 2015

122. Randall EC, Emdal KB, Laramy JK, Kim M, Roos A, Calligaris D, Regan MS, Gupta SK, Mladek AC, Carlson BL, Johnson AJ, Lu FK, Xie XS, Joughin BA, Reddy RJ, Peng S, Abdelmoula WM, Jackson PR, Kolluri A, Kellersberger KA, Agar JN, Lauffenburger DA, Swanson KR, Tran NL, Elmquist WF, White FM, Sarkaria JN, Agar NYR: Integrated mapping of pharmacokinetics and pharmacodynamics in a patient-derived xenograft model of glioblastoma. *Nature communications* 9: 4904, 2018

123. Miettinen M, Lasota J: Histopathology of gastrointestinal stromal tumor. *Journal of surgical oncology* 104: 865–873, 2011

124. Joensuu H, Hohenberger P, Corless CL: Gastrointestinal stromal tumour. *Lancet (London, England)* 382: 973–983, 2013

125. Serrano C, George S, Valverde C, Olivares D, García-Valverde A, Suárez C, Morales-Barrera R, Carles J: Novel Insights into the Treatment of Imatinib-Resistant Gastrointestinal Stromal Tumors. *Targeted oncology* 12: 277–288, 2017

126. Louis DN, Perry A, Wesseling P, Brat DJ, Cree IA, Figarella-Branger D, Hawkins C, Ng HK, Pfister SM, Reifenberger G, Soffietti R, von Deimling A, Ellison DW: The 2021 WHO Classification of Tumors of the Central Nervous System: a summary. *Neuro-oncology* 23: 1231–1251, 2021

127. Zong H, Verhaak RGW, Canoll P: The cellular origin for malignant glioma and prospects for clinical advancements. *Expert review of molecular diagnostics* 12: 383–394, 2012

128. Oronsky B, Reid TR, Oronsky A, Sandhu N, Knox SJ: A Review of Newly Diagnosed Glioblastoma. *Frontiers in oncology* 10: 574012, 2020

129. Villa C, Miquel C, Mosses D, Bernier M, Di Stefano AL: The 2016 World Health Organization classification of tumours of the central nervous system. *Presse medicale (Paris, France : 1983)* 47: e187–e200, 2018

130. Mortensen D, Ulhøi BP, Lukacova S, Alsner J, Stougaard M, Nyengaard JR: Impact of new molecular criteria on diagnosis and survival of adult glioma patients. *IBRO neuroscience reports* 13: 299–305, 2022

131. Stoyanov GS, Lyutfi E, Georgieva R, Georgiev R, Dzhenkov DL, Petkova L, Ivanov BD, Kaprelyan A, Ghenev P: Reclassification of Glioblastoma Multiforme According to the 2021 World Health Organization Classification of Central Nervous System Tumors: A Single Institution Report and Practical Significance. *Cureus* 14: e21822, 2022

132. Puchalski RB, Shah N, Miller J, Dalley R, Nomura SR, Yoon JG, Smith KA, Lankerovich M, Bertagnolli D, Bickley K, Boe AF, Brouner K, Butler S, Caldejon S, Chapin M, Datta S, Dee N, Desta T, Dolbeare T, Dotson N, Ebbert A, Feng D, Feng X, Fisher M, Gee G, Goldy J, Gourley L, Gregor BW, Gu G, Hejazinia N, Hohmann J, Hothi P, Howard R, Joines K, Kriedberg A, Kuan L, Lau C, Lee F, Lee H, Lemon T, Long F, Mastan N, Mott E, Murthy C, Ngo K, Olson E, Reding M, Riley Z, Rosen D, Sandman D, Shapovalova N, Slaughterbeck CR, Sodt A, Stockdale G, Szafer A, Wakeman W, Wohnoutka PE, White SJ, Marsh D, Rostomily RC, Ng L, Dang C, Jones A, Keogh B, Gittleman HR, Barnholtz-Sloan JS, Cimino PJ, Uppin MS, Keene CD, Farrokhi FR, Lathia JD, Berens ME, Iavarone A, Bernard A, Lein E, Phillips JW, Rostad SW, Cobbs C, Hawrylycz MJ, Foltz GD: An anatomic transcriptional atlas of human glioblastoma. *Science (New York, N.Y.)* 360: 660–663, 2018

133. Capper D, Jones DTW, Sill M, Hovestadt V, Schrimpf D, Sturm D, Koelsche C, Sahm F, Chavez L, Reuss DE, Kratz A, Wefers AK, Huang K, Pajtler KW, Schweizer L, Stichel D, Olar A, Engel NW, Lindenberg K, Harter PN, Braczynski AK, Plate KH, Dohmen H, Garvalov BK, Coras R, Hölsken A, Hewer E, Bewerunge-Hudler M, Schick M, Fischer R, Beschorner R, Schittenhelm J, Staszewski O, Wani K, Varlet P, Pages M, Temming P, Lohmann D, Selt F, Witt H, Milde T, Witt O, Aronica E, Giangaspero F, Rushing E, Scheurlen W, Geisenberger C, Rodriguez FJ, Becker A, Preusser M, Haberler C, Bjerkvig R, Cryan J, Farrell M, Deckert M, Hench J, Frank S, Serrano J, Kannan K, Tsirigos A, Brück W, Hofer S, Brehmer S, Seiz-Rosenhagen M, Hänggi D, Hans V, Rozsnoki S, Hansford JR, Kohlhof P, Kristensen BW, Lechner M, Lopes B, Mawrin C, Ketter R, Kulozik A, Khatib Z, Heppner F, Koch A, Jouvet A, Keohane C, Mühleisen H, Mueller W, Pohl U, Prinz M, Benner A, Zapatka M, Gottardo NG, Driever PH, Kramm CM, Müller HL, Rutkowski S, von Hoff K, Frühwald MC, Gnekow A, Fleischhack G, Tippelt S, Calaminus G, Monoranu CM, Perry A, Jones C, Jacques TS, Radlwimmer B, Gessi M, Pietsch T, Schramm J, Schackert G, Westphal M, Reifenberger G, Wesseling P, Weller M, Collins VP, Blümcke I, Bendszus M, Debus J, Huang A, Jabado N, Northcott PA, Paulus W, Gajjar A, Robinson GW, Taylor MD, Jaunmuktane Z, Ryzhova M, Platten M, Unterberg A, Wick W, Karajannis MA, Mittelbronn M, Acker T, Hartmann C, Aldape K, Schüller U, Buslei

R, Lichter P, Kool M, Herold-Mende C, Ellison DW, Hasselblatt M, Snuderl M, Brandner S, Korshunov A, von Deimling A, Pfister SM: DNA methylation-based classification of central nervous system tumours. *Nature* 555: 469–474, 2018

134. Sadik A, Somarribas Patterson LF, Öztürk S, Mohapatra SR, Panitz V, Secker PF, Pfänder P, Loth S, Salem H, Prentzell MT, Berdel B, Iskar M, Faessler E, Reuter F, Kirst I, Kalter V, Foerster KI, Jäger E, Guevara CR, Sobeh M, Hielscher T, Poschet G, Reinhardt A, Hassel JC, Zapatka M, Hahn U, von Deimling A, Hopf C, Schlichting R, Escher BI, Burhenne J, Haefeli WE, Ishaque N, Böhme A, Schäuble S, Thedieck K, Trump S, Seiffert M, Opitz CA: IL4I1 Is a Metabolic Immune Checkpoint that Activates the AHR and Promotes Tumor Progression. *Cell* 182: 1252–1270.e34, 2020

135. Ait-Belkacem R, Berenguer C, Villard C, Ouafik L, Figarella-Branger D, Chinot O, Lafitte D: MALDI imaging and in-source decay for top-down characterization of glioblastoma. *Proteomics* 14: 1290–1301, 2014

136. Ravi VM, Will P, Kueckelhaus J, Sun N, Joseph K, Salié H, Vollmer L, Kuliesiute U, von Ehr J, Benotmane JK, Neidert N, Follo M, Scherer F, Goeldner JM, Behringer SP, Franco P, Khiat M, Zhang J, Hofmann UG, Fung C, Ricklefs FL, Lamszus K, Boerries M, Ku M, Beck J, Sankowski R, Schwabenland M, Prinz M, Schüller U, Killmer S, Bengsch B, Walch AK, Delev D, Schnell O, Heiland DH: Spatially resolved multi-omics deciphers bidirectional tumor-host interdependence in glioblastoma. *Cancer cell* 40: 639–655.e13, 2022

137. Panitz V, Končarević S, Sadik A, Friedel D, Bausbacher T, Trump S, Farztdinov V, Schulz S, Sievers P, Schmidt S, Jürgenson I, Jung S, Kuhn K, Pflüger I, Sharma S, Wick A, Pfänder P, Selzer S, Vollmuth P, Sahm F, von Deimling A, Heiland I, Hopf C, Schulz-Knappe P, Pike I, Platten M, Wick W, Opitz CA: Tryptophan metabolism is inversely regulated in the tumor and blood of patients with glioblastoma. *Theranostics* 11: 9217–9233, 2021

138. Rončević A, Koruga N, Soldo Koruga A, Debeljak Ž, Rončević R, Turk T, Kretić D, Rotim T, Krivdić Dupan Z, Troha D, Perić M, Šimundić T: MALDI Imaging Mass Spectrometry of High-Grade Gliomas: A Review of Recent Progress and Future Perspective. *Current issues in molecular biology* 45: 838–851, 2023

139. Fernández R, Garate J, Lage S, Terés S, Higuera M, Bestard-Escalas J, López DH, Guardiola-Serrano F, Escribá PV, Barceló-Coblijn G, Fernández JA: Identification of Biomarkers of Necrosis in Xenografts Using Imaging Mass Spectrometry. *Journal of the American Society for Mass Spectrometry* 27: 244–254, 2016

140. Pace CL, Garrard KP, Muddiman DC: Sequential paired covariance for improved visualization of mass spectrometry imaging datasets. *Journal of mass spectrometry : JMS* 57: e4872, 2022

141. Erich K, Reinle K, Müller T, Munteanu B, Sammour DA, Hinsenkamp I, Gutting T, Burgermeister E, Findeisen P, Ebert MP, Krijgsveld J, Hopf C: Spatial Distribution of Endogenous Tissue Protease Activity in Gastric Carcinoma Mapped by MALDI Mass Spectrometry Imaging. *Molecular & cellular proteomics : MCP* 18: 151–161, 2019

142. Abu Sammour D, Cairns JL, Boskamp T, Marsching C, Kessler T, Ramallo Guevara C, Panitz V, Sadik A, Cordes J, Schmidt S, Mohammed SA, Rittel MF, Friedrich M, Platten M, Wolf I, von Deimling A, Opitz CA, Wick W, Hopf C: Spatial probabilistic mapping of metabolite ensembles in mass spectrometry imaging. *Nature communications* 14: 1823, 2023

143. Abu Sammour D, Marsching C, Geisel A, Erich K, Schulz S, Ramallo Guevara C, Rabe JH, Marx A, Findeisen P, Hohenberger P, Hopf C: Quantitative Mass Spectrometry Imaging Reveals Mutation Status-independent Lack of Imatinib in Liver Metastases of Gastrointestinal Stromal Tumors. *Scientific reports* 9: 10698, 2019

144. von Mehren M, Widmer N: Correlations between imatinib pharmacokinetics, pharmacodynamics, adherence, and clinical response in advanced metastatic gastrointestinal stromal tumor (GIST): an emerging role for drug blood level testing? *Cancer treatment reviews* 37: 291–299, 2011

145. Enzlein T, Cordes J, Munteanu B, Michno W, Serneels L, de Strooper B, Hanrieder J, Wolf I, Chávez-Gutiérrez L, Hopf C: Computational Analysis of Alzheimer Amyloid Plaque Composition in 2D- and Elastically Reconstructed 3D-MALDI MS Images. *Analytical chemistry* 92: 14484–14493, 2020

146. Ihaka R, Gentleman R: R: A Language for Data Analysis and Graphics. *Journal of Computational and Graphical Statistics* 5: 299–314, 1996

147. Palmer A, Phapale P, Chernyavsky I, Lavigne R, Fay D, Tarasov A, Kovalev V, Fuchser J, Nikolenko S, Pineau C, Becker M, Alexandrov T: FDR-controlled metabolite annotation for high-resolution imaging mass spectrometry. *Nature methods* 14: 57–60, 2017

148. Aimo L, Liechti R, Hyka-Nouspikel N, Niknejad A, Gleizes A, Götz L, Kuznetsov D, David FPA, van der Goot FG, Riezman H, Bougueleret L, Xenarios I, Bridge A: The SwissLipids knowledgebase for lipid biology. *Bioinformatics (Oxford, England)* 31: 2860–2866, 2015

149. Cordes J, Enzlein T, Marsching C, Hinze M, Engelhardt S, Hopf C, Wolf I: M2aia-Interactive, fast, and memory-efficient analysis of 2D and 3D multi-modal mass spectrometry imaging data. *GigaScience* 10, 2021

150. Rosin PL: Unimodal thresholding. *Pattern Recognition* 34: 2083–2096, 2001

151. Murray KK: Resolution and Resolving Power in Mass Spectrometry. *Journal of the American Society for Mass Spectrometry* 33: 2342–2347, 2022

152. Baddeley A, Rubak E, Turner R: Spatial point patterns: Methodology and applications with R. Chapman & Hall/CRC Interdisciplinary statistics series, Boca Raton, Florida: CRC Press, 2016

153. Kather JN, Marx A, Reyes-Aldasoro CC, Schad LR, Zöllner FG, Weis CA: Continuous representation of tumor microvessel density and detection of angiogenic hotspots in histological whole-slide images. *Oncotarget* 6: 19163–19176, 2015

154. Kulldorff M: A spatial scan statistic. *Communications in Statistics - Theory and Methods* 26: 1481–1496, 1997

155. Diggle P: A Kernel Method for Smoothing Point Process Data. *Applied Statistics* 34: 138, 1985

156. Chen YC: A tutorial on kernel density estimation and recent advances. *Biostatistics & Epidemiology* 1: 161–187, 2017

157. Cassese A, Ellis SR, Ogrinc Potočnik N, Burgermeister E, Ebert M, Walch A, van den Maagdenberg AMJM, McDonnell LA, Heeren RMA, Balluff B: Spatial Autocorrelation in Mass Spectrometry Imaging. *Analytical chemistry* 88: 5871–5878, 2016

158. Satopaa V, Albrecht J, Irwin D, Raghavan B: Finding a "Kneedle" in a Haystack: Detecting Knee Points in System Behavior 166–171

159. van den Berg RA, Hoefsloot HCJ, Smilde AK, van der Werf MJ, Westerhuis JA: Centering, scaling, and transformations: improving the biological information content of metabolomics data. *BMC genomics* 7: 142, 2006

160. Koeniger SL, Talaty N, Luo Y, Ready D, Voorbach M, Seifert T, Cepa S, Fagerland JA, Bouska J, Buck W, Johnson RW, Spanton S: A quantitation method for mass spectrometry imaging. *Rapid communications in mass spectrometry : RCM* 25: 503–510, 2011

161. Veselkov KA, Mirnezami R, Strittmatter N, Goldin RD, Kinross J, Speller AVM, Abramov T, Jones EA, Darzi A, Holmes E, Nicholson JK, Takats Z: Chemoinformatic strategy for imaging mass spectrometry-based hyperspectral profiling of lipid signatures in colorectal cancer. *Proceedings of the National Academy of Sciences of the United States of America* 111: 1216–1221, 2014

162. Kanawati B, Bader TM, Wanczek KP, Li Y, Schmitt-Kopplin P: Fourier transform (FT)-artifacts and power-function resolution filter in Fourier transform mass spectrometry. *Rapid communications in mass spectrometry : RCM* 31: 1607–1615, 2017

163. Fernandes AMAP, Vendramini PH, Galaverna R, Schwab NV, Alberici LC, Augusti R, Castilho RF, Eberlin MN: Direct Visualization of Neurotransmitters in Rat Brain Slices by Desorption Electrospray Ionization Mass Spectrometry Imaging (DESI - MS). *Journal of the American Society for Mass Spectrometry* 27: 1944–1951, 2016

164. Lein ES, Hawrylycz MJ, Ao N, Ayres M, Bensinger A, Bernard A, Boe AF, Boguski MS, Brockway KS, Byrnes EJ, Chen L, Chen L, Chen TM, Chin MC, Chong J, Crook BE, Czaplinska A, Dang CN, Datta S, Dee NR, Desaki AL, Desta T, Diep E, Dolbeare TA, Donelan MJ, Dong HW, Dougherty JG, Duncan BJ, Ebbert AJ, Eichele G, Estin LK, Faber C, Facer BA, Fields R, Fischer SR, Fliss TP, Frensley C, Gates SN, Glattfelder KJ, Halverson KR, Hart MR, Hohmann JG, Howell MP, Jeung DP, Johnson RA, Karr PT, Kawal R, Kidney JM, Knapik RH, Kuan CL, Lake JH, Laramee AR, Larsen KD, Lau C, Lemon TA, Liang AJ, Liu Y, Luong LT, Michaels J, Morgan JJ, Morgan RJ, Mortrud MT, Mosqueda NF, Ng LL, Ng R, Orta GJ, Overly CC, Pak TH, Parry SE, Pathak SD, Pearson OC, Puchalski RB, Riley ZL, Rockett HR, Rowland SA, Royall JJ, Ruiz MJ, Sarno NR, Schaffnit K, Shapovalova NV, Sivisay T, Slaughterbeck CR, Smith SC, Smith KA, Smith BI, Sodt AJ, Stewart NN, Stumpf KR, Sunkin SM, Sutram M, Tam A, Teemer CD, Thaller C, Thompson CL, Varnam LR, Visel A, Whitlock RM, Wohnoutka PE, Wolkey CK, Wong VY, Wood M, Yaylaoglu MB, Young RC, Youngstrom BL, Yuan XF, Zhang B, Zwingman TA, Jones AR: Genome-wide atlas of gene expression in the adult mouse brain. *Nature* 445: 168–176, 2007

165. Atkinson DE, Walton GM: Adenosine Triphosphate Conservation in Metabolic Regulation. *Journal of Biological Chemistry* 242: 3239–3241, 1967

166. Hayakawa E, Fujimura Y, Miura D: MSIdV: a versatile tool to visualize biological indices from mass spectrometry imaging data. *Bioinformatics (Oxford, England)* 32: 3852–3854, 2016

167. Derr RF, Zieve L: Adenylate energy charge: relation to guanylate energy charge and the adenylate kinase equilibrium constant. *Biochemical and biophysical research communications* 49: 1385–1390, 1972

168. de La Fuente IM, Cortés JM, Valero E, Desroches M, Rodrigues S, Malaina I, Martínez L: On the dynamics of the adenylate energy system: homeorhesis vs homeostasis. *PloS one* 9: e108676, 2014

169. O'Donnell VB: New appreciation for an old pathway: the Lands Cycle moves into new arenas in health and disease. *Biochemical Society transactions* 50: 1–11, 2022

170. Heidenreich NB, Schindler A, Sperlich S: Bandwidth selection for kernel density estimation: a review of fully automatic selectors. *AStA Advances in Statistical Analysis* 97: 403–433, 2013

171. Lindeberg T: Scale-Space Theory in Computer Vision, volume 256 of *The Springer International Series in Engineering and Computer Science*. Boston, MA: Springer US, 1994

172. Friedecký D, Mičová K, Faber E, Hrdá M, Široká J, Adam T: Detailed study of imatinib metabolization using high-resolution mass spectrometry. *Journal of chromatography. A* 1409: 173–181, 2015

173. Liu X, Ide JL, Norton I, Marchionni MA, Ebling MC, Wang LY, Davis E, Sauvageot CM, Kesari S, Kellersberger KA, Easterling ML, Santagata S, Stuart DD, Alberta J, Agar JN, Stiles CD, Agar NYR: Molecular imaging of drug transit through the blood-brain barrier with MALDI mass spectrometry imaging. *Scientific reports* 3: 2859, 2013

174. Edsgärd D, Johnsson P, Sandberg R: Identification of spatial expression trends in single-cell gene expression data. *Nature methods* 15: 339–342, 2018

175. Trede D, Kobarg JH, Oetjen J, Thiele H, Maass P, Alexandrov T: On the importance of mathematical methods for analysis of MALDI-imaging mass spectrometry data. *Journal of integrative bioinformatics* 9: 189, 2012

176. Karagiota A, Chachami G, Paraskeva E: Lipid Metabolism in Cancer: The Role of Acylglycerolphosphate Acyltransferases (AGPATs). *Cancers* 14, 2022

177. Wang B, Tontonoz P: Phospholipid Remodeling in Physiology and Disease. *Annual review of physiology* 81: 165–188, 2019

178. Deen SS, Riemer F, McLean MA, Gill AB, Kaggie JD, Grist JT, Crawford R, Latimer J, Baldwin P, Earl HM, Parkinson CA, Smith SA, Hodgkin C, Moore E, Jimenez-Linan M, Brodie CR, Addley HC, Freeman SJ, Moyle PL, Sala E, Graves MJ, Brenton JD, Gallagher FA: Sodium MRI with 3D-cones as a measure of tumour cellularity in high grade serous ovarian cancer. *European journal of radiology open* 6: 156–162, 2019

179. Torata N, Kubo M, Miura D, Ohuchida K, Mizuuchi Y, Fujimura Y, Hayakawa E, Kai M, Oda Y, Mizumoto K, Hashizume M, Nakamura M: Visualizing Energy Charge in Breast Carcinoma Tissues by MALDI Mass-spectrometry Imaging Profiles of Low-molecular-weight Metabolites. *Anticancer research* 38: 4267–4272, 2018

180. Golpelichi F, Parastar H: Quantitative Mass Spectrometry Imaging Using Multivariate Curve Resolution and Deep Learning: A Case Study. *Journal of the American Society for Mass Spectrometry* 34: 236–244, 2023

181. Minchinton AI, Tannock IF: Drug penetration in solid tumours. *Nature reviews. Cancer* 6: 583–592, 2006

182. Meyer M, Hohenberger P, Apfaltrer P, Henzler T, Dinter DJ, Schoenberg SO, Fink C: CT-based response assessment of advanced gastrointestinal stromal tumor: dual energy CT provides a more predictive imaging biomarker of clinical benefit than RECIST or Choi criteria. *European journal of radiology* 82: 923–928, 2013

183. Giordano S, Morosi L, Veglianese P, Licandro SA, Frapolli R, Zucchetti M, Cappelletti G, Falciola L, Pifferi V, Visentin S, D'Incalci M, Davoli E: 3D Mass Spectrometry Imaging Reveals a Very Heterogeneous Drug Distribution in Tumors. *Scientific reports* 6: 37027, 2016

184. Grüner BM, Winkelmann I, Feuchtinger A, Sun N, Balluff B, Teichmann N, Herner A, Kalideris E, Steiger K, Braren R, Aichler M, Esposito I, Schmid RM, Walch A, Siveke JT: Modeling Therapy Response and Spatial Tissue Distribution of Erlotinib in Pancreatic Cancer. *Molecular cancer therapeutics* 15: 1145–1152, 2016

185. Tsubata Y, Hayashi M, Tanino R, Aikawa H, Ohuchi M, Tamura K, Fujiwara Y, Isobe T, Hamada A: Evaluation of the heterogeneous tissue distribution of erlotinib in lung cancer using matrix-assisted laser desorption ionization mass spectrometry imaging. *Scientific reports* 7: 12622, 2017

186. Vandergrift GW, Lukowski JK, Taylor MJ, Zemaitis KJ, Alexandrov T, Eder JG, Olson HM, Kyle JE, Anderton C: Are Phosphatidic Acids Ubiquitous in Mammalian Tissues or Overemphasized in Mass Spectrometry Imaging Applications? *Analysis & Sensing* , 2023

187. van Nuffel S, Elie N, Yang E, Nouet J, Touboul D, Chaurand P, Brunelle A: Insights into the MALDI Process after Matrix Deposition by Sublimation Using 3D ToF-SIMS Imaging. *Analytical chemistry* 90: 1907–1914, 2018

Appendix

8.1 Supplementary Figures
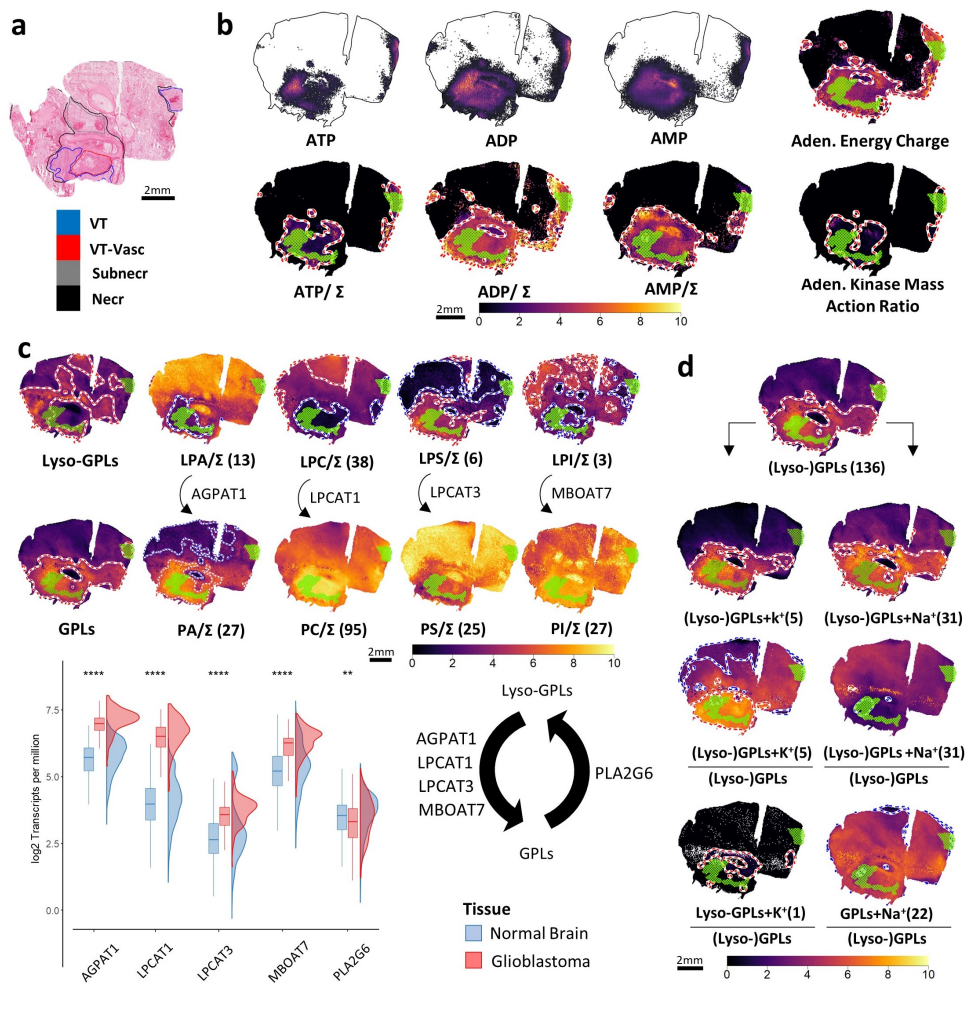
FIGURE 8.1: CPPMs of a technical replicate of the Glioblastoma (GB) tissue section showcased in **Figure 4.11**. **a)** H&E-stained image of the tissue section highlighting different GBM anatomical regions (VT: vital tumor; VT-Vasc: vital tumor with high vascularization; Subnecr: areas of pre-necrotic tissue; Necr: necrotic tissue). **b)** CPPMs enable basic arithmetic operations on SPPs. Green mesh indicates co-registered vital tumor regions. SPPs of $[ATP-H]^-$, $[ADP-H]^-$ and $[AMP-H]^-$ (FDR $\leq$ 0.2; upper row) and their sum-normalized CPPMs (bottom row; $\Sigma = [ATP-H]^- + [ADP-H]^- + [AMP-H]^-$). CPPMs also enable complex spatial quantitative scores such as adenylate energy charge $(([ATP-H]^- + 0.5 * [ADP-H]^-)/([ATP-H]^- + [ADP-H]^- + [AMP-H]^-)$; top right) and adenylate kinase mass action ratio $([ATP-H]^- * [AMP-H]^-/([ADP-H]^-)^2$; bottom right). **c)** CPPMs enable spatial investigation of glycerophospholipid remodeling (Lands' cycle) in GB by visualizing structurally similar lipids (FDR $\leq$ 0.5) within the same image space. Upper panel: CPPMs of all Lyso-GPLs compared to all GPLs (leftmost column). Lyso- and non-lyso-GPL pairs are normalized to their sum (ex. for LPC and PC, Σ represents the sum of all LPC and PC lipids). Lower panel is identical to the one shown in **Figure 4.11c**, replicated here for convenience. **d)** Analysis of the tissue's alkali ion milieu. Note that (Lyso-)GPLs refers to Lyso-GPLs plus GPLs. Numbers in parenthesis = METASPACE-verified[147] lipids (FDR $\leq$ 0.2). left column: CPPMs of all detected potassium adducts of (Lyso-)GPLs (PC, LPC, PE, LPE, PS, LPS, PI, LPI), CPPMs of all detected potassium adducts of (Lyso-)GPLs relative to the overall sum of all (Lyso-)GPL adducts and CPPMs of all detected potassium adducts of Lyso-GPLs relative to the overall sum of all (Lyso-)GPL adducts. right column: CPPMs of all detected sodium adducts of (Lyso-)GPLs, CPPMs of all detected sodium adducts of (Lyso-)GPLs relative to the overall sum of all (Lyso-)GPL adducts and CPPMs of all detected sodium adducts of GPLs relative to the overall sum of all (Lyso-)GPL adducts. Figure was adapted from Abu Sammour et al.[142] with permission from Springer Nature. Part **c** (lower panel) was contributed by A. Sadik.
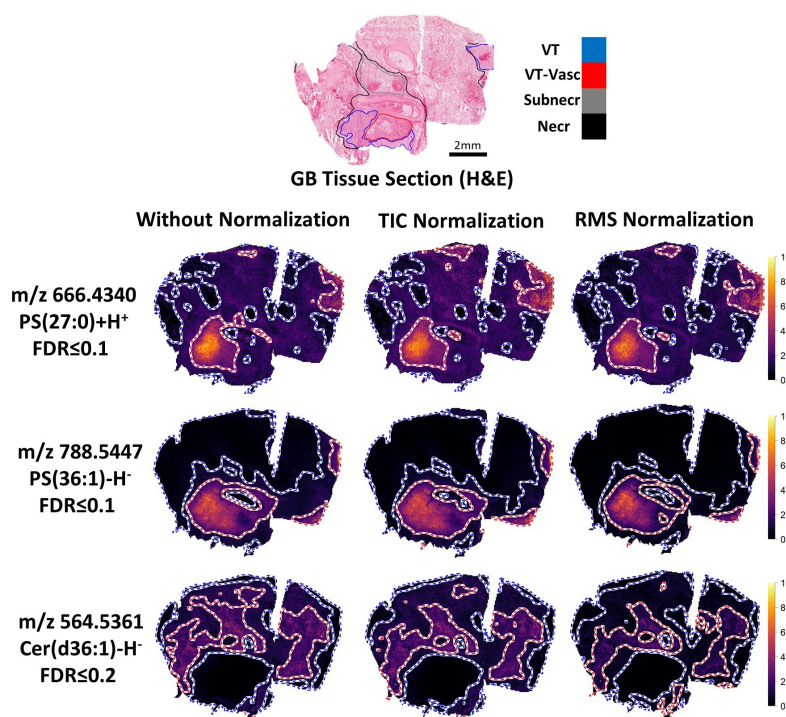
FIGURE 8.2: Comparison of the resulting molecular probabilistic maps (MPMs) of three exemplary lipids shown on a IDH-WT Glioblastoma (GB) serial tissue section measured with MALDI-FTICR-MSI based on raw data (without intensity normalization), total-ion-count (TIC) normalization and root mean squared (RMS) normalization. MPM hotspot and coldspot contours show good agreement irrespective of the normalization type or the lack thereof as also shown for the serial section of **Figure 4.25**. Figure was adapted from Abu Sammour et al.[142] with permission from Springer Nature.
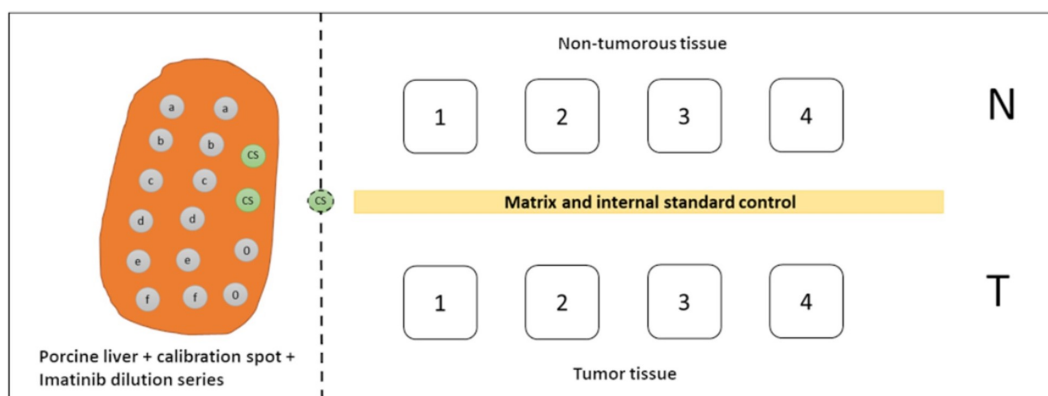
FIGURE 8.3: Layout of the sample slide used for MALDI-TOF-MSI and MALDI-FTICR-MSI quantification of imatinib in GIST. Two series of imatinib dilution spots (a = 25 pmol; b = 12.5 pmol; c = 6.25 pmol; d = 3.125 pmol; e = 1.5625 pmol; f = 0.78125 pmol; 0 = control) as well as two spots for mass calibration (CS; green) were spotted onto a porcine liver section mounted on the left side of each ITO slide. Per slide, normal tissue (N; upper row) and tumor tissue (T; lower row) of four tissue specimens were analyzed. Figure was adapted from Abu Sammour et al.[143] with permission from Springer Nature and contributed by C. Marsching.
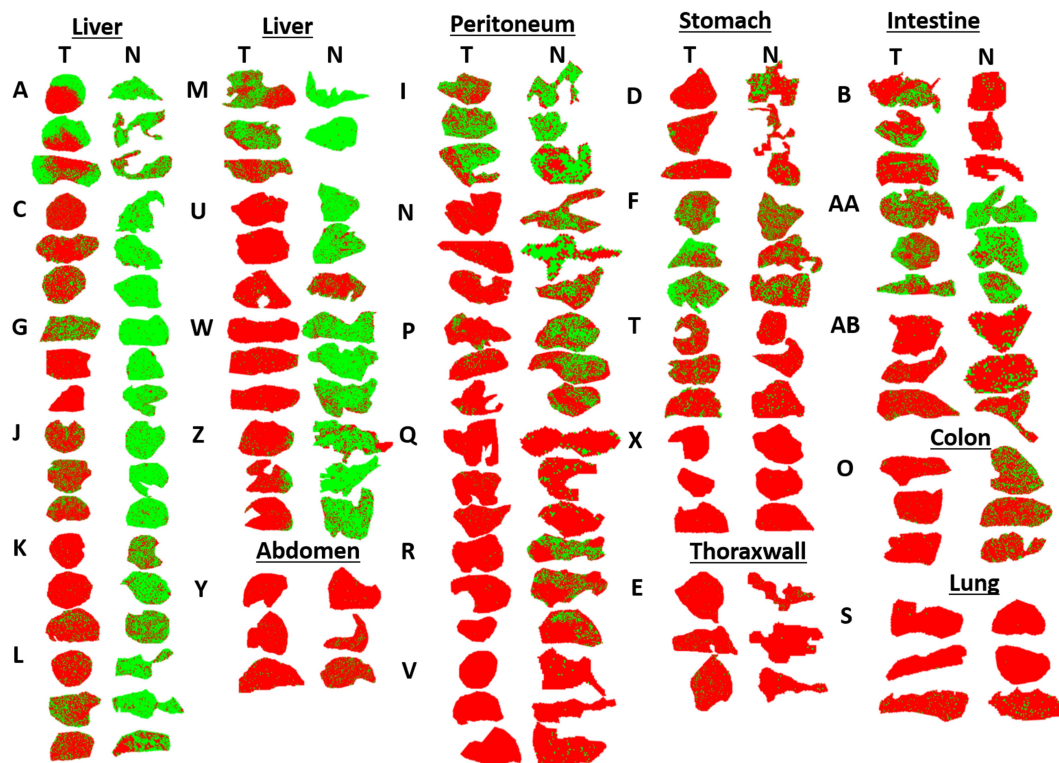
FIGURE 8.4: Imatinib detection and distribution in all tumor (T) and non-tumor (N) samples of the GIST study (not to scale). Green and red pixels indicate imatinib signal detection at SNR $\geq$ 3 and absence, respectively. Three cryosections were prepared per tissue specimen, and tissue specimens are coded by single or double letters. Tissues identified as stomach, colon or intestine are primary tumors. All others were metastases. Figure was adapted from Abu Sammour et al. [143] with permission from Springer Nature.

8.2 Supplementary Tables

TABLE 8.1: GIST patients clinical and pathological meta data as described in Abu Sammour et al.[143] Independent of therapeutic dosing, all patients received daily dosage of 400-800 mg imatinib until the day of surgery (n.i. = not identified; HPF = high power field). Table was adapted from Abu Sammour et al.[143] with permission from Springer Nature

Organ (ID)	Metastasis (m) or primary tumor (p)	Sex (f/m)	Age at surgery	Imatinib regime (months at that dose) (mg/day)	Mutations		mitosisactivity
					C-Kit	PDGFRA	
Liver (A)	m	f	44	91 / 400	Ex9;11;13;17	Ex18	50/50 HPF
Liver (C)	m	m	56	15/11/62 / 400/600/800	Ex17	—	n.i.
Liver (G)	m	f	47	17 / 800	Ex9;11;13;17	Ex18	n.i.
Liver (J)	m	m	50	82 / 800	Ex11;17	Ex18	36/50 HPF
Liver (K)	m	m	45	45 / 400	Ex11;13	—	11/10 HPF
Liver (L)	m	f	49	7/15 / 400/800	Ex11	—	1/50 HPF <7/1 HPF
Liver (M)	m	m	56	33/25 / 400/600	n.i.	n.i.	38/50 HPF
Liver (U)	m	m	62	n.i. / n.i.	Ex11	—	3/50 HPF
Liver (V)	m	f	67	31 / 400	Ex9;11;13;17	Ex12;14;18	92/50 HPF
Liver (W)	m	m	73	89 / 400	Ex9;11;13;17	Ex18	33/50 HPF
Liver (W)	m	m	73	88 / 400	—	—	33/50 HPF
Liver (Z)	m	m	49	n.i / n.i.	Ex11;13	Ex18	65/50 HPF
Peritoneum (I)	m	f	42	11 / 400	Ex11	—	12/50 HPF
Peritoneum (N)	m	m	84	72 / 400	Ex13	—	85/50 HPF
Peritoneum (P)	m	m	62	62 / 400	Ex12	—	4/50 HPF
Peritoneum (Q)	m	m	45	8 / 400	Ex11	—	147/50 HPF
Peritoneum (R)	m	m	76	36 / 400	Ex9;11;13;17	Ex18	30/50 HPF
Stomach (D)	p	f	76	10 / 400	Ex11	—	Not vital
Stomach (F)	p	m	52	6 / 400	Ex11	—	<1/50 HPF
Stomach (T)	p	m	69	13 / n.i.	—	—	90/50 HPF
Stomach (X)	p	f	87	7 / 400	Ex9;11;13;17	Ex18	10/50 HPF
Thorax wall (E)	m	m	76	26/5 / 400/800	Ex11;117	Ex12;14;18	115/50 HPF
Abdomen (Y)	p	m	43	n.i. / 400	—	Ex15	10/50 HPF
Intestine (B)	p	m	66	10 / 400	Ex13	—	5/50 HPF
Intestine (AA)	p	m	44	10 / 800	Ex9	—	4/50 HPF
Intestine (AB)	m	m	63	50 / 400	Ex9;11;117	Ex12;14;18	17/50 HPF
Lung (S)	m	m	74	28 / 400	Ex11	—	40/50 HPF
Colon (O)	p	f	80	12 / 400	Ex9;11;13;17	—	>5/50 HPF

8.3 Code Vignette

<div align="center">

moleculaR: Walkthrough

Denis Abu Sammour

2023-03-29

</div>

Introduction

The *moleculaR* R package provides a computational framework that introduces probabilistic mapping and point-for-point statistical testing of metabolites in tissue via Mass spectrometry imaging. It enables collective projections of metabolites and consequently spatially-resolved investigation of ion milieus, lipid pathways or user-defined biomolecular ensembles within the same image.

moleculaR comes pre-loaded with the SwissLipids database and with is capable of importing metabolite annotation results from the METASPACE platform to compute FDR-verified moleculaR probabilistic maps (MPMs) and collective projection probabilistic maps (CPPMs).

Installation & Loading Example Data

moleculaR can be installed via `devtools`, note that you need to set `build_vignettes=TRUE` to build this vignette during package installation. Once installed, *moleculaR* could be loaded using `library()`:

```r
# not run
install.packages("devtools")
devtools::install_github("CeMOS-Mannheim/moleculaR", build_vignettes=TRUE)


library(moleculaR)
```

Importing & Processing MSI Data

Under the hood *moleculaR* is mainly based on `MALDIquant`, `spatstat` and `Matrix` packages and provides some additional tools to help import and process any given MSI dataset. Please note that currently only *centroided* MSI data is supported. *moleculaR* expects two mandatory data inputs; a (processed) *imzML* file and an additional *tsv* file which contains a full continuous spectrum (with m/z and intensity columns) which either represents a random pixel within the imaging dataset or an average spectrum.

```r
#-- not run --#

# read MSI data
imzmlFile       <- "pathToFile.imzML"
msData          <- readCentrData(path = imzmlFile)

# single spectrum
spectrFile      <- "pathToFile.tsv"
msSpectr        <- readSingleSpect(spectrFile)
```

moleculaR also accepts one optional input which is the annotations results for the given dataset which the user could retrieve from METASPACE (https://metaspace2020.eu) provided, of course, that the same dataset has been previously uploaded there for annotation. When this input is provided, *moleculaR* takes these into

consideration to filter out detections which were not verified by METASPACE at a certain FDR specified by the user.

```
#-- not run --#

# load the metaspace annotations file
pathToMtspc     <- "pathToFile.csv"
mtspc           <- read.csv(file = pathToMtspc, skip = 2, header = TRUE,
                            colClasses = "character")
```

Finally, the SwissLipid database, which is provided with *moleculaR* ,must be loaded:

```
#-- not run --#

# load the processed swisslipids db
pathTosldb      <- system.file("extdata", "swisslipids-speciesOnly-sep2020.tsv",
                               package = "moleculaR", mustWork = TRUE)
sldb            <- loadSwissDB(pathTosldb)
```

For subsequent analysis, an S3 `fwhm` object must be created which will hold information about full width at half maximum (FWHM) as a function of m/z axis and will be used to estimate FWHM at any given m/z value (for more info see `?estimateFwhm`):

```
#-- not run --#

# estimate fwhm from msSpectr
fwhmObj         <- estimateFwhm(s = msSpectr)
```

Before applying any preprocessing methods, it is highly recommended to perform peak-binning and peak filtering on `msData`, subsequently the user may apply any preprocessing methods provided by `MALDIquant` (keeping in mind that this is a centroided dataset).

```
#-- not run --#

# bin peaks
msData          <-  MALDIquant::binPeaks(msData,
                                         #focusing on lipids:
                                         tolerance = getFwhm(fwhmObj, 400)/400,
                                         method = "relaxed")


# filter out peaks which occur in less than 1% of the time
# Note: use 'moleculaR::' namespace to distinguish it from MALDIquant::filterPeaks
# if MALDIquant is loaded.
msData          <- moleculaR::filterPeaks(x = msData, minFreq = 0.01)
```

Walkthrough - Example Data

moleculaR also comes pre-loaded with an example MALDI MSI dataset. **This dataset has been heavily reduced and filtered in order to make it available with the package. Consequently, the illustrations shown in this vignette are just to have an overview of the functionality of the different commands and might not be indicative of the molecular content of that tissue sample**. To load the example data (assuming that the package has been already loaded):

```
library(moleculaR)
```

```
data("processed-example-Data")

# to see the loaded objects
ls()
#> [1] "fwhmObj" "msData"  "mtspc"   "sldb"
```

`msData` represents a centroided MALDI MSI dataset stored as a list of `MassPeaks` objects (see `?MALDIquant::MassPeaks` for more details), `fwhmObj` is an S3 object of type `fwhm` storing the calculated full width at half maximum (FWHM) information of `msData` (see `?moleculaR::fwhm` for more details), `mtspc` is a data frame storing the associated annotations file (<0.2 FDR) which is downloaded directly from METASPACE (https://metaspace2020.eu) and `sldb` is a data frame storing the SwissLipids database filtered to only include the identifications outlined in `mtspc`.

Since *moleculaR* relies internally on spatial data, a spatial window can be created to represent the tissue boundaries:

```
spwin       <- createSpatialWindow(pixelCoords = MALDIquant::coordinates(msData),
                                   clean = TRUE,
                                   plot = TRUE)
```


Spatial Window

-
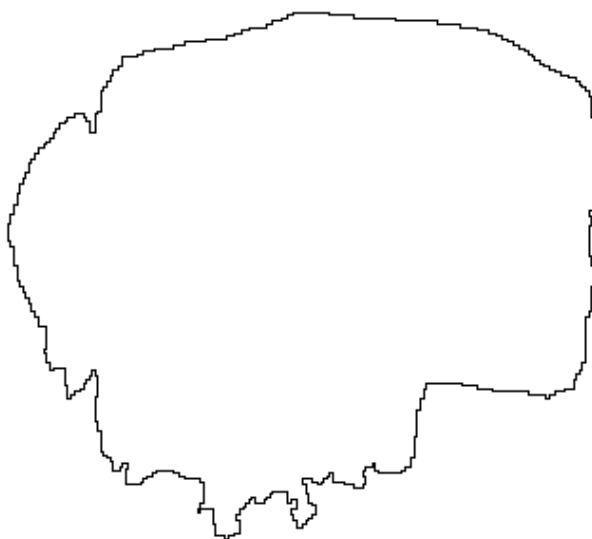
To investigate FWHM as a function of m/z axis one could simply plot `fwhmObj`:

```
plot(fwhmObj)
```

Estimated fwhm(m/z)

-
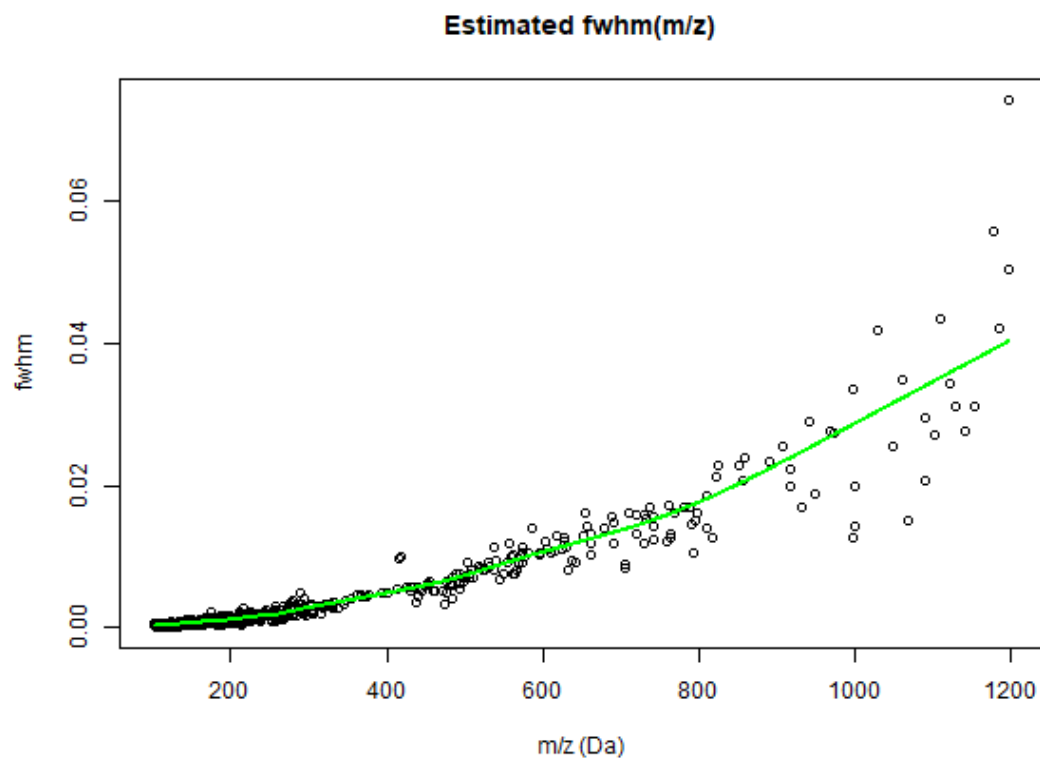
Or, to find the estimated FWHM at any given of m/z value one could simply pass `fwhmObj` to `GetFwhm` method:

```
# FWHM at m/z 400
getFwhm(fwhmObj, 400)
#> [1] 0.004822831
```

To speed up downstream analysis, *moleculaR* relies on a sparse matrix representation of the MSI data. To this end, `msData` has to be first converted to an S3 object of type `moleculaR::sparseIntensityMatrix`:

```
#// create sparse matrix representation
spData <- createSparseMat(x = msData)
```

Molecular Probabilistic Maps (MPMs)

moleculaR introduces the idea of molecular probabilistic maps (MPMs) the main goal of which is to reduce the reliance on user's subjective opinion on the extent of spatial distribution of analytes within a given tissue section. Instead MPMs provide a user-independent statistical testing on the likelihood that a certain spatial intensity distribution has a significant relative abundance (i.e. analyte hotspot) or deficiency (i.e. analyte coldspot) within the tissue space. To illustrate this, consider as an example a peak-of-interest (POI) of 788.5447 m/z.

```
# input by m/z value
queryMass        <- 788.5447
```

moleculaR provides `searchAnalyte` method to retrieve intensity values at a specific m/z with a mass-window dictated by the estimated FWHM at that same m/z value (see `?moleculaR::searchAnalyte` for more info). Moreover, `searchAnalyte` gives the user the possibility to choose which weighting method to choose, for example, setting the argument `wMethod="sum"` will generate the so called "ion image" as all peaks appearing within the estimated mass-window will be summed up (i.e. uniform mass-window weighting):

```
# compute the regular ion image - returns an AnalytePiontPattern
sppIonImage        <- searchAnalyte(m = queryMass,
                                    fwhm = getFwhm(fwhmObj, queryMass),
                                    spData = spData,
                                    spwin = spwin,
                                    wMethod = "sum")


# compute a raster image of the sppIonImage
ionImage           <- spp2im(sppIonImage)

# plot ion image
plotImg(ionImage)
```
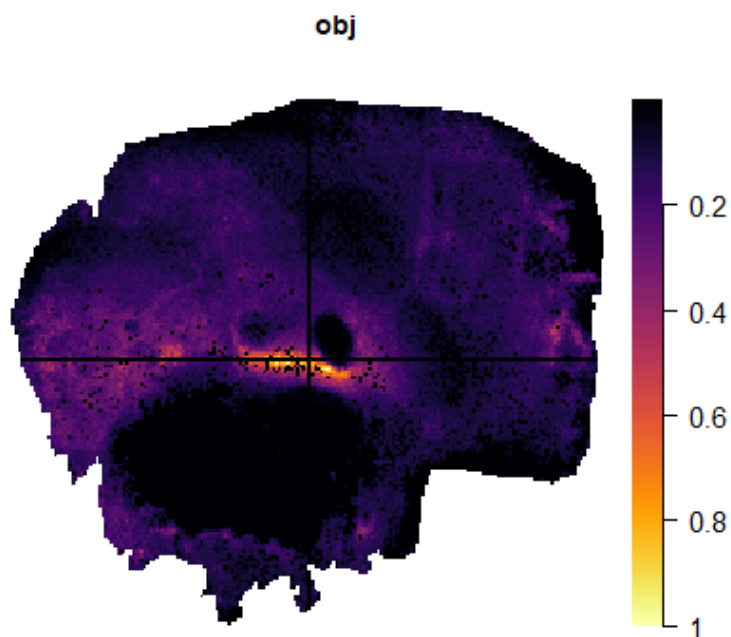

Now to compute a FWHM-dependent Gaussian weighted analyte point pattern representation, set `wMethod="Gaussian"`:

```
# compute spatial point pattern of the analyte
sppMoi          <- searchAnalyte(m = queryMass,
                                 fwhm = getFwhm(fwhmObj, queryMass),
                                 spData = spData,
                                 spwin = spwin,
                                 wMethod = "Gaussian")

# plot SPP
plotAnalyte(sppMoi, main = paste0("SPP of m/z ", round(queryMass, 4)))
```



```
-
```
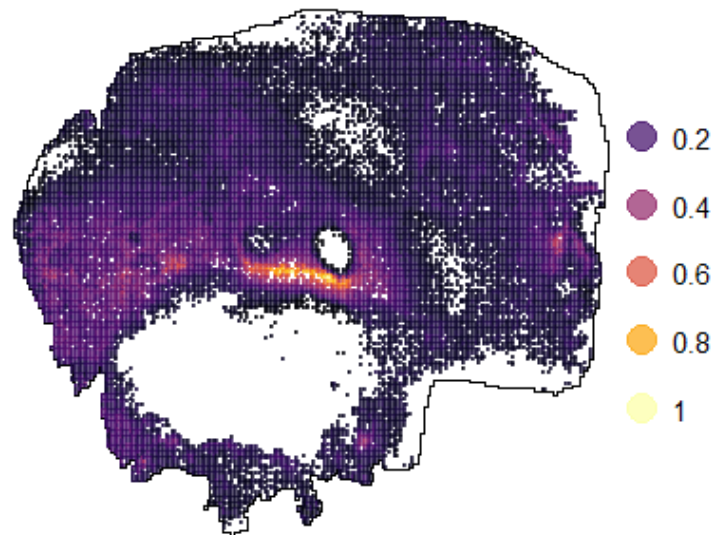
```
# plot the corresponding raster image
plotImg(spp2im(sppMoi), main = paste0("Raster image of m/z ", round(queryMass, 4)))
```

Raster image of m/z 788.5447

-
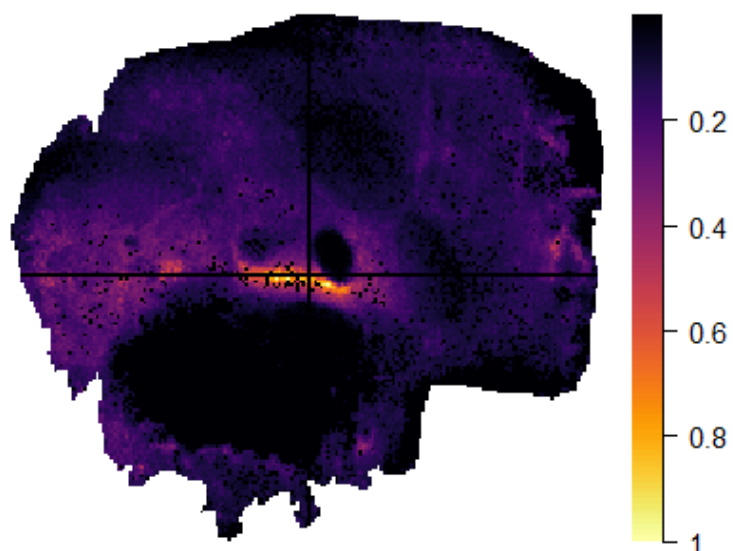
The `probMap` could then be called with the default parameters to calculate the corresponding MPM of the above POI (see `?probMap` for details) and the generic `plot` could be used on the result to plot a composite detailed illustration (see `?plot.molProbMap` for details):

```r
#// compute MPM - default parameters
probImg          <- probMap(sppMoi)


#// plot everything together
par(cex.lab = 2, cex.main = 2, cex.axis = 1.5)
plot(probImg, what = "detailed",  ionImage = ionImage)
```

m/z 788.5447

m/z 788.5447

$\rho_{CSR}(x,y)$

$\rho_{MOI}(x,y)$

m/z 788.5447 MPM

Corresponding Ion Image
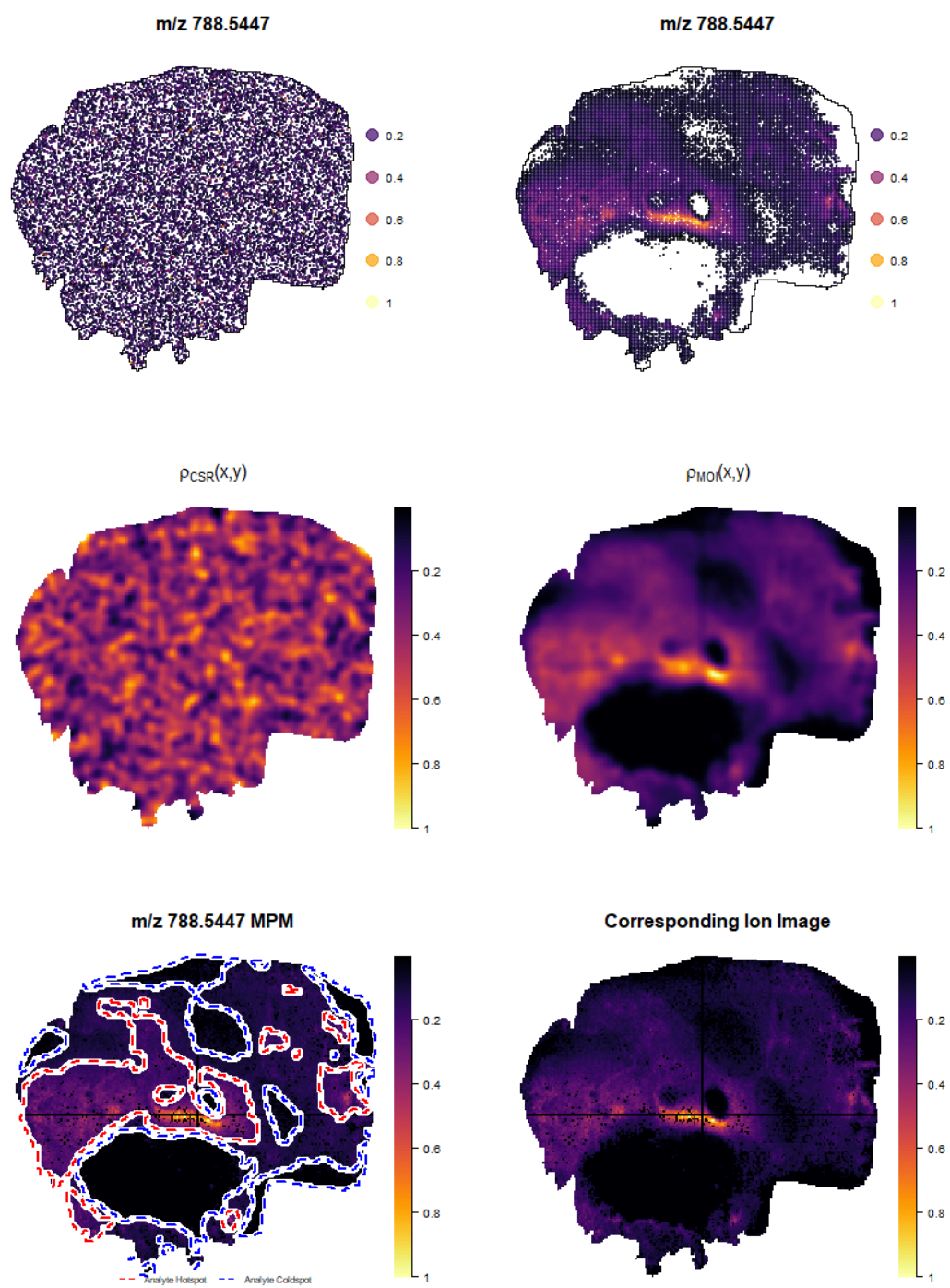
Collective Projections Probabilistic Maps (CPPMs)

Another concept introduced by *moleculaR* is the collective projections probabilistic maps (CPPMs) which, as the name implies, provides a framework for visualization of a set of analytes collectively in a single image space. This could be of interest when, for example, a user is interested in visualization a set of analytes with a certain similarity (structure, functionality, etc.).

CPPMs - Lipid Classes

As *moleculaR* is lipidome-focused in this example, the test MSI dataset is screened against the internal instance of the SwissLipids database and is optionally verified by an externally provided lipidome annotation file downloaded from METASPACE for the given MSI dataset (pre-loaded for the current example). The `batchLipidSearch` method then is used to do this screening (for more details see `?batchLipidSearch`):

```
cat("Batch lipid search is ongoing - this will take several minutes - \n")


lipidHits <- batchLipidSearch(spData = spData, fwhmObj = fwhmObj, sldb = sldb,
                                spwin = spwin,
                                 adduct = c("M+H", "M+Na", "M+K"),
                                 numCores = 4,
                                 verifiedMasses = as.numeric(mtspc$mz),
                                 confirmedOnly = TRUE, verbose = TRUE)


lipidHits
```

The results is an S3 object of type `spatstat::ppp` and `moleculaR::analytePointPattern` which contains all lipid identifications (against SwissLipids database) according to the provided `mtspc` annotation file. The metaData of the detected analytes are found in the `metaData` slot:

```
# show metaData
head(lipidHits$metaData)
#>            idx   mzVals mzConfirmed  mode    adduct lipidID      sumformula abbrev    ...
#> M+H   1659378808 327.1567   TRUE    positive   M+H  SLM:000055220  C13H25O7P  LPA(10:0) ...
#> M+H1  1659179733 299.1254   TRUE    positive   M+H  SLM:000055283  C11H21O7P  LPA(8:0)  ...
#> M+H2  1659302815 496.3398   TRUE    positive   M+H  SLM:000055318  C24H50NO7P LPC(16:0) ...
#> M+Na  1659222965 518.3217   TRUE    positive   M+Na SLM:000055318  C24H50NO7P LPC(16:0) ...
#> M+H3  1659375015 494.3241   TRUE    positive   M+H  SLM:000055319  C24H48NO7P LPC(16:1) ...
#> M+H4  1659320885 524.3711   TRUE    positive   M+H  SLM:000055322  C26H54NO7P LPC(18:0) ...
```

To list all lipid classes which were detected (and confirmed by METASPACE; if `confirmedOnly=TRUE`):

```
# Show all detected lipid classes
unique(lipidHits$metaData$lipidClass)
#>  [1] "LPA(x:x)" "LPC(x:x)" "LPC(O-x:x)" "LPE(x:x)" "LPS(x:x)" "PA(x:x)" "PA(O-x:x)"
#>  [8] "PC(x:x)" "PC(O-x:x)" "PE(x:x)" "PE(O-x:x)" "PG(x:x)" "PS(x:x)" "PS(O-x:x)"
#> [15] "TG(x:x)" "HexCer(tx:x)" "HexCer(dx:x)" "Hex2Cer(dx:x)" "SM(dx:x)" "PE-Cer(dx:x)"
#> "PGP(x:x)"
#> [22] "BMP(x:x) | LBPA" "SE(x:x)"   "PG(O-x:x)" "Cer(tx:x)" "TG(O-x:x)" "LPG(O-x:x)"
```

To generate class-specific lipid maps, `subsetAnalytes` could be used to filter `lipidHits` according to lipid classes. Note that `subsetAnalytes` subsetting is always based on the column names of `lipidHits$metaData`. Afterwards one could directly apply `probMap` method and produce a CPPM for all hit instances for a given lipid class. Note that for CPPMs it is highly recommended to apply z-score transformation to account for differences in ionization efficiency of the MOIs constituting the CPPM:

```r
# z-score transformation
lipidHits <- transformIntensity(lipidHits, method = "z-score")

# choose one lipid species
lipidClass <- "PA(x:x)"

# subset lipidHits
paHits <- subsetAnalytes(lipidHits, lipidClass == "PA(x:x)")


# compute MPM - default parameters
probImg    <- probMap(paHits)


#// plot everything together
par(cex.lab = 2, cex.main = 2, cex.axis = 1.5)
plot(probImg, what = "detailed")
```
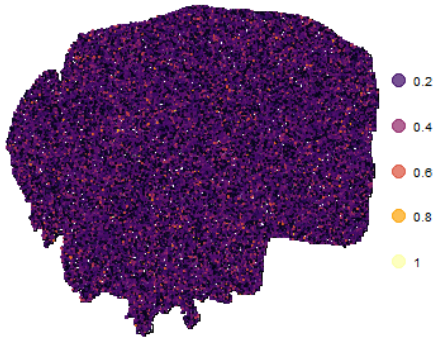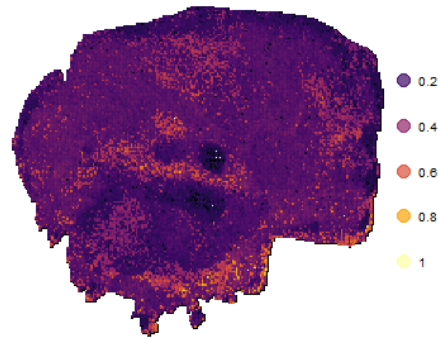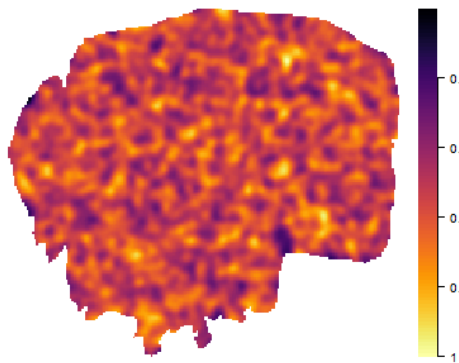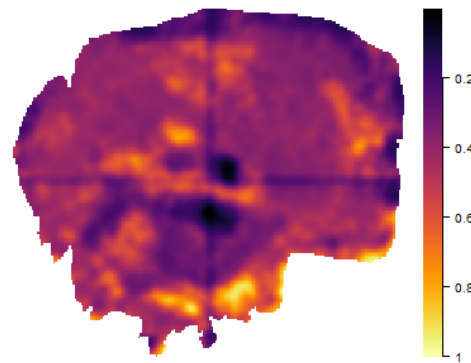
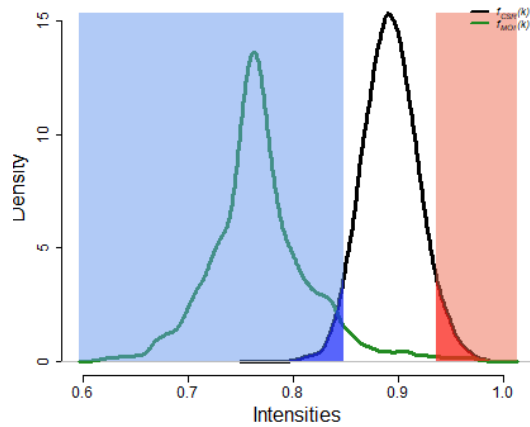**Collective SPP of 3 m/z Values**

Collective SPP of 3 m/z Values

$\rho_{CSR}(x,y)$

$\rho_{MOI}(x,y)$

$f_{CSR}(k)$ and $f_{MOI}(k)$ at bw $= 2.2$

CPPM of 3 m/z Values
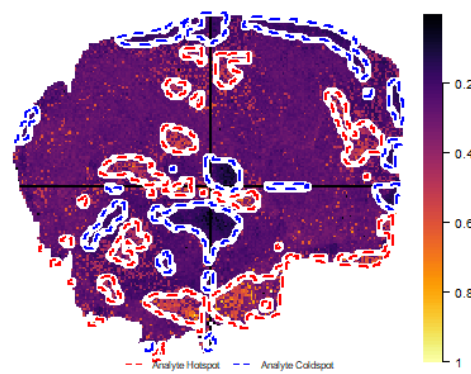
CPPMs - Ion Milieus

Same as with lipid class maps, one could create representations of a custom set of analytes. Suppose that ion milieus distribution of all (lyso)glycerophospholipids '(lyso)GPLs' which are the mian constituent of biological membraes. One could first subset `lipidHits` to include PA, PS, PE, PC, PI, PG, LPA, LPS, LPE, LPC, LPI, and LPG:

```
# create a subset representing lysoGPLs
ofInterest <- c("LPA(x:x)", "LPC(x:x)", "LPE(x:x)", "LPG(x:x)","LPI(x:x)", "LPS(x:x)",
                "PA(x:x)", "PC(x:x)", "PE(x:x)","PG(x:x)", "PI(x:x)", "PS(x:x)")
# subset lipidHits
lysoGPLs <- subsetAnalytes(lipidHits, lipidClass %in% ofInterest)
lysoGPLs
#> Marked planar point pattern: 5794229 points
#> Mark variables: idx, intensity
#> window: polygonal boundary
#> enclosing rectangle: [108.45, 305.55] x [139.45, 314.55] units

# detected classes
cat("detected lipid classes: \n")
#> detected lipid classes:
unique(lysoGPLs$metaData$lipidClass)
#> [1] "LPA(x:x)" "LPC(x:x)" "LPE(x:x)" "LPS(x:x)" "PA(x:x)"  "PC(x:x)"
#> [7] "PE(x:x)"  "PG(x:x)"  "PS(x:x)"
```

Then one could further use `subsetAnalytes` to subset `lysoGPLs` according to any analyte characterestic of the `metaData` table i.e.

```
# meta data table columns
colnames(lysoGPLs$metaData)
#>  [1] "idx" "mzVals" "mzConfirmed" "mode" "adduct" "lipidID" "sumformula" "abbrev"
#>  [9] "numDoubleBonds" "lipidClass" "chainLength"
```

To this end, one could visualize for example all [M+K]+ adducts of detected (lyso)GPLs:

```
# detected adducts
cat("detected adducts: ")
#> detected adducts:
table(lysoGPLs$metaData$adduct)
#>
#>  M+H  M+K  M+Na
#>  134   26   99
# subsetting
kHits          <- subsetAnalytes(lysoGPLs, adduct == "M+K")
# or NHits      <- subsetAnalytes(lysoGPLs, adduct == "M+Na")
# or HHits      <- subsetAnalytes(lysoGPLs, adduct == "M+H")
```

To apply CPPMs and plot the result for [M+K]+:

```
# compute CPPM
probImg    = probMap(kHits)

par(cex.lab = 2, cex.main = 2, cex.axis = 1.5)
plot(probImg, what = "detailed")
```
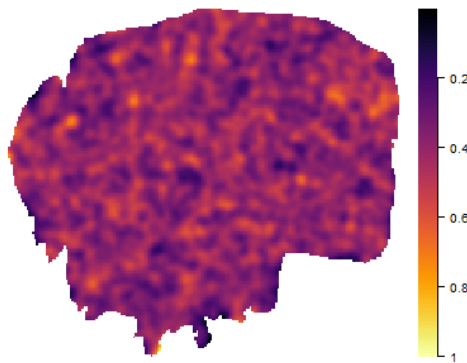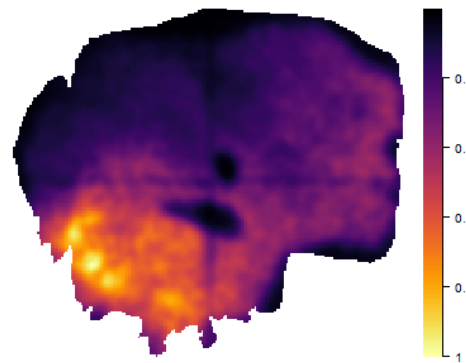
Collective SPP of 26 m/z Values
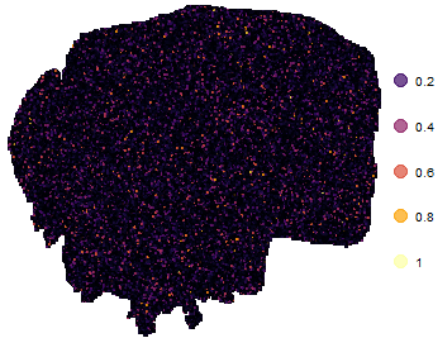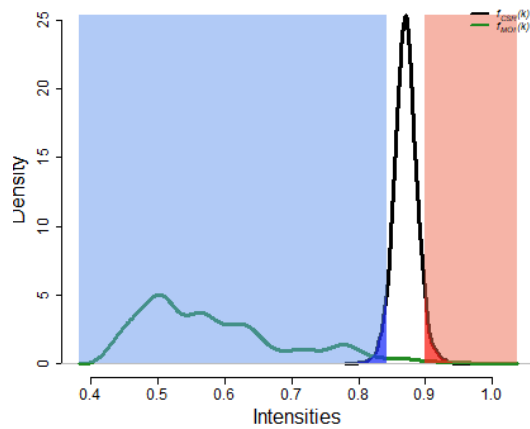
Collective SPP of 26 m/z Values
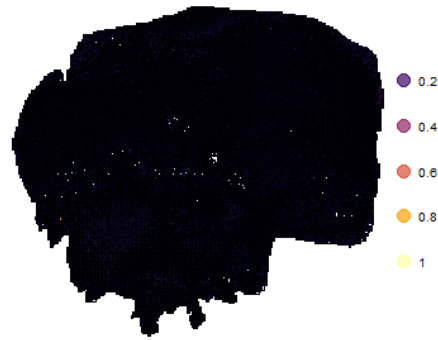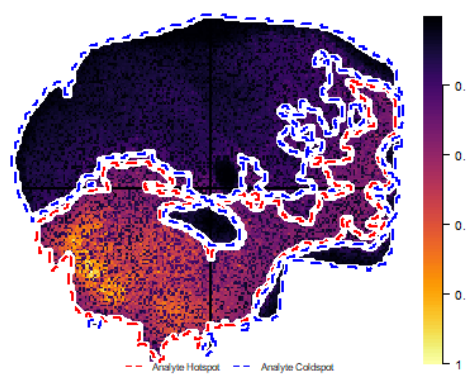
$\rho_{CSR}(x,y)$

$\rho_{MOI}(x,y)$

$f_{CSR}(k)$ and $f_{MOI}(k)$ at bw = 2.2

CPPM of 26 m/z Values

CPPMs - Lipid Saturation

The same technique could applied to investigate lyso(GPLs) saturation (saturated, mono-unsaturated, di-unsaturated and poly-unsaturated) within one image space by subsetting based on the number of double-bonds of the lipid fatty acid chain.

```r
detectedSaturation <- c("sat", "mono-unsat", "di-unsat", "poly-unsat")


# subsetting
satHits            <- subsetAnalytes(lysoGPLs, numDoubleBonds == 0)
# or monoHits       <- subsetAnalytes(lysoGPLs, numDoubleBonds == 1)
# or diHits         <- subsetAnalytes(lysoGPLs, numDoubleBonds == 2)
# or polyHits       <- subsetAnalytes(lysoGPLs, numDoubleBonds > 2)
```

input for the specific saturation

```r
# compute CPPM
probImg    = probMap(satHits)
#> Attempting to generate 1408331 random points

par(cex.lab = 2, cex.main = 2, cex.axis = 1.5)
plot(probImg, what = "detailed")
```
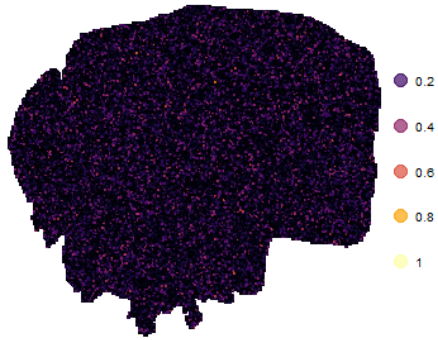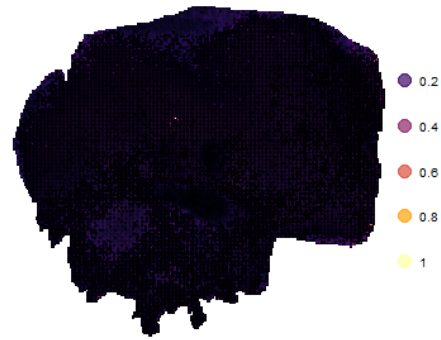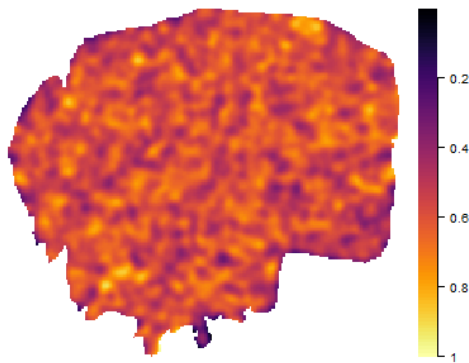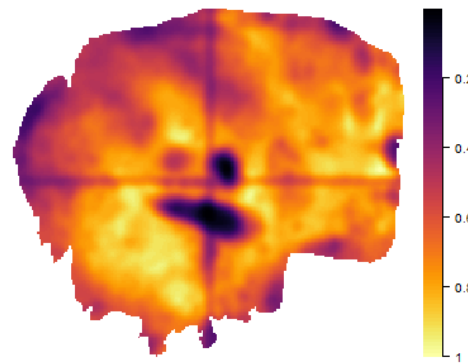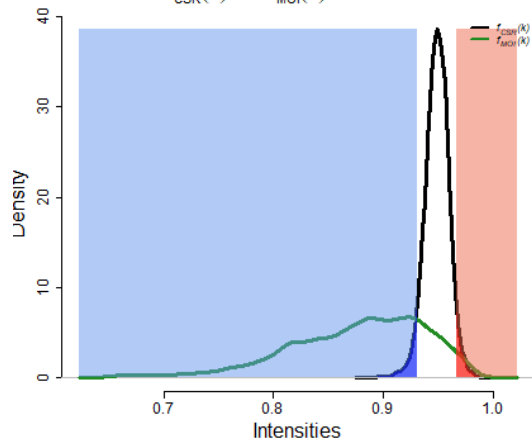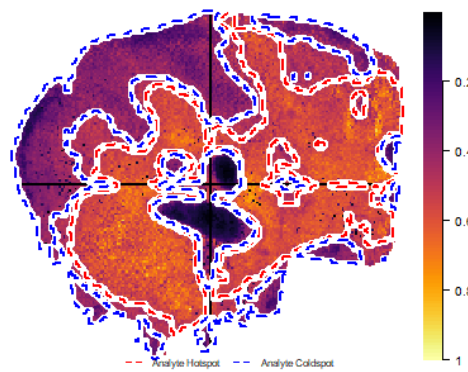
Session Information

```
sessionInfo()
#> R version 4.0.2 (2020-06-22)
#> Platform: x86_64-w64-mingw32/x64 (64-bit)
#> Running under: Windows 10 x64 (build 19044)
#>
#> Matrix products: default
#>
#> locale:
#> [1] LC_COLLATE=English_Germany.65001  LC_CTYPE=English_Germany.1252
#> LC_MONETARY=English_Germany.65001 LC_NUMERIC=C
#> [5] LC_TIME=English_Germany.65001
#> system code page: 65001
#>
#> attached base packages:
#> [1] stats     graphics  grDevices datasets  utils     methods   base
#>
#> other attached packages:
#> [1] moleculaR_0.9.0
#>
#> loaded via a namespace (and not attached):
#>  [1] terra_1.4-11         xfun_0.28            splines_4.0.2        lattice_0.20-45
#>  colorspace_2.0-2     spatstat.utils_2.2-0
#>  [7] vctrs_0.3.8          testthat_3.1.0       htmltools_0.5.2      viridisLite_0.4.0
#>  mgcv_1.8-38          utf8_1.2.2
#> [13] rlang_0.4.12         spatstat.data_2.1-0  pillar_1.6.4         glue_1.5.0
#> withr_2.4.2          sp_1.4-5
#> [19] lifecycle_1.0.1      stringr_1.4.0        spatstat.core_2.3-0  munsell_0.5.0
#> gtable_0.3.0         raster_3.5-2
#> [25] codetools_0.2-16     evaluate_0.14        knitr_1.36           fastmap_1.1.0
#> import_1.2.0         parallel_4.0.2
#> [31] fansi_0.5.0          highr_0.9            Rcpp_1.0.7           tensor_1.5
#> renv_0.13.0          scales_1.1.1
#> [37] desc_1.4.0           pkgload_1.2.3        abind_1.4-5          deldir_1.0-6
#> gridExtra_2.3        ggplot2_3.3.5
#> [43] digest_0.6.28        stringi_1.7.5        spatstat.sparse_2.0-0 polyclip_1.10-0
#> grid_4.0.2           rprojroot_2.0.2
#> [49] cli_3.1.0            tools_4.0.2          magrittr_2.0.1       goftest_1.2-3
#> tibble_3.1.6        crayon_1.4.2
#> [55] pkgconfig_2.0.3      ellipsis_0.3.2       Matrix_1.3-4         viridis_0.6.2
#> rpart_4.1-15        R6_2.5.1
#> [61] MALDIquant_1.20      spatstat.geom_2.3-0  nlme_3.1-153         compiler_4.0.2
```

Publications

Abu Sammour D, Cairns JL, Boskamp T, Marsching C, Kessler T, Ramallo Guevara C, Panitz V, Sadik A, Cordes J, Schmidt S, Mohammed SA, Rittel MF, Friedrich M, Platten M, Wolf I, von Deimling A, Opitz CA, Wick W, Hopf C: Spatial probabilistic mapping of metabolite ensembles in mass spectrometry imaging. *Nature communications* 14: 1823, 2023 **

Friedrich M, Sankowski R, Bunse L, Kilian M, Green E, Ramallo Guevara C, Pusch S, Poschet G, Sanghvi K, Hahn M, Bunse T, Münch P, Gegner HM, Sonner JK, von Landenberg A, Cichon F, Aslan K, Trobisch T, Schirmer L, **Abu Sammour D**, Kessler T, Ratliff M, Schrimpf D, Sahm F, Hopf C, Heiland DH, Schnell O, Beck J, Böttcher C, Fernandez-Zapata C, Priller J, Heiland S, Gutcher I, Quintana FJ, von Deimling A, Wick W, Prinz M, Platten M: Tryptophan metabolism drives dynamic immunosuppressive myeloid states in IDH-mutant gliomas. *Nature cancer* 2: 723–740, 2021

Abu Sammour D*, Marsching C*, Geisel A, Erich K, Schulz S, Ramallo Guevara C, Rabe JH, Marx A, Findeisen P, Hohenberger P, Hopf C: Quantitative Mass Spectrometry Imaging Reveals Mutation Status-independent Lack of Imatinib in Liver Metastases of Gastrointestinal Stromal Tumors. *Scientific reports* 9: 10698, 2019 **

Erich K, Reinle K, Müller T, Munteanu B, **Abu Sammour D**, Hinsenkamp I, Gutting T, Burgermeister E, Findeisen P, Ebert MP, Krijgsveld J, Hopf C: Spatial Distribution of Endogenous Tissue Protease Activity in Gastric Carcinoma Mapped by MALDI Mass Spectrometry Imaging. *Molecular & cellular proteomics : MCP* 18: 151–161, 2019

Weigt D, **Abu Sammour D**, Ulrich T, Munteanu B, Hopf C: Automated analysis of lipid drug-response markers by combined fast and high-resolution whole cell MALDI mass spectrometry biotyping. *Scientific reports* 8: 11260, 2018

Rabe JH, **Abu Sammour D**, Schulz S, Munteanu B, Ott M, Ochs K, Hohenberger P, Marx A, Platten M, Opitz CA, Ory DS, Hopf C: Fourier Transform Infrared Microscopy Enables Guidance of Automated Mass Spectrometry Imaging to Predefined Tissue Morphologies. *Scientific reports* 8: 313, 2018

Erich K*, **Abu Sammour D***, Marx A, Hopf C: Scores for standardization of on-tissue digestion of formalin-fixed paraffin-embedded tissue in MALDI-MS imaging. *Biochimica et biophysica acta*. Proteins and proteomics 1865: 907–915, 2017

Fülöp A, **Abu Sammour D**, Erich K, von Gerichten J, van Hoogevest P, Sandhoff R, Hopf C: Molecular imaging of brain localization of liposomes in mice using MALDI mass spectrometry. *Scientific reports* 6: 33791, 2016

**This dissertation.
*Equal contribution.

Curriculum Vitae

PERSONAL DATA

NAME:	Denis Abu Sammour
PLACE AND DATE OF BIRTH:	Rostov, Russia | 19.10.1987
FAMILY STATUS:	Married, two children

EDUCATION

10/2015 – Present	**Doctoral Candidate**
	Medical Faculty Mannheim, Heidelberg University, Mannheim, Germany
	Supervised by Prof. Dr. Carsten Hopf at the Center for Mass Spectrometry and Optical Spectroscopy (CeMOS), Mannheim, Germany
09/2013 – 09/2015	**Master of Science in Biomedical Engineering**
	Medical Faculty Mannheim, Heidelberg University, Germany
	Accumulated Grade: 1.6 (German Grading System)
09/2005 – 06/2010	**Bachelor of Science in Biomedical Engineering**
	Jordan University of Science and Technology, Jordan
	Accumulated Grade: 83.1%
07.2005	**General Secondary Education Certificate Examination, Jordan**
	Accumulated Grade: 90.1%

WORK EXPERIENCE

01/2018 – Present	**Team leader – Bioinformatics**
	Center for Mass Spectrometry and Optical Spectroscopy (CeMOS), Mannheim University of Applied Science, Mannheim, Germany
10/2015 – 12/2017	**Research Assistant - Bioinformatics**
	Center for Mass Spectrometry and Optical Spectroscopy (CeMOS), Mannheim University of Applied Science, Mannheim, Germany
08/2015 – 10/2015	**Project Assistant**
	Fraunhofer Institute, PAMB, Mannheim, Germany
09/2010 – 08/2013	**Medical Field Service Engineer and Application Specialist**
	Salbashian Group/Medical Division, Amman, Jordan
07/2009 – 09/2009	**Intern**
	Arab Medical and Scientific Alliance, Amman, Jordan

Acknowledgements

"If we knew what it was we were doing, it would not be called research, would it?"

– Albert Einstein

The last two pages of this dissertation and a culmination of years of hard work. Only few know how much effort it took to reach this point. I am glad I have made it this far. Looking back over the past years, I can't help but notice how privileged I have been to land into such a vibrant, diverse and multidisciplinary scientific community and to be surrounded by friendly, genuine and professional people, who contributed to my personal and professional growth and have been instrumental to the conclusion of this dissertation. I would like to take the opportunity to thank everyone who helped and supported me along the way and made this journey worthwhile.

First and foremost, I would like to express my sincere gratitude and appreciation to my supervisor and mentor Prof. Dr. Carsten Hopf, who offered me this opportunity to pursue my doctoral studies in the field of bioinformatics and computational science, a subject that I have grown to greatly love and enjoy. Through the years, he has relentlessly supported me, academically and personally, and has always been available for every question, hurdle and discussion, despite his extremely-packed schedules and even at the expense of his own personal time. He has been a reliable source of motivation, encouragement and guidance at every step of this journey. Working under his supervision and leadership has been a privilege.

I would also like to extend my gratitude to Prof. Dr. Ivo Wolf and Dr. Tobias Boskamp, both of whom have provided considerable guidance and support and have contributed greatly to my academic growth through countless discussions and interactions. I would also like to thank Natascha Heß-Mohr, Prof. Dr. Matthias Rädle, Prof. Dr. Julian Reichwald, Prof. Dr. Oliver Wasenmüller and Prof. Dr. Rüdiger Rudolf for creating such a vibrant research environment at CeMOS.

*"I wish there was a way to know you're in "the good old days",
before you've actually left them."*

– Andy Bernard (The Office)

I have been certainly lucky to land into a great team of friendly, helpful and professional individuals, many of whom have moved on to work in other places. My sincere gratitude goes to my colleagues, who became my dearest friends, Dr. Christian Marsching, Dr. Sandra Schulz, Dr. Katrin Erich, Dr. Carina Ramallo Guevara, Dr. Annabelle Füllöp, Matthias Schwartz, Dr. Qiuqin Zhou and Dr. Bogdan Munteanu for all the unforgettable times spent together in projects, discussions, "Kaffee und Kuchen" breaks, conferences, retreats but also traveling, picnics, gatherings, parties and complaining about work! Being part of such a group made this journey a lot more enjoyable and worthwhile and made my stay in Germany feel more like home.

I would like to thank all my past and current colleagues at CeMOS and elsewhere, Dr. David Weigt, Dr. Melissa Unger, Dr. Jan-Hinrich Rabe, Alexander Geisel, Dr. Thomas Enzlein, Jonas Cordes, James L. Cairns, Dr. Stefan Schmidt, Dr. Alexandra Iakab, Tobias Bausbacher, Miriam Rittel, Ralf Müller, Christian Croissant, Dr. Björn Fröhlich, Dr. Florian Richter, Livia Borggrefe and Dr. Yasemin Ucal for all their help and support throughout the years which made this journey a great learning experience. Special thanks to my colleague Shad A. Mohammed, who, being my only office-mate, has tolerated my complaining and stress in the last portion of my journey towards finishing this dissertation!

I would like to extend my thanks to my dear childhood friend Raji Sabbah, who, throughout all these years, never fails to call and reach out despite the great distances. Thanks also to my friend Talal Halilah, with whom I shared so many good times across countries. Finally, I would also like to thank my good old friends Anas Al-Qut, Ahmad Qadi, Musa Smadi, Ameen Snobar and Bilal Zaghloul who long ago encouraged me to pursue this academic path.

> *"As long as we are together; it doesn't matter to me."*
>
> – Marty (Madagascar)

As I usually tend to save the best for last, here I would like to express my deepest gratitude and appreciation to my wife Mariam, to whom this work in its entirety is dedicated. As I struggle to find words that could describe her contribution, I can only say she is the primary reason all this has worked out. Thank *you* Mariam for being there for me and for our daughters. Speaking of whom, I would also like to thank my two little daughters Sophia and Layla, who have given me a valuable lesson on where my priorities in life are. I would also like to thank my parents, Tamara and Ismail, my sister Asia and my parents-in-law, Elena and Nabil who always cheered for and supported me in every step.